



HAL
open science

Etude des mécanismes de vieillissement des batteries Li-ion en cyclage à basse température et en stockage à haute température : compréhension des origines et modélisation du vieillissement

Bramy Pilipili Matadi

► **To cite this version:**

Bramy Pilipili Matadi. Etude des mécanismes de vieillissement des batteries Li-ion en cyclage à basse température et en stockage à haute température : compréhension des origines et modélisation du vieillissement. Energie électrique. Université Grenoble Alpes, 2017. Français. NNT : 2017GREAI118 . tel-01792293

HAL Id: tel-01792293

<https://theses.hal.science/tel-01792293>

Submitted on 15 May 2018

HAL is a multi-disciplinary open access archive for the deposit and dissemination of scientific research documents, whether they are published or not. The documents may come from teaching and research institutions in France or abroad, or from public or private research centers.

L'archive ouverte pluridisciplinaire **HAL**, est destinée au dépôt et à la diffusion de documents scientifiques de niveau recherche, publiés ou non, émanant des établissements d'enseignement et de recherche français ou étrangers, des laboratoires publics ou privés.

THÈSE

Pour obtenir le grade de

DOCTEUR DE LA COMMUNAUTE UNIVERSITE GRENOBLE ALPES

Spécialité : **Matériaux, Mécanique, Génie civil, Electrochimie
(2MGE)**

Arrêté ministériel : 25 mai 2016

Présentée par

Bramy PILIPI MATADI

Thèse dirigée par **Yann BULTEL**, Professeur des Universités,
Grenoble INP

préparée au sein du **Laboratoire de Stockage Electrochimique
(CEA / LITEN)**
dans l'**École Doctorale I-MEP-2 - Ingénierie - Matériaux,
Mécanique, Environnement, Energétique, Procédés,
Production**

**Etude des mécanismes de vieillissement des
batteries Li-ion en cyclage à basse température et
en stockage à haute température : compréhension
des origines et modélisation du vieillissement**

**Study of the aging mechanisms of Li-ion batteries
under low temperature cycling and high
temperature storage: understanding of the origins
and aging modeling**

Thèse soutenue publiquement le **21 décembre 2017**,
devant le jury composé de :

Mme. Nathalie JOB

Professeur des Universités, LGC (Univ. de Liège), Rapporteur

M. Stéphane LARUELLE

Professeur des Universités, LRCS (Univ. de Picardie), Rapporteur

M. Pascal VENET

Professeur des Universités, Lab. Ampère (Univ. de Lyon 1), Président

Mme. Sylvie GENIÈS

Ingénieur de Recherche, LAP (CEA / LITEN), Examineur

M. Arnaud DELAILLE

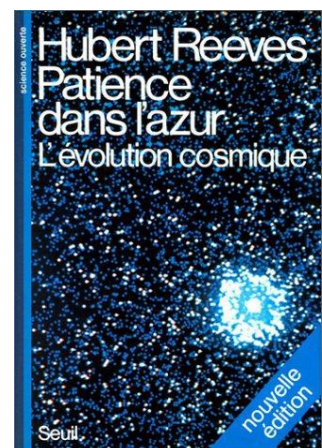
Chef de Laboratoire, LSEC (CEA / LITEN), Examineur

M. Yann BULTEL

Professeur des Universités, LEPMI (Grenoble INP), Directeur de thèse



« Si deux théories expliquent également bien un résultat, il convient de trancher en faveur de la plus simple »



Patience dans l'azur, Hubert REEVES

Acknowledgments

This manuscript is the fruit of three years of doctoral thesis conducted at the French Alternative Energies and Atomic Energy Commission (CEA), within the Laboratory for Electrochemical Storage based at the National Institute of Solar Energy (INES).

I would like to thank Professor Yann BULTEL for his leadership in this work. I express my gratitude to him for his scientific rigor and for his availability to supervise this manuscript and the articles published in the scientific journals notwithstanding his workload. I also thank him for his critical analysis of the results and their interpretations as well as for his supervision in calm and mastery.

My gratitude is also addressed to Dr. Arnaud DELAILLE, the Head of the Laboratory for Electrochemical Storage (LSEC), on the one hand, for giving me the opportunity to integrate his team since my end of university studies and on the other hand, for the confidence he has given me by offering me a thesis subject that is scientifically sound and offers interesting industrial perspectives. I have greatly benefited from his experience, his patience, but above all his great sense of listening and his remarkable ability to synthesize results.

I would also thank Dr. Sylvie GENIES, researcher at the Laboratory of Post-Mortem Analysis (LAP) and my co-supervisor for her immense contribution to the results of this thesis work and related articles. I express my gratitude for her availability despite her extremely busy schedule as well as for the major interest she has brought to the work of investigation and understanding of the mechanisms studied in this thesis. Thank you, Sylvie, for having trained me in electrochemistry and post-mortem analysis. I really benefited from your know-how, your experience, and your pertinent remarks throughout this scientific and professional experience.

Professors Nathalie JOB from the University of Liège, Pascal VENET from Ampère Laboratory at the University of Lyon 1 and Stéphane LARUELLE from the University of Picardie have honored me by accepting to examine this work. I hope they find here a sincere expression of my profound gratitude.

I would also like to thank Dr. Lise DANIEL, the Head of the Laboratory of Post-mortem Analysis, for having facilitated me to carry out analyzes in her laboratory and for her advice and suggestions to well lead this work. My gratitude goes particularly to Dr. Claude CHABROL for the DRX analyzes that she agreed to perform for me, to Dr. Michel BARDET for having disposed of his time to conduct the NMR analyzes, to Dr. Eric DE VITO for accepting to examine certain samples with FIB / ToF-SIMS and to Dr. Jean-Frédéric MARTIN, who has always been available for performing GC-MS analyzes. I would also like to thank Dr. Adrien BOULINEAU for the analysis under the transmission electron microscope.

The study on the polymerization of biphenyl and the coloration of separators would not have been complete without the expertise of Dr. Isabel JIMÉNEZ-GORDON and without the contribution of Xavier FLEURY. I am also grateful to them.

The data processing of the batteries was facilitated by the software tools enhanced by Dr. Maxime MONTARU, researcher at the Laboratory for Electrochemical Storage. I am very grateful to him for having trained me as much on his tools of automatic analysis as on the modeling of the batteries and for the precious time that he dedicated to explain the operation to me. The semi-empirical aging model could not have been done without the help and time spent by Karrick MERGO MBEYA. I am grateful for his immense contribution. Thanks to Laurent VINIT who set up the aging simulation platform as well to Dr. Clément EDOUARD and Stanislas GROSJEAN for the invaluable help they gave me in programming on MATLAB.

Of course, I would like to thank Catherine ARNAL, Baptiste JAMMET and Sébastien DUMENIL for the follow-up of my batteries aging tests. I would also like to thank Dr. Nicolas GUILLET and Dr. Mikaël CUGNET for helping me interpret some of the results.

A big thank you to all members of the Electrochemical Storage Laboratory for having enriched me with their knowledge in electrochemistry, for having devoted me of their time to answer my concerns and for sharing to me their knowledge. Thus, I am particularly indebted to Doctors Fathia KAROUI, Angel KIRCHEV, Jean-Marie KLEIN, Sothun HING and Romain TESSARD. By the same token, I would also like to thank everyone from the Electricity and Hydrogen Department for Transport, who participated in my thesis work. I thank in particular, David BRUN BUISSON for his help in the dismantling of Li-ion cells, Dr. Lionel PICARD and Dr. Nicolas MARIAGE.

My thanks also go to Dr. Chrystelle LEBOUIN, Senior Lecturer at Aix-Marseille University, for his teachings on Li-ion electrochemical storage batteries, through which my interest in this battery technology was born. My professors at the faculty of sciences of Aix-Marseille University, of which I value the great qualities, have ensured my follow-up during five years of formation. Let them be assured of my gratitude.

Finally, I thank God for the grace he has given me to conduct this work in good conditions. I extend my most sincere thanks to my parents, who have devoted all their lives to my education through sacrifices, to my dearest big brother for always supporting me, to my beloved fiancée who encouraged me every day throughout those years as well as to my childhood friends who have always been from the beginning.

To conclude, I dedicate this thesis work to my dearest little brother who knows how to handle anything.

To my dearest little brother.

Table of contents

General introduction	11
I. State of art and objectives of the study	15
1.1. Li-ion batteries	16
1.1.1. Evolution of the market of Li-ion batteries	16
1.1.2. Operating principles	17
1.1.3. The different types of materials chemistries.....	18
1.1.3.1. Positive electrodes	18
1.1.3.2. Negative electrodes.....	20
1.1.3.3. Electrolytes	21
1.2. Aging of Li-ion batteries	25
1.2.1. Economical point of view	25
1.2.2. Impact of aging on the battery.....	25
1.2.3. Types of aging	26
1.2.3.1. Calendar aging	26
1.2.3.2. Cycling aging	26
1.2.4. Mechanisms of aging	27
1.2.4.1. SEI growth.....	27
1.2.4.3. Metallic lithium deposition.....	29
1.2.4.4. Degradation of active material.....	29
1.2.4.5. Other aging mechanisms.....	30
1.3. Methods for the identification of aging mechanisms	31
1.3.1. Post-mortem investigations.....	31
1.3.2. Introduction of reference electrodes into commercial Li-ion cells.....	31
1.3.3. Incremental capacity measurements	32
1.4. Objectives of the study	35
II. Experimental setup	37
2.1. Li-ion cells reference studied: C/NMC KOKAM 16 Ah	38
2.2. Insertion of reference electrodes into 16 Ah commercial Li-ion pouch cells 41	
2.2.1. Types of reference electrodes.....	41
2.2.2. Insertion protocol of reference electrodes	41
2.2.2.1. Preparation of the reference electrode	41
2.2.2.2. Insertion of the reference electrodes	42
2.2.3. Electrochemical tests with the instrumented commercial cell.....	44
2.2.3.1. Evolution of the potential of electrodes.....	46
2.2.3.2. Internal resistance measurements	47
2.3. Protocols of check-ups for aging tests	51
2.3.1. Extended Check-Up test (ECU)	51
2.3.2. Short Check-Up (SCU)	52
2.4. Post-mortem analyses	53
2.4.1. Protocol of dismantling.....	54
2.4.2. Electrochemical characterizations of reassembled electrodes.....	55
2.4.3. Physico-chemical characterizations of harvested electrodes.....	56
2.4.4. Electrolyte analysis with GC-MS	58
2.4.5. Microscopy analysis	59
2.4.6. Chemical methods sensitive to electrode surface	60

2.4.7.	Chemical methods sensitive to electrode bulk.....	61
III.	Study of aging mechanisms at low temperature.....	65
3.1.	Cycling aging.....	66
3.1.1.	Cycling aging conditions	66
3.1.2.	Results of cycling aging tests.....	67
3.1.2.1.	Evolution of the capacity over aging.....	67
3.1.2.2.	Evolution of the internal resistance over aging	69
3.2.	Cycling aging at low temperature	71
3.2.1.	Evolution of the capacity during cycling.....	71
3.2.2.	Evolution of the internal resistance after cycling.....	73
3.3.	Ante-mortem analyses	74
3.4.	Post-mortem analyses	78
3.4.1.	State of health of commercial cells	78
3.4.1.1.	Visual inspections.....	78
3.4.1.2.	Surface morphology and chemical analysis with SEM / EDS	79
3.4.1.3.	Surface morphology analysis with TEM/EDS	81
3.4.2.	State of health of electrodes	84
3.4.2.1.	Electrochemical measurements of single components with coin half cells	84
3.4.2.2.	Determination of the state of lithiation of electrodes with XRD measurements	87
3.4.3.	Influence of the electrolyte	89
3.4.3.1.	Electrolyte analysis with GC-MS	89
3.4.3.2.	Influence of the composition of the electrolyte.....	91
3.4.4.	Influence of the films on graphite electrodes.....	94
3.4.4.1.	Detection of metallic Li with ⁷ Li NMR.....	94
3.4.4.2.	Chemical Investigation into the volume of graphite electrodes with FIB/ToF-SIMS.....	95
3.4.4.3.	Chemical Investigation of the SEI on graphite electrodes with XPS	97
3.5.	Representation of the mechanism leading to the hindrance of Li diffusion into graphite electrodes	102
3.6.	Conclusions.....	105
IV.	Study of aging mechanisms at high temperature	107
4.1.	Performance of cells in calendar aging.....	108
4.2.	Post-mortem analyses	111
4.2.1.	Visual inspections	111
4.2.2.	Deposits analysis with ⁷ Li NMR	114
4.2.3.	Effect of the biphenyl additive in the electrolyte	115
4.2.3.1.	Electrolyte analysis with GC-MS	115
4.2.3.2.	Post-mortem analysis with coin full cells: with and without biphenyl as an additive.....	118
4.2.3.3.	Post-Mortem analyses of coin cells: cyclic voltammetry	119
4.3.	Model of local Li deposition at high temperature.....	123
4.4.	Conclusions.....	125
V.	Aging modeling	127
5.1	Synthesis of aging mechanisms studied	128
5.2.	Semi-empirical aging modeling	129

5.2.1. Introduction	129
5.2.2. Model equations.....	129
5.2.2.1. Calendar aging	129
5.2.2.2. Cycling aging.....	132
5.2.2.3. Total capacity loss	133
5.2.3. Identification of model parameters	133
5.2.3.1. Calendar aging identification results.....	133
5.2.3.2. Cycling aging identification results	138
5.2.4. Model evaluation.....	141
5.2.4.1. Calendar aging validation results	141
5.2.4.2. Cycling aging validation results	145
5.2.5. Model validation	149
5.3. Prognostic aging model based on electrodes shifts	152
5.3.1. Principles and model descriptions.....	152
5.3.1.1. Loss of Lithium Inventory.....	153
5.3.1.2. Loss of Active Material on the Positive Electrode.....	155
5.3.1.3. Loss of Active Material on the Negative Electrode	157
5.3.1.4. Loss of Active Material on both electrodes	158
5.3.1.5. Synthesis of the impact of different aging mechanisms on peaks displacement.....	160
5.3.2. Identification of aging mechanisms during cycling at low temperatures 161	
5.3.3. Identification of aging mechanisms during storage at high temperatures 163	
5.3.3.1. Aging mechanism: SEI growth	166
5.3.3.2. Aging mechanisms: SEI growth and dry areas.....	167
5.3.3.3. Aging mechanisms: SEI growth, dry areas and local Li depositions 168	
5.4. Conclusions.....	171
Conclusions and perspectives	173
Appendix	179
<i>Appendix of the Chapter 2</i>	179
<i>Appendix of the Chapter 3</i>	183
<i>Appendix of the Chapter 4</i>	186
<i>Appendix of the Chapter 5</i>	190
List of illustrations	201
List of tables	205
References	207

General introduction

The lithium-ion (Li-ion) worldwide battery market is exponentially growing since the advent of this battery technology in the 90s. This tremendous growth is partly attributable to the international proliferation of electronic devices such as cameras, smartphones, laptops, tablets, hoverboards and electronic cigarettes.

Moreover, since the last decades, due to the technological advances, the use of Li-ion batteries has been exported to applications requiring higher power and energy. Their electric energy density has made them favorable candidates for electric and hybrid vehicles, whose global market is also tremendously growing.

The strong penetration of renewable energies, mainly photovoltaic and wind energy, in the energy mix requires adequate storage solutions, in order to overcome, for example, intermittency matters. Li-ion technology is also evaluated in these applications for the smoothing or forecasting of electricity production, for the provision of electricity at the peak of consumption, or for the support of grid frequency or voltage problems. Besides, the interest in Li-ion batteries now allows them to be integrated into stationary standalone applications, to replace lead-acid batteries.

In all these applications mentioned above, the use of Li-ion batteries requires the consideration of their endurance and safety issues. It is therefore essential to identify, understand and quantify mechanisms that may reduce their performance.

This methodology is necessary in particular to implement management strategies to overcome these lifetime problems or even for the redesign of more efficient cells. These optimal management laws derived from predictions obtained from the aging models of these batteries, which in turn must be developed on the basis of the understanding of degradation phenomena.

Some recent works - and in particular some experiments carried out by the laboratory that hosts this thesis - highlighted the very significant negative impact of the use of Li-ion batteries under low and high temperature conditions. More specially, it is rather cycling at low temperatures as well as storage at high temperatures that have been identified as the most critical conditions prone to accelerate aging.

The research works presented in this thesis explore issues related to the use of Li-ion battery technology under these two operating conditions. The aim is to provide a coherent understanding of the onset of the main aging mechanisms under these usage conditions, enriched by ante- and post-mortem investigations. Then, a semi-empirical aging model will be proposed, taking into account aging mechanisms identified.

In addition, a new approach for aging mechanisms identification through incremental capacity measurements will be undertaken. This tool makes it possible to obtain signatures specific to a given aging mechanism, not only on the basis of the cell voltage but also relatively to the potentials of each electrode.

This thesis was conducted within the Laboratory of Electrochemical Storage (LSEC) of the French Atomic Energy and Alternative Energies Commission (CEA) on the site of the National Institute of Solar Energy (INES), focused on understanding and aging modeling of electrochemical accumulators. The post-mortem analyzes were performed in the Laboratory of Post-Mortem Analyzes (LAP); in the Laboratory of Nanocharacterization and Nanosafety (L2N) and in the Laboratory of Magnetic Resonance (LRM).

This thesis manuscript is structured in five chapters corresponding to the different lines of research developed during this work.

The operating principle of the Li-ion battery and the different chemistries of both electrodes and electrolyte are described in the first chapter. A particular focus is given to overcharge protection agents, used as additives in the electrolytes of commercial Li-ion batteries. A bibliographic study on the main aging mechanisms which can reduce the performance this battery and methods for their identification are presented.

The second chapter is devoted to the experimental setup. Specifications of the commercial Li-ion cell studied in this thesis is given in the first part of this chapter. The steps leading to the insertion of Li metal used as reference electrode into this commercial cell as well as electrochemical tests performed are then described. This experiment has been set up in order to follow up the evolution of both electrodes potentials during aging. The protocols of checkups used in the aging campaign are presented. In addition, the various post-mortem investigations methods required for this thesis are meticulously detailed in the last section.

The study of aging mechanisms under cycling conditions at low temperature is addressed in the third chapter. Ante-mortem analyses consisting in the exploitation of cycling measurements obtained from the instrumented commercial cell are depicted. Results and interpretations emerged from post-mortem techniques are presented in a pedagogical way. The state of health of cells and of electrodes, and also the influence of the electrolyte are deeply examined. A schematic model explaining the onset of the aging mechanisms involved is proposed at the end of the chapter.

Unpredictable aging mechanisms observed during storage life of commercial Li-ion cells under high temperatures and states of charge conditions are detailed in the fourth chapter. The significant influence of an additive of the electrolyte used as an overcharge protection agent is noticed and investigated with required post-mortem methods. A graphic model, showing the onset of aging mechanisms identified, is scheduled in the last section.

The fifth chapter focus on the aging modeling. A semi-empirical aging model based on capacity evolution, is developed, taking into account aging mechanisms identified in this study. This predictive model has been evaluated and validated by comparison with experimental measurements. A prognostic aging model based on electrodes shifts, using incremental capacity peaks signatures, has been proposed in order to identify degradation modes.

I. State of art and objectives of the study

This work addresses the study of the aging of Li-ion batteries, and more particularly of Graphite/Nickel-Manganese-Cobalt (C/NMC) Li-ion. The uses of this battery technology are multiple and among which stand out, because of their great potential, both electrical mobility and stationary storage, including support for intermittent energies such as photovoltaic energy.

The first part of this chapter presents the evolution of the market of Li-ion batteries over the 25 years since the beginning of their marketing. The operating principle of the Li-ion battery and the different chemistries of positive electrode as well as negative electrode and electrolyte are described in detail thereafter. The end of this first section is dedicated to overcharge protection agents, used as additives in the electrolytes of commercial Li-ion batteries.

The second part proposes a bibliographic study on the main aging mechanisms studied in the framework of the thesis, through the description of the two main aging modes which can alter the performances of the batteries. Upstream, the impact of the aging of the Li-ion batteries from an economic point of view and from the point of view of autonomy is presented.

Then, the third part deals with the methods of identification of these aging mechanisms, through the various post-mortem analyzes required in the context of this research work and through ante-mortem tools such as the introduction of a reference electrode into a commercial cell and incremental capacity measurements.

The objectives of the study are presented in the fourth and last part.

1.1. Li-ion batteries

1.1.1. Evolution of the market of Li-ion batteries

The year 2017 corresponds to the 25th anniversary of the introduction of the lithium-ion (Li-ion) rechargeable battery into the battery industry. Sony Corporation marketed the first commercial Li-ion battery, manufactured based on research works conducted by the J. Goodenough's group [1] and R. Yazami's [2].

Since this discovery, the global market for Li-ion batteries became the fast growing one compared to that of other batteries technologies. Figures showing the evolution of the market of Li-ion batteries were presented by the Avicenne's group during the last Batteries event in 2016 [3].

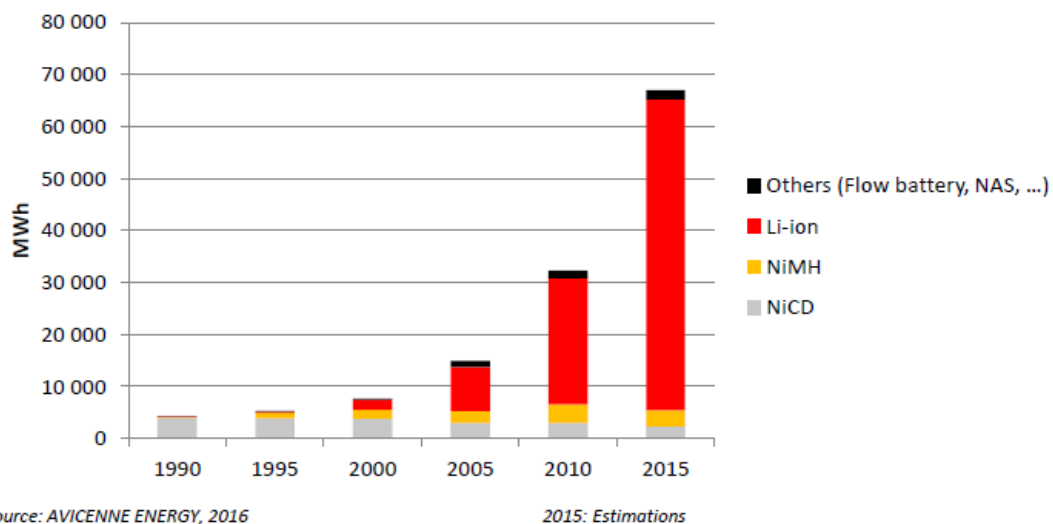


Figure I-1 : The worldwide battery market between 1990 and 2015 [3].

The global market for Li-ion batteries as illustrated in **Figure I-1**, represents the highest growth and the major part of industry investments since about ten years. We have nevertheless to add that the lead-acid technology, not represented in this figure, is very far behind (a little more than 350 000 MWh in 2015) and still hence the batteries technology the most used.

Li-ion batteries are mostly used in applications such as consumer electronic devices like mobile phones and computers, as seen in **Figure I-2**. Between 2000 and 2015, sales of Li-ion batteries went from less than 2 GWh to about 60 GWh. In 2000, cell phones represented 17 % of the total market (with in addition 17 % for portable electronics and 66 % for portable computers). Fifteen years later, the part corresponding to electronic devices became 50 % (with in addition 15 % for electric vehicles excluding China, 16 % for electric vehicles including China, 8 % for energy storage systems and 11 % attributed to other applications). Medical devices, power and gardening tools or e-bikes can be considered in the other applications category.

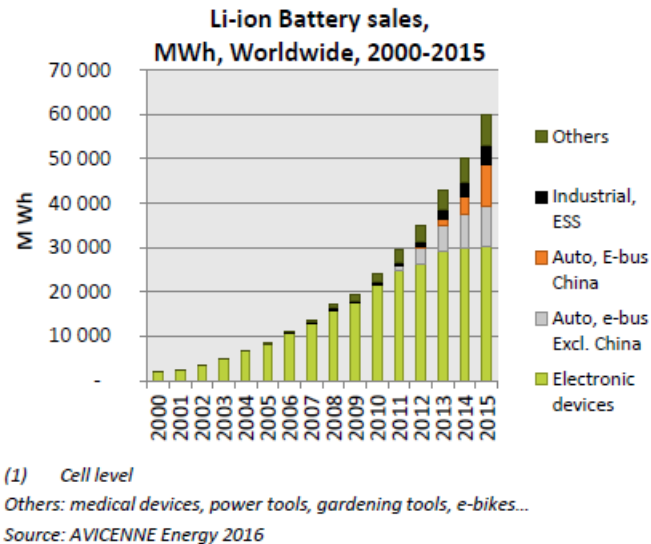


Figure I-2 : Li-ion technology main applications – M Wh [3].

The Li-ion technology challenges with established energy storage technologies such as lead acid in applications such as automotive products and storage systems where global efforts are undertaken to embrace smart grids. However, the market of Li-ion batteries for energy system storage (ESS) is at its beginning to take off.

In summary, the past 25 years have shown fairly rapid growth in sales and benefits of Li-ion batteries compared to all other rechargeable battery systems.

Recent works on new materials show that the Li-ion battery will be a formidable competitor for some years to come. However, despite its undeniable advantages, the Li-ion battery is still the subject of intensive research to improve its performance and its autonomy for applications requiring high energy densities, and especially in order to reduce its cost.

1.1.2. Operating principles

The Li-ion battery offers the best performance because of its high energy density. Its operation is based on the reversible exchange of Li cations between two materials of insertion. The negative electrode is generally made of graphite while the positive electrode is mostly composed of lithiated transition metal oxide.

The electrodes are composed of a current collector, usually aluminum for the positive electrode and copper for the negative electrode. A polymeric binder ensures the cohesion of the active particles and gives them a mechanical strength by adhering to the collector.

A porous polymeric membrane, allowing both electrical insulation and ionic conduction between the two electrodes, acts as a separator. The latter material is imbued with an electrolyte containing a lithium salt dissolved in a mixture of organic solvents, chosen so as not to be degraded at the electrodes at the operating potentials.

During charging, the Li cations coming from the positive electrode (then anode) are inserted into the negative electrode (then cathode) under the effect of a current applied from a generator. During the discharge, these Li ions migrate from the negative electrode (then anode) to the positive electrode (then cathode) at the same time as electrons are supplied to the external circuit. This makes it possible to recover the chemical energy stored in the form of electric energy.

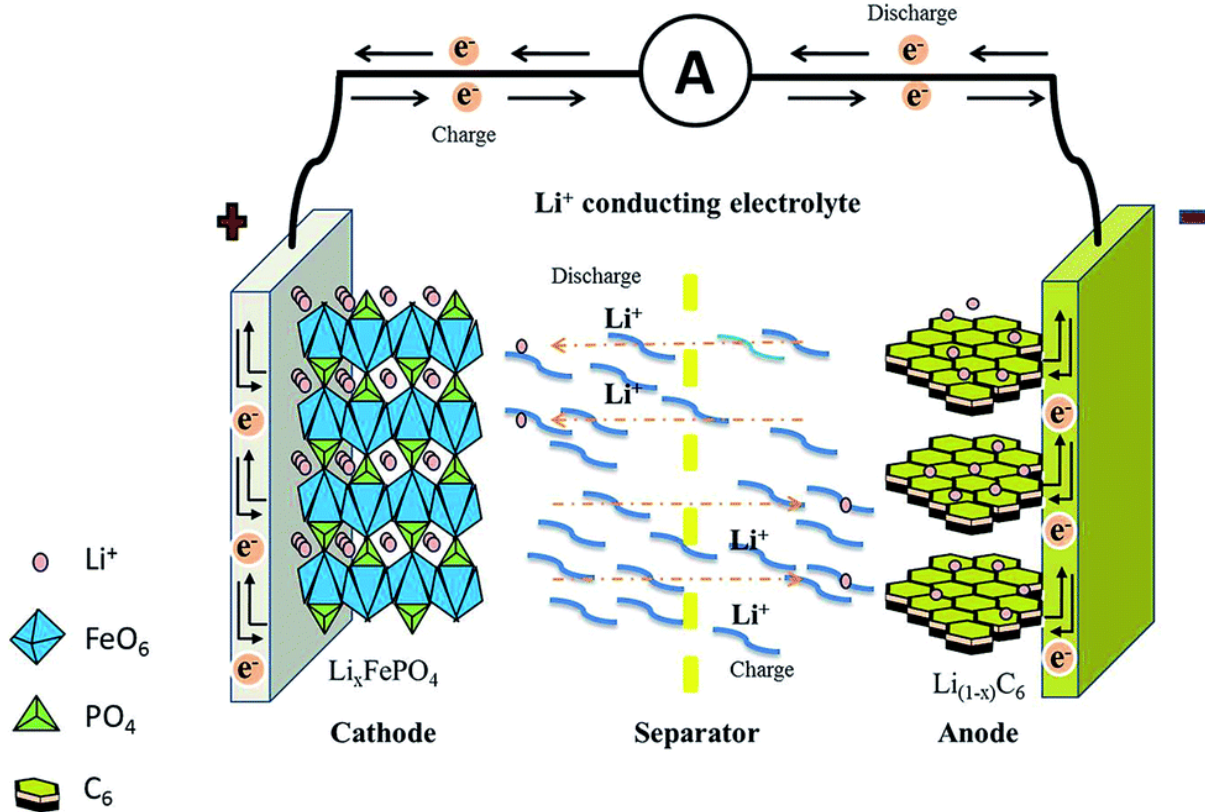


Figure I-3 : Schematic illustration of a typical Li-ion battery [4].

1.1.3. The different types of materials chemistries

1.1.3.1. Positive electrodes

1.1.3.1.1. Lithiated transition metal oxide

Lithiated transition lamellar oxides $\text{Li}_{(1-x)}\text{MO}_2$ are mostly used as material for the positive electrode of Li-ion batteries. Note that M may represent one or even more types of metals (Cobalt (Co), Nickel (Ni), Iron (Fe), Manganese (Mn)).

These materials have a crystallized host structure offering mono as well as bi and three-dimensional diffusion paths to facilitate the intercalation of the Li cations. The electrochemical insertion potential domains of most of these materials vary between 3 and 5 V relative to Li potential.

However, Co is very expensive and otherwise toxic. Once the rate of Li disinserted from that material becomes greater than or equal to 50 %, this material becomes unstable at high temperature and it releases oxygen. The release of oxygen can cause explosion if it reacts with electrolytic organic solvents.

The substitution of the Co in LiCoO_2 by Ni, Mn, Al made it possible to obtain materials such as $\text{Li}(\text{Ni}_x\text{Mn}_y\text{Co}_z)\text{O}_2$, called Lithium-Nickel-Manganese-Cobalt-Oxide (NMC) or $\text{Li}(\text{Ni}_x\text{Co}_y\text{Al}_z)\text{O}_2$, called Lithium-Nickel-Cobalt-Aluminium-Oxide (NCA). These new compounds are developed at a relatively lower cost, resulting in high mass capacity and good thermal tolerance. In the framework of this thesis, the commercial Li-ion cell used is based on $\text{Li}(\text{Ni}_{0.4}\text{Mn}_{0.4}\text{Co}_2)\text{O}_2$ as positive electrode.

1.1.3.1.2. Manganese oxides

Manganese oxide spinels $\text{Li}_{(1-x)}\text{Mn}_2\text{O}_4$ have also been developed to allow the intercalation of Li cations in the range of 3 and 4.2 V vs. Li^+/Li . The spinel $\text{Li}_{(1-x)}\text{Mn}_2\text{O}_4$ (Lithium-Manganese-Oxide as LMO) offers the advantages of low cost and non-toxicity. However, because of the risk of the Mn dissolving, this oxide is not suitable for temperature conditions above 55 °C.

1.1.3.1.3. Lithiated iron oxyphosphate

There is also another type of positive electrodes rather composed of phosphates of transition metals and more particularly of lithium-iron phosphate. The crystal structure of the $\text{Li}_{(1-x)}\text{FePO}_4$ (Lithium Ferro-Phosphate as LFP) is similar to that of olivine LiMgFeSiO_4 .

Although they are less dangerous in the case of abusive operation, these materials have the disadvantage of having a lower nominal voltage, about 3.2 V vs Li^+/Li .

The name olivine was originally given to a mineral group of silicates of olive green color. However, this designation has been extended to the isomorphic crystal structures of LiMgFeSiO_4 .

1.1.3.1.4. Crystalline structures

The three types of crystalline structures corresponding to the different families of positive electrodes materials are illustrated in the figure below.

Lithiated transition lamellar oxides $\text{Li}_{(1-x)}\text{MO}_2$ have a crystalline structure of lamellar type (A). Manganese oxide spinels such as LiMn_2O_4 present a crystalline structure of spinel type (B), while materials such as lithium-ion phosphate belongs to the category of crystalline structure of olivine type (C).

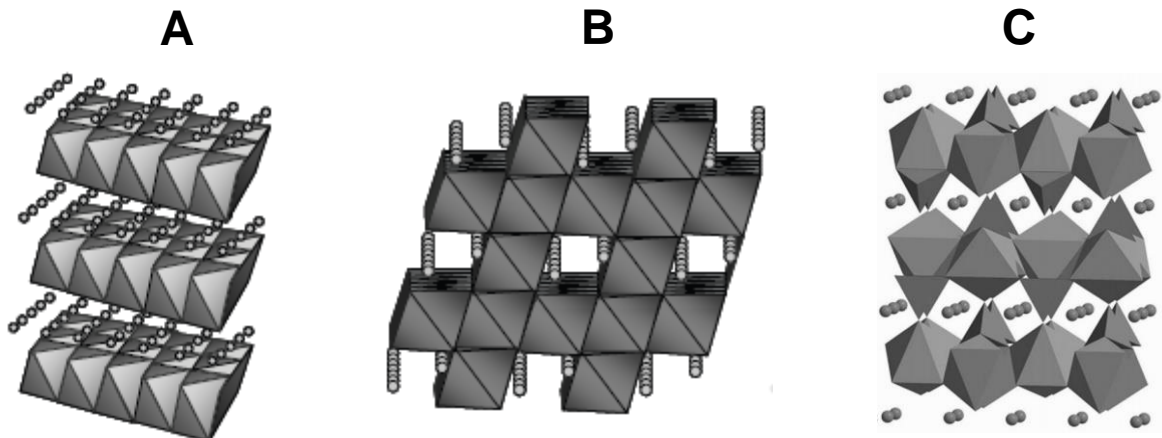


Figure I-4 : Crystalline structures for each type of positive electrode insertion material [5].

1.1.3.2. Negative electrodes

1.1.3.2.1. **Graphite**

Graphite is one of the most common negative electrodes used in commercial Li-ion batteries. This carbonaceous material is attractive because of its low cost and its very low electrochemical insertion potential leading to a very high cell voltage. It has an intercalation / deintercalation plateau between 0.05 and 0.1 V vs Li⁺/Li [6; 7; 8; 9]. Its mass capacity of 372 mAh/g and its high reversibility are additional factors that increase its attractiveness.

This high reversibility of the Li cation insertion within the graphite is related to the small spacing of the graphene planes (spaced at 0.335 nm) which constitute this material and which deviate during the intercalation of the Li (up to 0.370 nm for complete lithiation) [10].

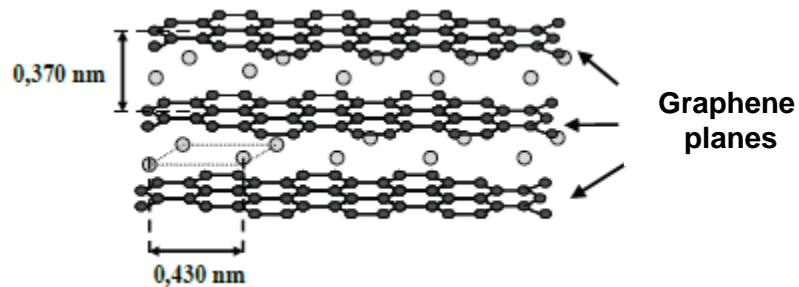


Figure I-5 : Plans of graphene between which the Li is inserted [10].

This small gap allows the conservation of the planar structure of the graphite. There is therefore no covalent bond but only electrostatic forces between the carbon planes, as showed in **Figure I-5**, in which the Li comes to be inserted.

It should be noted that many efforts are being made by researchers in the development of new high-capacity carbonaceous materials with a low rate of irreversible capacities.

Porous carbonaceous materials such as carbon xerogels prove to be promising candidates [11]. Nevertheless, these materials tend to irreversibly trap the Li ions in their porous structure during the first insertion / disinsertion cycle [12].

That is what limits their use at the present time. Consequently, current research is directed towards modifying the porous texture of these materials.

1.1.3.2.2. Lithium titanium oxide

Graphite has an insertion potential very close to the Li reduction one and is therefore exposed to the formation of lithium metal [1.2.4.3], which can pose a hazard to the safety of the battery. It is for this reason that the Lithium Titanate Oxide (LTO) appears as an interesting alternative electrode material to graphite, because it allows the Li to be inserted into electrochemical potentials greater than the electrochemical potential of lithium reduction. The Li insertion / disinsertion reaction in the LTO takes place in the same two-phase process as seen with the LFP. However, this material has a lower mass capacity, about 175 mAh/g in theory.

1.1.3.3. Electrolytes

1.1.3.3.1. Composition

The electrolyte used in Li-ion batteries consists of a mixture of aprotic organic solvents due to the instability of the graphite electrode in the presence of compounds with labile ¹ hydrogen.

In this mixture of solvents, most often composed of alkyl carbonates (ethylene, dimethyl, propylene carbonates), one or more lithium salts are solubilized in order to make possible the transfer of the Li cations. The most commonly used salts are lithium hexafluorophosphate (LiPF₆) and lithium bis (trifluoromethanesulfonyl) imide (LiTFSI).

Many additives are added to the electrolyte of commercial Li-ion batteries in order to improve their cycling ability. The use of certain additives such as vinylene carbonate (VC) optimizes the irreversible consumption of Li during the first charge of the battery. Its decomposition at high potential, before the solvents of the electrolyte, leads to the formation of a thin and homogeneous film on the surface of the graphite particles. As a result, the rate of consumed Li-ions is thus low, which reduces the irreversible capacity loss [13].

For safety reasons, the use of other types of additives (so-called "protectors") in the electrolyte of commercial Li-ion batteries is becoming more and more frequent [14]. Indeed, these molecules have the role of preventing overcharge. It should be noted that the overcharge incident in a Li-ion battery may induce a risk of thermal runaway.

¹ The more an atom (or group of atoms) detaches easily from a molecule, the more it is said to be labile.

These molecules must have an oxidation potential slightly higher than that of the limit potential corresponding to the cut-off of the charge at the positive electrode, considering that the overcharge takes place at the positive electrode.

More specially, aromatic compounds are the first molecules reported to act as a redox mediator during overcharge [15]. In the context of this thesis work, a crucial interest will be devoted on the stability of an aromatic compound, the biphenyl, used as a safety electrolyte additive for overcharge protection. Aging mechanisms, caused with the use of this molecule in the electrolyte of the commercial cell studied in this thesis, will be discussed.

1.1.3.3.2. Overcharge protection agents

Overcharge protection agents are additives used in the electrolyte of Li-ion batteries for preventing the overcharge reactions of both electrodes by sacrificial reactions as seen in **Figure I-6**.

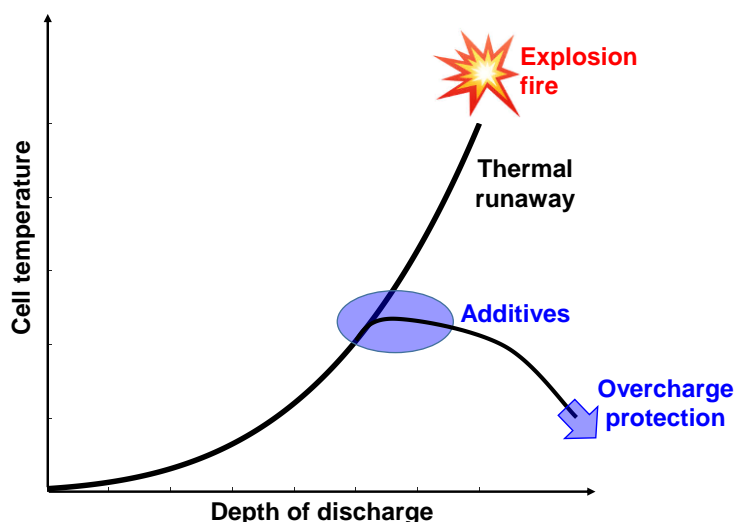


Figure I-6 : Principle of overcharge agents based on the representation made by J. Garche et al. [16].

According to J. Garche et al. [16], two types of compounds need to be distinguished: redox shuttle type and shutdown type.

On one hand, the concept of redox shuttle type agents such as 2,4 – Difluoroanisole (DFA) consists in the oxidation of a compound R, having a reversible redox potential (0.1 – 0.2 V higher than the cathode potential at end-of-charge), to compound O on the cathode, and then O migrates to the anode in order to be reduced to original form R. The principal of operation is described in the **Figure I-7 (A)**.

These types of agents are used in the electrolyte of Li-ion batteries rather conceived for low current applications since the diffusion coefficient of a cation radical produced by oxidation controls current density.

On the other hand, aromatic compounds such as biphenyl (BP – C₁₂H₁₀), having no reversible electrochemical characteristic, polymerize on the cathode during overcharge and the liberated protons migrate to the anode generating hydrogen gas (see in **Figure I-7 (B)**). Note that, biphenyl is the most overprotection agent used as an additive in commercial Li-ion cells.

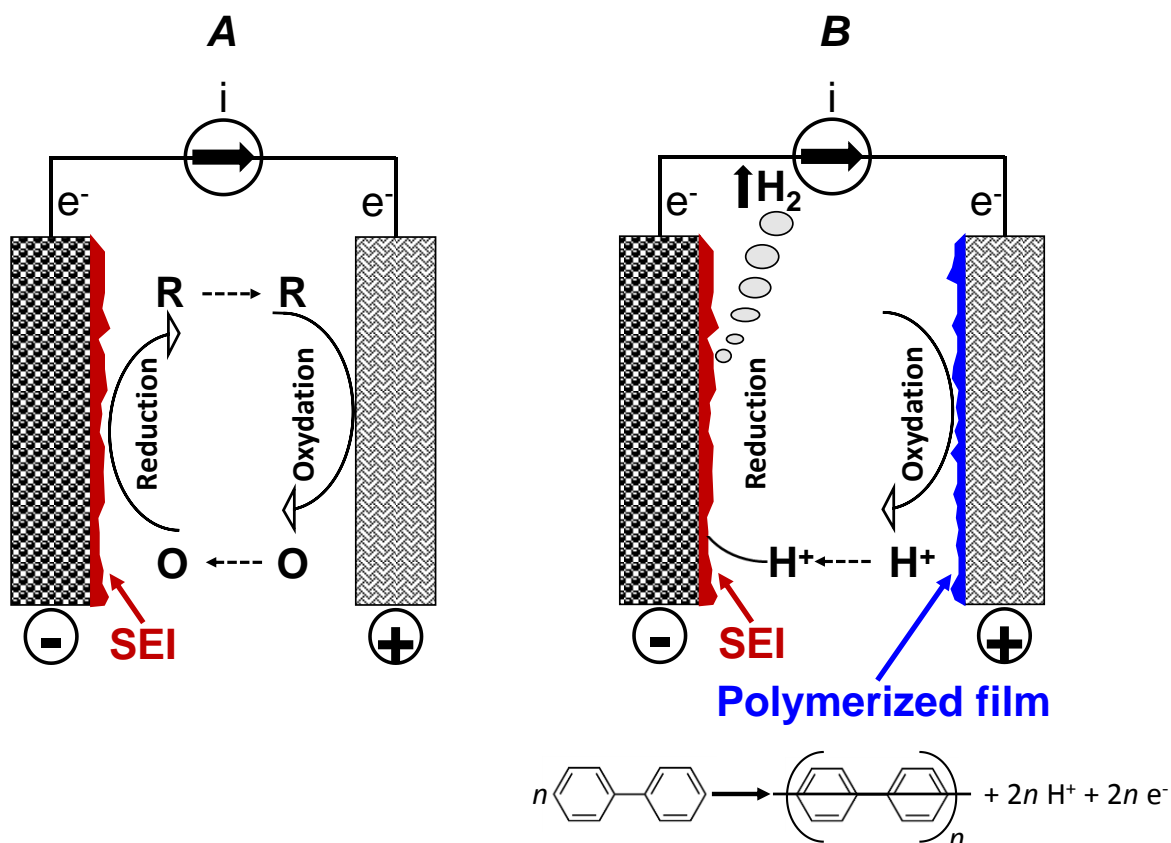


Figure I-7 : Overcharge agents: mechanism of redox shuttle type (A) and mechanism of shutdown type (B) based on the representation made by J. Garche et al. [16].

In the case of cylindrical cells, the hydrogen reaction leads to the rise of the internal pressure which activates pressure-activated intermitted devices, called Current Interrupt Device (CID). In the case of prismatic cells, the current shutdown is activated by the increase of the internal resistance which depends on the polymerized film and the meltdown of polyethylene separators. The activation of pressure-sensitive internal electrical disconnect devices makes the cell inoperative and protects it from any overcharge abuse [17; 18; 19; 20].

Since these compounds become active from a specific potential, their oxidation potential are thus related to the cathode potential. J. Garche et al. [16] mentioned the appropriate oxidation potential of these additives in the range of 4.5 – 4.6 V vs. Li⁺/Li in the case of lithium cobalt oxide (LiCoO₂) cathodes (4.3 V vs. Li⁺/Li at 100 % of SOC). This value of potential is consistent with the one (4.5 V vs. Li⁺/Li) reported by C.-H. Doh et al. [21].

K. Abe et al. [22] used cyclic voltammetry measurements to determine the cathodic limits of biphenyl (4.45 V vs. Li⁺/Li) with LiCoO₂ and LiMnO₄ used as cathodes. The base electrolyte was 1 M LiPF₆-EC:EMC (3:7 by volume). Y. Zhang et al. [23] rather performed overcharge tests at 20 ± 5°C and their results showed that biphenyl can electrochemically polymerize at the overcharge potential of 4.5 – 5.5 V vs. Li⁺/Li to form a layer on the cathode surface. They used different amounts of biphenyl (from 0.5 to 4 % wt) in an electrolyte based on 1 mol L⁻¹ LiPF₆ in EC:DMC:EMC (1:1:1, by volume). The electrochemical behavior of biphenyl was also examined using microelectrode cyclic voltammetry by L. Xiao et al. [24]. Their results revealed that the monomer must be able to polymerize at a potential just above 4.3 V vs. Li⁺/Li and quite below 5.0 V vs. Li⁺/Li. In addition, it was also found that the use of biphenyl as an electrolyte additive did not significantly influence the normal performances of the cell. These findings are consistent with N-S. Choi et al. [25] suggestions.

In summary, based on all the reports above, the polymerization potential of biphenyl is determined at room temperature in the range of 4.3 – 5.5 V vs. Li⁺/Li. However, few experimenters have worked on the thermal behavior of these gassing agents used as electrolyte additives in Li-ion cells subjected to high temperatures storage. In this thesis, the stability of overcharge agents under high temperature conditions will be discussed as well as its impact on the aging of the cell.

1.2. Aging of Li-ion batteries

1.2.1. Economical point of view

It is worth mentioning the inevitable degradation of battery performance that implies the need to reduce the impact of aging for a given application.

For the electric vehicle, for example, it should be remembered that the cost of the lithium battery pack is about 800 € / kWh [26]. As a result, an all-electric vehicle package, of the order of 22 kWh to obtain 150 km of autonomy approximately, currently costs about half of the total price of the vehicle.

Recently, a team of British researchers published an article [27] concerning a techno-economic study of a United Kingdom (UK) residential property photovoltaic (PV) storage system. The detailed cost-benefit analysis and the battery model showed that the use of Li-ion batteries for a PV-residential storage system connected to the grid is economically not yet viable, by considering the degradations of the battery and its replacement. This even with attractive subsidies and feed-in tariffs.

Given this high cost, manufacturers must ensure the durability of the battery and that its replacement is the least frequent possible. In other words, the anticipation of the aging mechanisms that may occur in the battery is necessary in order to promote the commercialization of electric vehicles or PV applications, and in order to forecast possible warranty costs [28].

1.2.2. Impact of aging on the battery

The aging mechanisms of Li-ion batteries are highly dependent on the materials used. A better understanding of these phenomena allows an optimal management of the battery while avoiding its use in abuse conditions. The complexity of the physicochemical reactions occurring within the cell, responsible for degradation, makes it difficult to understand the aging process. These physicochemical processes operate in an interdependent way: the degradation of a component influences the properties of the other constituents.

It is essential to differentiate self-discharge from the aging of a battery. Self-discharge refers to the reversible loss of energy stored in the cell when not in use. A simple recharge of the battery is sufficient to return it at its original level. This phenomenon manifests itself differently depending on the storage conditions and remains low for Li-ion cells, ie around 2 % per month, although this value may be greater according to storage conditions [29].

Aging is rather equivalent to irreversible deterioration of performance. In fact, it results in a decrease in capacity and / or an increase in the internal resistance of the cell [30] which is directly related to the available power. As a general rule, this phenomena reduces the battery lifetime.

Usually, the end of the life of a battery is generally defined by a loss of 20 % of capacity and / or when its internal resistance increases by 30 % [31].

The state of health (SOH) of a battery translates losses of performance of a battery due to aging, and is expressed by the next relation:

$$\text{SOH}(\%) = \frac{Q_{\text{tot},t}}{Q_{\text{tot},t0}} \times 100 \quad (1.1)$$

where $Q_{\text{tot},t}$ (Ah) is the current total capacity and $Q_{\text{tot},t0}$ (Ah) the total capacity measured at the beginning of life (BOL).

The state of charge (SOC) is an indicator of the available capacity in the battery.

$$\text{SOC}(\%) = \frac{Q_{r,t}}{Q_{\text{tot},t}} \times 100 \quad (1.2)$$

where $Q_{r,t}$ (Ah) is the remaining capacity and $Q_{\text{tot},t}$ (Ah) the current total capacity.

It should be remembered that the use of the battery combines both the phases of rest, discharging and recharging. Thus, two types of aging need to be distinguished: calendar aging (at rest) and cycling aging (in operation). Furthermore, we can underline that the aging mechanism observed in calendar mode, mainly the SEI growth, is not inhibited in cycling. This is the reason why some researchers distinguish "pure calendar" (at rest) from "calendar in cycling", referring in fact not to the battery usage mode but to its aging mechanism.

1.2.3. Types of aging

1.2.3.1. Calendar aging

The degradation of the performance of a battery over time when it is not electrically stressed corresponds to the so-called "calendar" aging mode. It results in an irreversible loss of capacity observed in the difference between its capacity after a full recharge and its capacity before storage. In this case, the storage temperature and the charge level (relative to the cell voltage) are the two factors affecting the life of the battery.

1.2.3.2. Cycling aging

A cycle of a battery corresponds to a discharge / charge, usually partial but sometimes complete in the case of battery test (between 0 and 100 % of SOC), followed by a recharge over an equivalent state of charge. In the case of cycling, the SOC parameter can range in a SOC window (ΔSOC) since the electrical stresses due to the cycling conditions lead to a dynamic interval of the SOC.

In addition to the range of SOC, cycling aging may be influenced by other factors such as the temperature and the charging / discharging current rates (C-rate). This mode of aging is also of course a function of the number of repeated cycles

undergone by the battery, and therefore of the quantity of charge exchanged. Finally, the self-heating of the battery due to the passage of current may induce an increase of the battery temperature during cycling and can thus accelerate the degradation processes.

1.2.4. Mechanisms of aging

The aging of Li-ion batteries is largely studied and can be related to complex inter-dependencies from intrinsic cell components on one hand (electrodes materials, electrolyte composition [32; 33; 34; 35; 36; 37; 38; 39; 40]) and from extrinsic criteria on the other hand (temperature, applied charge / discharge current-rate, charge/discharge cut-off voltages, depth of charge/discharge, cell design [41; 42; 43; 44]).

1.2.4.1. SEI growth

At the level of graphite electrode, the Li is inserted devoid of its sphere of solvation which is constituted by the organic molecules of the electrolyte. This phenomenon of desolvation is carried out during the diffusion of the Li in an interfacial passivation layer present on the surface of graphite particles. This layer is called passivation film or Solid Electrolyte Interphase (SEI) in analogy to the passivation layer formed on the surface of lithium metal in lithium batteries.

However, unlike the latter, formed chemically by contact between Li metal and the electrolyte, the passivation layer on the carbon has rather an electrochemical origin. Indeed, it is formed during the first charge called "activation charge", performed at the batteries factory well before marketing. This layer permeable to Li has a very important role for the stability of the electrode itself. Without the desolvating power of the SEI, the Li ion would be inserted with its sphere of solvation, which would result in a complete destruction of the structure of graphite, called exfoliation (see in **Figure I-8**).

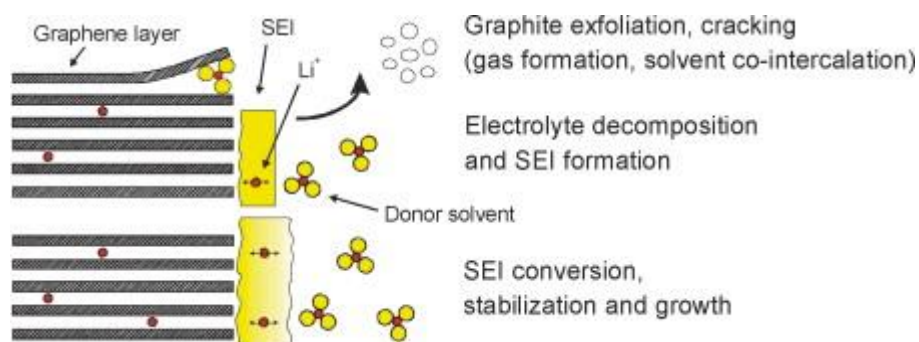


Figure I-8 : Development of the SEI at the graphite electrode [45].

Nevertheless, the formation of this layer consumes Li ions on the surface of graphite at low potential. Thus, that growth of the SEI over the lifetime of the battery leads to capacity loss and an increase in resistance at the cell level.

Repeated cycling can induce rupture of this layer because of volume expansion of graphite during cycling. This phenomena thus reactivates the reduction of the electrolyte by its contact with the free graphite surfaces formed. The lithium consumption leads to a Loss of Lithium Inventory (LLI).

1.2.4.2. Pore clogging

J.C. Burns et al. [46] showed that the SEI growth within graphite would be responsible for the sharp change in the slope of the capacity loss curve observed at the end of life (EOL). This rapid rollover capacity failure is caused by the development of a kinetic hindrance in the negative electrode, as the number of cycles increases. The authors have performed cycling tests at 30 °C and at a rate of 1 C with 18650-sized 2 Ah cells based on graphite and $\text{Li}[\text{Ni}_{1/3}\text{Mn}_{1/3}\text{Co}_{1/3}]\text{O}_2$ (NMC) electrodes.

In fact, they suggested that electrolyte degradation products created at the positive electrode can migrate to the negative electrode where they are reduced as a solid layer of unwanted material on the front surface of the negative electrode.

With the increase of the number of cycles, this layer becomes thicker enough to considerably reduce Li ions transport into the bulk of the negative electrode since electrode pores are filled with reduced oxidation products (see in **Figure I-9**).

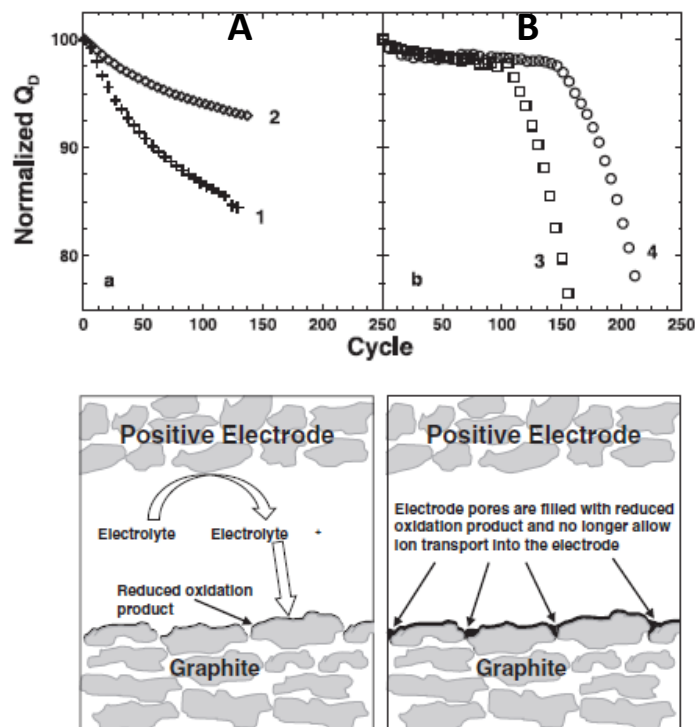


Figure I-9 : Example of gradual capacity loss (A) and fast rollover capacity loss (B) due to the reduction of porosity on graphite electrode [46].

Moreover, the authors showed that cells cycled at 23 °C led to rollover failure after only 700 cycles, while the cells at 60 °C did not (over 1600 cycles were performed). This effect was attributed to the Li-ions transport through that film due to improved kinetics observed at 60 °C.

At the level of the graphite electrode, the reduction of the porosity can finally lead to metallic lithium depositions on the surface due to the high polarization that will be created at the surface of the negative electrode.

1.2.4.3. Metallic lithium deposition

Batteries can be used sometimes at low temperature, typically below 10 °C. In such conditions, it is well known that the performance of Li-ion batteries is reduced in most of the cases. The kinetics of Li intercalation-deintercalation is affected due to the limited mobility of Li cations in the electrolyte [47]. Moreover, C.-K. Huang et al. [48] suggested that the poor low-temperature performance of Li-ion cells is exclusively related to the reduced Li diffusivity in carbon electrodes and not in organic electrolytes neither SEI.

As mentioned above, the graphite domain of intercalation / deintercalation of Li is very close to the Li reduction potential. The increase of the graphite electrode resistance under the effect of low temperature and / or by applying a high charge current rate (C-rate) could drive its potential to fall below 0 V vs Li⁺/Li. Consequently, graphite is therefore exposed to the formation of Li metal.

Li deposition on the carbon anode is due to low Li cation diffusion in the anode [49]. In the literature, Li plating is reported to be the main cause of Li-ion batteries aging at low temperature and/or at high charge rate [50; 51; 52; 53; 54; 55; 56; 57; 58; 59].

Li carbonate compounds can be formed in case of contact between the metallic Li and the electrolyte on the surface of the SEI. On the whole, the loss of the exchangeable Li leads to an irreversible loss of the capacity of the Li-ion battery only in the case the dendrite formed is disconnected from the electrode. It is thus called “dead Li” and in that case, this Li can visually be observed although the cell is opened at discharged state.

1.2.4.4. Degradation of active material

The degradation of active material involves all physico-chemical mechanisms through which some of the active intercalation sites become inactive at either the negative electrode or the positive electrode.

In the literature, D. Aurbach [60] particularly described a failure mechanism of graphite electrodes characterized by the deactivation of graphite particles, covered by insulating surface films. In fact, the author suggested that the reduction of propylene carbonate (PC) within crevices in the edge planes of graphite particles, leads to the formation of species of type R(OCO₂Li)₂ and the release of propylene gas.

This phenomenon results in the cracking of particles, exposing the new reactive surface capable of reacting further with solution species. Therefore, the graphite particles are deactivated since they are electrically insulated by the formation of an insulating film. This deactivation of the particles due to their electrical disconnection from the bulk of the electrode is a notable capacity-fading mechanism of graphite electrodes, especially at elevated temperatures.

This type of failure mechanism is considered as a loss of active material (LAM). LAM from the positive electrode may also be caused by particle isolation or Li ions trapping in the oxide constituting the positive electrode material.

1.2.4.5. Other aging mechanisms

The electrolyte can oxidize at low voltages at the negative electrode to form a passivation layer and / or a gas production such as methane, and at high voltages at the level of the positive electrode to create a deposit capable of covering its active surface. This phenomenon leads to a non-homogeneous distribution of the current and reduce the conductivity of Li ions [61].

Experimental works have demonstrated that the degradation of the positive electrode materials is caused by the phase changes activated during the intercalation and deintercalation of the Li ions. This can distort the crystalline structure and strongly influence the lifetime of active materials of the positive electrode under cycling conditions [62; 63].

Mechanisms of dissolution and chemical decomposition are also observed in the presence of certain materials such as those based on Manganese. J. Vetter et al. [45] have shown that this phenomenon is a function of the SOC of the cell.

The mechanical integrity of the current collectors can also be affected by high potentials and thus reduce the mobility of the electrons towards the external circuit due to the non-uniform distribution of current density. Besides, during the insertion / disinsertion of the Li as the number of cycles increases, the active material can detach from the collector on some of its zones.

1.3. Methods for the identification of aging mechanisms

1.3.1. Post-mortem investigations

It is possible to detect depositions on the electrode surface in the μm size range using optical microscopy methods. S.J. Harris et al. [64] described *in situ* measurements of Li transport in an operating cell using an Olympus SZX12 optical microscope in order to study the graphite lithiation, Li plating and Li dendrite growth. C. Uhlmann et al. [65] observed the growth and relaxation of macroscopically plated Li using an optical confocal microscopy whilst applying current. J. Steiger et al. [66] used a light microscope to observe the modification of the SEI at crystalline defects and the dissolution of electrodeposited Li filaments. *In situ* optical investigations to analyze Li metal plating have also been performed by other authors such as O. Crowther et al. [67] and H. Wu et al. [68]. However, the detection of particle cracks is limited by the resolution of optical microscopes which corresponds to a range of 0.2 μm [69]. The SEI growth or the morphology of Li deposition (dendritic, granular or foamy) on the surface of graphite particles can also be observed with electron microscopy images.

The visual inspection may be sufficient to attest of the LAM at the surface of the electrodes. Besides, the use of coin half-cells based on harvested materials can be necessary to measure the capacity loss in the case of active host material loss on a given electrode.

The different post-mortem methods used in this thesis for the identification of aging mechanisms are very well discussed in the second chapter.

1.3.2. Introduction of reference electrodes into commercial Li-ion cells

In addition to required post-mortem techniques, the detection of metallic Li deposition may also be achieved by measuring the potential of the negative electrode using a reference electrode. Such measurements are possible using a reconstruction of both negative and positive electrodes recovered from a commercial cell into a three-electrodes full cell with an additional reference electrode [70; 71; 72; 73].

However, measurements obtained from a reconstructed Li-ion cell may be influenced by several factors such as the necessity of removing one of the two coating faces of each electrode (in the case of bifacial coated electrodes) recovered from the commercial cell, the protocol of washing electrodes, the nature of the electrolyte which may be different from the original one used in the commercial cell and the pressure between the different layers (electrodes and separators).

Besides, the assembly of reconstructed 3-electrodes full cells is performed in an anhydrous room. The exposure of electrodes, especially graphite, to the atmosphere of the anhydrous room has a negative impact on electrochemical impedance spectroscopy curves (see in **Figure I-10**).

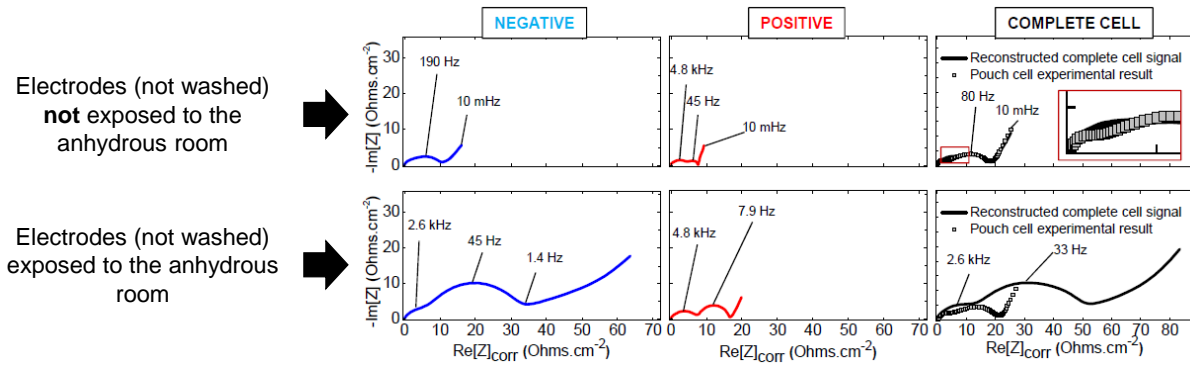


Figure I-10: Impact of the exposure of electrodes to the atmosphere of the anhydrous room before assembling into reconstructed 3-electrodes system.

Some authors studied the introduction of reference electrodes into commercial *cylindrical 18650 cells*. In 2000, G. Nagasubramanian [74] worked on the contribution of the impedance of each electrode in the total cell impedance increase of commercial 18650 cells at different temperatures ranging from 35 °C to -40 °C. Another electrolyte based on {ethylene carbonate (EC), propylene carbonate (PC) and diethyl carbonate (DEC) (1:1:2 v/v) containing 1 M LiPF₆} was added to the cell with the reference electrode for impedance studies.

In 2014, Jeffrey R. Belt et al. [75] investigated the voltage characteristics of the individual electrodes throughout calendar aging and duty cycle aging regimes with a reference electrode introduced into commercial cylindrical 18650 cells with a capacity of 1.2 Ah. The researchers added an electrolyte similar to the electrolyte found in the cell. As mentioned above, we believe that exposing the cell to an electrolyte which is different from the original used in the cell may influence the results and then the interpretation.

However, one case of an insertion of reference electrodes into commercial Li-ion *pouch-cells* is reported in the literature. E. McTurk et al. [76] compared two procedures of insertion of reference electrodes into manufactured 740 mAh Li-ion pouch cells (Kokam SLPB 533459H4). The authors investigated the effects of the two procedures of insertion onto the measurements of the potential of both electrodes and the cell voltage *in operando* over 20 cycles performed at 40 °C at a rate of C / 10. However, the suitability of this method for longer-term cycling tests and the effects of thermal conditions were not assessed. Moreover, the relation between electrodes behavior with aging and any aging mechanism is not dealt at all.

1.3.3. Incremental capacity measurements

It is also possible to identify aging mechanisms with Incremental Capacity Analysis (ICA) ($\Delta Q/\Delta U$ vs U). This method has been used by several authors as a powerful tool, sometimes as an alternative to post-mortem investigations. Several works on this subject have been conducted by Dubarry's group. In some cases, it is possible to obtain meaningful trends with differential voltage (DV) [77].

In this thesis, we have observed more noteworthy signatures with IC than with DV so that we focus only on the use of IC curves

M. Dubarry et al. [78] studied the evolution of peaks of incremental capacity (IC) of commercial Li-ion cells curves under loss of active material (LAM), under discharge and under charge. In another paper [79], the authors proposed a prognostic aging model able to simulate scenarios of major degradation modes, including loss of lithium inventory (LLI) as well as ohmic resistance increase (ORI) and their corresponding IC signatures. Impacts on the IC curves, characteristic to each aging mode were more pointed out in a further research work [80]. Other authors have also used IC measurements to provide qualitative analysis for aging mechanism identification [81; 82; 83; 84; 85; 86].

On one hand, it has been shown [79] that LLI results in a non-proportional and successive decrease of the peaks from the highest potentials to their disappearance, whereas a LAM rather results in the reduction of all peaks proportionally to their initial value.

On the other hand, a shift of all the peaks indicates an increase in resistance, as in the case of the SEI growth. However, the same shift of peaks has been pointed out in the case of LAM only on the negative electrode (NE). It should be noted that LAM on the NE and LLI show similar IC signatures because they share a common theme that the graphite cannot be lithiated to the same level as it was initially.

In the case of a Graphite / LFP Li-ion cell, each peak identified on the IC curves may be attributed to the intercalation / deintercalation of the Li-ions into the graphite electrode, convoluted with a large plateau corresponding to the phase transformation at the LFP electrode. Thus, a peak can be easily assimilated to a graphite insertion plate (see in **Figure I-11**).

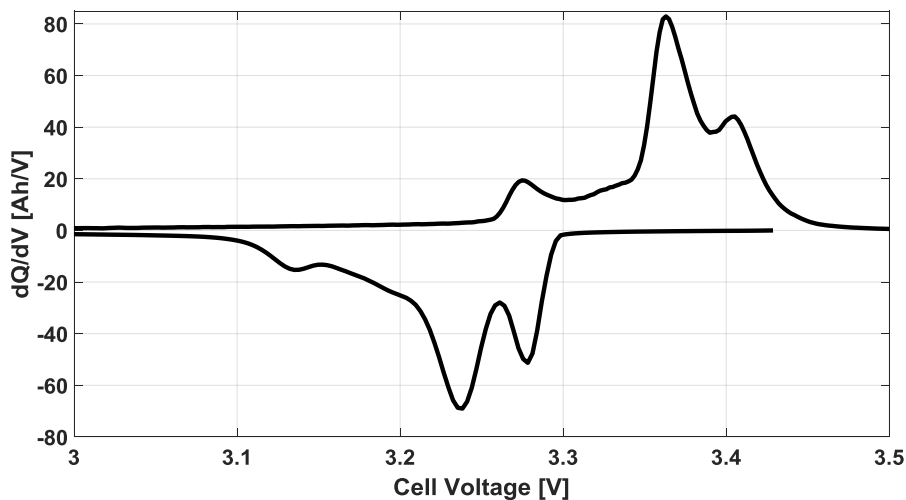


Figure I-11 : Incremental capacity of a Graphite / LFP Li-ion cell obtained at the rate of C / 10. (This Figure originates from an internal project of the Laboratory).

For other Li-ion chemistries such as Graphite / NMC studied in this thesis, it is not obvious to distinguish, based on the IC curves obtained from the cell voltage, the peaks corresponding to one or the other electrode, since the evolution of the potential of the NMC does not have any plateau (see in **Figure I-12**).

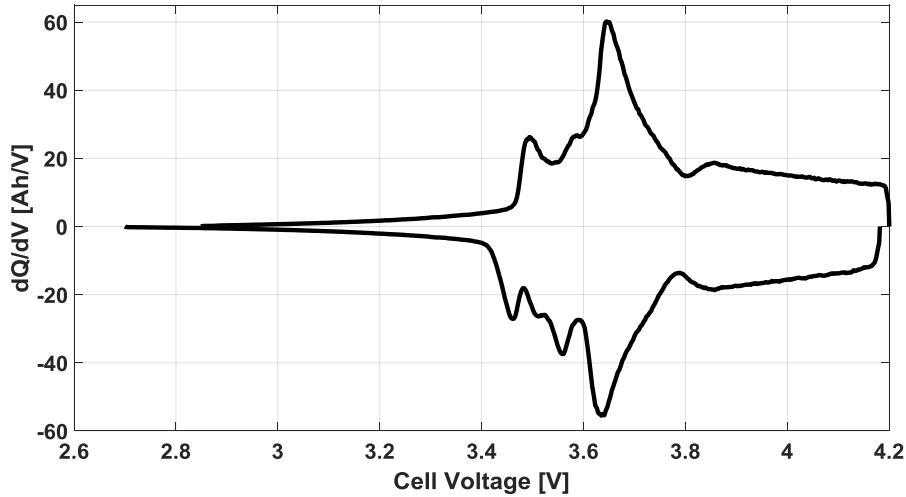


Figure I-12 : Incremental capacity of a Graphite / NMC Li-ion cell obtained at the rate of C / 25. (This Figure originates from this thesis work).

However, in this case, it is possible to correspond a given peak to a given electrode by analyzing the IC curves obtained on the potentials of the electrodes. This measurement is only possible by having the cell voltage measurements and the potential measurements of each electrode at the same time. The presence of a reference electrode into a commercial cell will make it possible to obtain such measurements.

1.4. Objectives of the study

The performance of Li-ion batteries is highly dependent on the physicochemical and thermal properties of the materials of the various components, among which electrodes and electrolyte play a leading role. A better understanding of the reaction mechanisms and limiting factors associated with the use of these materials under the various usage conditions of the battery remains essential.

Moreover, this research theme represents a significant economic interest regarding the growth of the Li-ion battery market for more applications. Despite intensive research undertaken over the last 25 years, the subject is far from being fully understood. Understanding fundamental problems such as the influence of the electrolyte or the structure of the electrodes is a decisive factor in extending the life of the batteries currently marketed.

The overview of current bibliographic research shows that some areas have already been the subject of fruitful research. For example, many researchers have been interested in the mechanism of lithium metal deposition on the graphite electrode. Nevertheless, some clues were only very rarely explored. This is the case in particular with the use of reference electrodes into commercial cells in order to monitor the evolution of electrode potentials. This technique will be studied in this work, in addition to the multiple post-mortem techniques used.

Indeed, the losses of performance observed at low temperatures are often, by misuse of language, quite easily attributed to the mechanism of reduction of lithium. In the same way, irreversible capacity losses measured after storage at high temperatures are often explained by the SEI growth. However, in these various conditions of use, the composition of the materials of the electrochemical system is very little considered.

In this way, the objective of this thesis is to consolidate new knowledge on the aging mechanisms of Li-ion accumulators, on the one hand, under the conditions of cycling at low temperature and, on the other, in the high temperature storage conditions.

I. State of art and objectives of the study

II. Experimental setup

This second chapter is structured into four sections.

The characteristics of the commercial Li-ion cell studied in this thesis is presented in the first section. Common specifications mentioned in the datasheet as well as geometrical dimensions are detailed. The different applications addressed by this commercial cell are quoted.

The second section is devoted to the protocol corresponding to the introduction of Li metal used as reference electrode into the commercial cell. The step of the preparation as well as of the insertion of reference electrodes are detailed. This section ends with the presentation of preliminary electrochemical tests (protocols and results) performed with the instrumented cell.

The protocols of check-up tests used in this thesis, for measuring the evolution of the performance of cells, after cycling tests or calendar storage phase, are described in the third section.

This Chapter ends with the description of the different post-mortem investigations techniques required in the framework of this research work. The protocol of cells dismantling as well as the required precautions and the operating principle specific to each method are detailed. In addition, a brief state of the art about the interest of each of the methods in Li-ion batteries field is presented.

2.1. Li-ion cells reference studied: C/NMC KOKAM 16 Ah

KOKAM is one of pioneers in supplying small to large format Super Lithium Polymer Battery (SLPB) cells ranging from 2 Ah to 240 Ah. Commercial high power Li-ion polymer pouch cells (Kokam SLPB 78205130H) have been chosen by the laboratory to be used in this work. With a nominal capacity of 16 Ah, an energy density of 146 Wh/kg and a weight of 406 g, this Li-ion cell has the following geometrical dimensions: width = 207 mm, length = 137 mm and thickness = 7.8 mm. The Alternating Current – Internal Resistance (AC-IR) measured at 1 kHz is indicated at 1.1 mΩ in the datasheet. A voltage range of 2.7 – 4.2 V is allowed with a nominal voltage at 3.7 V. Additional specifications are presented in **Table II-1**.

Items	Specification			Remarks
Current (maximum)	Charge	Continuous	48 A (3 C)	@ 23 ± 3 °C
		Continuous	128 A (8 C)	@ 23 ± 3 °C
	Discharge	Peak	240 A (15 C)	<10 sec, > SOC 50 %
Cycles @ 1C/1C, to 80 % of capacity	Up to 4000			80 % DOD or 3.4 ~ 4.1 V (@ 23 ± 3 °C)
Charging Temperature ^(a)	0 ~ 10°C		<0.3 C	
	10 ~ 35°C		< 3 C	
	35 ~ 45°C		< 1 C	
Discharging Temperature ^(b)	-10 ~ 55°C			
Storage Temperature	-20 ~ 25°C		1 year	@ 60 ± 25 %
	25 ~ 40°C		3 months	R.H.
	40 ~ 60°C		<1 week	SOC 50 ± 5 %

Table II-1 : Common specifications of 16 Ah commercial Li-ion pouch cells (Kokam SLPB 78205130H).

(a) : 0 °C ↓ or 45 °C ↑ : charge protection temperature (shut down required)

(b) : -10 °C ↓ or 55 °C ↑ : discharge protection temperature (shut down required)

On one hand, the datasheet mentions that this commercial Li-ion cell addresses applications as diverse as transportation (fully / plug-in electric vehicles), military, aviation, industrial machinery, marine, grid storage or telecom.

On the other hand, it recommends to do not charge the cell over 0.3 C in a temperature range of 0 ~ 10 °C. Besides, the storage time in a temperature range of 40 ~ 60 °C must be less than one week.

In applications such as defense, space and other systems under severe conditions, batteries may be used at low temperature, typically below 10 °C [87].

So it is necessary to study further the impact of current rates on aging mechanisms limiting the performance under such conditions.

Besides, the use of Li-ion cells in electric vehicles, for example, requires long rest time (calendar aging) and regular charge / discharge phases (cycling aging). Similar operating conditions can also be encountered in photovoltaic applications. It is therefore imperative to perform protocols including long-time storage at high temperature in the aim to test the battery in ‘real life’ conditions.

Concerning materials of this commercial Li-ion cell, graphite is the negative electrode and Nickel Manganese Cobalt (NMC) oxide is the positive electrode while the separator is constituted by microporous polyethylene film. **Figure II-1** illustrates a photograph of a 16 Ah Kokam cell.



Figure II-1 : 16 Ah commercial Li-ion cell (Kokam SLPB 78205130H).

The internal order of electrodes in this cell is shown in **Figure II-2**. The cell stack consists in total of 25 positive electrodes and 24 negative electrodes. Besides, 23 positive electrodes are coated on both sides and the two ones at the ends of the stack are coated only on one side, while all negative electrodes are coated on both sides by active material. The separator exhibits z-folding. The electrodes in the middle of the stack (#10-17) will be used to take samples for further analysis.

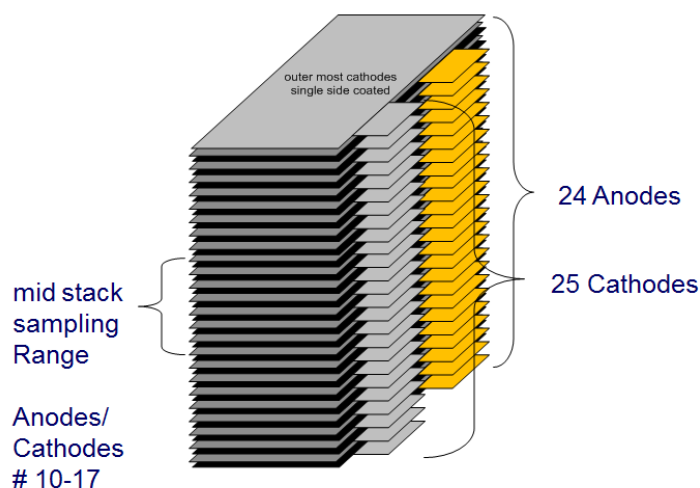


Figure II-2 : Internal order of electrodes inside the 16 Ah commercial Li-ion cell (Kokam SLPB 78205130H).

The surface of a single positive and negative electrode is respectively 199.97 cm^2 and 206.01 cm^2 as pointed out in **Figure II-3**. The current collector at the negative electrode is based on copper with a tab made of nickel-plated copper, while the current collector and the tab at the positive electrode is made of aluminum.

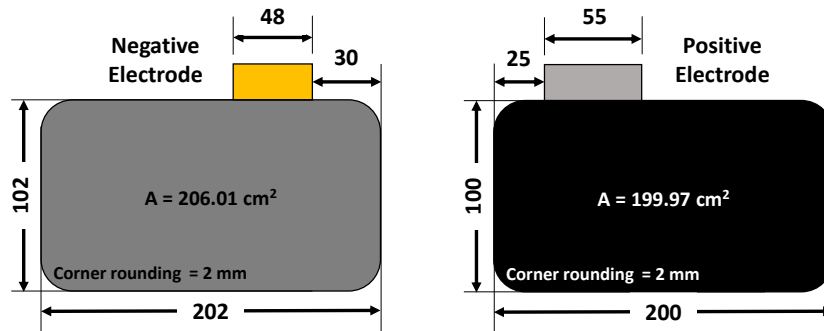


Figure II-3 : Dimensions of positive and negative electrodes in the 16 Ah commercial Li-ion cell (Kokam SLPB 78205130H).

2.2. Insertion of reference electrodes into 16 Ah commercial Li-ion pouch cells

2.2.1. Types of reference electrodes

The electrochemical couple constituting the reference electrode must present a plateau of potential on a wide range of SOC and be stable in the electrolyte. The major difficulty is to have a stable potential over time in order to perform reliable long-term characterizations during electrochemical tests.

In Li-ion cells, different redox couples are used as a reference electrodes: biphasic insertion materials [88] like $\text{LiFePO}_4/\text{LiFePO}_4$ (LFP) ($U_{\text{plateau}} = 3.32 \text{ V vs. Li}^+/\text{Li}$), $\text{Li}_4\text{Ti}_5\text{O}_{12}/\text{Li}_7\text{Ti}_5\text{O}_{12}$ (LTO) ($U_{\text{plateau}} = 1.55 \text{ V vs. Li}^+/\text{Li}$) as well as alloys [89; 90] such as $\text{Li}_x\text{Bi}/\text{Bi}$ ($U_{\text{plateau}} = 0.80 \text{ V vs. Li}^+/\text{Li}$), $\text{Li}_x\text{Al}/\text{Al}$ ($U_{\text{plateau}} = 0.36 \text{ V vs. Li}^+/\text{Li}$).

LTO was previously validated by M. Dollé and al. [91] as the reference electrode optimum material for performing three electrodes impedance measurements. The Li_xAl alloy is less reactive than lithium and then less reactive to the electrolyte and it should therefore have a more stable potential over time than Li^+/Li [92].

The most commonly material used as reference electrode is metallic lithium Li^+/Li ($U_{\text{plateau}} = 0 \text{ V vs. Li}^+/\text{Li}$) even though its stability may be insufficient over long time [93; 94; 95; 96]. The SEI which will be spontaneously developed on the surface of reference electrode could shift its measured potential and impedance, over a longer period of time. Nevertheless, for short time characterizations, it is still efficient.

2.2.2. Insertion protocol of reference electrodes

2.2.2.1. Preparation of the reference electrode

The insertion of reference electrodes is performed inside a glove box under Argon atmosphere. A lithium metal foil having a surface of 16 mm^2 ($4 \text{ mm} \times 4 \text{ mm}$) and a thickness of $50 \mu\text{m}$ is used as reference electrode.

Before being inserted into the cell, the lithium metal is folded in half and protected by a Celgard 2400 separator film for security reasons. The material thus covered by the separator is then drenched into the electrolyte in order to ensure that lithium is perfectly glued to the separator. This electrolyte, commonly called LPX, is based on 1:1:1 wt ethylene carbonate (EC), dimethyl carbonate (DMC) and ethyl methyl carbonate (EMC) + 1 LiPF_6 . The amount of electrolyte (LPX) soaked on the separator which envelops the reference electrode remains very negligible compared to the total amount of the original electrolyte present inside the commercial cell. An influence of the LPX electrolyte on the results is therefore unlikely.

The reference electrode is then attached on a copper grid having a thickness of $38 \mu\text{m}$. The gluing is reinforced with an Epoxy resin. The copper grid is then in turn stuck to a nickel tab as illustrated in **Figure II-4**. A Kapton tape (in orange) is positioned to hold the separator in place.

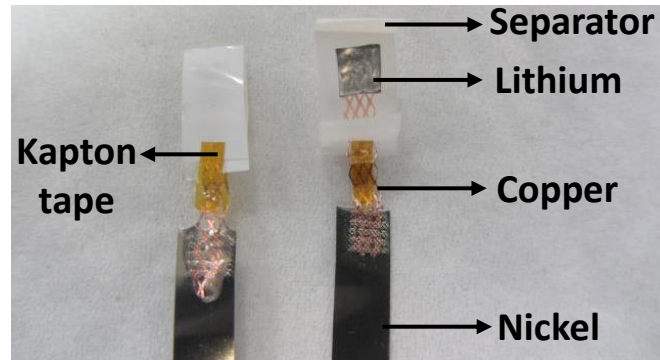


Figure II-4 : Illustration of the reference electrode which will be inserted inside the 16 Ah commercial Li-ion cells (Kokam SLPB 78205130H).

Based on the lithium metal density (0.534 g/cm^3), on its standard atomic weight (6.941 g/mol) and considering the Faraday's law ($F = 96485 \text{ C/mol}$), it is possible to estimate the amount of lithium in the electrode compared to commercial cell capacity. Then, normalized to the nominal capacity of the commercial cell (16 Ah), this value is 0.033 Ah and represents only 0.21 % of the capacity of the commercial cell.

The presence of the copper grid prevents the formation of loops in electrochemical impedance spectroscopy (EIS) measurements, which may be caused by the corrosion of Nickel if the tab was inside the cell [97; 98; 99; 100; 101].

2.2.2.2. Insertion of the reference electrodes

First of all, for safety reasons, cells are discharged at room temperature until the minimum voltage of 2.7 V is reached. Using a ceramic knife, a cutting of about 1 cm is performed on the side of the cell casing by which it is possible to access to the electrodes.

A ceramic clamp is used to spread the components so as to insert the reference electrode in the middle of the stack between opposite electrodes. This operation is done very quickly and very delicately.

Figure II-5 presents the required steps to respect in order to insert reference electrodes into commercial cells. Once the reference electrode is introduced into the battery, external incisions are isolated.

A mold is then prepared in order to encapsulate the cell, always for safety reasons and/or prevent any leakage. The solution for successful encapsulation is composed of a mixture of 104 g of epoxy resin and 42 g of epoxy hardener. The cell is then placed in the mold and the solution is then poured over it until the entire cell is completely submerged. Thereafter, the cell is allowed to stand in this configuration for 24 hours. The cell is fully resined at the end of the instrumentation and it can be taken out of the glove box for electrochemical measurements. The second reference electrode is used as backup.

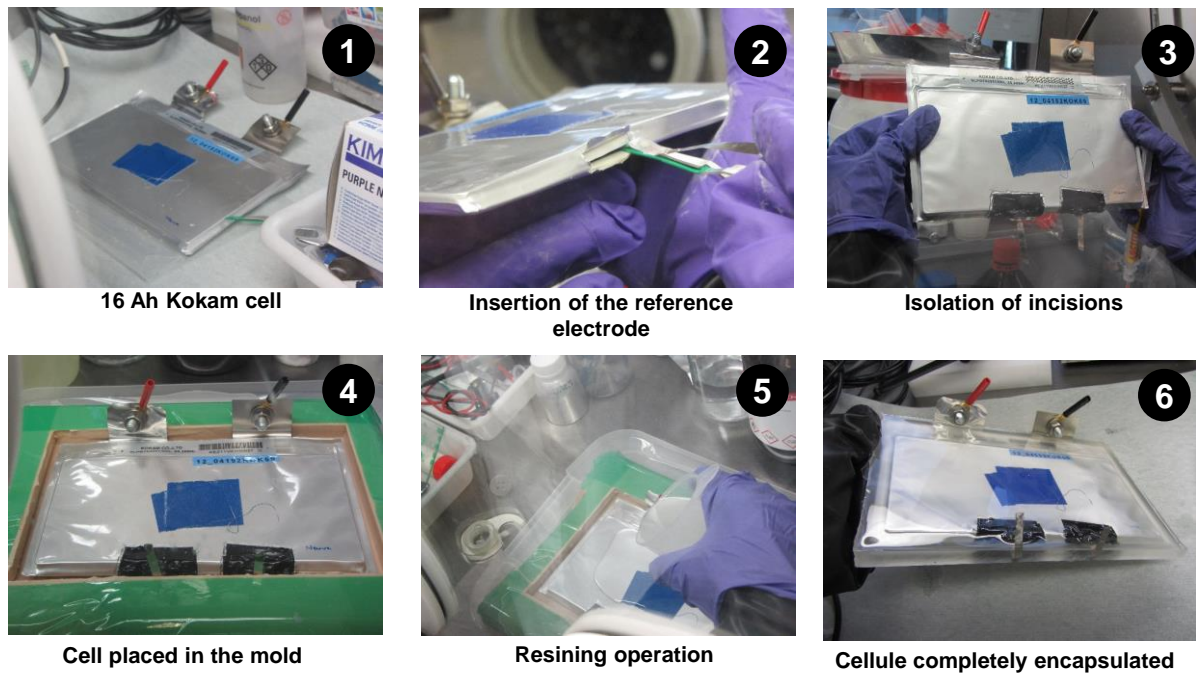


Figure II-5 : Steps of insertion of reference electrodes into the 16 Ah commercial Li-ion cell (Kokam SLPB 78205130H).

As seen in **Figure II-6**, EIS measurements were performed before and after the introduction of the reference electrode into the commercial, in order to evaluate the impact of the instrumentation. These EIS measurements were carried out, while the cell was inside the glove box, using a Solartron equipment (30 kHz – 10 mHz with $\Delta V = 10$ mV).

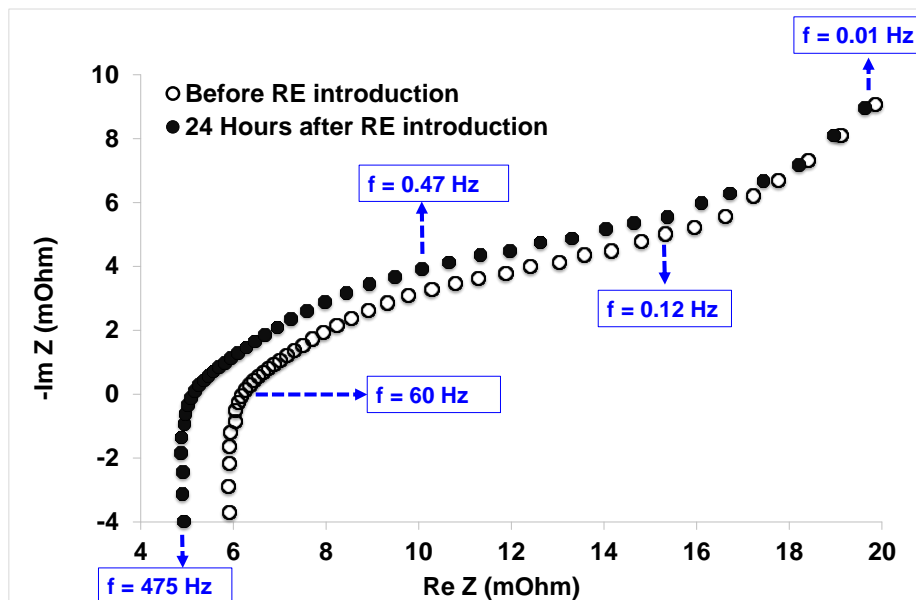


Figure II-6 : Impedance curves before and after the insertion of the reference electrodes into the first commercial 16 Ah pouch-cell.

A small difference between the two impedance measurements can be noticed. It should be noted that after the first measurement, the cell was disconnected from the Solartron in order to introduce the reference electrode.

Then, after the instrumentation, the cell was again reconnected to perform the other impedance measurement. This difference in behavior can therefore be attributed to the operations of disconnecting and reconnecting of the cell between the two measurements. However, this did not disrupt the measurements obtained with cycling tests.

In this work, three fresh 16 Ah commercial Li-ion cells have been instrumented with reference electrodes at different periods from one another. The first one has been subjected to electrochemical tests performed respectively at 25 °C, 45 °C and 5 °C at different C-rates in order to ensure proper functioning of the inserted reference electrodes. Data obtained from these measurements at the beginning of life (BOL) have been used in order to develop an aging prognostic model based on electrodes behaviors. After the preliminary electrochemical tests, the same instrumented cell was used for cycling tests at low temperature in order to follow up the evolution of both electrodes in such conditions.

The other two instrumented cells have been subjected to calendar aging at high temperature for complementing the understanding of aging mechanisms involved in such conditions.

2.2.3. Electrochemical tests with the instrumented commercial cell

Electrochemical tests are performed respectively at 25 °C, 45 °C and 5 °C at different charge C-rates (respectively 1 C, C / 25, C / 10, C / 5, C / 2, 2 C, 2.5 C and 1 C) as presented in **Figure II-7**.

For all the C-rates except C / 25, the charge ends with a constant voltage (CV) phase which starts when the cut-off voltage of 4.2 V is reached and stops when the current drops to C / 20. Unfortunately, the test bench used for these measurements does not allow to charge over 40 A. The discharge rate is set in all cases at 1 C.

The protocol is established such that the electrical test begins and ends with a charge at 1 C, the discharge being always at 1 C, so as to limit the impact of the discharge rate and especially to compare the evolution of both electrodes potentials and the capacity between the beginning and the end of the test. This will make it possible to check the stability of the reference electrode for each temperature.

As a result, no derivation of the reference electrode is then observed during these preliminary tests. There is a good correspondence between the cell voltage measured at the cell terminals and the voltage calculated by the difference of the potential between both electrodes which is obtained with the reference electrode.

The protocol also includes pulses with a duration of 30 s implemented in charge as well as in discharge at a rate of 1 C at every 10 % of SOC in order to measure the internal resistance. Note that as capacity, energy or self-discharge, internal resistance is also an important criteria for the determination of the performance of Li-ion batteries.

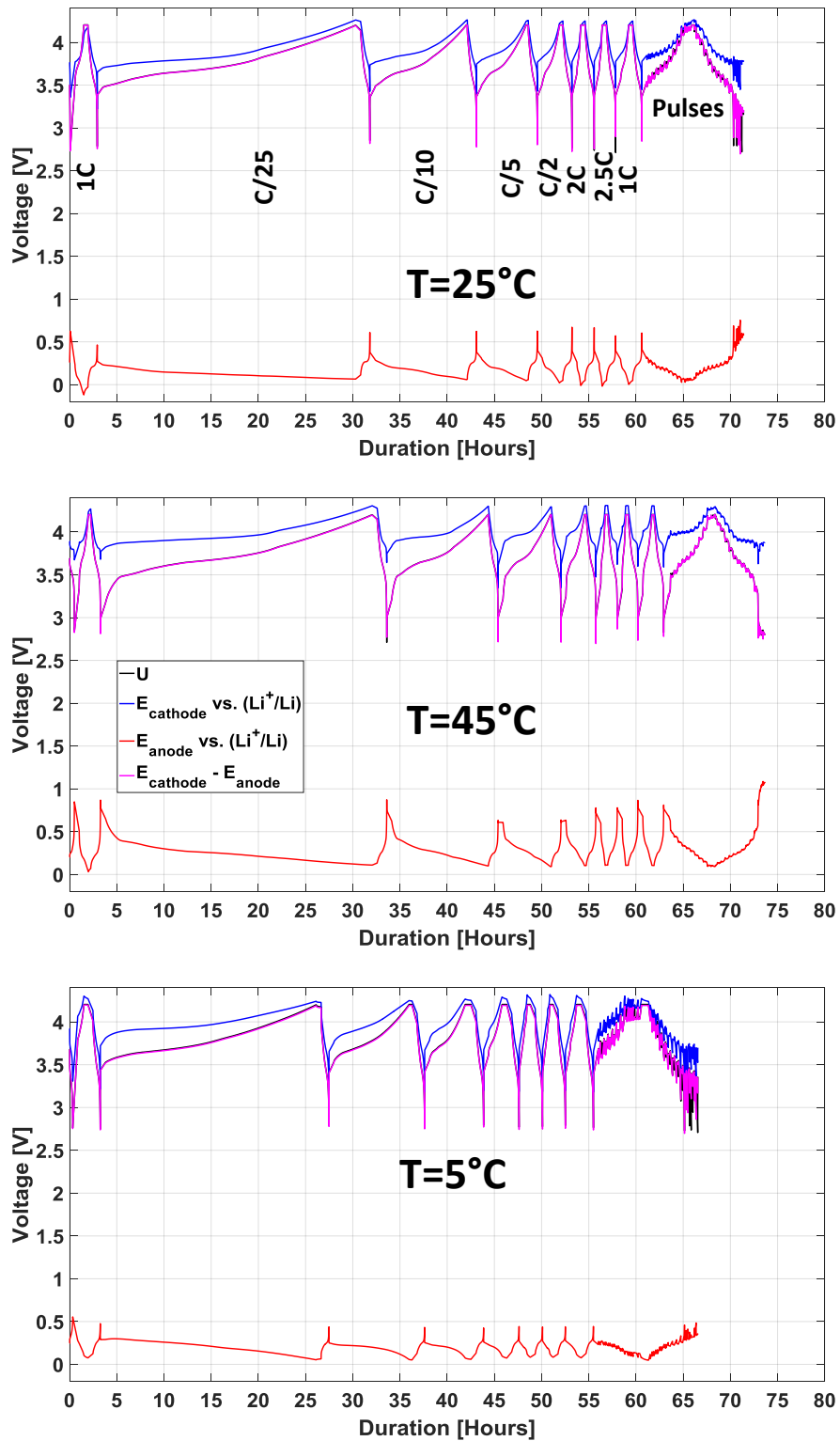


Figure II-7 : Electrochemical characterizations performed at 25 °C, 45 °C and 5 °C at different C-rates with the 16 Ah commercial Li-ion cell instrumented with Li metal as reference electrode.

2.2.3.1. Evolution of the potential of electrodes

Figure II-8 illustrates, for the three temperatures, the evolution of the potential of both electrodes (compared to the Li potential) in function of C-rates in charge.

A resistive effect is remarked on the behavior of the potential curves corresponding to the positive electrode when C-rates become higher. This trend is less distinct on the behavior of the negative potential curves.

As it can be perceived, the potential curves of the positive electrode are higher at 5 °C than at the other two temperatures. It is worth mentioning that the potential of the graphite, contrary to what was expected, does not go below the 0 V / Li even when the current is equal to 40 A (2.5 C). Note that the small hook, ascent on the negative potential and descent on the positive potential curves, represents the CV phase. It is well observed at 25 °C and at 45 °C, although the difference of behavior between the first C-rate (in dark blue) at 1 C and the last C-rate (in claret red).

At 5 °C, the ascent hook on the negative electrodes is less pronounced for high C-rates and besides, less outstanding difference of behavior between the first and the last C-rate at 1 C is distinguished.

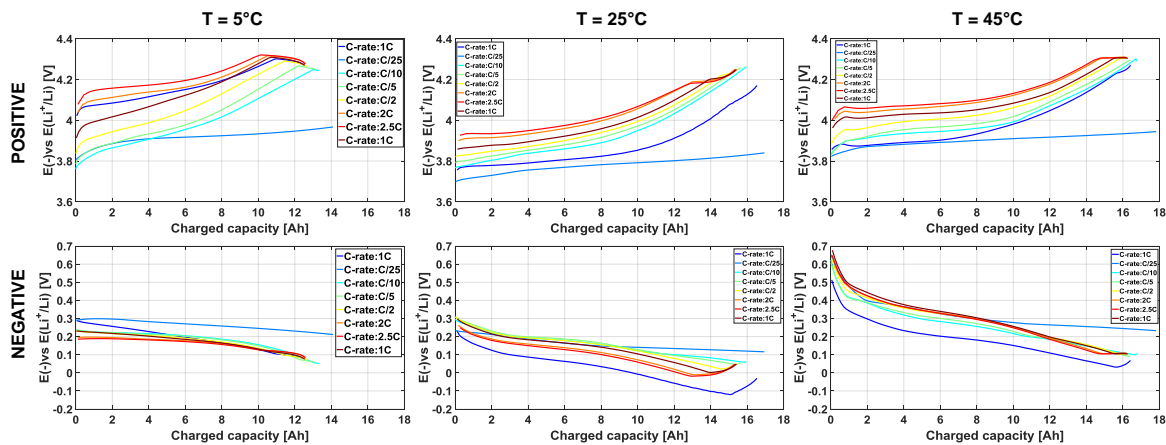


Figure II-8 : Evolution of the potential of each electrode compared to the lithium potential in function of the charge current and the temperature.

Figure II-9 shows the evolution of the potential of both electrodes (compared to the Li potential) in discharge. This figure demonstrates that the Li electrode does not drift at all in discharge. Note that the discharge rate has been maintained at 1 C. This observation permits to confirm that the difference of the potential behavior observed between the first and the last charge at 1 C is not due to a derivation of the reference electrode. There may be another effect to elucidate. The correct operation of the reference electrode could be therefore validated.

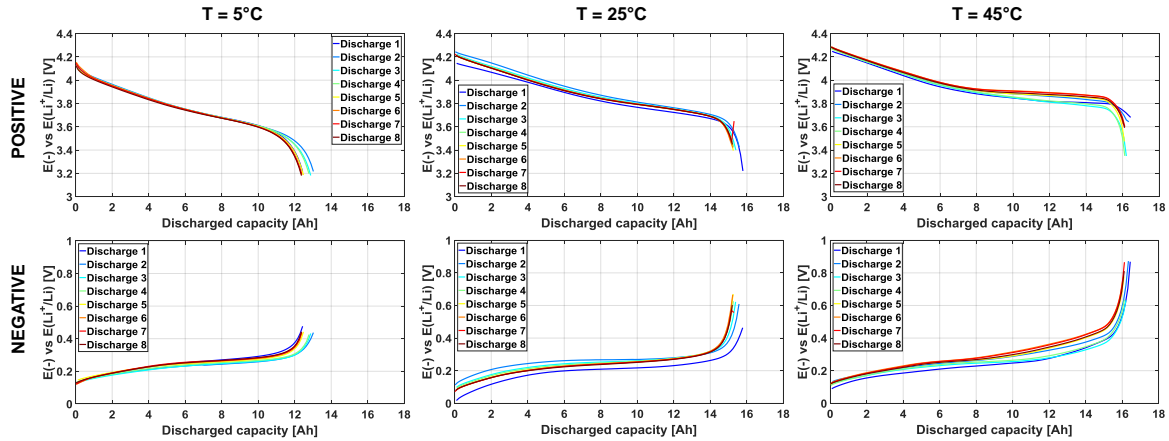


Figure II-9 : Evolution of the potential of each electrode compared to the Li potential in function of the discharge current (1 C) and the temperature.

2.2.3.2. Internal resistance measurements

The internal resistance of a cell can be determined by alternating current (AC) methods, electrochemical impedance spectroscopy methods, thermal loss methods and direct current pulse methods as reported by H.-G. Schweiger et al. [102].

In this work, the internal resistance is calculated by pulses measurements.

B. V. Ratnakumar et al. [103] demonstrated that the direct current resistance is easy to implement in the pulse conditions. This measurement is influenced by the duration and the current of the pulse and the SOC of the cell. In addition, reduction of pulse current and pulse duration was determined to reduce the influence of discharge and charge on creating a feigned² resistance [102].

H.-G. Schweiger et al. [102] performed charge pulses with a duration between 0.1 s and 18 s and a C-rate in the range of 1 C to 20 C. B.V. Ratnakumar et al. [103] employed a current pulse with of a magnitude at 0.4 C and with a duration of 60 s. Besides, the authors observed similar trends with pulses programmed for 60 s as with shorter pulses of 30 ms duration.

In our case, as illustrated in **Figure II-10**, the internal resistance at different SOC is determined by direct current methods by applying a constant current charge / discharge pulse with duration of 30 seconds and a current rate of 1 C. A rest period of 30 minutes is set up after the pulse in order to reach the open circuit voltage (OCV) for a specified SOC.

² A feigned resistance refers to the resistance calculated with the increase of the pulse length. This feigned increase of internal resistance is mainly caused by the voltage change due to the discharge or charge of the measuring pulse.

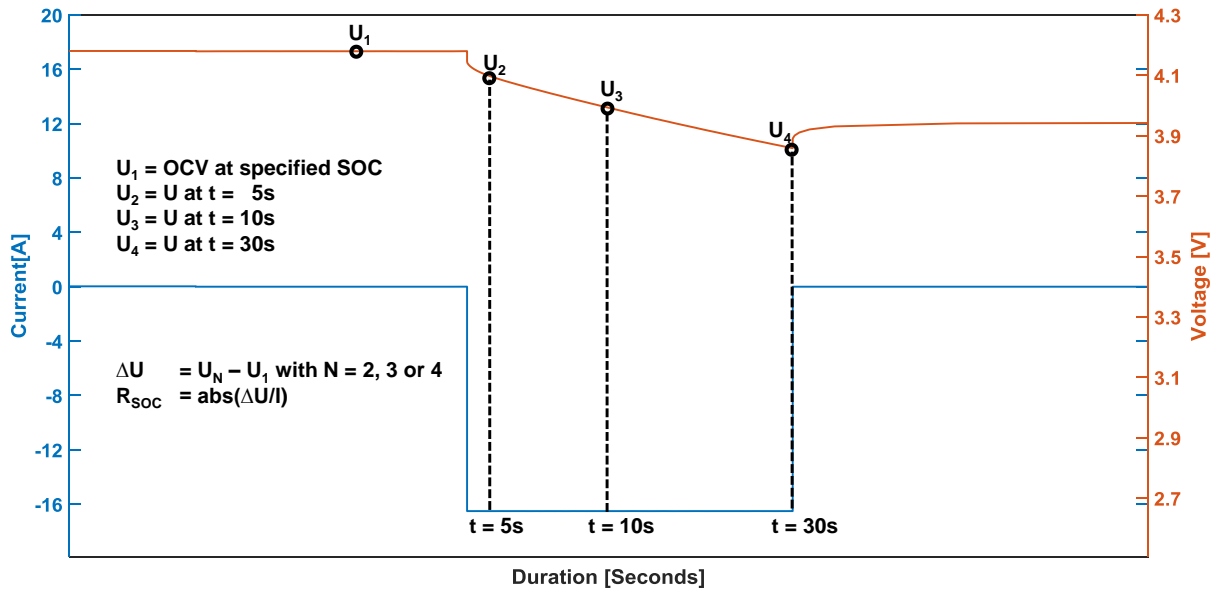


Figure II-10 : Measurement of internal resistance according to direct current test procedure.

Figure II-11 compares internal resistance measurements obtained directly from the cell and those calculated by the addition of the resistance of each electrode which is determined through the reference electrode, respectively at 25 °C, 45 °C and 5 °C. Internal resistance (measured at 10 s) is expressed in function of the SOC and the duration of the pulse.

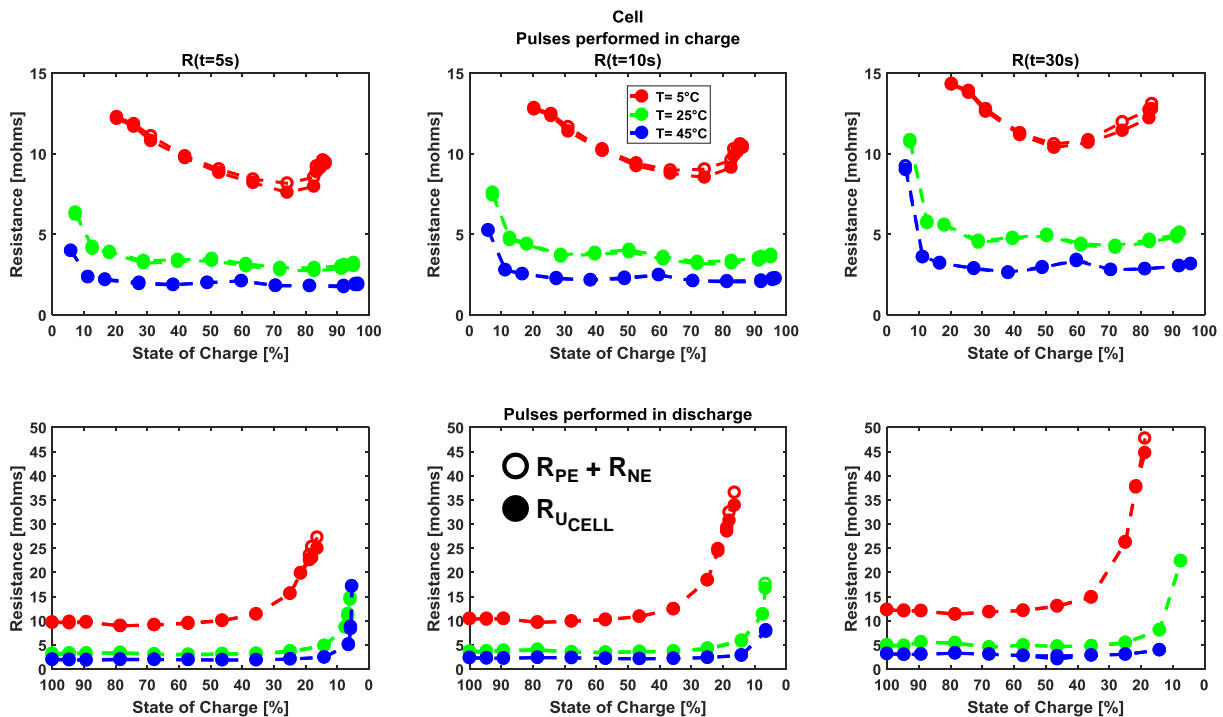


Figure II-11 : Comparison of the DC resistance obtained directly from cell and those calculated by addition of the DC resistance of each electrodes for different temperatures.

Note that values of the SOC are estimated in function of the total charged or discharged capacity at the end of the charge or discharge pulses, respectively. Thus, at 5 °C, as the resistance increases faster than at 25 °C or 45 °C, the voltage limits are more rapidly reached. As a result, the corresponding capacity is lower than at the other temperatures and consequently the range of SOC is reduced.

There is a good correspondence between values of resistance directly measured from the cell and those calculated based on the resistance of each electrode. It should be pointed out that the data are well superimposed.

These results are consistent with the literature, about the influence of the temperature behavior on the internal resistance [104; 105; 106]. As expected, the value of DC internal resistance increases when pulse duration increases

Figure II-12 and **Figure II-13** respectively show resistance measurements corresponding to the positive and to the negative electrode at the beginning of life in function of the SOC and for different temperatures. It is noticeable that at 5 °C the resistance is higher than at other temperatures, in charge as in discharge.

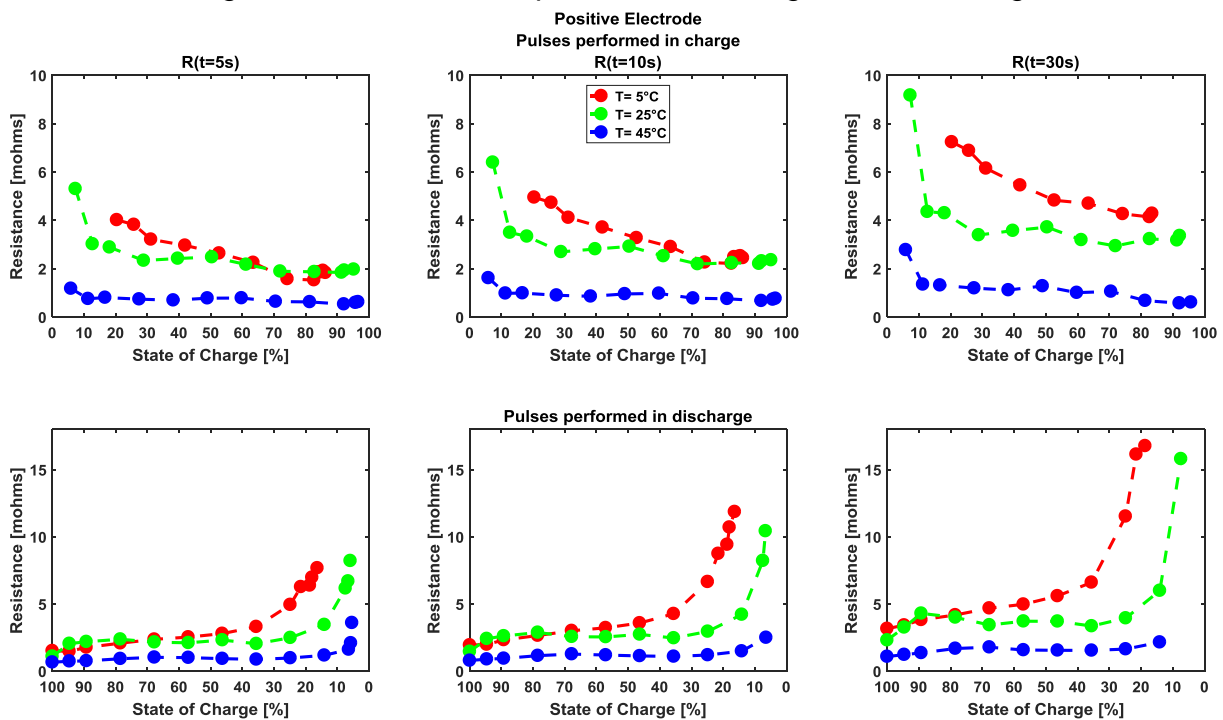


Figure II-12 : DC resistance corresponding to the positive electrode in function of the SOC and for the different pulses duration (5s, 10s and 30s).

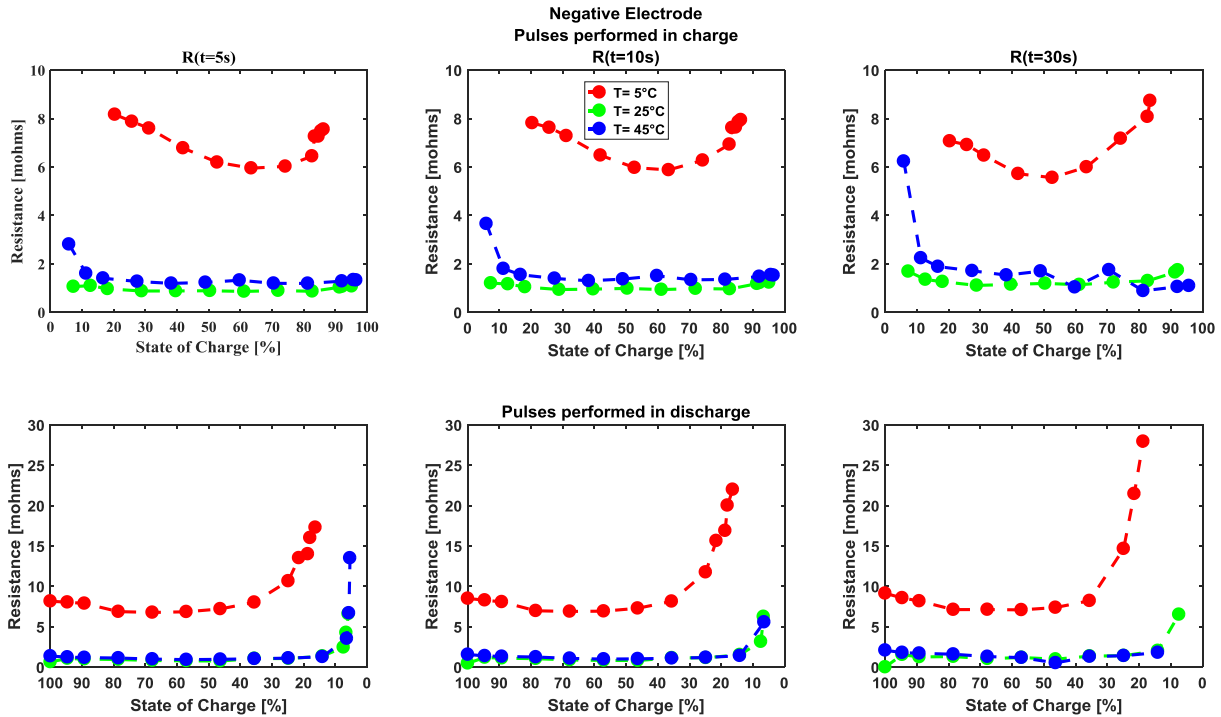


Figure II-13 : DC resistance corresponding to the negative electrode in function of the SOC and for the different pulses duration (5 s, 10 s and 30 s).

It is possible to construct a DC resistance mapping as a function of the temperature and the SOC. For that, we considered that the resistance varies linearly as a function of the SOC to interpolate the measurements of resistances over the whole range of SOC [105]. For the temperature variations, we applied an exponential type interpolation between 5 °C to 45 °C. **Figure II-14** shows the mapping, obtained with interpolations in function of the temperature and the SOC, of DC resistances measured during pulses in charge at 10 s, corresponding to the complete cell and to each electrode.

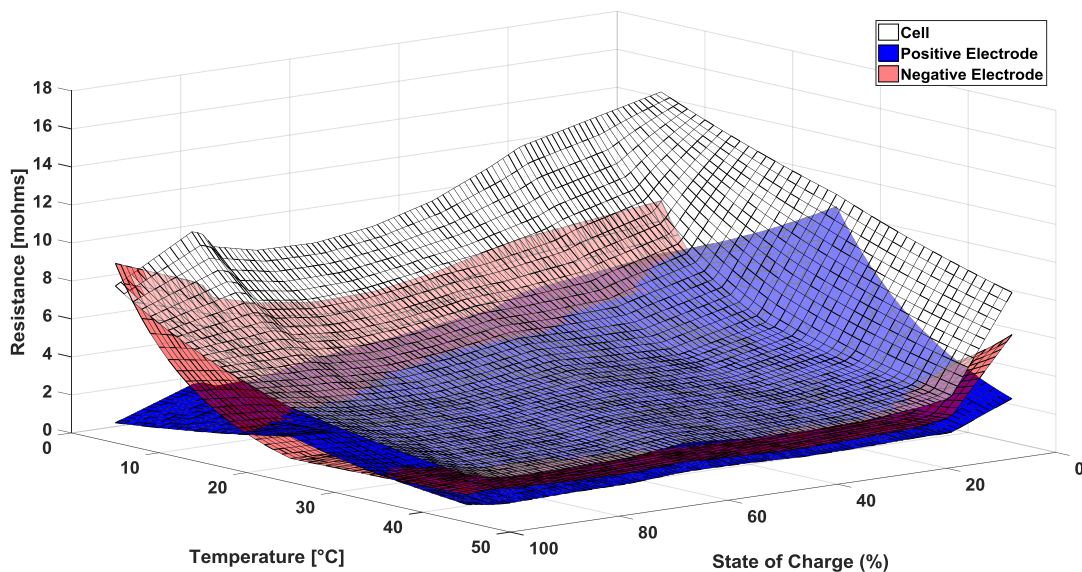


Figure II-14 : Mapping of DC resistances measured during pulses in charge at 10 s

2.3. Protocols of check-ups for aging tests

A considerable part of the aging data of lithium-ion batteries used in this thesis originates from the European Mat4Bat project [107]. In this project, one of the objective of Europe was to increase battery lifetime by 20 to 30 % for electric vehicles. For this reason, Li-ion batteries were tested according to protocols used in automotive firms. In the field of automotive, there are standard tests to control the aging of batteries. The majority of them are defined by scientific communities, such as the FreedomCar consortium, to facilitate comparison of the results of major United States manufacturers.

Within the framework of the Mat4Bat Project, two purely electrical tests, namely check-up tests at 25 °C, have been defined for controlling the evolution of the state of health of cells after each aging phase. They are based on standard models but have also some specificities.

2.3.1. Extended Check-Up test (ECU)

As illustrated in **Figure II-15**, Extended Check-Up (ECU) test, which lasts nearly 6 days, is programmed at the beginning of the life (BOL) of the cell, in the middle of life (defined here by a state of health of 90 %) and then at the end of life (EOL) (defined by a state of health of 80 %). This protocol includes different sequences that are described in the following paragraphs.

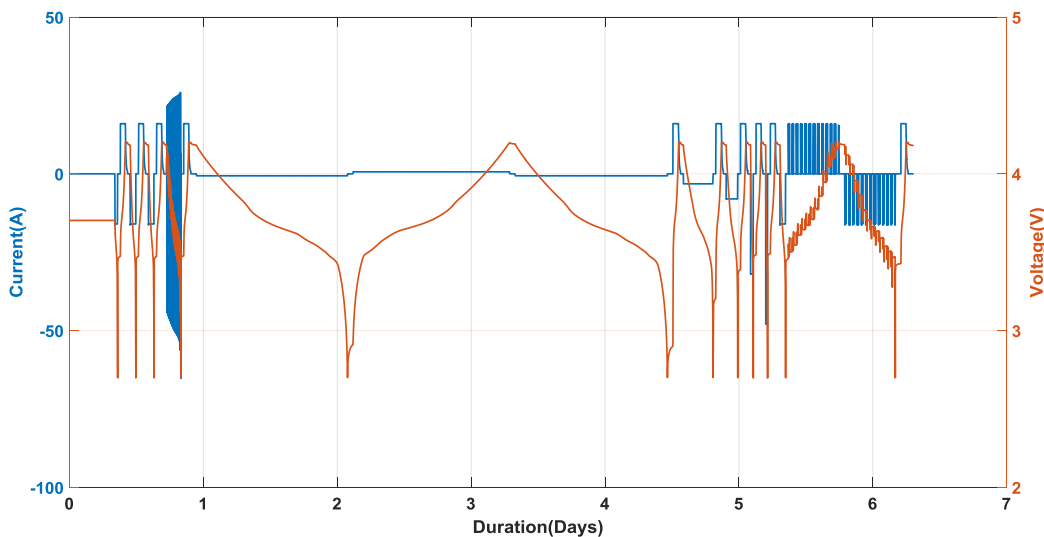


Figure II-15 : Protocol of Extended Check-Up (ECU) test performed at 25 °C at the beginning of life, at the middle of life and at the end of life of the commercial cell.

2.3.2. Short Check-Up (SCU)

With a shorter duration than the ECU, the Short Check-Up (SCU) only incorporates a part of sequences included in the ECU. Capacity tests at different C-rates other than at 1 C have been removed. Pulses are only performed in discharge. This regular test is necessary to evaluate the state of health of the Li-ion cells during aging. It is scheduled every 200 cycles.

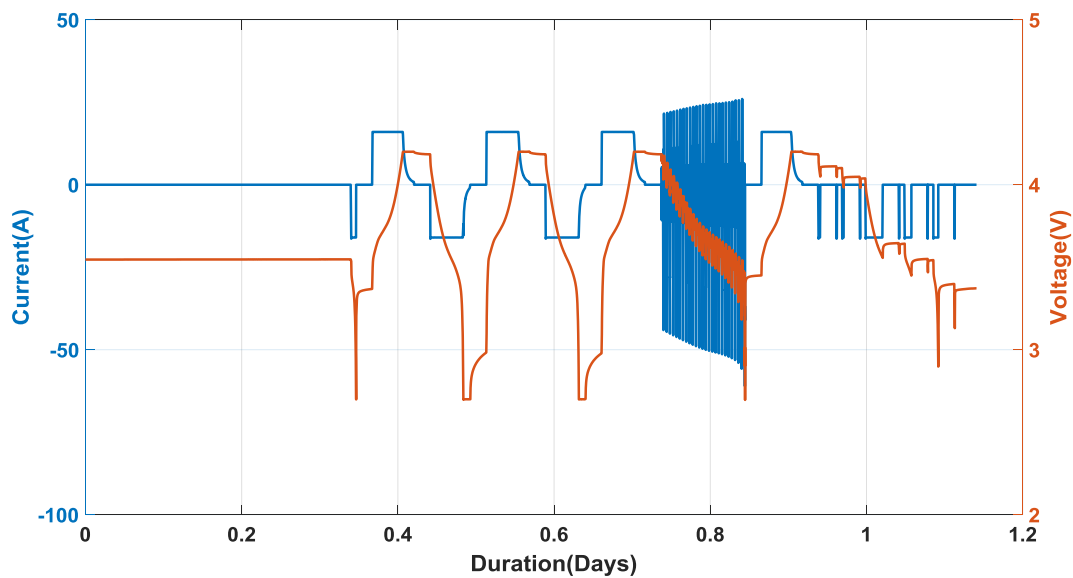


Figure II-16 : Protocol of Short Check-Up (SCU) test performed at 25 °C after every 200 cycles

The description of each sequence of the checkups can be found in the *Appendix of the Chapter 2*.

2.4. Post-mortem analyses

Post-mortem analyses are required in order to elucidate the functioning of electrochemical systems. To go further in the investigations of aging mechanisms affecting the performance of Li-ion batteries, post-mortem electrochemical and physico-chemical analyses with a diversity of complementary techniques have been used for this research work. Particular attention is focused on each stage: from the disassembly of cells to the post-mortem characterizations and then resulted interpretations, through various methods of sampling specific to each technique. An overview of the individual steps in post-mortem analysis is illustrated in **Figure II-17**. Fresh and aged battery materials as well as positive electrodes, negative electrodes, separators and electrolyte are meticulously inspected.

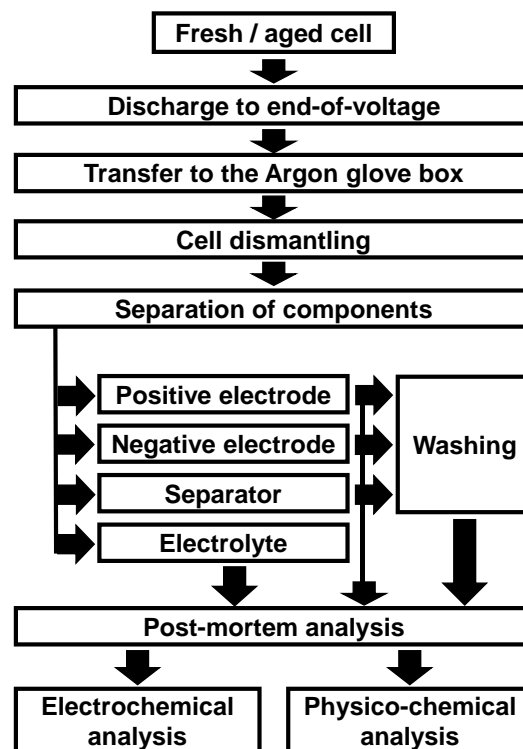


Figure II-17: Flow chart for the disassembly of Li-ion cells and analysis of components.

To pursue these investigations on aging mechanisms of Li-ion cells, two main complementary groups of post-mortem analyses can be considered as follows: electrochemical analyses of reassembled electrodes and physico-chemical analyses of harvested components. For pedagogical reasons, different physico-chemical methods required for this work have been featured to form additional categories as following:

- ❖ Electrolyte analysis
- ❖ Microscopy analysis
- ❖ Chemical methods sensitive to electrode surface
- ❖ Chemical methods sensitive to electrode bulk.

2.4.1. Protocol of dismantling

The opening of Li-ion batteries must be carried out at a full discharged state for safety reasons and under controlled atmosphere in order to avoid unexpected material changes not caused by aging. Hence, most experimenters discharge the cells until the end-of-voltage is reached (SOC = 0 %) prior to disassembly in an Argon-filled glove box [108; 109; 110; 111; 112]. The dismantling at lower potential energy state minimizes the amount of charge in the event of an accidental short circuit as reported by N. Williard et al. [113]. Note that battery dissections may cause abuse unfortunate events such as thermal runaway leading to an explosion [114]. So that, in some cases, a deep discharge consisting in discharging the cell until 0 V might be useful always for safety reasons [115].

In our case, cell sizes are measured in order to follow any size variation and hint for gas generation. Prior dismantling, cells are discharged at a rate of C/10 until 2.7 V is reached. The same discharge procedure is repeated after a rest of 5 minutes. This discharge procedure is to be performed 3 hours before the cell opening. Commercial Li-ion pouch cells are opened using a ceramic knife in an Argon-filled glove box for safety reasons. Careful cuts are realized avoiding shortcuts between electrodes to obtain reliable results. The electrode pairs in the middle of the pouch cells are considered for analysis as shown in the **Figure II-2**.

After disassembling the cell, both electrodes and separator are washed in pure high concentrated (99.999 %) dimethyl carbonate (DMC) as mentioned in different papers [108; 109; 110].

The washing procedure is useful to remove residual crystallized Li salts or non-volatile solvents in the aim of avoiding increasing the percentage of certain elements (Li, F, P) with some physico-chemical characterizations such X-Ray Photoelectron Spectroscopy (XPS) and thus biasing the interpretation.

Indeed, as reported by N. Williard et al. [113], if the electrodes are not cleaned, a given amount of electrolyte residue, mostly composed of a Li salt, will be left on the surface of the electrodes after evaporation of the organic solvents.

Moreover, as reported by T. Waldmann et al. [116], this washing procedure may reduce corrosion risks of the samples since LiPF_6 reacts with H_2O and O_2 . It will thus protect sensitive analytical equipment in the case samples would be exposed to air.

The nature of solvents and/or washing duration may influence results and then interpretations.

In 2007, D. P. Abraham et al. [117] supported that electronically insulating surface films formed on the surface of the anode can pore-clog or isolate graphite particles and therefore could lead to the capacity loss. The authors experimented that the capacity of aged negative electrodes could be restored by DMC rinsing.

In 2011, N. Williard et al. [113] evoked the fact that soaking disassembled electrodes in DMC or similar solvent may lead to an absence of particular SEI components.

More recently, L. Somerville et al. [118] demonstrated that DMC washing for 1 minute removes lithium fluoride (LiF) and lithium phosphofluorides (Li_xPF_y) functionalities from deeper strata of the SEI. Otherwise, when only visual inspections is required, it is not necessary to perform electrodes washing process.

2.4.2. Electrochemical characterizations of reassembled electrodes

Electrochemical measurements using reconstruction methods for electrodes built into half and full cells with reference electrode are powerful to determine the reversible capacity of each electrode, the lithium content in each one and obviously the SOC in the operation range. Electrochemical measurements with coin cells are suitable to investigate the influence of the electrolyte (solvents and/or additives) on the performance of the Li-ion cell.

First of all, N-Methyl-2-pyrrolidone (NMP) is used to remove the coating of one side from electrodes extracted from commercial cells so as to have only one active face. Some experimenters rather use laser blanking for removing coating [119].

Single components are then assembled in different types of laboratory coin cells under argon atmosphere for electrochemical characterizations as illustrated in the **Figure II-18**. It is very important to duplicate laboratory coin cells for each condition that is planned to be studied in order to verify the reproducibility of results.

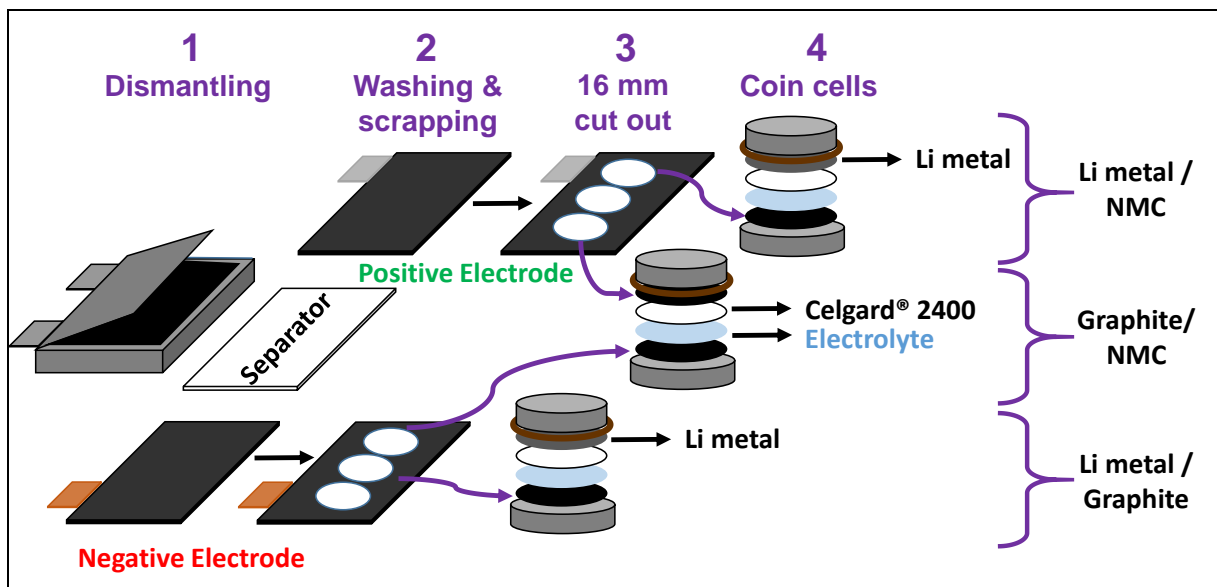


Figure II-18 : Scheme of the cell disassembly and coin cells types for post-mortem electrochemical analyses.

Coin half cells consist of graphite-based electrode (16 mm) or NMC-based electrode (16 mm) from the commercial cell and Celgard® 2400 separator (18 mm) with a metal lithium electrode used as counter electrode. For investigating the capacity of each electrode, we used the standard LPX electrolyte based on 1:1:1 wt

EC:DMC:EMC + 1 M LiPF₆. Note that the capacity of lithium De/Re-Intercalation into both graphite and NMC electrodes recovered from aged cells can be investigated with coin half-cells. For graphite/Li metal coin half cells, the first electrochemical test generally starts with a charge step in order to extract lithium from graphite (delithiation) whereas for the NMC/Li cells, the first test starts with a discharge to insert Li to the positive electrode (lithiation). The corresponding capacities are then the residual capacities of the electrodes.

Coin full cells consist of graphite-based electrode (16 mm), NMC-based electrode (14 mm) both from the commercial cell and Celgard® 2400 separator (18 mm). Different types of electrolyte based on solvents and additives can be used to study the influence of the electrolyte composition.

2.4.3. Physico-chemical characterizations of harvested electrodes

In this research work, physico-chemical methods have been selected in function of the aging mechanisms involved and available technical resources. **Figure II-19** presents the process of sampling and the scan ability specific to each post-mortem technique that has been used in this thesis.

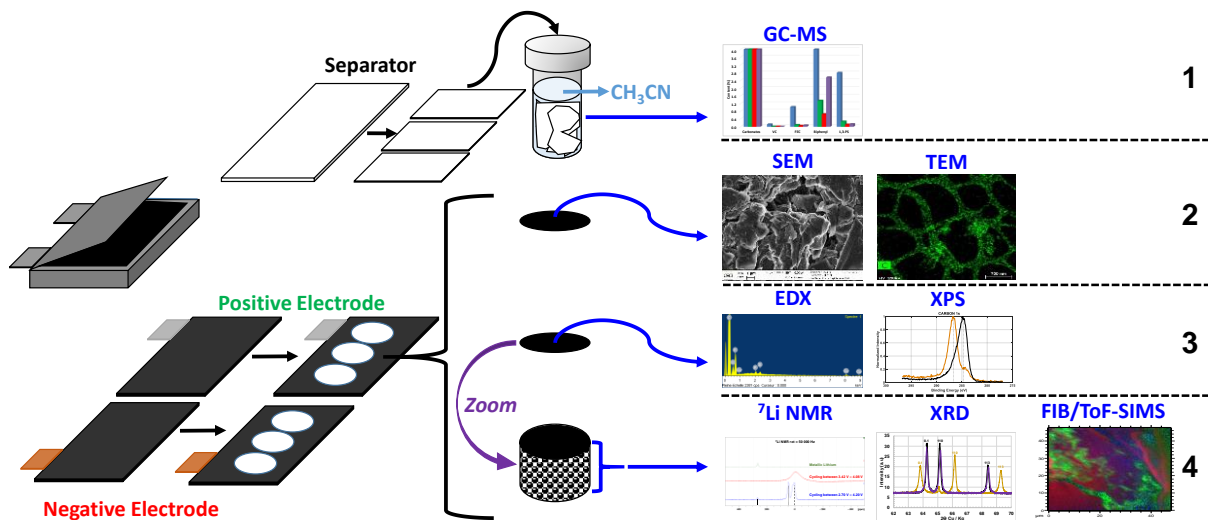


Figure II-19 : Overview of components inside the commercial 16 Ah Li-ion pouch cell and various methods of sampling specific to each physico-chemical method for post-mortem analyses. (1) Electrolyte analysis; (2) Electron microscopy methods; (3) chemical methods sensitive to electrode surface; (4) chemical methods sensitive to electrode bulk.

Original electrolyte from commercial Li-ion cells has been analyzed with Gas Chromatography – Mass Spectrometry (GC-MS).

Electron microscopy methods such as Scanning Electron Microscopy (SEM) and Transmission Electron Microscopy (TEM) are suitable for revealing the structure of smaller objects with a higher resolving power than light microscopes.

Energy Dispersive X-ray spectroscopy (EDX) and X-ray Photoelectron Spectroscopy (XPS) are used in order to determine the chemical composition of the analyzed area. These latest two techniques can be grouped and considered as chemical methods sensitive to electrode surface.

Lithium Nuclear Magnetic Resonance (^7Li NMR) has been used for detecting occurrence of metallic lithium deposition on graphite electrodes. X-Ray Diffraction (XRD) is usually applied for determining the state of lithiation of electrodes. *In situ* XRD analysis is also performed on the fresh electrode to create a “calibration” curve that links lattice parameters value with SOC values.

In addition, coupling Focused Ion Beam (FIB) to Time-of-Flight Secondary Ion Mass Spectrometry (ToF-SIMS) is used to inspect cavities / pores / inter-particles of graphite electrodes. ^7Li NMR, XRD and ToF-SIMS constitute the category of chemical methods sensitive to electrode bulk. Schematics of principle of each analysis method is given in the **Figure II-20** as reported by T. Waldmann et al. [116].

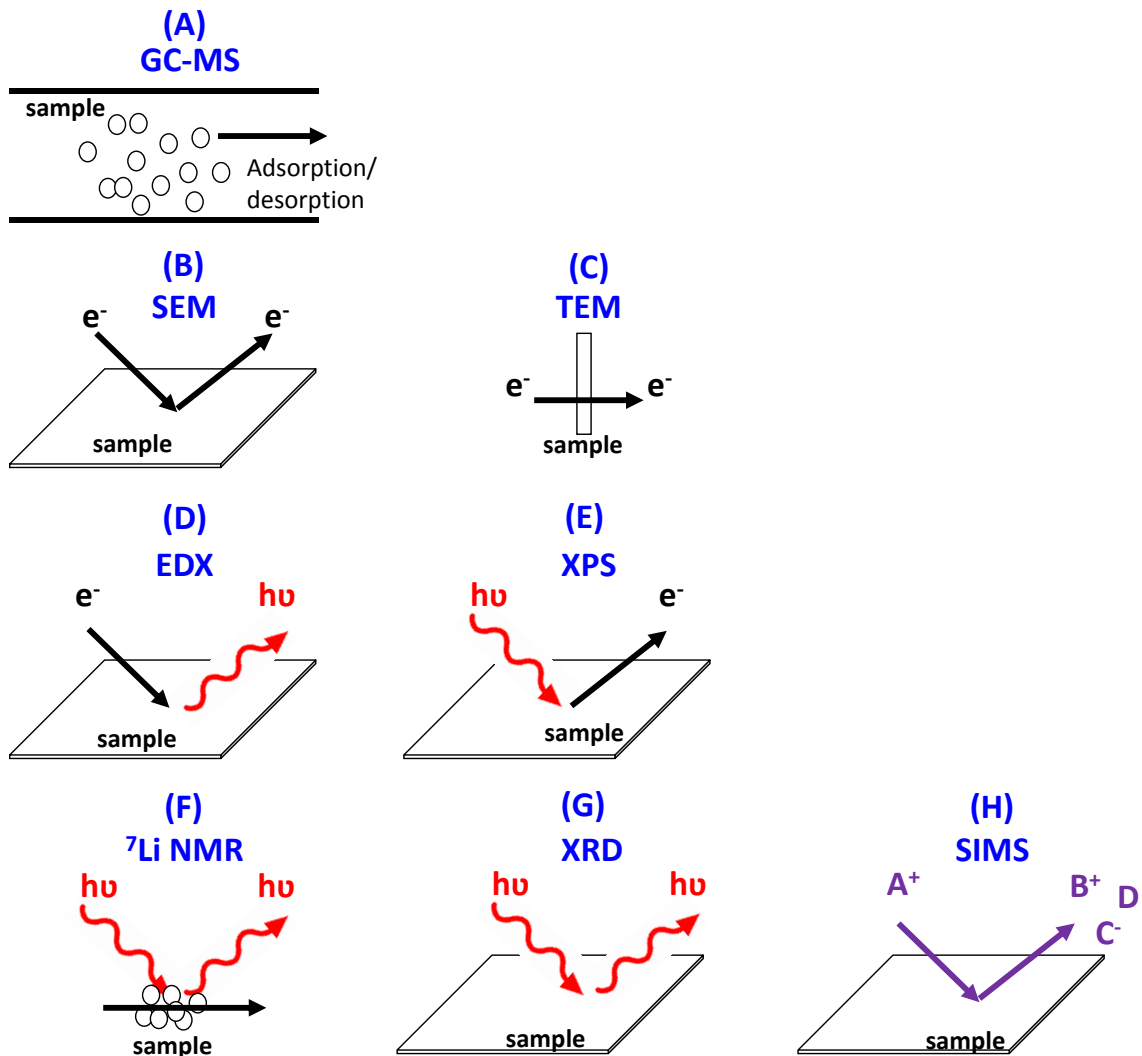


Figure II-20 : Schematics of principle of each analysis method.

2.4.4. Electrolyte analysis with GC-MS

The purpose here is to detect the components of the original electrolyte harvested from the commercial Li-ion cell and/or the gas generated in order to identify a possible correlation between the evolution of these components with aging and the aging mechanism involved. Many studies have implemented chromatography techniques to analyze electrolytes and gases generated during batteries aging.

In chromatography, the sample containing one or more species is carried by a mobile phase current (liquid, gas or supercritical fluid) in contact with a stationary phase (paper, gelatin, silica, polymer, grafted silica, etc.). The various constituents of the mixture travel at different speeds, causing them to separate. The separation is based on differential partitioning between the mobile and stationary phases (see in **Figure II-20 - A**) [116].

G. Gachot et al. [120] used Gas Chromatography – Mass Spectrometry (GC-MS) technique as a tool to explore highly volatile compounds originated from the electrolyte. In another paper [121], these same authors implemented the coupling of GC-MS and Fourier transform infrared (FTIR) analytical tools to detect gaseous and volatile soluble species recovered from a swollen commercial battery.

It is of course possible to couple gas chromatography to other methods such as Flame Ionization Detector (FID) for the quantification of detected elements [122] or Thermal Conductive Detector [123] (TCD) to identify inorganic gas in the generated gases.

In this paper, GC-MS was performed on samples harvested from the electrolyte. During the cell opening, a piece of separator was rapidly immersed in CH₃CN as a carrier solvent for at least 2 hours. Note that commercial cells usually do not have electrolyte excess so that during dismantling of the cell, the electrolyte could rapidly evaporate in the glove box. The solution is then transported to the GC-MS split / splitless injector without air exposure.

We note that the probability of some components of the electrolyte being quickly volatilized during the opening of the cell under Argon atmosphere is not negligible. The list of components identified from the original electrolyte is consequently not exhaustive. For this experiment, an Agilent GC-MS with a 30 cm column, an internal diameter of 0.25 mm and a film of 0.25 μm is used. The injector temperature is 280 °C. The furnace of the column passes from 40 °C to 200 °C at 10 °C/min. The result is given in total ion count (TIC) of the mass detector (model 5975C / electronic impact).

2.4.5. Microscopy analysis

2.4.5.1. Scanning Electron Microscopy

Scanning Electron Microscopy (SEM) still a suitable tool for providing high resolution images however that resolution may be limited by spherical aberration of the electron lenses [124]. The operating principle of a SEM equipment requires the exclusive using of electrons (see in **Figure II-20 - B**). The detector has a considerable influence on the image contrast since it collects either backscattered or secondary electrons.

SEM is used to observe the morphology of materials at their surface. The SEI growth on graphite electrode has been observed by T. Waldmann et al. [109] with SEM. Moreover, the morphology of Li depositions (dendritic, granular or foamy) has been distinguished by H. Honbo et al. [125] with images obtained from SEM. This method is often completed with Focused Ion Beam (FIB) technique for 3D visualizations.

In this paper, a SEM equipment with a transfer chamber is used to avoid exposure to the air, for surface analysis. SEM analyses are performed on samples of fresh and aged electrodes recovered from commercial Li-ion cells.

2.4.5.2. Transmission Electron Microscopy

In Transmission Electron Microscopy (TEM) technique, a beam of electrons is transmitted through the analyzed material to form an image (see in **Figure II-20 - C**). Higher acceleration voltages for the electrons are commonly used with this technique contrary to SEM. It is suggested that reducing the accelerating voltage and increasing acquisition speed are necessary to avoid the beam damage as demonstrated on NMC materials by F. Lin et al [126].

Unlike optical microscopes, the resolution is not limited by the wavelength of the electrons, but by the aberrations due to the magnetic lenses. Furthermore, TEM method requires a scrupulous samples preparation since the piece of the material to be analyzed needs to be as clean as possible and the thinner it is, the better it is for investigations.

In Li-ion batteries, TEM technique can be used to detect the phase of distribution in the electrode which provides insights to heterogeneous phase transformation mechanisms. In this context, Y. Shao-Horn [127] studied the phase transformations of O_3 and O_2 layered Li_xCoO_2 , $O_3 Li_xNiO_2$, $O_3 Li_xMnO_2$ and spinel $Li_x[Mn]_2O_4$ underwent during electrochemical cycling with TEM. Moreover, high-resolution TEM imaging can permit direct visualization of atomic arrangements and modifications associated with structural defects and modifications [128]. Some experimenters rather performed *In situ* TEM in order to get real-time live images for understanding the structural and chemical evolution during lithium reaction process [129; 130].

In this research, it is not planned to examine the lithiation process in Li-ion battery electrodes. We required to TEM technique to investigate the state of structural and chemical bonding especially in graphite electrode after aging of commercial Li-ion cells as complementary tool to SEM analyses.

2.4.6. Chemical methods sensitive to electrode surface

2.4.6.1. Energy Dispersive X-ray Spectroscopy

In general, as in our case, a scanning / transmission electron microscope is combined with an Energy Dispersive X-ray spectroscopy equipment for providing in the same time the chemical composition of the surface of the sample which is inspected with SEM / TEM, sometimes in the form of map superposed with SEM / TEM images.

In the literature, Z. Zeng et al. [96] performed *in situ* TEM combined with EDX mapping to visualize electrochemical lithiation and delithiation of Au anodes in a commercial LiPF₆/EC/DEC electrolyte for Li ion batteries. The presence of numerous internal pores in LiCoO₂ and graphite active particles has been observed with SEM/EDX equipment by S. J. Harris et al. [131].

Furthermore, EDX mappings allowed the localization of lithium deposition or dendrites [132; 133]. In recent past, M. Klett et al. [134] showed experimental evidence of uneven surface film formation across the depth of a porous graphite electrode from EDX mappings.

Note that the main principle in spectroscopy is that each element has a unique atomic structure allowing a unique set of peaks on its electromagnetic emission spectrum. With EDX, the sample being studied is irradiated with electrons and this incident beam leads to the emission of X-ray photons (see in **Figure II-20 – D**). The energy of released X-rays are characteristic of the atomic structure of the emitting element.

EDX is also useful for example to detect if any electrode has been contaminated during an electrochemical process by any element originating from the opposite electrode [109]. However, due to its low atomic mass and its low energy of characteristic radiation, Li is not detectable with EDX. ThermoFisher Scientific group [135] estimated that detecting lithium would require to build an EDX equipment with spectral performance of which the zero width should be lower than 30 eV and could discriminate a 52 eV energy event. Nonetheless, the minimum accelerating voltage in EDX is estimated between 3 kV and 5 kV.

2.4.6.2. X-ray Photoelectron Spectroscopy

X-ray Photoelectron Spectroscopy (XPS) is based on the principle of irradiating the sample with a beam of X-rays while measuring at the same time the number of electrons ejected from the material and the kinetic energy as shown in **Figure II-20 – E**. Only Hydrogen and Helium cannot be detected with XPS.

In post-mortem analyses for battery materials, XPS can be combined with ion sputtering to access the depth of the material. Unfortunately, XPS is limited in the range of nanometers of the surface. Thence, for battery electrodes, XPS cannot detect the material of the current collector.

Most of experimenters use XPS for investigating the chemical composition through the solid electrolyte interphase (SEI) which are developed on the surface of graphite electrode [136; 137; 138; 139; 140; 141].

Extensive chemical investigation are conducted with XPS in this study with the same objective than papers mentioned above. The aim is to analyze the chemical composition of the SEI formed on graphite electrodes after aging process and to compare with findings resulted from other post-mortem methods.

To do this, XPS spectroscopic analyses of the surface of graphite electrodes are carried out on a PHI Versaprobe II spectrometer. Spectroscopic and profilometric analyses of the SEI layer are performed with the following parameters: take-off angle = 45°, pass energy = 23.5 eV.

2.4.7. Chemical methods sensitive to electrode bulk

2.4.7.1. Lithium Nuclear Magnetic Resonance

Characteristics of Li inserted into carbon or deposited on its surface can be determined from Nuclear Magnetic Resonance (NMR). This method is able to characterize material in solid state as well as in liquid state. The sample is placed in a magnetic field. When subjected to electromagnetic radiation (radiofrequency), most often applied in the form of pulses, some atomic nuclei can absorb the energy of the radiation and then release it during relaxation (see in **Figure II-20 – F**).

In the literature, using a calibration of NMR spectra, R. Castaing et al. [142] were able to detect the presence of lithium fluoride (LiF), explaining 15 % of the electrode slippage, on both electrodes after cycling of Li₄Ti₅O₁₂|LiFePO₄ Swagelok (commercial name of a 3-electrode cell device) cells.

W.-C. Oh [143] used ⁷Li NMR to analyze Li inserted into artificial carbon material.

From the electrolyte point of view, the thermal decomposition of Li battery electrolytes composed of LiPF₆ in organic carbonates was studied by W. Li and Brett L. Lucht's group [144; 145].

In this thesis, Solid-state Magic Angle Spinning (MAS) NMR measurements were performed on a Bruker AVANCE DSX 200 MHz spectrometer (4.7 T, ⁷Li Larmor frequency $\nu_0 = 77.78$ MHz) equipped with a 1.3 mm Bruker CPMAS probe head. The ⁷Li MAS NMR spectra were recorded at different MAS spinning frequencies in the range 36 – 60 kHz with direct ⁷Li excitation.

Different repetition delays for transient accumulation were tested in the range of 1 to 30 s in order to obtain quantitative data. A ⁷Li 90°-pulse width of 2.2 μ s was used, corresponding to the nucleus magnetization turn angle of about 75-80°. High power proton decoupling was also used but did not improve the quality of the spectra since proton and lithium are not directly linked neither through bond nor through space interactions. All spectra were acquired with room temperature bearing air, corresponding to a sample temperature in the range of 50 – 70 °C.

Aqueous LiCl solution was used as a chemical shift reference set to 0 ppm. A sample of Li metal was recorded in order to measure its chemical shift (265 ppm). For illustration of ionic Lithium, a sample of Li_3PO_4 was also recorded.

2.4.7.2. X-Ray Diffraction

X-Ray Diffraction (XRD) is an analysis technique based on X-ray diffraction by the material, especially when it is crystalline. XRD is an elastic diffusion that means without loss of photon energy as seen in **Figure II-20 – G**.

In Post-Mortem analysis, XRD technique is usually used for investigating structural changes of electrodes materials after aging.

XRD measurements are performed in order to verify the structure and the state of lithiation of both negative and positive electrodes before and after aging. Samples of both electrodes are analyzed.

Not washed samples ($\Theta = 14$ mm) are recovered from electrodes and protected by a well dried Kapton film. X-ray diffractograms are recorded with a BRÜKER D8 Advance apparatus using $\text{Cu K}\alpha$ radiation.

In situ XRD analysis is also performed on the fresh NMC to create a “calibration” curve that links lattice parameters value with SOC values [146; 147; 148; 149]. So, the lithium rate of the aged cathodes can be estimated using the lattice parameters of the structure after aging.

For this experiment, powder of NMC is recovered by scratching the fresh electrode, washed five times with NMP and rinsed two times with DMC and then mixed with 30 % wt of super P (carbon black). It is cycled against lithium in conventional liquid electrolyte *in situ* XRD cell connected to a VSP Bio-Logic EC Lab cycler unit.

The cycling protocol consists in an alternation of 2 steps: a 2 hours step of cycling at C/20 and 4 hours of relaxation. An X-Ray diffractogram is acquired during the last 3 hours of each relaxation step. This is repeated until the end of charge at 4.3 V vs. Li and the end of discharge at 2.6 V vs. Li.

2.4.7.3. Focused Ion Beam / Time-of-Flight Secondary Ion Mass Spectrometry

Basically, the Time-of-Flight Secondary Ion Mass Spectrometry (ToF-SIMS) is a ionization method that allows molecular surface analysis. The surface of the sample is bombarded by a pulsed source of mono or multi-atomic primary ions (Ga^+ , Au^+ , C_60^+ ...) having an energy of a few keV. As a result, secondary ions are emitted from the first surface monolayer of that material (see in **Figure II-20 – H**).

The latter ions are focused and accelerated with the same kinetic energy in the analysis tube. It is the physical principle of the ToF analyzer that analyzes in parallel all the secondary ions emitted. The mass spectra obtained represent the intensity of the secondary ions as a function of their masses. The use of a ToF analyzer makes it possible to obtain a very good mass resolution. By means of a device for scanning the primary ion beam, it is possible to obtain a mapping of the various molecular elements and species present on the surface, with sub-micron resolution.

Though being a surface sensitive technique, ToF-SIMS is thoroughly used for the study of the surface of bulk materials. In this context, by performing an *in situ* focused ion beam (FIB) cut to access to the depth of the sample, it is then possible to explore chemical composition of the bulk of the material. That is an original way to carry out an *in situ* FIB cut in the analysis chamber of a ToF secondary ion mass spectrometer.

Note that ToF-SIMS is a sophisticated technique that allows a better understanding of the SEI chemical structure. C. G. Marxer et al. [150] reported that ToF-SIMS analysis is more sensitive than the XPS, particularly for the detection of fluorine, for which the yield is very high.

E. Peled's group are pioneers in the use of ToF-SIMS measurements applied for Li-ion materials. In 2000, they demonstrated, by using ToF-SIMS measurements, direct evidence for the existence of polymers (or long oligomers) in the SEI formed on Highly Oriented Pyrolytic Graphite (HOPG) in LiPF₆ - EC, DEC solutions; a (CH₂)_n sequence was proved [151]. Heavy organic fragments (up to 900 g/mol) were found mainly at the surface of the basal SEI. The thickness of the SEI on the basal plane was found to be 3 – 5 times smaller than that on the cross section. In another paper [152], they showed that the SEI on the cross-section is dominated by lithium and fluorine while the passivation film on the basal plane is more composed of organic materials.

In this study, chemical investigation in the understanding of mechanisms involved have been performed with ToF-SIMS combined with *in situ* FIB, as successfully used in a previous work [153]. Samples were transferred directly from the glovebox to the IONTOF ToF-SIMS preparation chamber by using a sealed transfer vessel to avoid exposure to air. Here, the aim was to analyze in depth electrodes samples recovered from aged commercial cells. Analyzes were essentially performed in negative polarity mode because most of elements (Carbon, Phosphorus, Fluorine, Oxygen) are more sensitive to "negative" ionization except for the lithium which is however relatively well detected.

In order to extract maximum information from FIB-SIMS analysis, a data processing protocol for images is proposed. The raw image corresponding to the substrate (addition of signals C/C2/C3 and so on) is retained. The carbon may come from the SEI layer but especially from graphite particles, in particular the fragments C2/C3 and so on. For elements in smaller quantities (Li, F, P, O), in connection with SEI, the corresponding images are normalized with respect to the "graphite" image. This minimizes contrast related to topology.

III. Study of aging mechanisms at low temperature

This third chapter is divided into five main sections.

General cycling conditions and results obtained in the framework of the Mat4Bat project, from which a considerable part of the aging data used in this thesis originate from, are described and commented in the first section of this chapter.

The second subdivision is focused on the cycling aging performed at low temperature. The protocol of the test as well as the evolution of the capacity during cycling and the evolution of the internal resistance after cycling are reported.

Ante-mortem analyses based on cycling measurements obtained from the commercial cell instrumented with Li metal as reference electrode are detailed in the third section of this chapter.

Results obtained from different post-mortem techniques required in the investigation of the aging mechanism studied in this chapter and the corresponding interpretations are presented in the fourth part. The state of health of cells as well as that of electrode, and also the influence of the electrolyte as well as that of films formed on graphite electrode are minutely investigated.

This Chapter ends with a schematic model representing the aging mechanism involved. This representation has been proposed based on results obtained in this study.

3.1. Cycling aging

3.1.1. Cycling aging conditions

Within the framework of the Mat4Bat project, several research institutes have carried out an aging campaign of Li-ion batteries under different conditions, both in cycling and in calendar. The objective of Europe is to increase battery lifetime by 20 to 30 % for electric vehicles, with a target of 4000 cycles of 80 % depth of discharge (DoD).

It is with this perspective that experimenters decided to develop appropriate aging test protocols and conditions which are therefore adapted to the actual use profiles of electric vehicles. In line with this, for studying cycling aging, the following conditions were studied:

- 3 conditions for temperatures : 5 °C, 25 °C and 45 °C
- 4 SOC windows : { 0 – 80 %; 0 – 100 %; 10 – 90 %; 20 – 100 %}
- 3 charge current rates: 1 C (16 A), 2 C (32 A) and 3 C (48 A).

The discharge current rate remains set at 1 C. The consortium decided to manage cycling SOC windows in function of the corresponding voltage thresholds, in order from one part to simplify the tests protocol and avoid then experimental errors from one experimenter to the other, but also from the other part because this is exactly the way that current BMS (Battery Management System) deal with the end-of-charge / end-of-discharge thresholds.

The correspondence between voltage thresholds and the SOC limits were measured in the beginning of life (BOL) at 25 °C, and so these voltage ranges do not correspond rigorously to specified SOC ranges for other temperatures, C-rates, or after aging. Once again, the aim was to simplify the protocol while being representative of the current BMS.

SOC windows (%)	Voltage thresholds (V)
0 - 100	2.70 - 4.20
0 - 80	2.70 – 3.98
10 - 90	3.42 – 4.08
20 - 100	3.49 – 4.20

Table III-1 :Correspondence between SOC windows and voltage thresholds at 25 °C as defined for cycling aging by the consortium in the Mat4Bat project.

In total, 42 Li-ion cells with a capacity of 16 Ah were distributed accordingly to different research institutes such as Vlaamse Instelling voor Technologisch Onderzoek (VITO), Zentrum für Sonnenenergie–und Wasserstoff-forschung (ZSW), Karlsruhe Institute of Technology (KIT), École d'ingénieurs généraliste La Rochelle (EIGSI), CIDETEC and CEA (Commissariat à l'Énergie Atomique et aux Énergies Alternatives). Experimental conditions for cycling aging are illustrated in **Table III-2**.

T (°C)	Charge / discharge current rates			Total
	1C = 16 A	2C = 32 A	3C = 48 A	
5	1C/1C {10-090%} x2 CIDETEC	1C/1C {10-090%} x2 CIDETEC	1C/1C {10-090%} x2 CIDETEC	6
25	1C/1C {10-090%} x2 CEA 1C/1C {00-100%} x2 KIT	2C/1C {10-090%} x2 ZSW 2C/1C {00-100%} x2 KIT	3C/1C {10-090%} x2 ZSW 3C/1C {00-100%} x2 KIT	12
45	1C/1C {00-080%} x2 VITO 1C/1C {20-100%} x2 VITO 1C/1C {10-090%} x2 CEA 1C/1C {00-100%} x2 EIGSI	2C/1C {00-080%} x2 VITO 2C/1C {20-100%} x2 VITO 2C/2C {10-090%} x2 CEA	3C/1C {00-080%} x2 VITO 3C/1C {20-100%} x2 VITO 3C/1C {10-090%} x2 CEA 3C/3C {10-090%} x2 CEA 3C/1C {00-100%} x2 EIGSI	24
Total	14	12	16	42

Table III-2 : Illustration of experimental conditions for cycling aging of commercial Li-ion cells in the framework of the Mat4Bat project.

3.1.2. Results of cycling aging tests

3.1.2.1. Evolution of the capacity over aging

Figure III-1 presents the evolution of the state of health (SOH) of commercial 16 Ah Li-ion cells in cycling aging in function of the full equivalent cycles (FEC) in the framework of the Mat4Bat project. Note that FEC are calculated by dividing the total discharged capacity throughput measured at the end of the cycling test per the nominal capacity which is 16 Ah. This method allow to make reliable comparisons between different conditions of cycling.

At 45 °C, cycling between [3.49 V – 4.20 V] (20 % - 100 %) and [2.70 V – 4.20 V] (0 % - 100 %) leads to a more accentuated aging state while cycling between [3.42 V – 4.08 V] (10 % - 90 %) and [2.70 V – 3.98 V] (0 % - 80 %) presents a similar trend in aging.

The end-of-voltage of 4.2 V appears here to have a negative influence on the performance of cells. Contrary to what it was expected, it seems that cycling between [2.70 V – 4.20 V] (0 % - 100 %) is less degrading than cycling between [3.49 V – 4.20 V] (20 % -100 %) even though in the first case the DoD is more important.

It may be assumed that the proportion of calendar aging in the second case would be more important considering the fact that the cycling duration is shorter and therefore faster than in the case of complete cycling. The cell would therefore spend more time at higher SOC, knowing that the calendar aging is accelerated with high SOC.

It is clear that the choice of the minimum and maximum limits of the SOC windows has a strong impact on the loss of performance. For all SOC windows conditions, a low influence of the charge C-rates emerges. It has been possible to perform up to 5000 FEC with the condition [3.42 V – 4.08 V]. Finally, above 80 % of the SOH, aging curves show rather a linear trend while beyond 80 %, a sudden break in slope is observed whatever the operating conditions.

III. Study of aging mechanisms at low temperature

At 25°C, as expected, fully cycling leads to a pronounced aging state than cycling between [3.42 V – 4.08 V] (10 % - 90 %). There is a less evident influence of the charge C-rate for both cycling strategies. It has been able to perform cycling over 4000 FEC without observing the SOH going below 70 %.

At 5 °C, there is a clear influence of the charge C-rate between 1 C and 2 C, but much less between 2 C and 3 C. The loss of capacity is abrupt at the beginning of aging and then seems to stabilize whatever the C-rate conditions.

Since this behavior is quite specific and interesting to investigate, we decided to go further in the understanding of the aging mechanisms observed during cycling aging test at low temperature (5 °C).

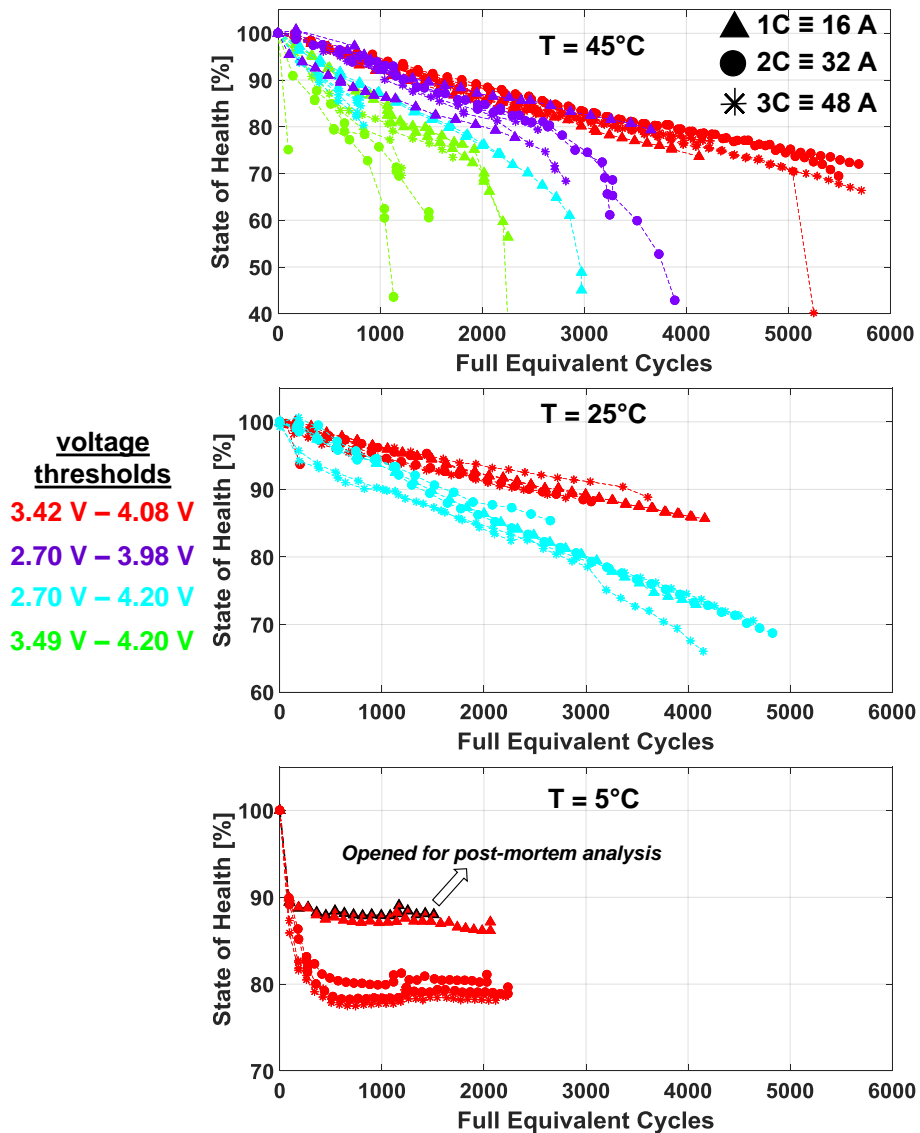


Figure III-1 : Evolution of the SOH of commercial 16 Ah Li-ion cells in cycling aging in the framework of the Mat4Bat project.

3.1.2.2. Evolution of the internal resistance over aging

Another indicator of the SOH of the cell could be the internal resistance. For our approach, information about internal resistance is considered only as an instrument for a SOH evaluation but is not really used for measuring the state of aging.

Note that as discussed in the previous chapter, the internal resistance at different SOC is determined by direct current methods by applying a constant current charge / discharge pulse with duration of 30 seconds and a current rate of 1 C.

We choose here in the **Figure III-2** to represent the evolution of the increase of DC resistance over aging as function of the capacity decrease and the FEC.

DC resistances were measured with pulses performed in discharge at a rate of 1 C, at 10 seconds and at 40 % of SOC.

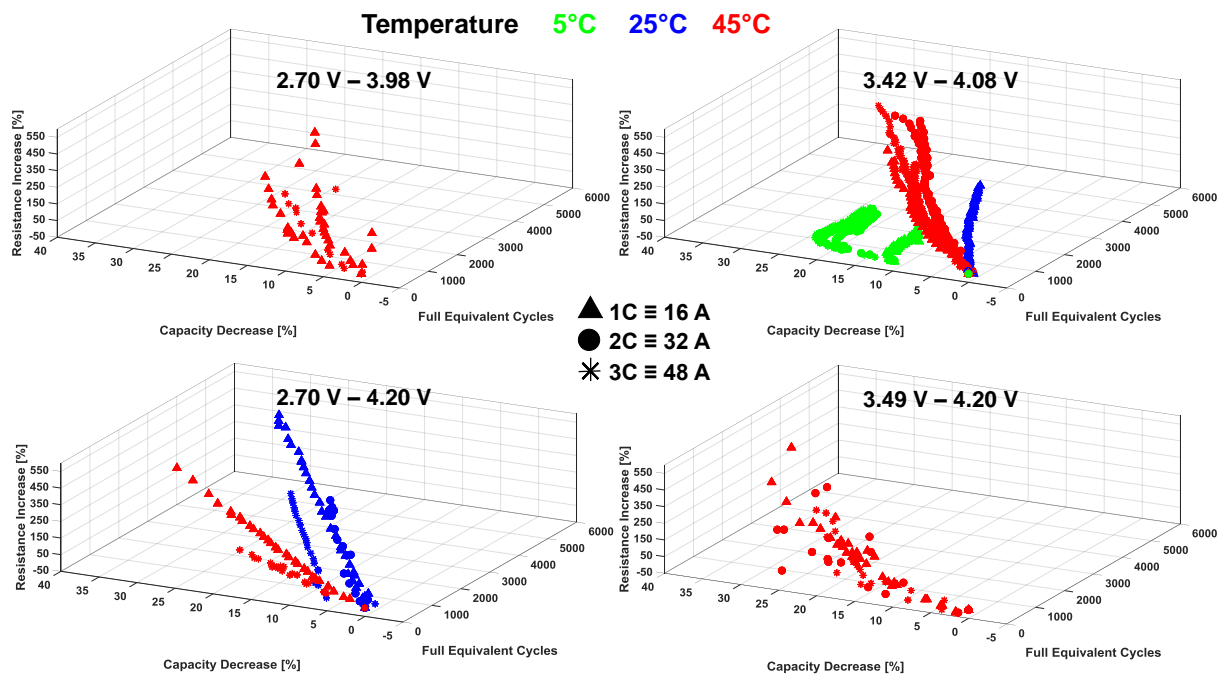


Figure III-2 : Evolution of the increase of DC resistance over aging as function of the capacity decrease and the equivalent cycles.

The first remark is that the DC resistance increases strongly at 45 °C whatever the cycling voltage thresholds. However, when the cycling end-of-voltage is 4.2 V, it seems to be higher with a less number of equivalent cycles.

For example, the DC resistance increases up to 350 % after 2700 FEC with the condition of cycling at the rate of 1 C / 1 C between 2.7 V and 4.2 V, while the loss of capacity is about 35 %. In contrary, this DC resistance has increased up to 150 % after more than 4000 FEC with the condition of cycling at rate of 1 C / 1 C between 3.42 V and 4.08 V leading to a loss of capacity of 25 %.

The same observation is found for cycling at 25 °C. Indeed, the DC resistance increases strongly when the end-of-voltage is more than 4.08 V. It has increased over 550 % at a rate of 1 C for the condition [2.70 V – 4.20 V] with a loss of capacity of higher than 35 % after 4000 FEC, while for the condition [3.42V – 4.08 V] the

increase is estimated at only 17 % (with 14 % of capacity loss) after the same number of FEC which is 4000. The loss of capacity is then mainly related to the internal resistance increase.

For the cycling at 5 °C between 3.42 V and 4.08 V, the abrupt loss of capacity observed between the two first consecutive check-ups (performed at 25° C) is not accompanied by a DC resistance increase whatever the C-rates. The increase in DC resistance begins very late compared to the loss of capacity. There is even a decrease in the DC resistance (passage below 0 %) at the beginning of aging even though a capacity loss is observed. In this case, the loss of capacity is hence not correlated with the increase of the DC resistance.

In the literature, it is reported that the elevated temperatures accelerate the degradation of the positive electrode and the formation of passivation films on the negative one. The SEI was found to be the main contributor to the increase in the cell internal resistance [154]. A Li-ion cell experienced a significant power loss due to impedance rise. But, J. Vetter et al. [45] reviewed and evaluated Li-ion batteries aging mechanisms. They reported that impedance rise can be caused by the following mechanisms:

- ❖ Electrolyte decomposition (→ formation of the SEI on the negative electrode) leading to capacity fade and power fade, reduced by stable SEI (additives) and enhanced by high temperatures and high SOC;
- ❖ Decrease of accessible surface area due to continuous SEI growth leading to power fade, reduced by stable SEI (additives) and enhanced by high temperatures and high SOC;
- ❖ Changes in electrodes porosity leading to power fade, reduced by external pressure or even stable SEI (additives) and enhanced by high cycling rate and high SOC;
- ❖ Current collector corrosion leading to power fade, maybe reduced by current collector pretreatment and enhanced by overdischarge and low SOC.

It may then be assumed that the DC resistance increase, observed above at 25 °C and at 45 °C could be related to the formation of SEI on graphite electrodes. The part of calendar aging should be important in these conditions than at 5 °C (cycling between 3.42 V and 4.08 V), since calendar aging is favored by high SOC and high temperatures storage conditions [155; 156; 157; 158; 159].

Nonetheless, based on checkups measurements, the condition of cycling at 5 °C between 3.42 V – 4.08 V did not show a notable increase of the DC resistance accompanying a capacity decrease. In order to go further in the investigations, we performed an additional cycling tests at 5 °C between 2.70 V – 4.20 V.

Results obtained with this latest condition constitute the main theme discussed in this chapter and developed in details in the following sections. All the other results will be discussed again in the chapter 5 devoted to aging modeling.

3.2. Cycling aging at low temperature

3.2.1. Evolution of the capacity during cycling

Four cells are considered for cycling tests performed at 5 °C between 2.7 V and 4.2 V (0 % - 100 %) at a rate of 1 C in charge as in discharge. A CTS Binder was used as a thermal chamber.

One commercial cell is instrumented with a reference electrode based on Li metal as described in the previous chapter. **Figure III-3** presents the evolution of the charged and the discharged capacities (A), Faraday Efficiency (B) and Energy Efficiency (C) measured at each cycle during cycling at 5 °C for the all four cells. For the cell #2, cell #3 and cell #4, the charge ends with a CV phase which starts when the cut-off voltage is reached and stops when the current drops to C/20.

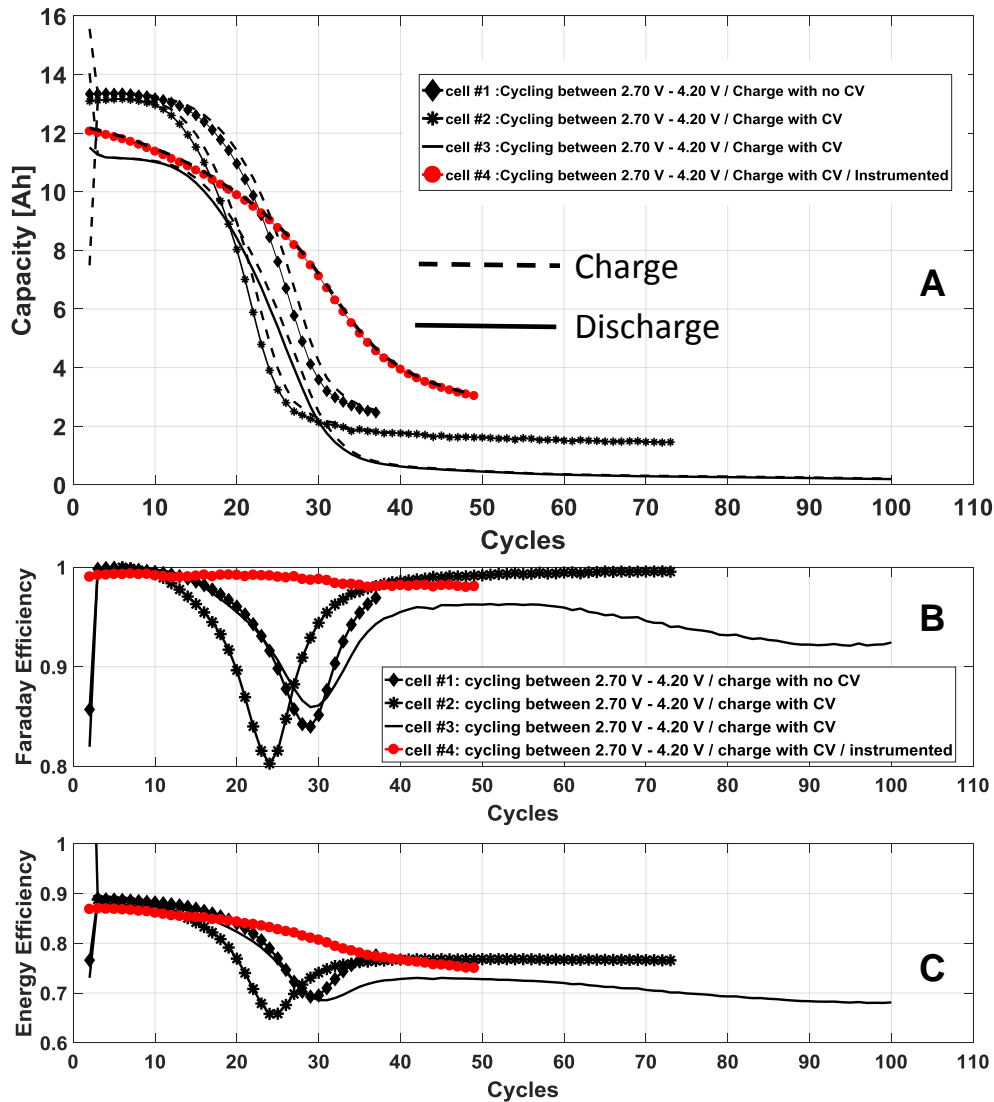


Figure III-3 : Evolution of the charged capacity (A), Faraday Efficiency (B) and Energy Efficiency (C) measured at each cycle during cycling test at 5 °C between 2.7 V and 4.2 V (A).

III. Study of aging mechanisms at low temperature

A considerable and fast loss of performance is observed even before reaching the first 50 cycles for the all 4 cells. This unexpected capacity fade is also observed with the commercial Li-ion cell instrumented with a reference electrode. These results reflect a good reproducibility. There is no real influence of the CV phase in charge.

In addition, the charged capacity is slightly higher than the discharged one at each cycle (see in **Figure III-3 – A**) until the capacity goes below around 4 Ah, except for the cell instrumented with the reference electrode (in red color).

This behavior has an incident on the Faraday efficiency curves (see in **Figure III-3 - B**). Indeed, all the non-instrumented cells present a particular signature which is characterized by a sudden drop in Faraday efficiency from the beginning of cycling until a minimal value is reached (localized between the 24th and 29th cycle). Thereafter, this parameter increases up to the initial value of 100 %

From that moment when the values of both capacities become equivalent, the performance and the Faraday efficiency curves stabilize. This trend is not observed with the instrumented cell because from the beginning to the end of cycling, the charged and discharged capacities seems to be much more superimposed.

However, the fact that the Faraday efficiency drops indicates that some of the electrons no longer participate in the main reaction inside the Li-ion cell, which is the Li intercalation / de-intercalation mechanisms into electrodes. It indicates the presence of irreversible parasitic(s) reaction(s) during cycling.

Moreover, in this phase where the Faraday efficiency is dropping down, observing that, from one cycle to another, the discharged capacity remains lower than the charged capacity, demonstrates that it is more the mechanism of delithiation of the negative electrode which is particularly implicated.

Indeed, at each cycle, the amount of Li ions restituted by the graphite electrode (delithiation) remains lower than the amount of Li ions that was been intercalated (lithiation). Thus, from the moment when the quantity of available Li strongly decreases, the loss of the retained capacity, between two successive charge / discharge cycles, becomes almost derisory. This could explain the rise of the Faraday efficiency curves which seems to tend towards 1 after the sudden fall.

When the Energy efficiency is considered (see in **Figure III-3 - C**), the same behavior can be noticed for all the non-instrumented cell. Furthermore, for the instrumented cell (in red), the energy efficiency continues to decrease. This behavior could indicate an increase of the internal resistance of the cell knowing that the energy depends on the cell voltage.

It is then clear that there is another reaction than Li de/intercalation, which is involved in the fast loss of performance observed with this cycling condition. This mechanism will be investigated in details in the following sections.

It should be pointed out that no definitive explanation has been given for the different behavior of the instrumented cell in terms of Faraday and Energy efficiencies. However, the loss of capacity is otherwise reproducible with the other non-instrumented cells.

3.2.2. Evolution of the internal resistance after cycling

This irreversible loss of capacity measured at 25 °C is about 75 % for all the cells and it is accompanied with a considerable internal resistance increase higher than 400 %. Note that the DC resistance measurements were unfortunately performed only for the cell #1 and the cell #4.

For the cell # 1, the DC resistance has risen from 3.54 mΩ (1st CU) to 19.69 mΩ (2nd CU – after cycling), representing an increase of 456 %. For cell # 4, it has risen from 3.54 mΩ (1st CU) to 19.37 mΩ (2nd CU – after cycling), representing an increase of 447 %. These DC resistance were measured at 40 % of SOC and at 10 s.

In contrast to the condition of cycling between 3.42 V and 4.08 V where the loss of capacity was not necessarily accompanied by a DC resistance rise, we rather observe here that cycling between 2.7 V and 4.2 V not only leads to an impressive loss of capacity after at least 50 cycles, but also leads to a considerable increase of the internal resistance over 400 %.

This behavior was rather observed with cycling tests performed at high temperature where a SEI formation is suggested to be the main aging cause.

Be that as it may, charging at low temperatures increases DC resistance which can lowered the potential of graphite below 0 V vs. Li⁺/Li, leading to a likely Li metal deposition on the anode surface, known as Li plating [160]. However, metallic Li and subsequent electrolyte decomposition by metallic Li is not reported to be a mechanism that increases the impedance of Li-ion cells. It appears therefore very interesting to investigate on the mechanisms responsible of the fast loss of performance observed when fully cycling is performed at 5 °C.

3.3. Ante-mortem analyses

Table III-3 shows that the irreversible loss of capacity measured at 25 °C is on average of about 75 % for all the first four cells. These results reflect a good reproducibility. There is no real influence of the CV phase in charge. Profiles of current, voltage and capacity of the all four cells are presented in the *Appendix of the Chapter 3*.

Cells	Voltage limits (v)	Charge with CV	FEC	Capacity @25°C (Ah)		SOH (%)	Status
				BOL	EOL		
1	2.70 – 4.20	No	38	17.30	3.49	20.2	Backup
2		Yes	100	16.96	4.01	23.6	Swollen
3		Yes	73	17.24	4.84	28.0	Post-mortem
4		Yes	50	17.18	4.24	24.7	Ante-mortem Instrumented
5	3.42 – 4.08	Yes	1509	17.27	15.20	88.0	Post-mortem

Table III-3 : Protocol of cycling at 5 °C according to the following voltage limits strategies.

The condition of cycling between 3.42 V and 4.08 V (cell #5 – CIDETEC) involves a capacity loss limited to 4 % after 100 FEC (see in **Figure III-1**). Furthermore, this capacity fade stabilized quickly, and as a result, it has been possible to extend the number of cycles up to 1509 FEC without any important additional capacity loss defect, about 12 % before dismantling. So, for the same conditions of temperature, there is a considerable difference in loss of performance due to the end-of-voltage limits.

After cycling, the cell #1 has been stored as backup in a climate chamber at 12 °C while the cell #2 has swollen itself few days after be placed inside the same climate chamber.

Post-mortem investigations were then investigated with the cell #3 and the cell #5 while ante-mortem analyses were performed with the commercial Li-ion battery instrumented with a reference electrode (cell #4).

In this part, we will exploit the measurements of each electrode obtained from the instrumented cell #4.

Figure III-4 and **Figure III-5** illustrate the separate evolution of the potential of both positive and negative electrodes during cycling test performed at 5 °C between 2.7 V and 4.2 V in function of the discharged capacity and the charged capacity, respectively. Those measurements are obtained from the instrumented cell with Li metal as counter electrode.

In **Figure III-4**, it is shown that the end-of-discharge potential of both positive and negative electrodes are more and more high as the number of cycles increases. This observation could not be made without the contribution of the reference electrode.

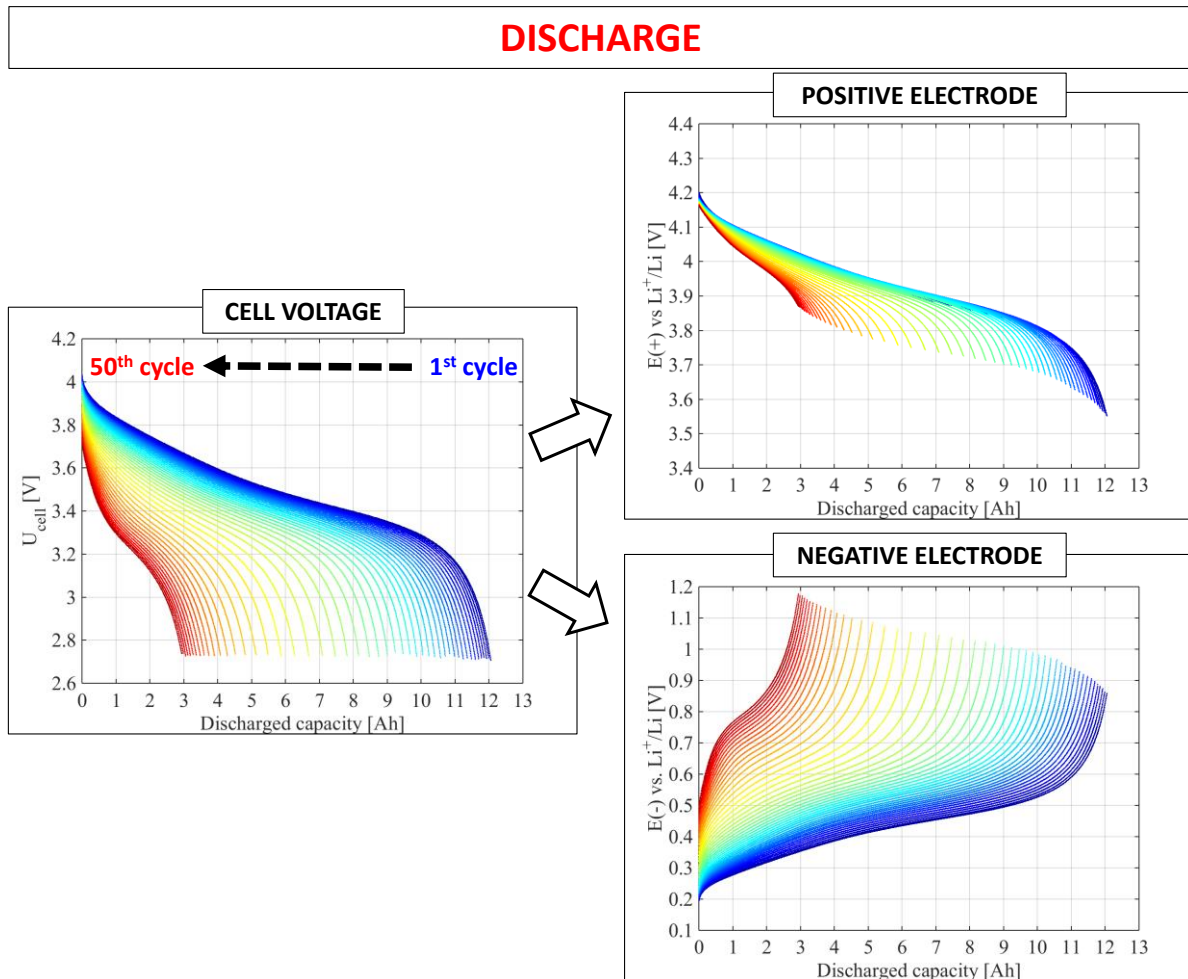


Figure III-4 : Evolution of the potential of both positive and negative electrodes corresponding to discharge during cycling aging test at 5 °C.

Figure III-5 shows that the potential of the negative electrode only goes slightly below 0 V vs. Li^+/Li for the last cycles, and consequently after the observation of the sudden loss of capacity. Furthermore, as the number of cycles increases, the cell is practically charged only in CV mode. This means that the cell maximum voltage of 4.2 V is very quickly reached at each cycle because of the internal resistance increase during cycling at 5 °C.

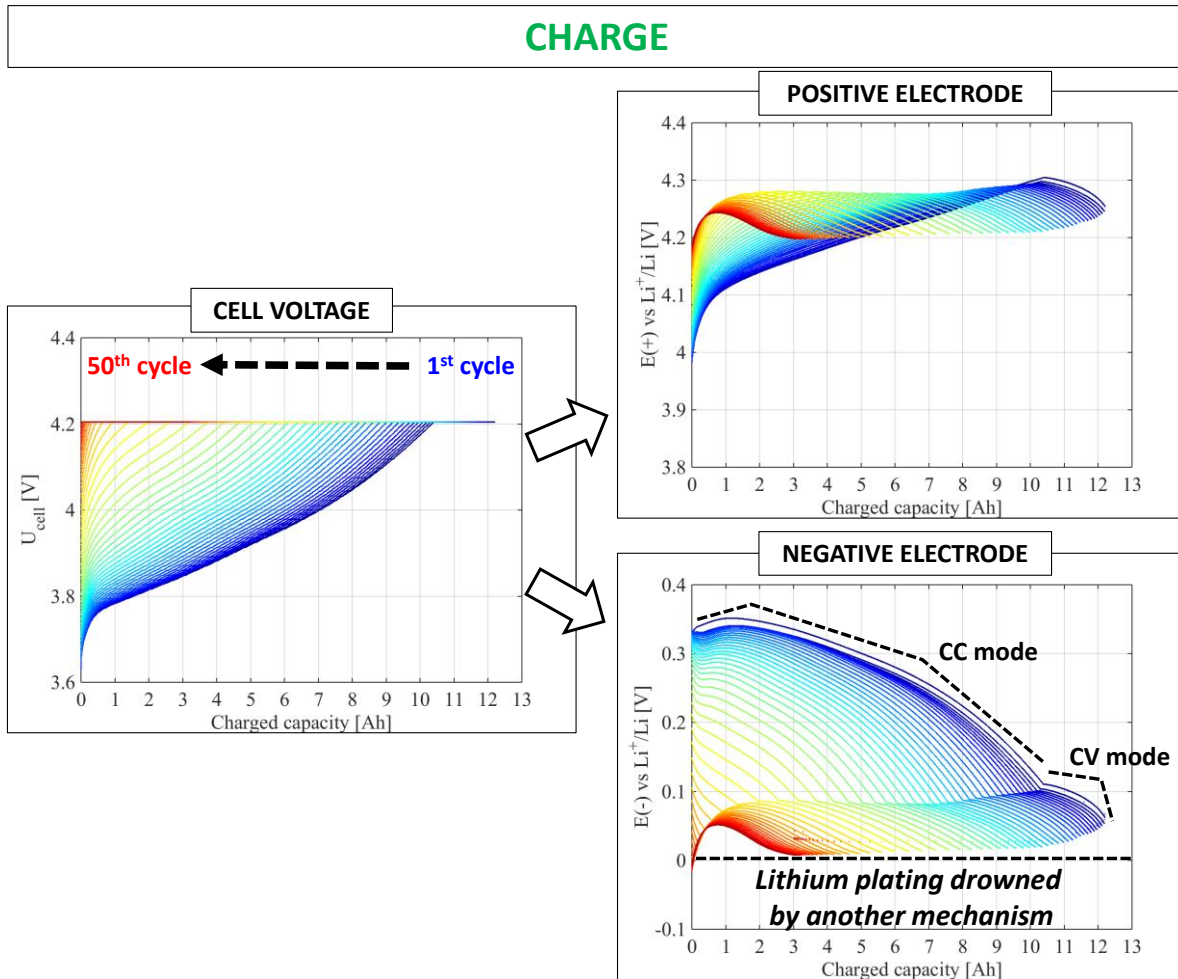


Figure III-5 : Evolution of the potential of both positive and negative electrodes corresponding to charge during cycling aging test at 5 °C.

Very important information can be obtained by exploiting with more interest the end-of-charge / discharge potentials of each of the two electrodes in order to understand the mechanism that occurs during cycling.

Figure III-6 shows the evolution of the end-of-charge / discharge potential in function of number of cycles of both positive and negative electrodes during cycling aging test at 5 °C.

The figure at the bottom left shows that the potential of the negative electrode only goes below 0 V vs. Li⁺/Li over the last 6 cycles.

On one hand, the end-of-charge potential of the negative electrode decreases from 110.04 mV vs. Li⁺/Li (1st cycle) to -6.14 mV vs. Li⁺/Li (50th cycle) as a decrease of about 116.18 mV as shown in **Figure III-6**. As a result, the end-of-charge potential of the positive electrode drops from 4.305 V vs. Li⁺/Li (1st cycle) to 4.185 V vs. Li⁺/Li (50th cycle) too. This latter phenomena could be interpreted by the fact that graphite is more and more lithiated at the end of the charge, during cycling.

III. Study of aging mechanisms at low temperature

On the other hand, the end-of-discharge potential of the positive electrode is increasingly high as the number of cycles increases as shown in **Figure III-6**.

It rises from 3.557 V vs. Li⁺/Li (1st cycle) to 3.872 V vs. Li⁺/Li (50th cycle). It seems that NMC is less and less lithiated at the end of the discharge, during cycling. Consequently, the end-of-discharge potential of the negative electrode increases from 0.8583 V vs. Li⁺/Li (1st cycle) to 1.177 V vs. Li⁺/Li (50th cycle), representing an increase of 0.319 V.

It is then assumed that it is more and more difficult to extract more Li ions from graphite particles to intercalate to the positive electrode. This means that less and less Li ions are exchanged during the cycling. In addition, the potential of graphite electrode goes slightly below 0 V vs. Li⁺/Li, especially over the last 6 cycles, however an irreversible capacity fading is observed since the beginning of cycling. Regarding this latter results, the risk of Li plating seems to be unlikely in such conditions.

This mechanism will be thoroughly investigated with post-mortem analyses.

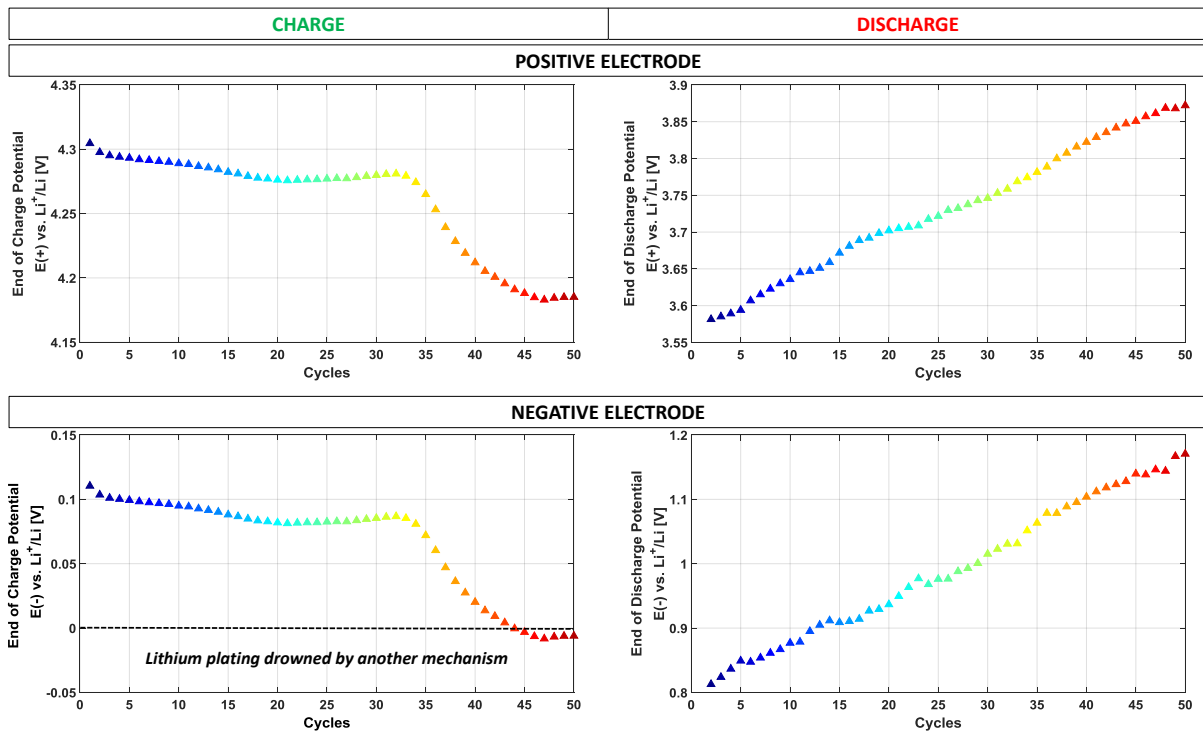


Figure III-6 : Evolution of the end-of-charge / discharge potential in function of number of cycles of both positive and negative electrodes during cycling aging test at 5 °C.

3.4. Post-mortem analyses

3.4.1. State of health of commercial cells

3.4.1.1. Visual inspections

A fresh 16 Ah Li-ion cell, cell #3 (cycled between 2.7 V - 4.2 V) and cell #5 (cycled between 3.42 V - 4.08 V) (as described in **Table III-3**) were disassembled in discharged state for investigations of aging mechanisms involved. Visual inspections of both negative and positive electrodes and separators are presented in **Figure III-7**. No notable degradation is observed on both NMC electrodes. Separators from both cells are still white. Contrary to expectations, no Li plating is visually observed on the surface of the graphite electrodes.

Cycling aging at T=5°C and at 1 C	Components			Comments
	NMC	Separator	Graphite	
<p>Cell n°3</p> <p>$U_{min}=2.70V$ $U_{max}=4.20V$</p> <p>38 FEC</p> <p>SOH = 22%</p> <p>Duration = 3 days</p>				No Lithium deposition
				Lithiated
<p>Cell n°5</p> <p>$U_{min}=3.42V$ $U_{max}=4.08V$</p> <p>1509 FEC</p> <p>SOH = 88%</p> <p>Duration = 328 days</p>				No Lithium deposition

Figure III-7 : Visual inspections of both negative and positive electrodes and separators of 16 Ah C/NMC commercial Li-ion pouch cells after cycling at 5 °C.

In the literature, some authors reported that metallic Li deposited on the surface of the graphite electrode can diffuse into the active material during the relaxation time by chemical reaction to form graphite intercalation compounds resulting in a capacity recovery.

J. Fan et al. [161] suggested that the Li deposited on the negative surface during the low-temperature charging of a commercial graphite/LiCoO₂ Li-ion cell can rapidly diffuse into graphite during the room temperature rest, while it cannot diffuse during 4 hours rest at -20 °C.

V. Zinth et al. [162] observed, after few cycles performed at -20 °C and at a rate of C/30 and C/5, the plated Li diffusion into graphite in commercial graphite/LiNi_{1/3}Mn_{1/3}Co_{1/3}O₂ cells during a 20 hours rest period at -20 °C by in situ neutron diffraction investigations. The authors evoked the diffusion of metallic Li leading to an ongoing transformation to LiC₁₂ and LiC₆ with a capacity recovery estimated to 17 %.

Recently, T. Waldmann et al. [163] discussed the chemical intercalation of Li plating into adjacent graphite particles during a rest period at 25 °C resulting also in a partly capacity recovery.

By contrast, in our case, after the last check-up, cells that have been stored at 12 °C during two weeks before dismantling did not show any capacity recovery. So, a potential diffusion of plated Li into graphite particles during rest time resulting in a capacity recovery cannot be evoked in our case.

To go further, the graphite electrode recovered from the cell #5 presents a black color with no visible defect detected on the surface while, the graphite electrode taken from the cell #3 seems rather presenting a lithiated state due to the brown color [164; 165; 166; 167] on the surface although the cell has been dismantled in a discharged state.

This observation is reproducible on all the 24 bifacial negative electrodes. Additional post-mortem analyses have been performed for investigating this unexpected mechanism.

3.4.1.2. Surface morphology and chemical analysis with SEM / EDS

Figure III-8 shows SEM images of graphite electrodes recovered from a fresh commercial Li-ion cell and from the cell #3.

The unaged graphite sample presents a normal graphite material appearance, with a crushing aspect on its surface, certainly due to the calendaring effect during industrial manufacturing.

The graphite sample of the aged cell presents visually an unexpected brown color attributed to a lithiated state and particles on the surface looking like “sticks”. The appearance of these “filaments” is quite similar to Li deposition in dendritic morphologies observed by H. Honbo et al. [168]. The detection of the occurrence of metallic Li depositions with ⁷Li NMR is well discussed in the section [3.4.4.1].

Table III-4 presents the percentage of each element detected with Energy-dispersive X-ray spectroscopy (EDS) that confirms that there is no contamination by elements originating from the positive electrode. Li element could not be detected by EDS as it is a light element.

III. Study of aging mechanisms at low temperature

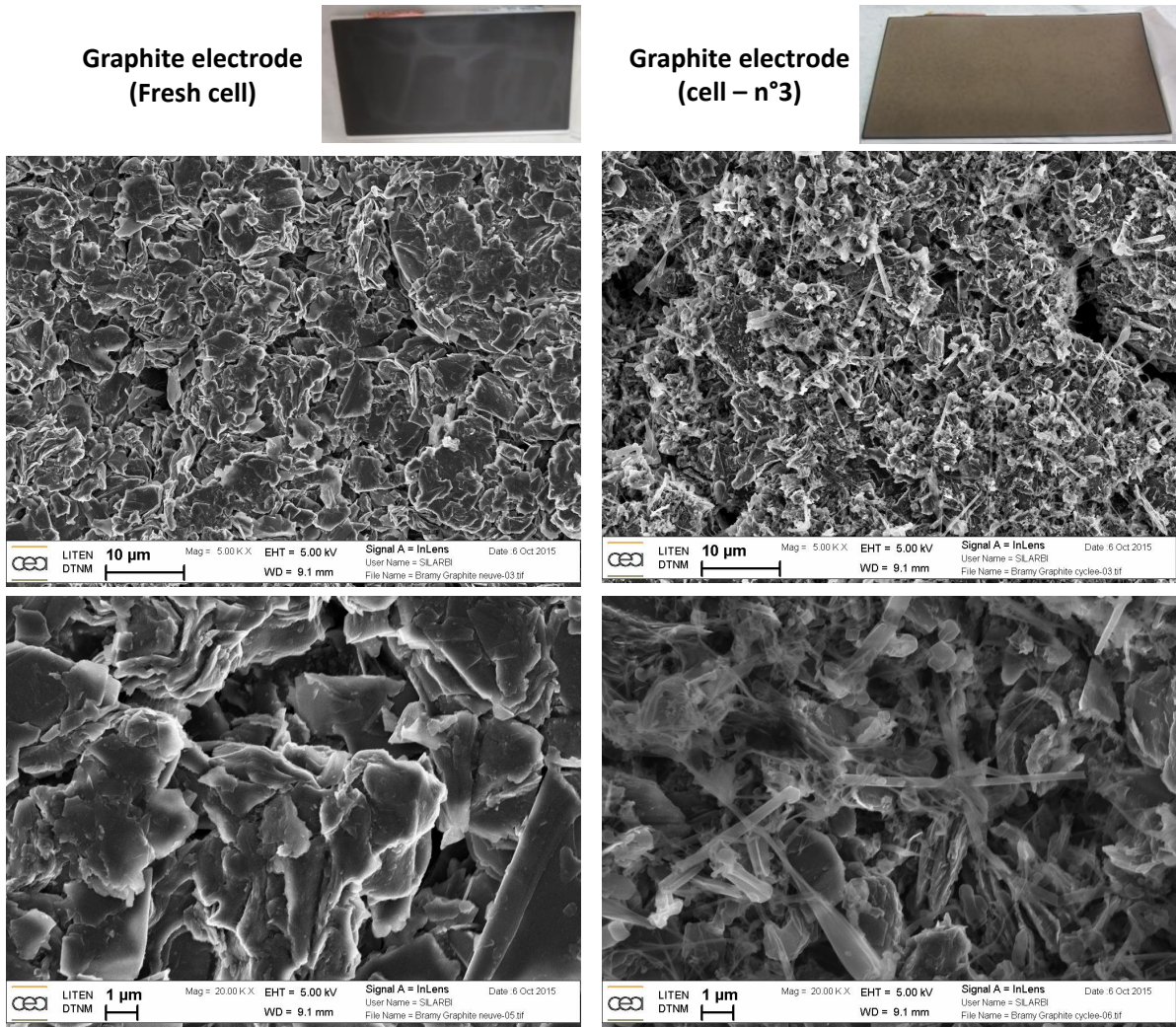


Figure III-8 : SEM analysis performed on a sample of graphite electrode recovered from the fresh commercial cell and on a sample graphite electrode from the cell #3 (after cycling between 2.7 V and 4.2 V).

Element		C	O	F	P	S	Cu
% at.	Fresh cell	82.78	7.69	9.17	0.23	0.12	0
	Cell #3	73.53	16.48	8.87	0.55	0.57	0

Table III-4 : Percentage of each element detected with SEM / EDS on samples of graphite electrodes respectively recovered from a fresh cell and from the cell #3.

3.4.1.3. Surface morphology analysis with TEM/EDS

We required to TEM technique to investigate the state of structural and chemical bonding especially in graphite electrode after aging of commercial Li-ion cells as a complementary tool to SEM analysis.

Figure III-9 presents TEM images obtained from a sample of graphite electrode respectively recovered from the cell #5 (cycled between 3.42 V and 4.08 V) and from the cell #3 (2.7 V and 4.2 V).

The surface film on top of graphite particles from the cell #5 has a size of about 1500 nm with a higher concentration of carbon, fluorine and oxygen, as confirmed in **Figure III-10**, suggesting a standard SEI more likely to contain species such as Li_2CO_3 , Li alkyl carbonates or LiF as supported by M. Nie et al. [169].

A similar film is observed on top of graphite particles recovered from the cell #3. Besides, additional particles with dendritic morphology high concentrated with carbon, oxygen and fluorine, as seen in **Figure III-11**, are also found on the surface of this electrode. This observation is consistent with SEM images suggesting dendrites Li formation and will be discussed in the following sections.

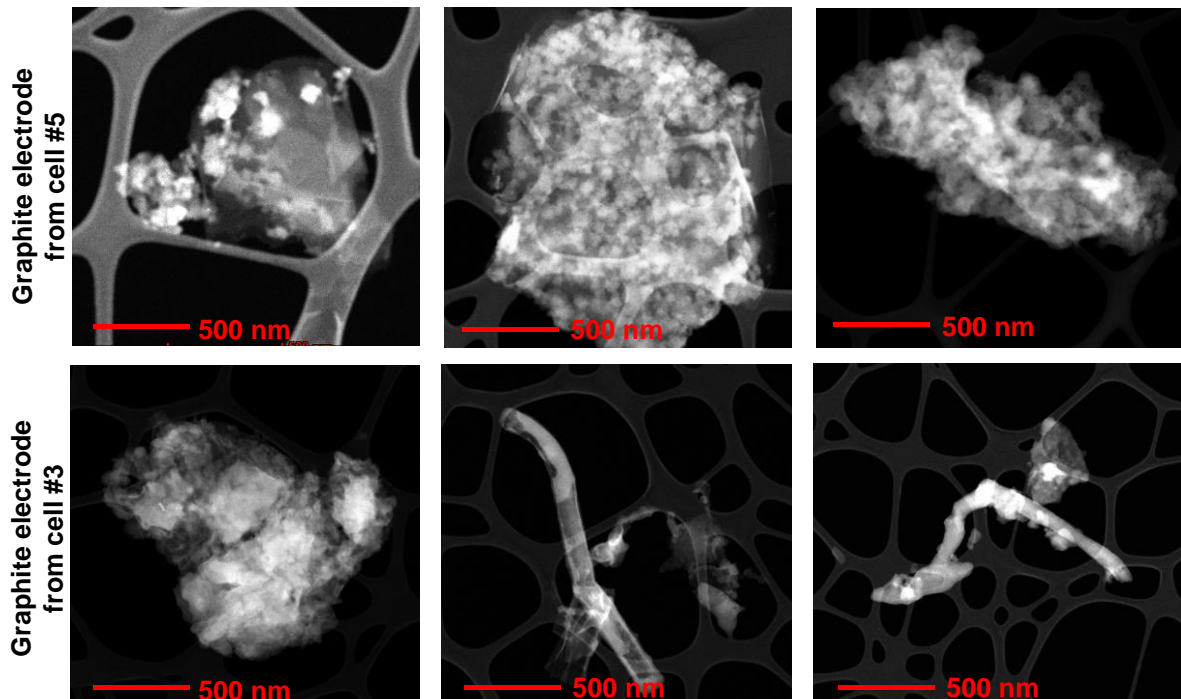


Figure III-9 : TEM images obtained from a sample of graphite electrode respectively recovered from the cell #5 (cycling between 3.42 V and 4.08 V) and from the cell #3 (2.7 V and 4.2 V).

III. Study of aging mechanisms at low temperature

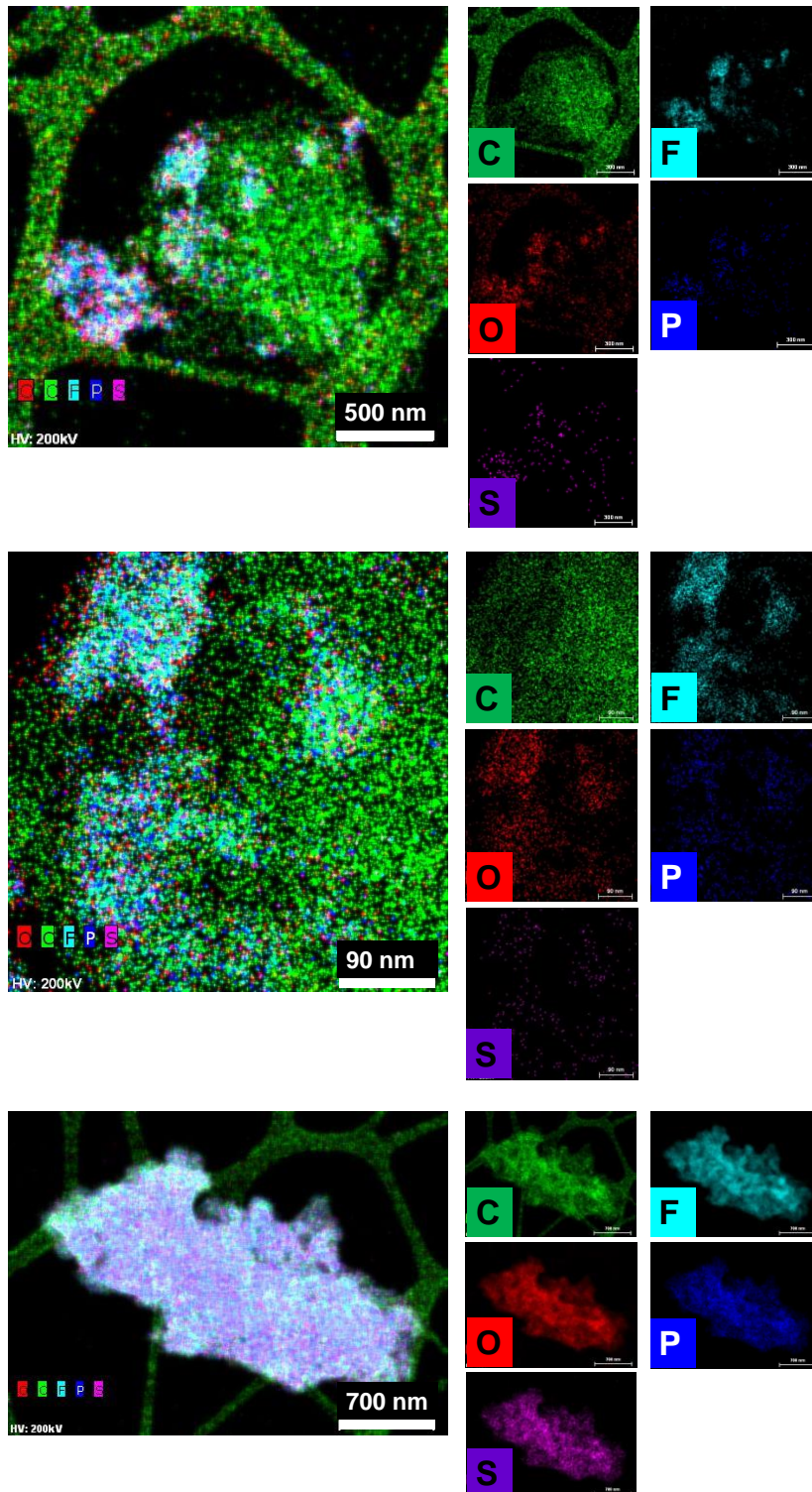


Figure III-10 : TEM / EDS analysis of a sample of graphite electrode recovered from the cell #5.

III. Study of aging mechanisms at low temperature

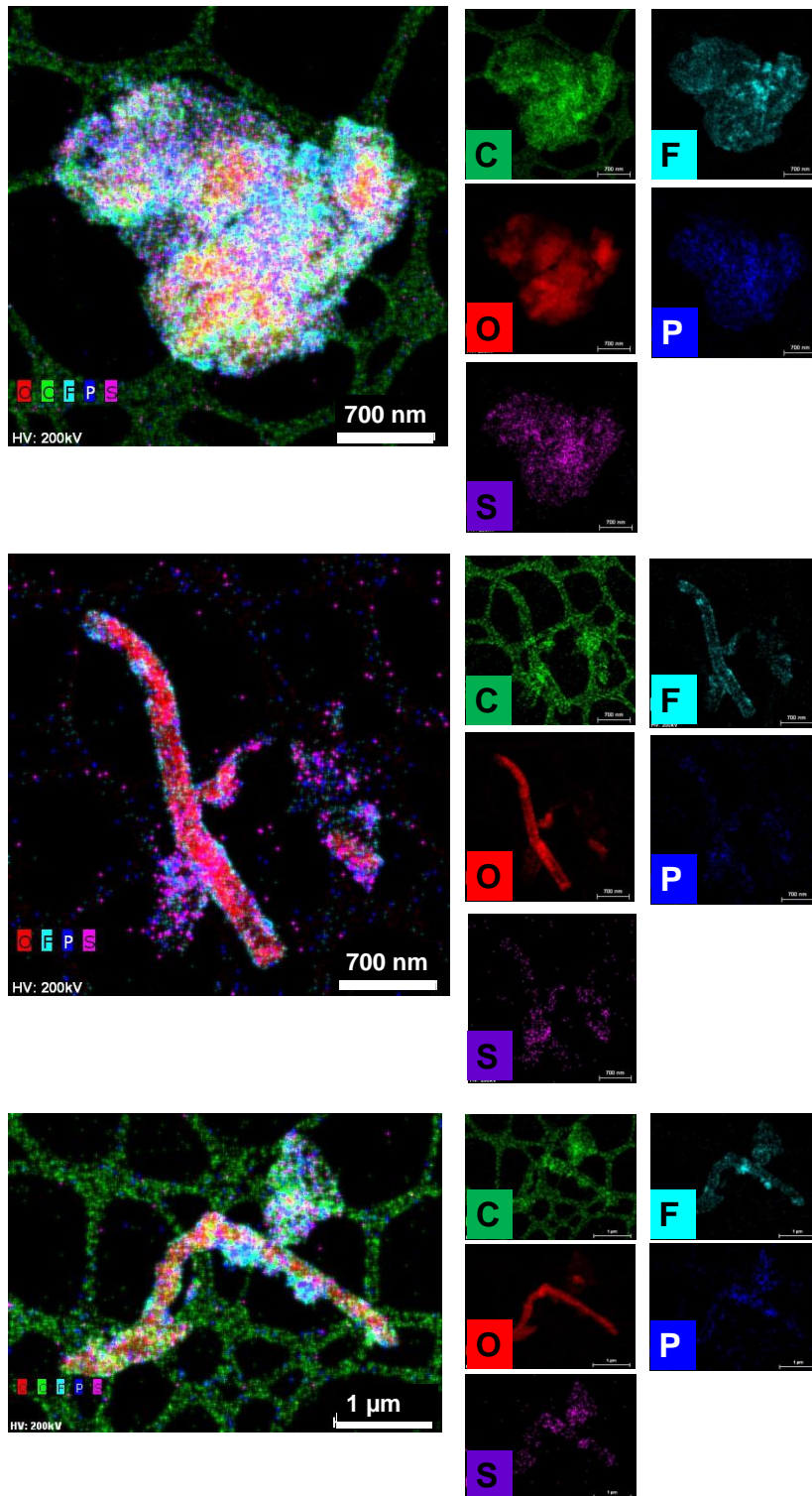


Figure III-11 : TEM / EDS analysis of a sample of graphite electrode recovered from the cell #3.

3.4.2. State of health of electrodes

3.4.2.1. Electrochemical measurements of single components with coin half cells

We aim to determine the residual capacity remained in each electrode after the cell #3 dismantling. As it seems difficult to extract Li ions from the graphite electrode to intercalate to the positive electrode, this investigation conducted with coin half-cells is also performed to determine whether the Li de/intercalation mechanisms into each of harvested electrodes remains possible after aging.

Three CR2032 Graphite/Li metal coin half-cells (A, B and C) are assembled in 1:1:1 wt EC:DMC:EMC + 1 M LiPF₆ electrolyte as presented in **Table III-5**.

The nominal capacity of each coin half-cell is 3.3 mAh with $V_{min} = 0.02$ V and $V_{max} = 1.5$ V. The first Graphite/Li metal coin half-cell (A) is based on a fresh graphite electrode while the two others (B and C) contain graphite samples recovered from the aged cell (cell #3).

In parallel, two CR2032 NMC/Li metal coin half-cells (D and E), based on a fresh (D) and an aged (E) NMC electrode respectively, are assembled (see in **Table III-5**). The nominal capacity of each NMC/Li metal coin half-cell is 2.88 mAh with $V_{min} = 2.6$ V and $V_{max} = 4.1$ V.

Graphite / Li metal			
		Capacity (mAh) measured at 0.1 C	
		1st charge	1st discharge
Graphite from the fresh cell	coin half-cell A	0	2.602
Graphite from the aged cell (cell #3)	coin half-cell B	0.153	1.360
	coin half-cell C	0.202	1.475
NMC / Li metal			
		Capacity measured (mAh)	
		1st discharge	1st charge
NMC from the fresh cell	coin half-cell D	0	2.411
NMC from the aged cell (cell #3)	coin half-cell E	2.289	2.478

Table III-5 : Post-mortem electrochemical measurements (performed at 25 °C) of single components (from the cell #3) with coin half cells.

Electrochemical characterizations are performed at 25 °C, at different C-rates according to the following order: 0.1 C, 0.2 C, 0.5 C, 1 C, 2 C, 5 C, 8 C, 0.2 C and 0.1 C at least. Charges at 0.1 C are performed with a CV phase until the current reaches C / 50. Between charge and discharge, a rest of 30 minutes is programmed.

III. Study of aging mechanisms at low temperature

Each C-rate is repeated 5 times except the first C-rate at 0.1 C which is repeated only 3 times.

It should be noted that the charge process of the Graphite / Li metal coin half-cells corresponds to delithiation process in graphite electrode since graphite functions as the cathode in this configuration.

The protocol of NMC / Li metal coin half cells starts with a discharge step while that of the Graphite/Li metal coin half cells starts with a charge step performed at a rate of 0.1 C which is a low C-rate. The aim is to delithiate those electrodes so that the residual capacity of each of the respective electrodes, after dismantling of the cell, can be determined. Thereafter, the capacity of these coin half cells is also measured at other C-rates.

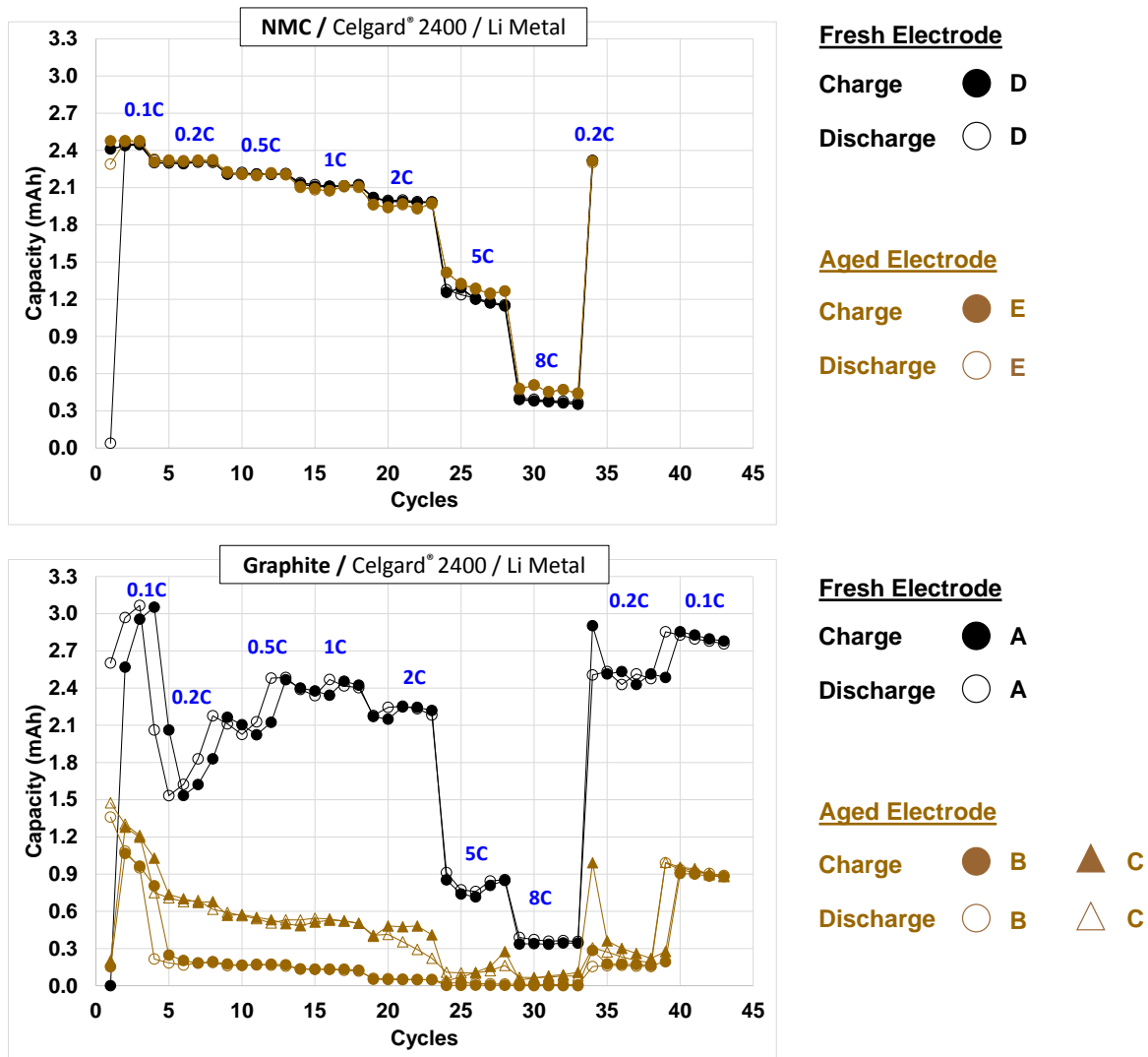


Figure III-12 : Electrochemical characterizations at 25 °C with Graphite / Li metal and NMC / Li metal coin half-cells.

III. Study of aging mechanisms at low temperature

The first discharged and charged capacities are respectively 0 mAh and 2.411 mAh for NMC/Li metal coin half-cell based on fresh electrode (D) (as presented in **Figure III-12** and mentioned in **Table III-5**). This result confirms that the fresh NMC electrode was fully lithiated before dismantling.

For the NMC / Li metal coin half-cell based on aged electrode (E), the first discharged and charged capacities are respectively 2.289 mAh and 2.478 mAh. This electrode was therefore not fully lithiated during the last discharge before dismantling. Li remained thus into graphite electrode. In any case, this aged positive electrode exhibits good cycling when further cycled vs. Li metal. No loss of capacity of Li intercalation with this electrode is observed.

On one hand, the first charged and discharged capacities are respectively 0 mAh and 2.602 mAh for the Graphite / Li metal coin half-cell based on fresh electrode (A). It is a confirmation that the fresh graphite was fully delithiated. It then is not possible at all to more delithiate.

On the other hand, the first charged and discharged capacities are respectively 0.153 mAh and 1.3602 mAh for the Graphite / Li metal coin half-cell based on aged electrode (B). Similarly, the first charged and discharged capacities are respectively 0.202 mAh and 1.4752 mAh for the other one sample (C). In fact, even by applying a low charge C-rate, it appears very difficult to delithiate this aged electrode, which nevertheless remains lithiated as described above. Moreover, by applying a low discharge C-rate thereafter, it is difficult to insert more Li into the graphite, which is certainly fully lithiated.

It should be noted that Li de/re-intercalation mechanisms into aged graphite particles are not totally obstructed since a part of Li, about 0.9 mAh, is recovered at a very low rate (0.1 C) as seen in **Figure III-12** with Graphite/Li metal half coin cells based on harvested graphite materials. Indeed, this capacity of about 0.9 mAh measured at 0.1 C represents about 1/3 of the capacity of the fresh graphite at the same C-rate which is about 2.8 mAh. It then may be assumed that the other 2/3 of Li can be accessed and then delithiated from graphite at C-rates lower than 0.1 C (e.g. 0.01 C).

Finally, it appears clearly here that only the negative electrode is involved in the loss of capacity.

3.4.2.2. Determination of the state of lithiation of electrodes with XRD measurements

3.4.2.2.1. XRD Studies of the cathode material

Samples of positive electrodes respectively recovered from the fresh 16 Ah Li-ion cell, from the cell #3 (dismantled after full cycling at 5°C) and from the cell #5 (dismantled after cycling at 5 °C between 3.42 V – 4.08 V) are analyzed with XRD measurements. All samples possess a layered structure described in the R-3m space group for which lattice parameters *a* and *c* are calculated.

In situ XRD measurements are performed on a sample of the fresh NMC electrode. This technique is used to obtain lattice parameters of the R-3m rhombohedral phase as a function of the SOC and the Li content *x* in NMC.

In the literature, as reported by I. Buchberger [170] et al, various methods have been used to demonstrate that the lattice parameters are correlated to the Li content of the NMC electrode such as chemical or electrochemical delithiation combined with Inductively Coupled Plasma, XRD, Neutron Diffraction, or combinations of these methods. But to quantify the Li-loss, an *in situ* XRD calibration curve is suitable to correlate the transferred electrochemical charge to the Li content of NMC and its lattice parameters. This can be obtained using *in situ* XRD during charging and discharging of NMC electrode.

Figure III-13 illustrates XRD measurements performed on positive electrodes (left figure) and the calibration curve obtained from *in situ* measurements with a fresh NMC sample (right figure).

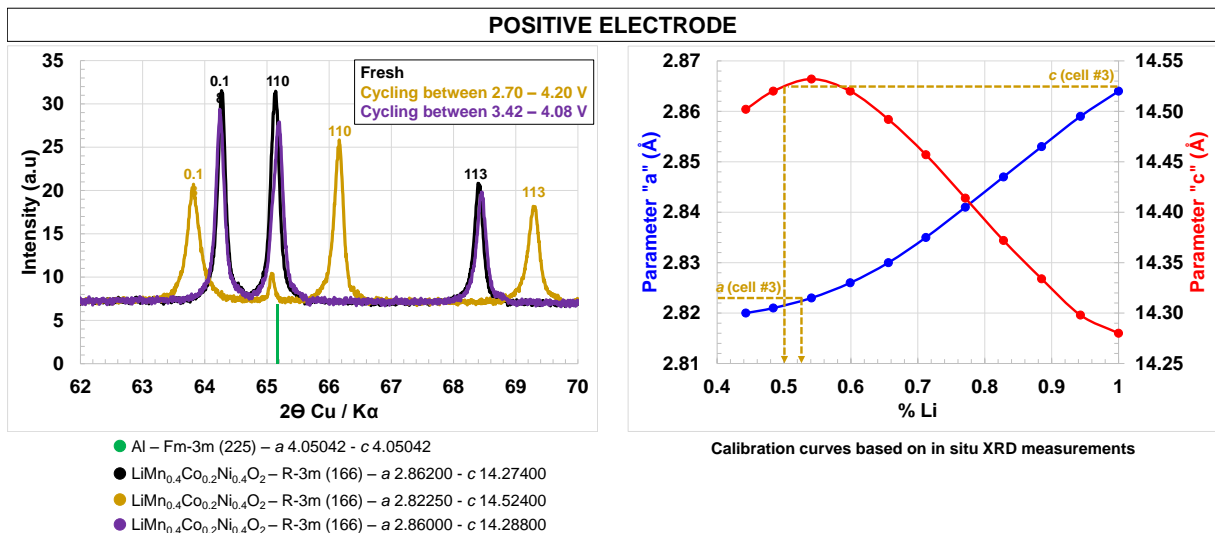


Figure III-13 : XRD studies of the cathode Li_x(Mn_{0.4}Co_{0.2}Ni_{0.4})O₂ material. In situ XRD measurements are performed on a sample of a fresh cathode electrode in order to obtain a calibration curve of lattice parameters in function of Li rate.

III. Study of aging mechanisms at low temperature

The left figure presents the contribution of $K\alpha_1$ of the reflections 018, 110 and 113 for the fresh and cycled samples. The Aluminum collector peaks are visible.

Lattice parameters obtained from the NMC recovered from the cell #5 are equal to those determined from the fresh cathode while those obtained with the NMC electrode recovered from the cell #3 have significantly evolved.

The NMC samples respectively recovered from the fresh cell and the cell #5 present the expected lithiated state, while the cathode from the most degraded cell is highly delithiated. We hypothesize that the rate of $\text{Li}^+ x = 1$ for the fresh material failing to dispose of a sample of pristine commercial cathode material.

Note that the value of the a parameter has decreased from 2.862 Å (fresh - lithiated) to 2.823 Å (aged - delithiated) and the value of the c parameter has increased from 14.274 Å (fresh - lithiated) to 14.524 Å (aged - delithiated). This reflects a less lithiated state in the structure of the cathode material recovered from the cell #3.

The decrease of a and the increase of c with delithiation are in good agreement with the observations of S.-C. Yin et al. using Neutron Diffraction studies on $\text{Li}_{1-x}\text{Ni}_{1/3}\text{Mn}_{1/3}\text{Co}_{1/3}\text{O}_2$ samples [171].

J. Choi et al. [172] further investigated the variations of the lattice parameters with Li content (1-x) in $\text{Li}_{1-x}\text{Ni}_{1/3}\text{Mn}_{1/3}\text{Co}_{1/3}\text{O}_2$ using XRD measurements. They reported that the c parameter increases with decreasing Li content due to an increasing electrostatic repulsion across the Van der Waals gap between the $(\text{Ni}_{1/3}\text{Mn}_{1/3}\text{Co}_{1/3})\text{O}_2$ sheets.

As suggested by several authors [173; 174; 175], it is also possible to calculate the Li content into a NMC sample by reporting the corresponding values of lattice parameters on the calibration curves determined with the fresh NMC *in situ* XRD measurements.

This technique confirms that the NMC electrode recovered from the aged cell is less lithiated although the cell was disassembled in discharged state. The estimated rate of Li in that NMC electrode is about 0.5. It should be noted that if the amount of disinserted Li becomes greater than 0.5, that is to say in the event of overdischarge, an irreversible structural modification of the material would occur.

3.4.2.2.2. XRD Studies of the anode material

XRD measurements have also been conducted on graphite samples respectively recovered from the fresh cell, the cell #3 (cycling between 2.70 V and 4.20 V) and the cell #5 (cycling between 3.42 V and 4.08 V) as presented in **Figure III-14**.

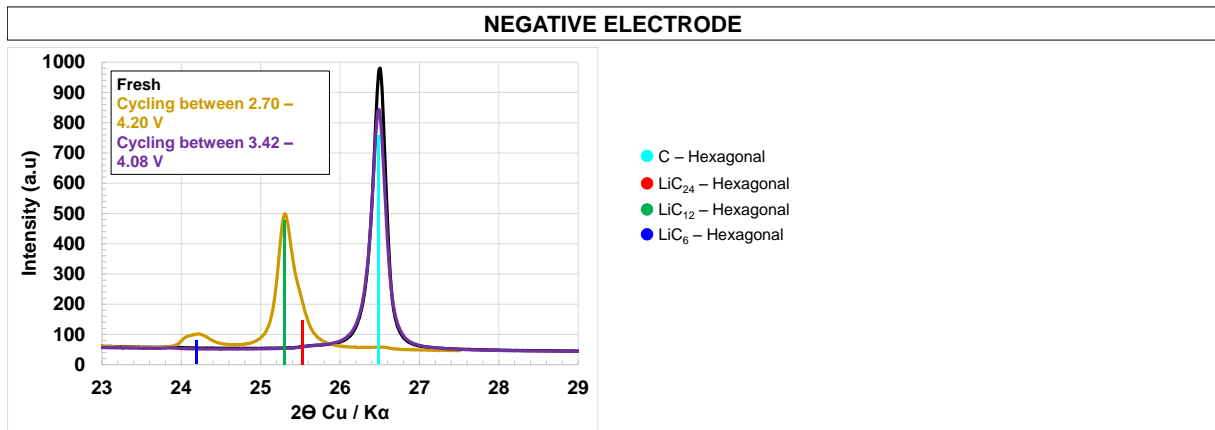


Figure III-14 : XRD studies of the anode material.

Signals corresponding respectively to the graphite electrode recovered from the cell #5 and from the fresh cell have the same signature.

The relative intensity of the hexagonal graphite peaks have decreased for the most aged material (cell #3) compared to the fresh material. Nevertheless, what is astounding is the concurrent presence of intercalation compounds (LiC₆, LiC₁₂ and LiC₂₄) found into the aged graphite.

This result reveals that a considerable part of exchangeable Li is trapped as graphite intercalation compounds. It is consistent with the brown color on the surface of graphite electrode as shown in **Figure III-7**, and with results obtained with coin half-cells electrochemical measurements in **Figure III-12**.

3.4.3. Influence of the electrolyte

3.4.3.1. Electrolyte analysis with GC-MS

In order to follow the evolution of each component with aging, GCMS analyzes are performed on a sample of the electrolyte recovered from a fresh commercial Li-ion cell and on a sample recovered from the cell #3.

Original electrolyte components of the commercial pouch cell can be identified from the fresh electrolyte analysis as following: solvents (Ethyl Methyl Carbonate (EMC) and Ethylene Carbonate (EC)) and many additives (Vinylene carbonate (2 % wt VC), Fluoroethylene Carbonate (5 % wt FEC), Biphenyl (7 % wt BP) and 1,3-Propane Sultone (0.1 % PS)).

M. Nie et al. [169] suggested that incorporation of VC (3 % wt) inhibits the reduction of EC to generate Li Ethylene Dicarboxylate (LEDC) and LiPF₆ to generate LiF while incorporation of FEC (3 % wt) results in the generation of a thinner SEI.

III. Study of aging mechanisms at low temperature

The use of PS and VC improves retention capacity for cycling at high temperature and lower impedance. These additives modify the reduction reactions at the negative electrode by inhibiting the production of ethylene and modifying the structure of the SEI. They reduce by more than 60 % the evolution of gas during the formation of ethylene as reported by B. Zhang et al. [176]. Biphenyl is rather used as a fire-retardant in Li-ion batteries. Aging mechanisms associated to the use of this additive will be discussed in the next chapter.

Table III-6 illustrates the content of each detected element.

Content (%) of each component			
		Fresh	cyc@5°C
Solvents	EMC	53.52	23.65
	EC	32.53	24.05
Additives	VC	0.10	0
	FEC	0.88	0.15
	Biphenyl	10.57	10.57
	1,3-PS	2.40	0.52
Decomposition products	DMC	0	3.34
	DEC	0	17.04
	EGMC	0	0.79
	2-ethoxycarbonyloxyethyl methyl carbonate	0	2.30
	DEDOHC	0	1.77
TOTAL		100	84.18
Gas and/or not detected material		0	15.82

Table III-6 : Content (%) of each component of the electrolyte detected with GC-MS analysis performed on samples recovered from a fresh cell and from cell #3.

The analysis of the electrolyte retrieved from the cell #3 reveals the presence of additional components identified as electrolyte decomposition products. Dimethyl Carbonate (DMC), Diethyl Carbonate (DEC), Ethyleneglycol bis-(methyl carbonate) (EGMC), 2-ethoxycarbonyloxyethyl methyl carbonate and Diethyl 2,5-dioxhane dicarboxylate (DEDOHC).

The content of solvents has decreased significantly at 5 °C and VC additive is totally consumed with aging. FEC and 1,3-PS show lower concentrations. In any case, the degradation of solvents content and the apparition of many electrolyte degradation products during cycling is clearly identified.

According to the literature, DMC and DEC are generated by the reduction of EMC solvent on lithiated graphite surface [177; 178]. The presence of EGMC is caused by the reaction between lithium alkoxides and EC [179]. The origin of the apparition of the carbonates has not been identified.

The organic electrolytes used in Li-ion batteries have oxidation potentials around 4.7 V vs. Li⁺/Li and reduction potentials close to 1.0 V vs. Li⁺/Li [180]. But, the intercalation potential of Li into graphite is between 0.05 V and 0.1 V vs. Li⁺/Li, which is below the reduction potential of the electrolyte. Charging at low temperatures increases internal resistance which can lowered the potential of graphite below the stability window of the electrolyte, leading to the decomposition of the electrolyte at the graphite surface.

3.4.3.2. Influence of the composition of the electrolyte

The investigation consists in testing electrolytes of different chemical composition with coin full cells based on electrodes recovered from a fresh 16 Ah commercial Li-ion cell. Electrolytes are synthesized based on components detected from a fresh electrolyte with GCMS as shown in **Table III-6**. The aim is to identify the impact of each element of the electrolyte on the fast loss of performance observed in cycling at 5 °C.

The electrolyte #1 corresponds to the original composition of the fresh commercial electrolyte. For the others compositions, an additive is removed successively in order to study the influence on cycling performance. The electrolyte #6 does not retain any additives. Only DMC is added as solvent in order to obtain a standard electrolyte.

Twelve CR2032 Graphite/NMC coin full cells are assembled: two coin full cells per type of electrolyte as described in **Table III-7** in order to verify the reproducibility. The nominal capacity of each coin full cell is 2.88 mAh with $V_{min} = 2.7$ V and $V_{max} = 4.2$ V. Cycling are performed between 2.7 - 4.2 V at a rate of 1 C in charge (with a CV phase) as in discharge.

Electrolyte	Solvents	Additives
E1	1:1:1 EMC:EC + LiPF ₆ 1 M	BP + PS + FEC + VC
E2		BP + PS + FEC
E3		BP + PS
E4		BP
E5		PS
E6	1:1:1 EMC:EC:DMC + LiPF ₆ 1 M	

Table III-7 : Composition of different electrolytes based on elements detected from the fresh electrolyte with GC-MS [3.4.3.1].

As with 16 Ah commercial pouch-cells, the reference capacity of each coin full cell is measured at 25 °C at the beginning of life (BOL) and after the cycling period. After cycling, all the coin full cells are dismantled at a discharged state as it was the case for 16 Ah commercial pouch-cells.

Figure III-15 presents the evolution of the charged capacity measured at each cycle during cycling test at 5 °C between 2.7 V and 4.2 V with coin full cells based on six different types of electrolyte composition.

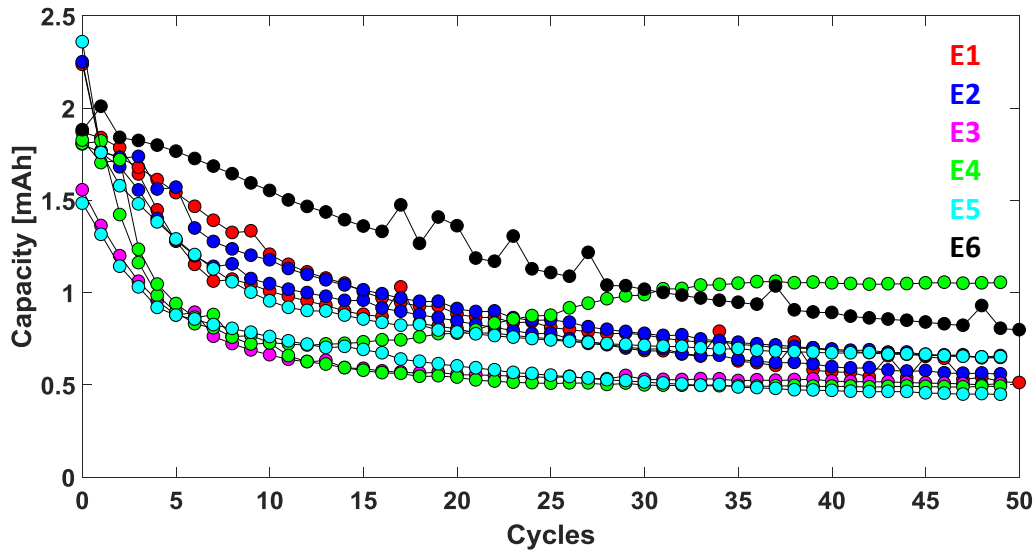


Figure III-15 : Evolution of the charged capacity measured at each cycle during cycling test at 5 °C between 2.7 V and 4.2 V with coin full cells based on six different types of electrolyte composition.

Unfortunately, for the electrolytes E3 and E6, one of the two coin full cells did not work. Nevertheless, the same signature of a fast decrease of performance in only 50 cycles, already observed with commercial cells as seen in **Figure III-3**, is also put into evidence here with the all coin full cells. As seen in **Table III-8**, fast performance fade is observed whatever the nature of the electrolyte.

Loss of capacity (%)	Electrolyte					
	1	2	3	4	5	6
0.1 C	57	52	47	31	38	49
0.2 C	54	47	40	29	38	48
0.5 C	54	46	43	22	38	47
1 C	50	43	38	20	34	45

Table III-8 : The average of capacity loss of coin full cells per type of electrolyte.

Figure III-16 illustrates visual inspections of components of those coin full cells based on different composition of electrolyte after cycling at 5 °C. Coin full cells are disassembled at a discharged state after a discharge applied at a rate of 0.1 C as it was the case for the 16 Ah commercial cells.

Electrolytes		NMC		Separator		Graphite	
		Coin cell #1	Coin cell #2	Coin cell #1	Coin cell #2	Coin cell #1	Coin cell #2
E1							
EC+EMC+ LiPF ₆ 1M	BP+PS+FEC+VC						
E2							
EC+EMC+ LiPF ₆ 1M	BP+PS+FEC						
E3			Failed		Failed		Failed
EC+EMC+ LiPF ₆ 1M	BP+PS						
E4							
EC+EMC+ LiPF ₆ 1M	BP						
E5							
EC+EMC+ LiPF ₆ 1M	PS						
E6			Failed		Failed		Failed
EC+EMC+DMC+ LiPF ₆ 1M							

Figure III-16 : Visual inspections of both negative and positive electrodes and separators of coin full cells after cycling at 5 °C and at a rate of 1 C between 2.7 V and 4.2 V.

It is remarkable to observe that there is no interesting defect on the positive electrode and on the separator which remained white.

In addition, the graphite remained lithiated regardless the composition of the electrolyte for the all coin full cells. This mechanism is therefore reproducible for 16 Ah commercial Li-ion cells as with coin full cells. Areas that have not been in contact with the opposite electrode remained in black color. No metallic Li is visually observed. This result demonstrates that there is no notable influence of the nature of the electrolyte in this aging mechanism. It is therefore the graphite electrode that would only be involved.

In the literature, J. C Burns and J. R. Dahn [46; 181] explained that electrolyte oxidation products might migrate to the negative electrode where they are reduced and eventually shut it down. They showed that near end of life, pores of a highly compacted graphite might become filled by reduced products originating from oxidized electrolyte resulting in a catastrophic performance fade of the cell. Consequently, as the access of Li into pores is blocked, Li plating occurs on surface of the anode and Li inventory is reduced at each cycle and cell fails quickly. This mechanism was rather reported for temperature higher than 20 °C [1.2.4.2].

Based on this assumption, it appears necessary to perform further investigations, especially on the surface and in the bulk of the graphite electrode.

3.4.4. Influence of the films on graphite electrodes

3.4.4.1. Detection of metallic Li with ^7Li NMR

^7Li NMR under fast magic angle spinning appears to be useful for ex situ and post-mortem analyses of battery electrodes. **Figure III-17** illustrates ^7Li NMR measurements performed on graphite electrodes retrieved respectively from the cell #3 and the cell #5.

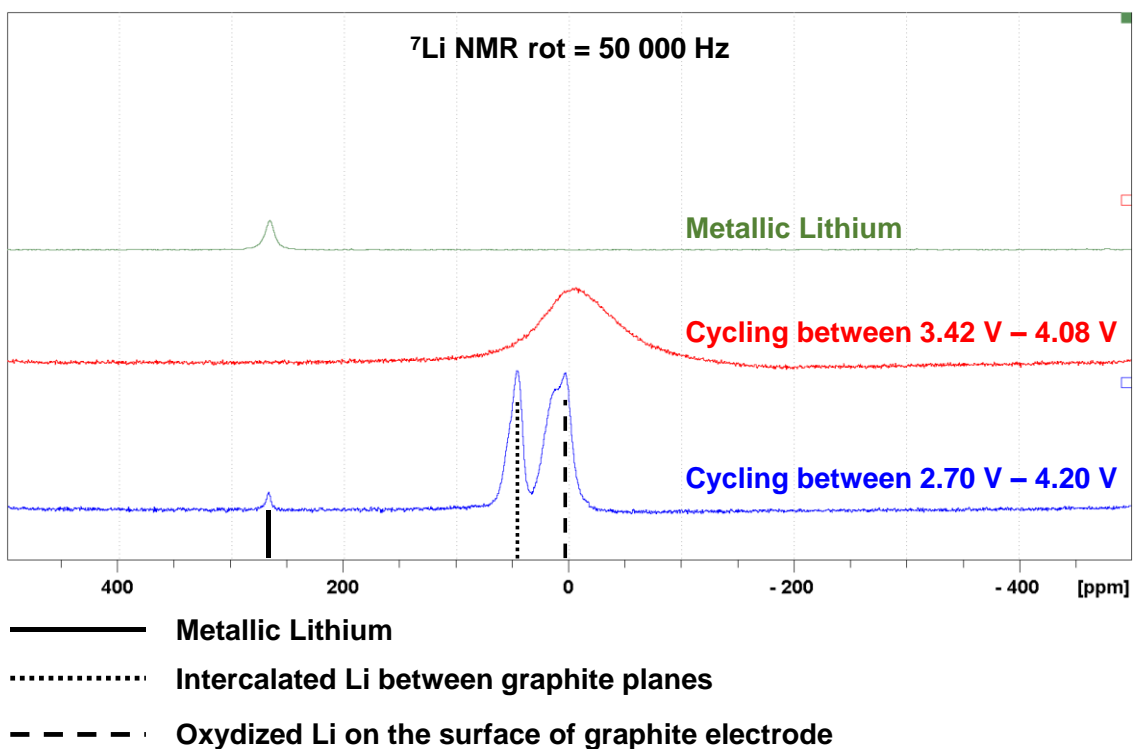


Figure III-17 : ^7Li NMR analysis on graphite electrodes.

The presence of metallic Li is detected with a lower intensity only on the most degraded graphite with a specific signal centered at 260 ppm.

The high signal at 0 ppm is assigned to Li in diamagnetic compound complexes with graphite derivatives for instance or diamagnetic inorganic salts indicating the presence of the SEI [40].

There is an additional high intensity peak at 50 ppm, corresponding to intercalated Li between graphite planes. W.-C. Oh [182] reported that a Knight shift of 44.32 ppm corresponding to the LiC_6 compound indicates an electrical field gradient at the Li nucleus site with a quasi-axial symmetry.

^7Li NMR is a chemical method sensitive to bulk electrode as described by T. Waldman et al. [116]. These results demonstrated that metallic Li deposition (“dead Li”) is not the main aging mechanism involved. In addition, these observations are consistent with coin half cells results [3.4.2.1] which showed that Li ions were trapped in graphite electrode.

Moreover, the peak corresponding to Li trapped into graphite planes and that one attributed to oxidized Li on the surface of the electrode are higher than that one corresponding to metallic Li. This result is in agreement with measurements obtained with reference electrode [3.3] which showed that graphite potential went below 0 V vs. Li^+/Li only over the last 6 cycles, well after the capacity of the cell failed.

The fact that metallic Li (not visually observed) is detected in small amounts on the surface of the graphite electrode may be congruent with dendrites observed on SEM and TEM images (see in **Figure III-8** and **Figure III-9**).

Whatever, it appears here that Li remains in large amounts trapped in the form of graphite intercalation compounds (as confirmed by XRD in **Figure III-14**) and the negative electrode may be hindered by a film composed of electrolyte degradation products (as shown with GC-MS in **Table III-6**).

3.4.4.2. Chemical Investigation into the volume of graphite electrodes with FIB/ToF-SIMS

Figure III-18 presents normalized elemental mappings of graphite electrodes recovered from the cell #3 and from the cell #5.

For the cell #5 (cycled between 3.42 V and 4.08 V), Li signal is weak and presents almost no contrast, confirming the near absence of Li. Fluorine is mainly detected at the surface of the electrode (left part of the image – outlined in red) which indicates the presence of SEI, and also slightly around graphite grains.

For the cell #3 (cycled between 2.7 V and 4.2 V), fluorine mapping is different: the observed contrast is representative of a higher concentration in the regions corresponding to the cavities between or within particles.

III. Study of aging mechanisms at low temperature

This is an indication that in that case, the inter-particles cavities are filled with electrolyte degradation products. Moreover, Li mapping presents a signal contrast fitting the graphite particles mapping (see carbon mapping), confirming Li trapping into the graphite particles.

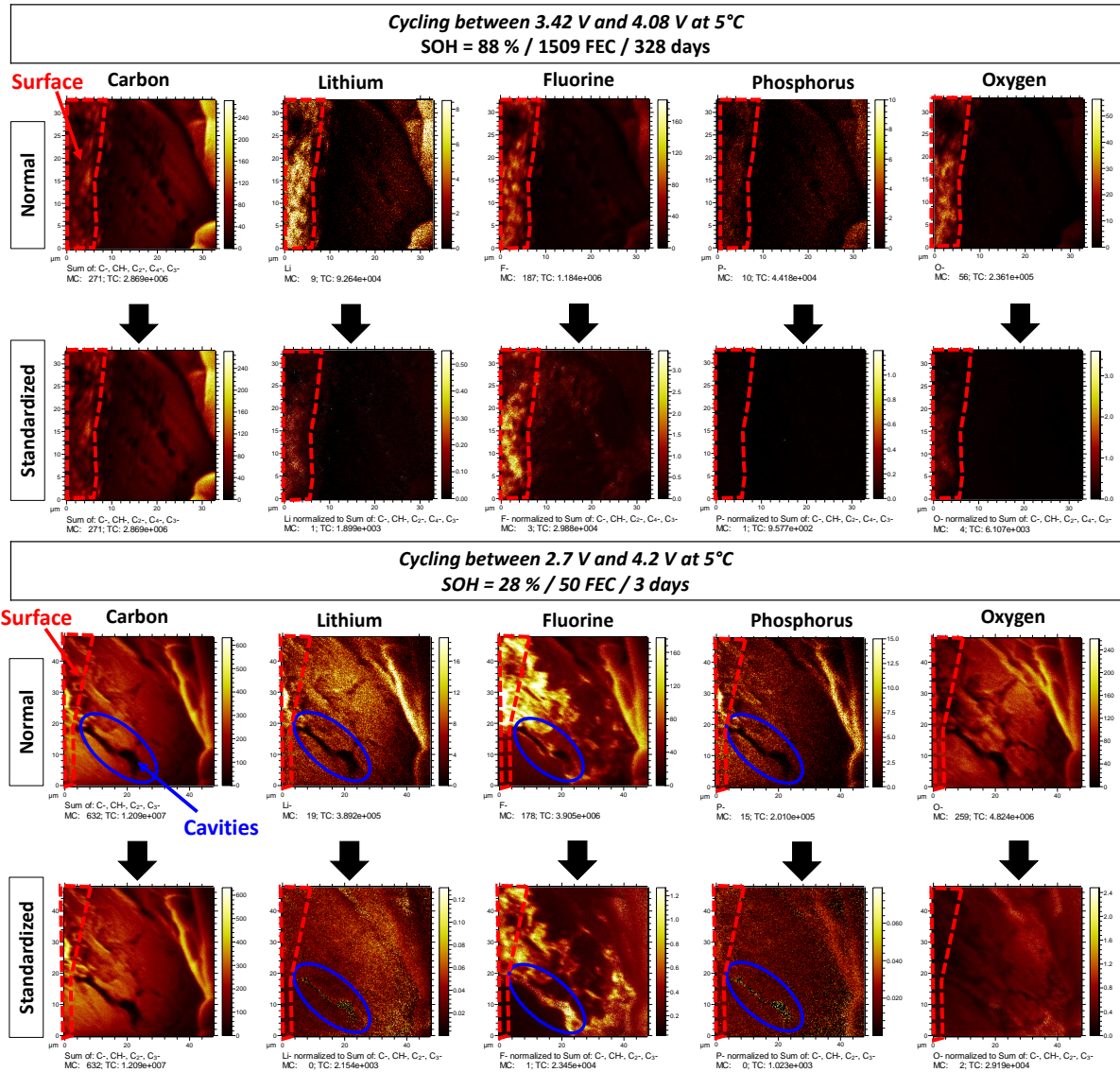


Figure III-18 : ToF-SIMS images: Standardization of the rate of each characteristic element in function of the graphite "carbon" rate.

3.4.4.3. Chemical Investigation of the SEI on graphite electrodes with XPS

We aim to further investigate graphite electrodes recovered from the cell #3 and cell #5 which were subjected to FIB-SIMS analyzes suggesting electrolyte degradation compounds in significant quantities into the electrode porosity.

In the literature, it is reported that the elevated temperatures accelerate the formation of passivation films on anode. The SEI growth was found to be rather favored by high SOC and high temperature storage conditions.

In the case of this study, it would be unlikely to suggest a growth of the regular SEI favored at 5 °C. In contrast to the typical nanometer SEI film reported in the literature, the formation of an untypical layer composed of electrolyte decomposition products obstructing the graphite electrode pores and then de/re-lithiation mechanisms seems to be more appropriate.

The objective of XPS is to compare the chemical composition of the films at the surface of both graphite electrodes, respectively retrieved from the cell #3 and the cell #5.

3.4.4.3.1. Spectroscopic analysis

Figure III-19 presents the XPS spectroscopic analysis results for both graphite electrodes.

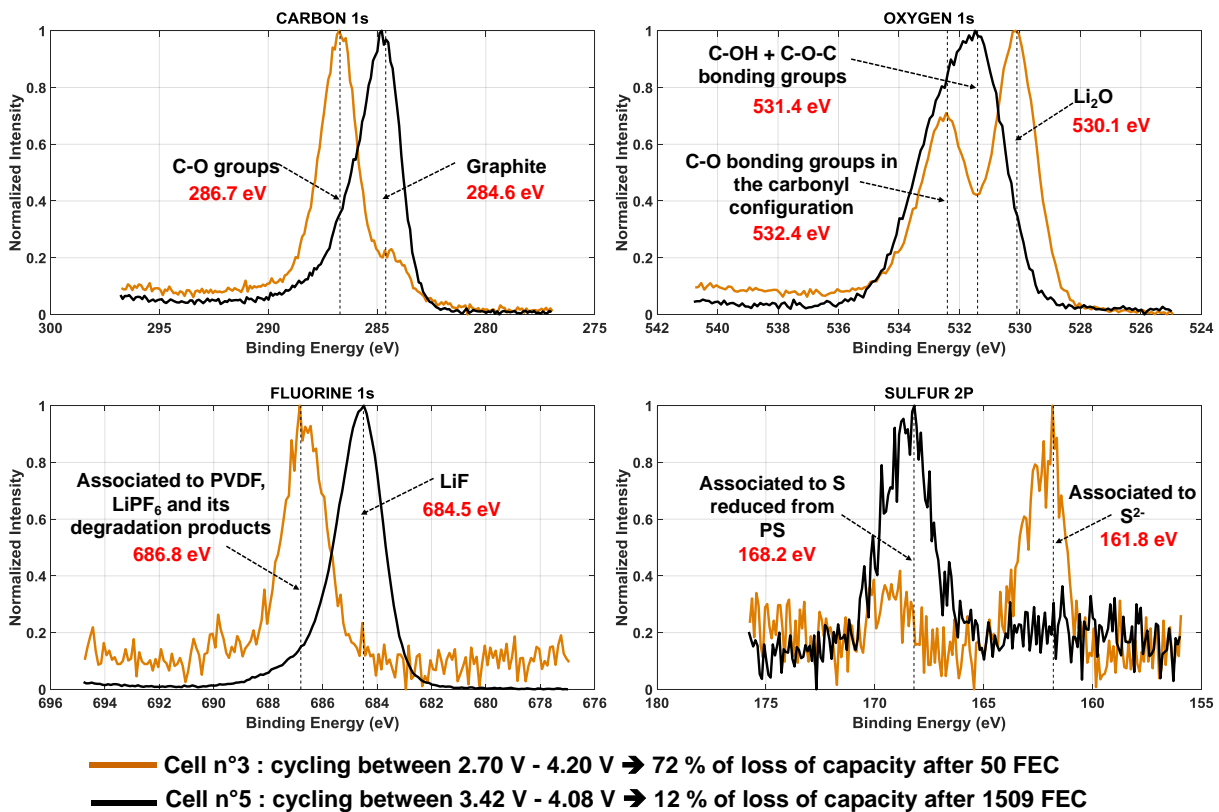


Figure III-19 : Spectroscopic analysis of graphite electrodes with XPS technique

C 1s analysis –

The C 1s spectrum of graphite from the cell #5 presents one asymmetric peak, whose maximum is at 284.6 eV. This peak can be related to the presence of the active material (graphite particles) probably mixed with carbon black [183; 184]. Its relative high intensity confirms that the passivation layer is thin (regular SEI), probably no more than 2 or 3 nm.

In contrast, the C 1s XPS spectrum of graphite from the cell #3 presents one main peak at 286.7 eV associated to C-O groups, and a tiny shoulder of lower intensity at 284.6 eV. This is a clear indication of the presence of a thicker layer screening the photoelectrons originated from the graphite particles. It can be assumed that this thick layer is composed of the expected SEI and the accumulation of electrolyte degradation products impeding carbon pores.

F 1s analysis –

The F 1s spectra of both electrodes show 2 peaks located at different binding energies. The sample from the cell #5 presents one intense peak at 684.5 eV which can be explained by the presence of LiF [184; 185] compounds while the surface of the electrode #3 is characterized by a peak of lower intensity at the same binding energy. This could indicate the absence of the LiF compounds in the composition of the regular SEI formed on the graphite surface. Nevertheless, this hypothesis remains unlikely. The most likely explanation is that the presence of a layer formed over the LiF compounds, suspected to hinder graphite electrode pores, is shielding the photoelectrons originated from these Li fluoride compounds as it has been observed with carbon particles.

Besides, this graphite electrode shows one intense peak at 686.8 eV, which may be associated to PVDF, LiPF₆ and its degradation products such as Li phosphofluorides [184].

O 1s analysis –

The O 1s XPS spectra are quite different between both electrodes.

Graphite electrode from the cell #5 presents a wide shoulder centered at a higher binding energy (531.4 eV): this is typical of SEI with a wide range of oxidized species and C-OH and/or C-O-C bonds [184; 186; 187].

Graphite electrode from the cell #3 presents two well separated peaks. The lower binding energy peak (530.1 eV) is associated with Li₂O [184; 188], while the other one (532.4 eV) corresponds to C-O bonding groups in the carbonyl group or Li carbonate molecule [185].

S 2p analysis –

The peak associated to the sample retrieved from the cell #5 is located at a higher binding energy of 168.2 eV, which is typical of S reduced from 1,3 propane sultone [186]. Surprisingly, the S 2p of the graphite electrode from the cell #3 presents a lower binding energy peak (161.8 eV), which is assigned to S²⁻ [186].

The respective passivation films compositions are given in **Table III-9**.

Element		C	O	F	P	S	Li
% at.	Cell #3	24.7	19.3	1.8	0	0.5	53.7
	Cell #5	24.1	10.5	32.7	2	0.5	30.3

Table III-9: Percentage of each element detected with XPS on the surface of samples of graphite electrodes respectively recovered from the cell #3 (cycled between 2.70 V and 4.20 V) and from the cell #5 (cycled between 3.42 V and 4.08 V).

Graphite electrode recovered from the cell #5 presents a Li/F ratio close to 1, relative to the high presence of amounts of LiF (confirmed by F 1s spectra). Other elements (C, O, and P) are probably related to the presence of (poly(ethylene oxide)) PEO-type oligomers, ROCO_2Li and $\text{Li}_x\text{PO}_y\text{F}_z$ compounds.

On the contrary, the composition of the electrode of the cell #3 presents high amounts of Li and a very high Li/F ratio. R. Castaing et al. [142] reported that LiF may be dissolved in the electrolyte instead of being deposited at the surface of active material grains. Recently, L. Somerville et al. [118] demonstrated that DMC washing for 1 minute can remove LiF and Li_xPF_y functionalities from deeper strata of the SEI.

LiF may be here probably screened by another layer based on accumulation of electrolyte degradation products constituting an additional layer over it (LiF) or modified by reacting with these compounds as confirmed by XPS F 1s spectrum which validates the presence of Li_xPF_y species instead.

Note that ToF-SIMS analysis showed that inter-particles cavities were filled with fluorine. C. Marxer et al. [150] reported that ToF-SIMS analysis is more sensitive than the XPS, particularly for the detection of fluorine, for which the yield is very high.

3.4.4.3.2. Profilometric analysis

Figure III-20 presents XPS profilometric analyses of the surface of both graphite electrodes.

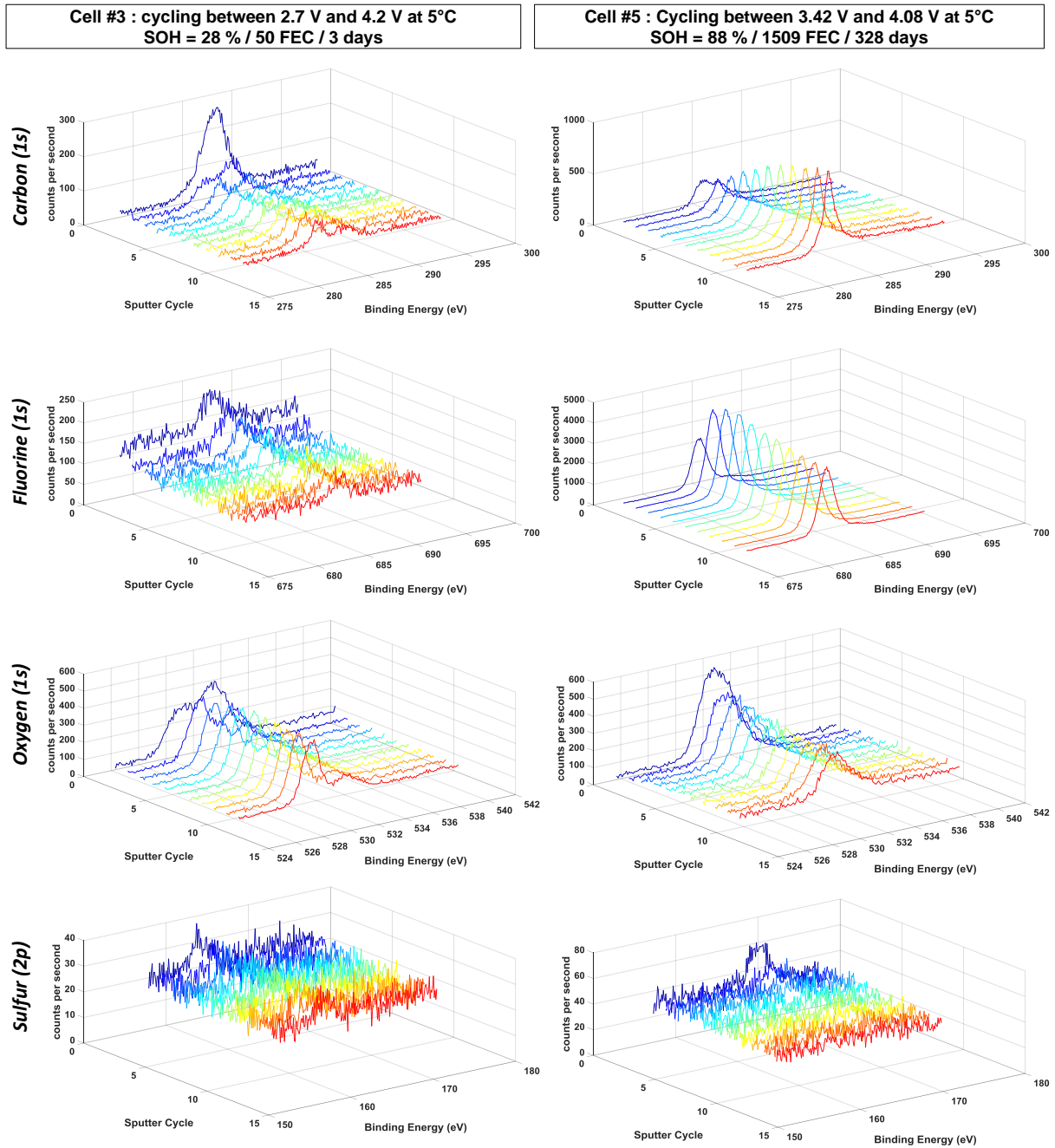


Figure III-20 : Profilometric analysis graphite electrodes with XPS technique.

C 1s analysis –

The concentration profile for the graphite electrode of the cell #5 shows that the peak corresponding to the graphite contribution increases with the number of sputter cycles.

For the graphite electrode of the cell #3, C 1s profile concentration shows the extinction of the peak at higher binding energy (286.7 eV) after the first sputtering step, confirming the thinness of the film formed by C-O species on the surface of the remained lithiated graphite electrode (cell #3).

After the first sputtering step, the intensity of the carbon peak becomes constant. More sputtering steps would be required to remove completely the thick layer above and then to see the increase of the peak corresponding to graphite.

F 1s analysis –

F 1s profiling concentrations show that LiF is not present even in the internal part of the SEI, in the case of electrode of the cell #3: it has probably been degraded with cycling or it may be assumed that it had reacted with other degradation products. Otherwise for the other electrode (cell #5), LiF remains present throughout the SEI.

O 1s analysis –

On one hand, the O 1s XPS profiling concentrations show a decrease of the peak corresponding to species identified as C-O bonding groups at 532.4 eV for the aged graphite (cell #3).

On the other hand, a decrease of the wide shoulder centered at 531.4 eV is also observed for the non-degraded graphite (cell #5).

S 2p analysis –

For the non-degraded graphite (cell #5), the peak observed at ~168.2 eV disappears after the first sputtering step: this suggests that this contribution is linked to some traces of the electrolyte deposition at the surface which are quickly removed with sputtering. On the contrary, for the aged graphite, the numerous sputtering steps do not remove the peak observed at 161.8 eV which remains until the end of the profile. This strongly suggests that this peak is due to the presence of a degraded (reduced) product of PS in the whole depth of the SEI.

The thickness abraded by step of abrasion cannot be known with certainty and precision. For this, it would be necessary to "calibrate" the abrasion with a layer of SEI of similar composition and of known thickness for the chosen abrasion conditions.

This technique remains a "relative" semi-quantitative tool, that is, from one analysis to another, for similar abrasion conditions, it is possible to compare the thicknesses between them (to say that a layer is thicker in one case than the other).

3.5. Representation of the mechanism leading to the hindrance of Li diffusion into graphite electrodes

We found in this chapter a new explanation, different from the usual metallic Li deposition expected in cycling at low temperature, to explain the very fast capacity fade observed on Kokam 16 Ah cells in such conditions (i.e. 75 % over only 50 cycles). **Figure III-21** presents a scheme that explains the formation of an untypical layer constituted by electrolyte degradation products occurring during cycling of 16 Ah commercial Li-ion cells at 5 °C between 2.7 V and 4.2 V.

The evolution of the state of the graphite electrode is represented here at the end of discharges as the number of cycles increases. During cycling at 5 °C, the regular SEI layer as reported in the literature does not grow since its growth is rather favored by high temperatures and high SOC's.

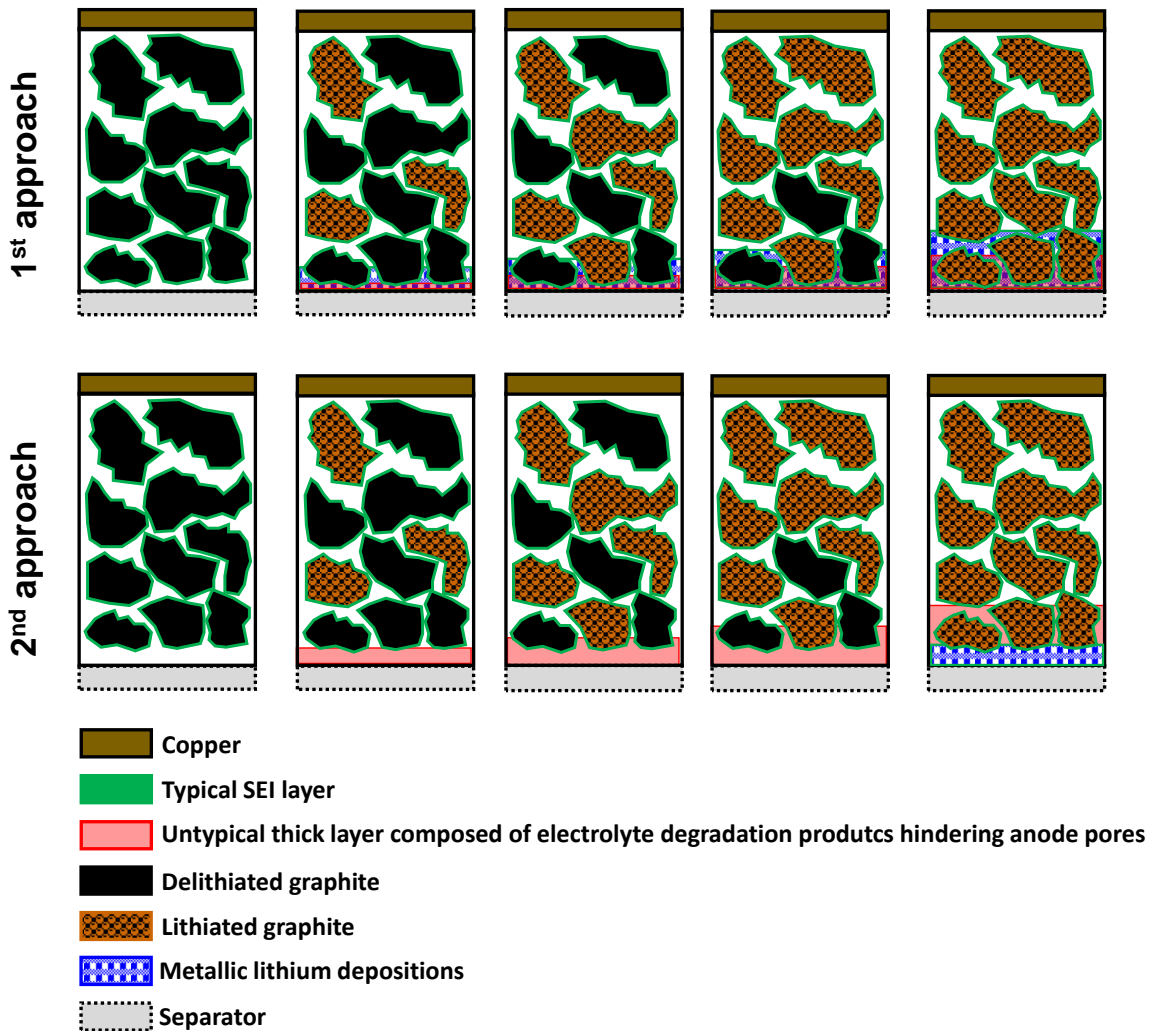


Figure III-21 : Representation of the mechanism leading to the hindrance of Li diffusion into graphite electrodes, observed during cycling at 5 °C between 2.7 V and 4.2 V.

Charging at low temperatures increases internal resistance which can lower the potential of graphite below 0 V vs. Li⁺/Li. As a result, the potential of the graphite electrodes falls below the stability window of the electrolyte during charging.

On one hand, it leads to the decomposition of the solvents of the electrolyte forming a specific layer on top of and within the graphite electrode. Note that the analysis of the electrolyte with GC-MS shows a strong degradation of solvents and the apparition of many degradation products.

On the other hand, local metallic Li depositions are facilitated under such conditions.

As the number of cycles increases, this untypical layer grows and hinders more and more the pores of the graphite electrode. As a result, de/re-intercalation mechanisms are then significantly reduced into the negative electrodes. Consequently, some areas of the graphite electrode remain lithiated. Due to the presence of this growing layer clogging anode pores, it is then more and more difficult to extract more Li cations from graphite particles in order to intercalate into the positive electrode, as seen with the evolution of the end-of-charge / discharge potentials of both electrodes pointed out in **Figure III-6**.

On one hand, this mechanism leads to an irreversible and catastrophic capacity loss of about 75 % in only 50 cycles, as illustrated in **Figure III-3** and in **Table III-3**.

On the other hand, it causes a strong increase of the internal resistance by 400 %, as shown in section [3.2.2]. Moreover, visual inspections in **Figure III-7** show that graphite electrodes remain unexpectedly lithiated although the cell was dismantled after a discharge performed twice at rate of 0.1 C. The positive electrode was therefore not fully lithiated during the last discharge before dismantling.

In the case of metallic Li depositions, two approaches needs to be considered. Li depositions could be formed either all along cycling or at the very end.

The first approach would be that a part of metallic Li (deposited inside the volume of the electrode) formed all along cycling have been reversible. With this hypothesis, the measured anode potential (as seen in **Figure III-5** and **Figure III-6**) during cycling may not reflect the occurrence of localized Li plating, since it remains the average electrode potential. This supposition is in agreement with Li plating model developed by X.-G. Yang et al. [189].

The researchers demonstrated that the clogging of anode porosity induces localized Li plating formation all along cycling. By the end of cycling, serious Li plating leads to localized pore clogging resulting in a sharp resistance rise which would dramatically deteriorate the power capability of the cell. The growth of the layer clogging anode pores was found to be the dominant aging mechanism in this linear aging stage. Both numerical and experimental results were obtained for 3500 cycles performed at room temperature between 2.8 V and 4.2 V (charge at a rate of 1 C and discharge at a rate of 2 C) using graphite/NMC622 Li-ion cell with a nominal capacity of 12.4 Ah.

The second approach rather stipulates that as the entrance of Li ions into pores of graphite electrodes is obstructed by the growing of the layer made of electrolyte degradation products, Li plating occurs on surface of the anode due to the high polarization, as explained by J. Dahn [46; 181], and Li inventory is reduced at each cycle and cell fails rapidly.

This assumption is consistent with measurements obtained with the cell instrumented with reference electrodes which show that during cycling the potential of the negative electrode only goes below 0 V vs. Li⁺/Li over the last 6 cycles (see in **Figure III-5** and **Figure III-6**). This theory validates that the measurements with the reference electrode are potentially sufficient to reflect the occurrence of Li plating. This approach is also supported by ⁷Li NMR results where metallic Li is detected with a lower peak (**Figure III-17**).

Whatever the approach, the chemical composition of the layer hindering graphite electrodes given by XPS suggests the presence of C-O bonding species; Li₂O; Li carbonates; PVDF, LiPF₆ and its degradation products (Li_xPO_yF_z compounds).

In recent past, M. Klett et al. [134] showed experimental evidence of uneven surface film formation across the depth of a porous graphite electrode obtained from a commercial 26650 LiFePO₄/graphite cell cycled with 3.75 C and 100 % depth of discharge (DoD) at 22 °C. After cycling, the capacity loss was 34 %, nevertheless the authors did not precise the number of cycles performed.

From their EDX mapping, it was found that the film was enriched, on one hand, in carbonates species clogging the pores in the electrode closest to the separator and on the other hand, in fluorine which appears evenly distributed throughout the electrode depth. The authors performed ToF-SIMS analysis which showed that this uneven film has similar decomposition species than the standard SEI, though with higher amounts of PO and PO₂ fragments. The film formation led to the reduction of the current distribution in the porous electrode and then it caused an inefficient material utilization.

In this chapter, we have discussed a similar mechanism but rather observed during cycling at 1 C and at 5 °C. Besides, the chemical composition of this untypical layer as described above seems to be identical in both studies.

This might mean that even at room temperatures, for certain types of graphite electrodes and by applying strong charge rates, the same mechanism of degradation could be observed. However, all the papers mentioned above do not discuss about the fact that most of Li ions are lost in the form of graphite intercalated compounds. We have shown that graphite remained lithiated and thus it becomes difficult to delithiate it because of the hindrance of pores on the surface.

3.6. Conclusions

A fast loss of performance around 75 % was observed during fully cycling at 5 °C (in only 50 cycles). Graphite electrodes of 16 Ah commercial Li-ion cells remained unexpectedly lithiated after dismantling at a discharged state. Electrochemical measurements with full coin cells demonstrated that there is no influence of the nature of the electrolyte in the aging mechanism. The evolution of the end-of-charge / discharge potentials of both electrodes during cycling showed difficulties to extract more Li cations from graphite to intercalate to the positive electrode.

The analysis of the electrolyte with GC-MS showed a strong solvents decomposition and the apparition of many degradation products which have accumulated on graphite electrodes during cycling to form an untypical layer hindering the pores of the anode. As a result, Li de/re-intercalation mechanisms are then obstructed into the negative electrode presenting lower porosity.

Based on XPS results, it can be assumed that this thick layer impeding the electrode porosity is mainly formed by C-O bonding species; Li_2O ; Li carbonates; PVDF, LiPF_6 and its degradation products ($\text{Li}_x\text{PO}_y\text{F}_z$ compounds).

Metallic Li is detected in very negligible amounts as seen with ^7Li NMR analysis suggesting that it is not really the main aging mechanism involved. Some dendrites are well distinguished on the surface of the remained lithiated graphite with SEM and TEM images.

The fact that graphite remained lithiated may be explained by the hindering of the electrode porosity, preventing diffusion of the remaining cyclable Li into the electrode depth. Moreover, the higher reduction level imposed by the cycling conditions may induce a drastic degradation of the electrolyte. These results are consistent with the interpretation in FIB-SIMS which suggests the obstructing of the porosity of the graphite electrode. It can be concluded that the length of this diffusion pathway (which directly depends on the electrode engineering) is one of the key parameters affecting the formation of the untypical layer found in this study to be the main aging mechanism in cycling at low temperature.

III. Study of aging mechanisms at low temperature

IV. Study of aging mechanisms at high temperature

In this chapter, we discuss unexpected aging mechanisms observed during calendar life of commercial Li-ion cells suggested to high temperatures and high states of charge conditions.

Performance of cells in calendar aging are presented in the first branch of this fourth Chapter. The evolution of the state of health as well as that of the increase of the resistance of cells are discussed with details.

The second part of this Chapter is dedicated to post-mortem analyses required in order to investigate aging mechanisms involved. The effects of overcharge protection agents such as Biphenyl used as an electrolyte additive are figured out.

By the end of this Chapter, a schematic model, illustrating the development process of aging mechanisms observed, is scheduled in accordance with the understanding provided by the results of the various analyzes.

4.1. Performance of cells in calendar aging

Twenty nine 16 Ah commercial C/NMC Li-ion cells are aged in calendar mode using 3 different states of charge (SOC), namely SOC=50 %, 90 % and 100 % and 4 different temperatures, namely 5 °C, 25 °C, 45 °C and 60 °C, as illustrated in **Table IV-1**.

T (°C)	SOC (%)			Total
	50	90	100	
5	x2 CIDETEC		x3 CIDETEC	5
25	x2 EIGSI	x3 EIGSI	x3 EIGSI	8
45	x2 CEA	x3 CEA	x3 CEA	8
60	x2 VITO	x2 VITO	x3 VITO	7
			x1 CEA**	1
Total	8	8	13	29

Table IV-1 : Calendar aging conditions (** condition without any periodic check-up test but only two check-ups, at BOL and EOL respectively).

Therefore, as for cycling tests, the same electrical checkup tests performed at 25 °C are also used here in order to measure the capacity of the cell after each calendar phase.

Thus, periodic check-ups are performed at 25 °C every 8 weeks for cells stored at 5 °C and 25 °C, every 6 weeks for cells stored at 45 °C and every 4 weeks for cells stored at 60 °C. It is indeed well known that the calendar aging of Li-ion batteries is favored by high SOC and high temperatures during storage time [190; 191]. That is why we decided to manage the periodicity of the experimental control tests, which consists in reducing the time between two checkups for more severe aging conditions in order to limit the decrease in capacity between the two tests (and conversely for less severe aging conditions).

An additional cell ** was stored at 60 °C and 100 % of SOC without any periodic electric check-up tests during 4 months.

The duration corresponds to time of storage of other cells aged at 60 °C. In this case, a test of capacity is performed at low charge rate at 25 °C after the 4 months of storage according to the following protocol: residual discharge performed at a rate of C / 25 until 2.7 V. After a rest of 30 minutes, a charge is performed at rate of C / 25 until 4.2 V followed by a last discharge at C / 25 until 2.7 V.

** condition without any periodic check-up test but only two check-ups, at BOL and EOL respectively

IV. Study of aging mechanisms at high temperature

The aim of this additional test being to measure the influence of intermediate checkups on the aging. This is the reason why we decided to limit the charge C-rate to C / 2 5 instead of 1 C during the classical ECU and SCU.

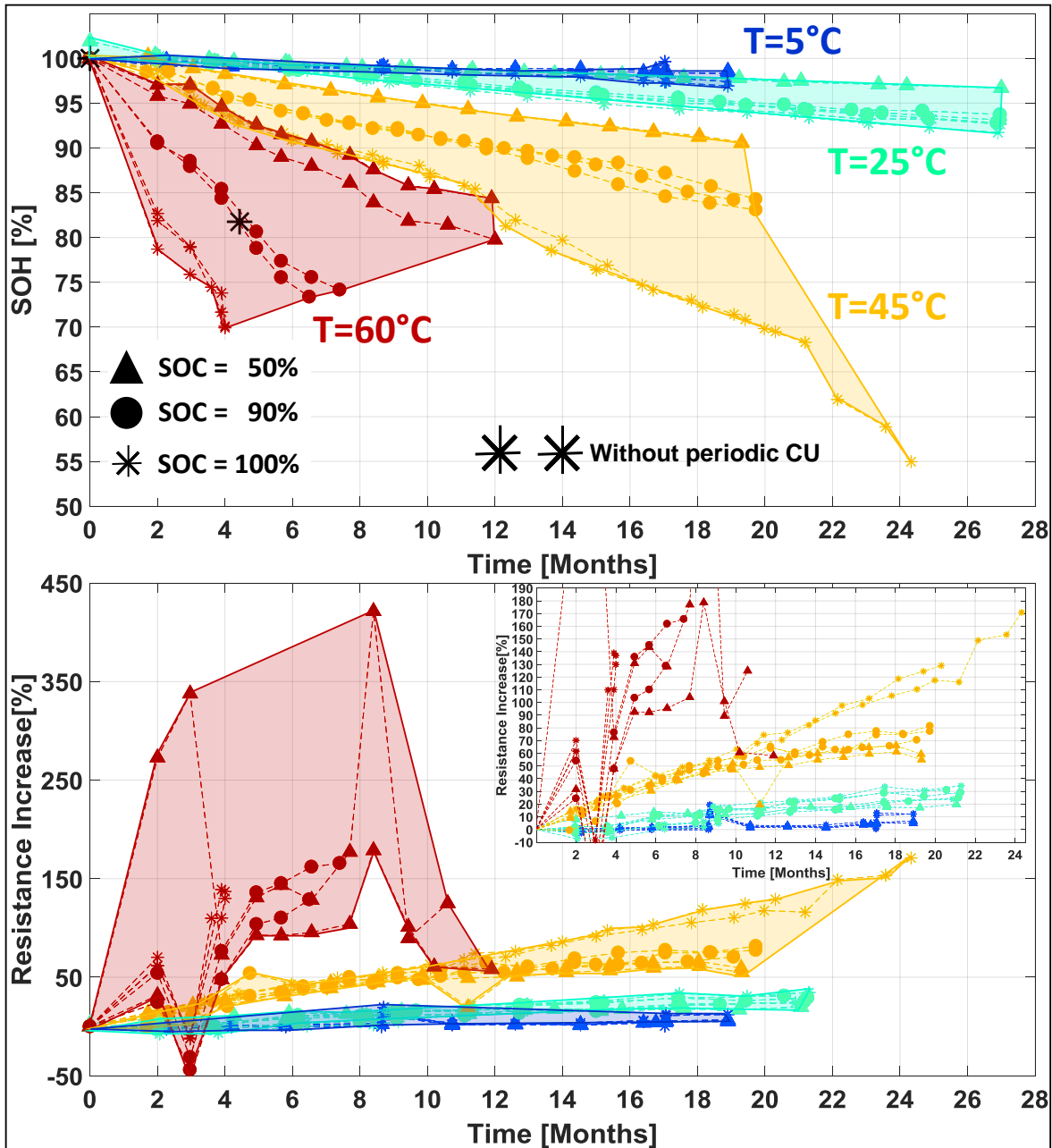


Figure IV-1 : Evolution of the state of health and the resistance increase of 16Ah commercial Li-ion cells in calendar aging.

The evolution of the SOH and the resistance increase of the 16 Ah calendar aged commercial batteries is presented in **Figure IV-1**.

For the SOH, the reference capacity is the discharged capacity measured during periodic checkup tests at a rate of 1 C. The resistance is determined based on pulses measurements, more especially at 40 % of SOC and at 10 s.

IV. Study of aging mechanisms at high temperature

For the cell stored 4 months without periodic standard checkups, the capacity at 1 C at the second check-up (after storage time) is estimated as a function of the capacity measured at C / 25 multiplied by a ratio since for this specific cell, the maximum C-rate used during its second check-up is C / 25 as mentioned above.

This ratio is thus determined by dividing the value of the capacity measured at 1 C on that measured at C / 25 obtained at the first check-up (before storage time) and it is equal to 1.002. In addition, since no pulses measurements were performed on that particular cell, no resistance values can be obtained.

Nevertheless, it can be observed that the degradation of Graphite/NMC Li-ion batteries in calendar aging mode is favored by high SOC and high temperatures storage conditions. These results are consistent with previously reported results [192; 193; 194; 195].

For high temperatures, the strong difference observed between SOC = 90 % and SOC = 100 % in calendar aging of Graphite/NMC Li-ion cells has already been observed in the literature. The influence of the SOC on the aging is not linear with the SOC. The main hypothesis is the influence of the corresponding voltages.

Regarding the curves corresponding to resistance increase, the influence of the temperature and the SOC is also ascertained.

Cells stored at 5 °C showed a resistance increase less than 10 % (with a capacity loss limited to 2 % in 19 months for cells aged at 100 % of SOC).

These results confirm that aging at low temperature does not lead to the increase of the resistance of the cell. Furthermore, they corroborate the fact that the considerable rise of the resistance observed after full cycling at 5 °C, as discussed in the previous Chapter, was definitely not related to the growth of the regular SEI but rather to the accumulation of important electrolyte degradation products into anode porosity.

The cells aged at SOC = 100% and at 5 °C, 25 °C, 45 °C and 60 °C have been selected for further post-mortem analyses.

4.2. Post-mortem analyses

4.2.1. Visual inspections

Visual inspections of aged components have raised several interesting features as shown in **Figure IV-2**. The electrodes and the separator are still wetted by the electrolyte at the moment of dismantling, at any aging conditions.

Calendar ageing SOC=100%		Components			Comments
		Graphite	Separator	NMC	
With periodic check-up tests	T=5°C SOH (1C)=100% Duration = 9 months				No Lithium deposition
	T=25°C SOH (1C)=100% Duration = 9 months				No Lithium deposition
	T=45°C SOH (1C)=93% Duration = 10 months				Lithium deposition
	T=60°C SOH (1C)=72% SOH (C/25)=75% Duration = 4 months				Lithium deposition
Without periodic check-up tests	T=60°C SOH (C/25)=82% Duration = 4 months				No Lithium deposition

Figure IV-2 : Visual inspections of negative and positive electrodes and separators of commercial 16 Ah Graphite/NMC pouch cells (at discharged state) aged in calendar mode (SOC=100%).

Electrodes and separators aged in the calendar condition at low temperature ($T = 5\text{ }^{\circ}\text{C}$) present no visible change. This is in accordance with the low capacity loss observed at $5\text{ }^{\circ}\text{C}$ (see **Figure IV-1**).

For the cells stored at $25\text{ }^{\circ}\text{C}$, the separator presents only a light brown color on the side in contact with positive electrodes whereas there is no notable visible change detected on the electrodes.

IV. Study of aging mechanisms at high temperature

Harvested positive electrodes of cells stored at 45 °C present a black color with circular grey stains. The separator presents a brown color with white circular areas.

Graphite electrodes present concentric lithiated deposits which are symmetric to the circumference of white zones found on the brown separators and grey stains found on NMC electrodes. This symmetrical correlation between separator white zones, stains on NMC electrodes on one side and circular lithiated deposits on graphite on the other side is exposed in **Figure IV-3**. Those lithiated deposits, insoluble with DMC or acetonitrile, can be removed with friction and are very reactive with water.

Inside of some of these concentric lithiated deposits, the graphite appears to have a high lithiated state compared to the rest of the surface. This indicates that lithium is no more exchangeable in those areas where graphite particles remained lithiated despite the discharge before dismantling.

Similar observations are done on the cells aged in calendar mode at higher temperature, more pronounced for cells stored at 60 °C with periodic checkup tests. In this cell, the graphite electrode reveals an important concentration of Li metal deposition around the symmetrical areas.

Additionally to the cells aged with periodic check-ups, a cell was aged at 60 °C and 100 % of SOC without checkups as detailed above.

The post mortem study reveals that the brown separator shows the same white symmetrical areas and the corresponding grey stains observed on both positive and negative electrodes. However, there are no presence of metallic lithium on graphite electrodes. We can hence conclude that the metallic lithium deposition occurred only during the checkup.

Both cells aged with or without periodic check-up tests have been stored in the same condition (at 60 °C and at 100 % of SOC; during 4 months and until a SOH of 75 % and 82 % respectively). This small difference of SOH between the two cells can most likely be attributed to the lithium loss caused by the intermediate checkup tests which are leading to the metallic lithium deposits.

Contrary to visual inspections of graphite electrodes originating from 16 Ah Li-ion cells cycled at 5 °C between 2.7 V and 4.2 V at rate of 1 C where no Li depositions were visually found (graphite remained lithiated - see in the previous Chapter), we rather observe here the presence of localized metallic lithium deposition in large amounts, although cells were opened at discharged state.

In the literature, Jalkanen et al. [\[196\]](#) suggested the presence of lithium deposition after cycling at high temperature. As far as we know, there is no published works reporting this aging mechanism at high temperature operating conditions during calendar aging.

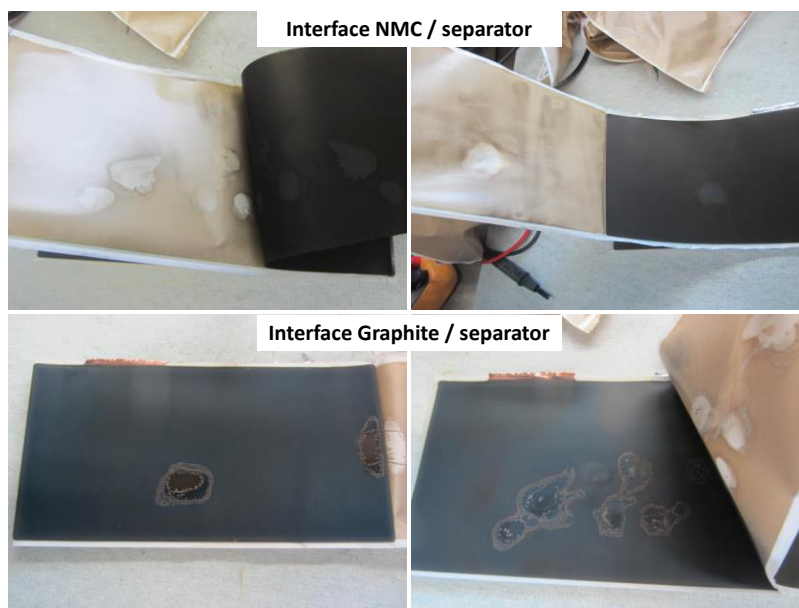


Figure IV-3 : Calendar aging at 45 °C and at 100 % of SOC.

According to the literature, at least two explanations can be proposed regarding the brown coloration found on the separator. It could be due to either remaining lithiated graphite and/or linked to the thermal and electrochemical degradation of LiPF_6 [197; 198].

Nagasubramanian [197] observed discoloration of the electrolyte containing LiPF_6 and based on solvents such as ethylene carbonate (EC) and ethyl methyl carbonate (EMC) at 60 °C while electrolyte containing $\text{LiN}(\text{SO}_2\text{C}_2\text{F}_5)_2$ showed very little discoloration even at 120 °C.

Zhang et al. [198] reported that 1.2 M LiPF_6 3:3:4 PC/EC/EMC electrolyte had changed its color to brown after 2 weeks of storage at 60 °C.

Similarly, a piece of a fresh separator has been immersed in an electrolyte composed by 1 M LiPF_6 EC/EMC at 45 °C for one month. In this experiment, we observed that the electrolyte became brown but the separator stayed white. So, it can be concluded that the thermal decomposition of LiPF_6 is not sufficient to modify the color of the separator. Brown color appears only when the separator is in contact with electrodes as confirmed by visual inspections. Namely, the upper surface of separator not in contact with electrodes is still white.

To go further in the understanding of the emergence of the distinct brown coloration of the separator, a piece of polyethylene in contact with lithiated graphite electrode and another piece in contact with delithiated NMC electrode were stored in an electrolyte composed by 1 M LiPF_6 EC/EMC during one month at 45 °C.

It was observed that only polyethylene in contact with delithiated NMC has changed its color to brown. This latest observation is consistent with results published by D.J. Xiong et al. [199]. Moreover, during storage at 60 °C, the experimenters observed that pouch bags containing only a lithiated graphite electrode and electrolyte produced no

gas while pouch bags containing only a delithiated NMC111 electrode (initial voltage of 4.2 V) and electrolyte produced a significant amount of gas. They suggested that predominant gas produced in the positive electrode was CO₂ (determined by GC-MS) which is thereafter consumed at the negative electrode.

It is thus reasonable to assume that white areas found in large amounts on brown separators retrieved from cells aged at 45 °C and 60 °C have thus not been in close contact with the delithiated NMC surface.

This contact disconnection is probably due to the progressive formation of gas bubbles caused by the degradation of the electrolyte inside the cell. Gas formation may be due to the electrolyte components oxidation at the NMC electrode maintained at high potential (calendar storage at SOC = 100 %) and high temperature as reported in the literature [199].

4.2.2. Deposits analysis with ⁷Li NMR

Figure IV-4 illustrates ⁷Li NMR measurements performed on graphite electrode retrieved from the cell aged in calendar mode at 60 °C and 100 % of SOC.

Samples were chosen as followed:

- 1) In the region of lithiated deposits (area A), only at the extreme surface of the electrode.
- 2) In the region of lithiated deposits (area A), all the thickness of the electrode.
- 3) At the electrode surface in any region without lithiated deposits (area B).

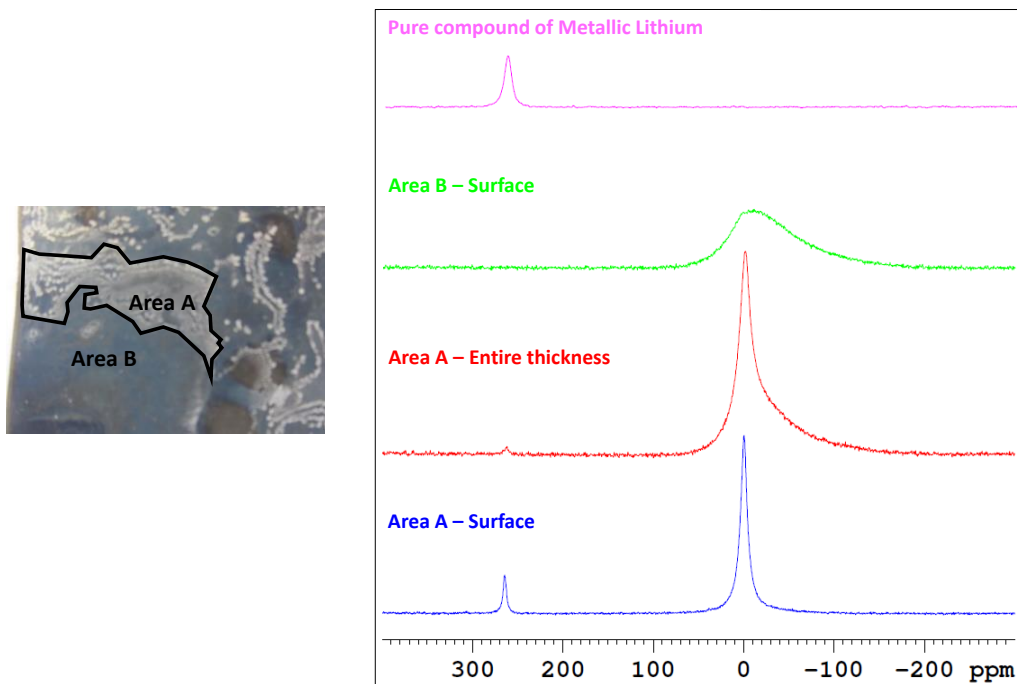


Figure IV-4 : ⁷Li NMR analysis on graphite electrode after calendar aging at 60°C and 100 % of SOC with periodic checkups.

With a specific signal centered at 260 ppm, the ^7Li NMR spectra demonstrated the presence of metallic lithium only where lithiated deposits could be picked out. This signal is visible both when the material was collected by scraping the surface (area A) of the electrode or by taking the thickness (area A) of the electrode. In the latter case the intensity of the signal was lower because of dilution effects.

According to the literature, the observed signal corresponds to a clear signature of Li metal with this technique [200; 201].

For the other spectrum, a signal at 0 ppm can be observed. This signal is narrow when it corresponds to a sample scraped at the surface of lithiated deposits (area A). However, if the sample is taken in the thickness (area A) of lithiated deposits, a broad shoulder appears at higher field in the range 0 to -100 ppm.

Very interestingly, if the sample is taken at the surface (area B) outside lithiated deposits, only the broad signal is observed.

On one hand, taking into account the NMR data reported in literature for ^7Li , the signal at 0 ppm can easily be assigned to Li in diamagnetic compound complexes with graphite derivatives for instance or diamagnetic inorganic salts.

On the other hand, the broad signal ranging from 0 to 100 ppm could be assigned to paramagnetic inorganic compounds including Ni, Mn Cr or Co.

In summary, there is a low intensity peak corresponding to metallic lithium (260 ppm) when the entire thickness of the area A is considered. In addition, the peak corresponding to lithium in oxidized form (at 0 ppm) seems to be the sum between the one observed with area A (scraping surface) and the one observed with area B (entire thickness).

4.2.3. Effect of the biphenyl additive in the electrolyte

4.2.3.1. Electrolyte analysis with GC-MS

Additionally to analysis of electrode materials, the evolution of electrolyte components during aging was followed by GC-MS. A quantitative analyses of the electrolyte composition recovered from a fresh cell and from cells respectively aged in calendar mode (100 % of SOC) at 25 °C and 45 °C with intermediate electric check-up tests during storage and at 60 °C without any periodic capacity test is presented in the *Appendix of the Chapter 4*.

Unfortunately, no GCMS has been performed for the aging condition related to cell aged at 60 °C and 100 % of SOC with periodical checkups.

The content of each carbonate in %, normalized regarding the quantity of EC and in **Figure IV-5** accordance with time of storage (divided by the storage time), is presented in. Note that, as illustrated in **Table A** (*in the Appendix of the Chapter 4*), GC-MS analysis showed no decomposition of EC with aging except at 60 °C.

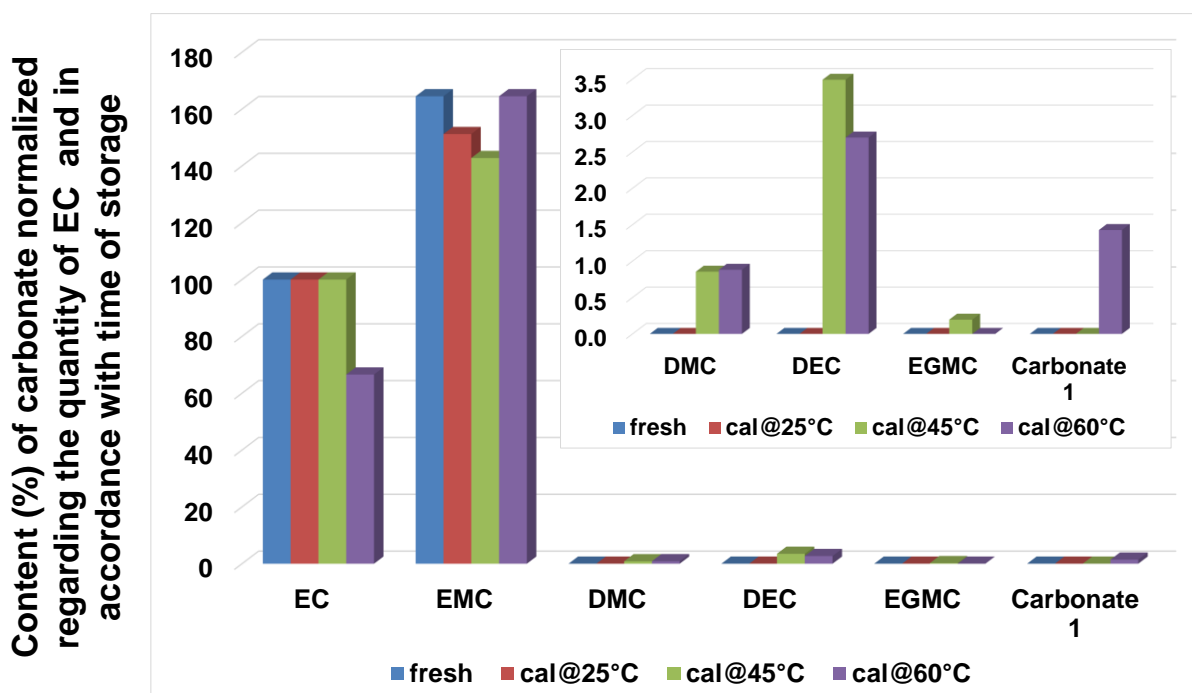


Figure IV-5 : Content of each carbonate in % normalized regarding the quantity of EC and in accordance with time of storage.

In the previous Chapter, we observed a considerable decrease of solvents content in the electrolyte, after cycling at low temperature, leading to the apparition of many electrolyte degradation products.

In the present Chapter, the decomposition of solvents seems to be less important. Electrolyte degradation products (DMC, DEC, EGMC, Carbonate 1^[3]) are detected, in a negligible amount, for cells aged at 45 °C and at 60 °C.

The content of each additive in %, per time of storage presented in **Figure IV-6**, was calculated based on the sum of all detected carbonates including those detected as degradation products at high temperature.

VC additive is totally consumed with aging, FEC and 1,3-PS show lower concentrations. Biphenyl concentration has decreased significantly at 45 °C and at 60 °C. The decrease seems to be more at 45 °C than at 60 °C. This could be due to a shorter aging time and no periodic check up in the case of the cell aged at 60 °C. It should be noted that metallic lithium is known to react with the electrolyte. The decrease of other additives can also be correlated to temperature.

³ Carbonate 1 : 2-ethoxycarbonyloxyethyl methyl carbonate

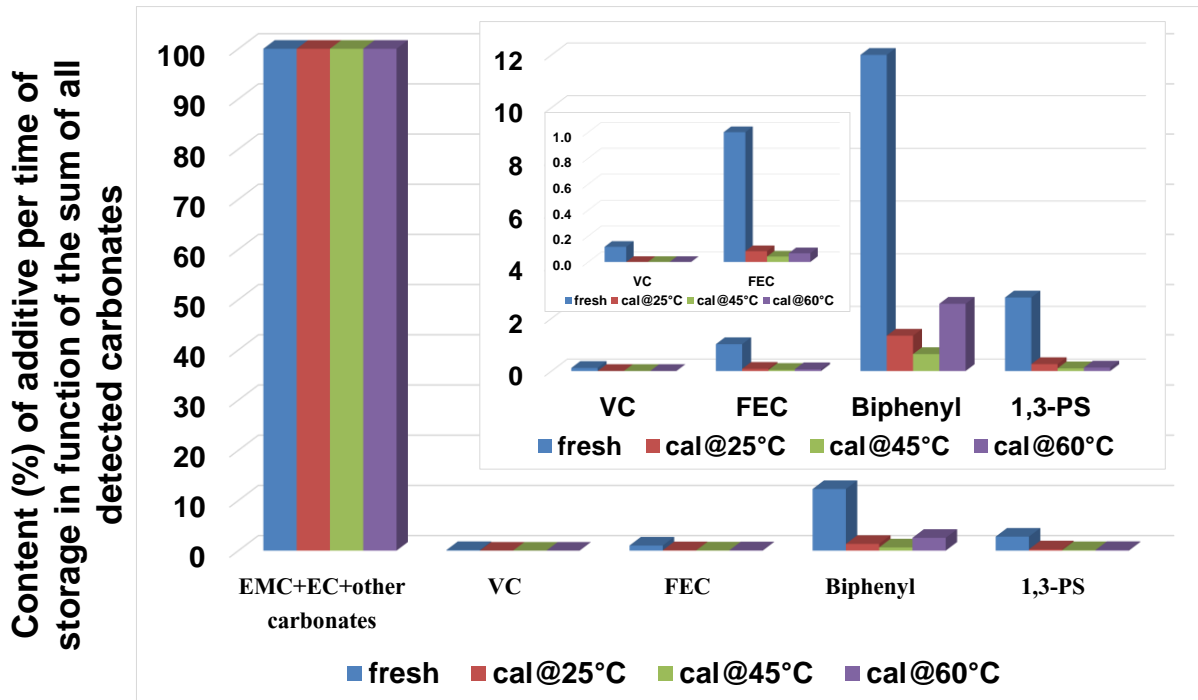


Figure IV-6 : Content (%) of additive per time of storage in function of the sum of all detected carbonates.

We have explained in the first Chapter that biphenyl is an aromatic compound that shows no reversible electrochemical behavior but give overcharge protection effects. This shutdown compound polymerizes on the cathode during overcharge and the liberated protons (H^+) migrate to the anode, generating hydrogen gas (H_2). Biphenyl is suitable for use as an overcharge protective additive and its polymerization generates gas increasing the internal cell pressure. This phenomenon enables to disconnect the cell in case of overcharge. For example, the excessive gas pressure would open the safety cap for certain cell designs [202].

However, up to our knowledge, the literature does not mention polymerization of biphenyl at high temperature in a Graphite/NMC lithium-ion system. The decreasing in the biphenyl concentration results from its polymerization process. This leads to drying-out areas of the separator visible in form of white stains which will be symmetrically impregnated on the surface of both electrodes (see in **Figure IV-3**).

4.2.3.2. Post-mortem analysis with coin full cells: with and without biphenyl as an additive

Coin full cells are used to investigate the effect of the biphenyl additive in the electrolyte. Two types of CR2032 coin full cells with pristine NMC-based electrode (cathode), pristine graphite-based electrode (anode) and Celgard® 2400 separator are assembled.

The first coin cell is based on 1:1:1: wt EC:DMC:EMC + 1 M LiPF₆ electrolyte (LPX). The second coin full cell contains the same electrolyte (LPX) with additional 2 wt % of biphenyl.

Before aging, a formation cycle was performed at 25 °C under galvanostatic charge-discharge cycle (voltage range: 2.7 - 4.2 V) then C/2 in CC-CV charge. The CV mode starts when the cell voltage reaches the maximum of 4.2 V and stops when the current drops to C/50. Thereafter, coin cells were stored at 45 °C and 100 % of SOC for 24 days. The calendar phase includes a periodic electric check-up test performed at 25 °C every 4 days.

Figure IV-7 shows the visual inspections of coin cell components after the storage at 45 °C and at 100 % of SOC during 24 days with a periodic checkup test every 4 days. Similar white zones are observed in the case of coin cells containing biphenyl as an additive in the electrolyte. Depositions of metallic lithium are found on the graphite electrode originating from this coin cell.

These circular depositions are similar to those observed with the commercial 16 Ah pouch cells aged at 45 °C and 60 °C (see in **Figure IV-2**). Therefore, this result confirms that the reaction of the biphenyl additive is the origin of the local lithium depositions observed on the graphite electrodes of the commercial 16 Ah C/NMC Li-ion cells in calendar aging at 45 °C and 60 °C at 100 % of SOC.

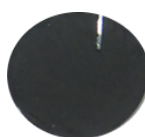
Electrolyte composition	Components			Comments
	Pristine Graphite	Celgard® 2400 Separator	Pristine NMC	
1:1:1: wt EC:DMC:EMC + 1M LiPF ₆				No Lithium deposition
1:1:1: wt EC:DMC:EMC + 1M LiPF ₆ + 2%wt of Biphenyl				Lithium deposition

Figure IV-7 : Visual inspection of Graphite/NMC coin cells components after 24 days of calendar aging at 45 °C and 100 % of SOC.

4.2.3.3. Post-Mortem analyses of coin cells: cyclic voltammetry

Cyclic voltammetry measurements have been performed in order to measure the voltage of the biphenyl polymerization at elevated temperatures.

Three coin half-cells with pristine NMC-based electrode (cathode), metal lithium based electrode (anode), Celgard® 2400 separator and 1:1:1 wt EC:DMC:EMC + 1 M LiPF₆ electrolyte with 2 wt% of biphenyl are assembled. A fourth coin half-cell does not contain biphenyl.

Cyclic measurements are performed with a Biologic system between 3 and 5.2 V with a rate of 1 mV/s respectively at 25 °C, 35 °C and 45 °C. At the end, coin half-cells were disassembled in an Argon-filled glove box for a visual inspection in a discharged state. Cyclic voltammetry measurements have been performed in order to measure the polymerization potential of this aromatic component at elevated temperatures.

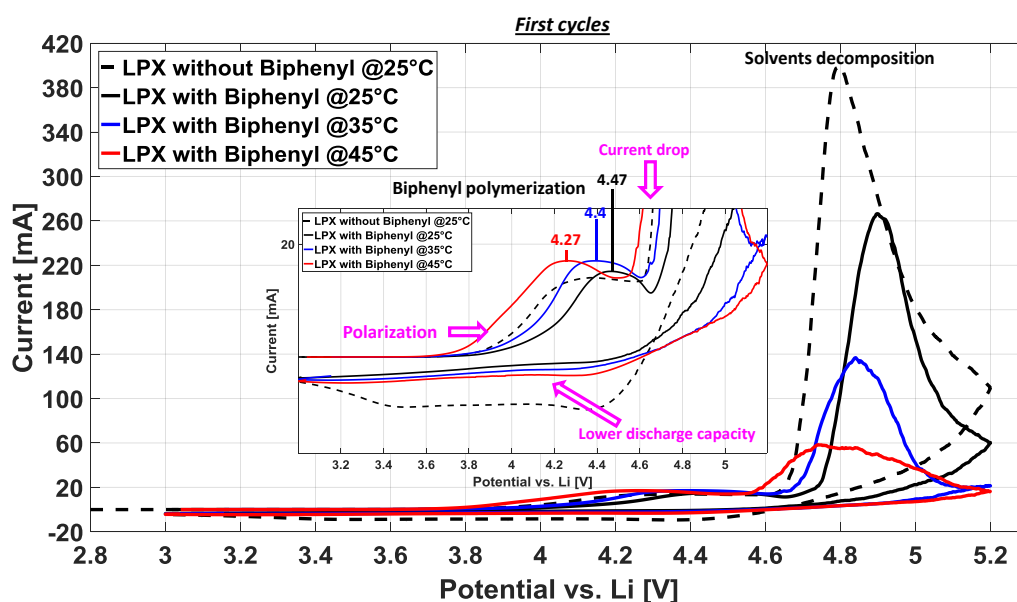


Figure IV-8 : First cycles of CV measurements. Effects of the temperature increasing on biphenyl polymerization potentials.

Figure IV-8 highlights that the polymerization of biphenyl occurs around 4.47 V vs Li/Li⁺ at 25 °C, 4.4 V vs. Li/Li⁺ at 35 °C and 4.27 V vs Li/Li⁺ at 45 °C.

It should be mentioned that the voltage range related to the electrochemical activity of the positive electrode is the same as that of the biphenyl polymerization. For example, for the coin half-cell without biphenyl, the electrochemical activity of the NMC electrode starts at around 3.8 V to reach a maximum at 4.381 V.

The second peak at higher potential (with higher intensity) corresponds to the decomposition of electrolyte solvents.

IV. Study of aging mechanisms at high temperature

For the biphenyl-free coin half-cell, since the electrode is not covered with polymer, the NMC is still in contact with the electrolyte, so that solvents continue to degrade. Therefore, the peak corresponding to the oxidation of the solvents is very high.

For biphenyl-containing coin half-cells, the intensity of this second peak is less important as the temperature increases.

Indeed, the positive electrode is all the more protected since the quantity of electrodeposited biphenyl is important, in this case, in the decreasing way at 45 °C, 35 °C and then at 25 °C. Consequently, this protection of the electrode, by the polymer deposited on its surface, has the effect of reducing the probability of decomposition of solvents. This explains the low intensity of the peak related to the oxidation of solvents observed with the coin half-cell containing biphenyl tested at 45 °C.

Indeed, a greater amount of biphenyl (7 % wt as in KOKAM) would certainly have led to a complete passivation of the electrode after polymerization, so that the peak associated with the decomposition of the solvents would not have been seen. In that case, the potential for decomposition of solvents would either be shifted to very high potentials or downright unobserved.

In this thesis, we used a smaller amount of biphenyl (2 % wt) for economic reasons. Moreover, it was sufficient to demonstrate the mechanism studied in this chapter.

Figure IV-9 show that the solvents decomposition of the electrolyte of the coin half-cell without biphenyl continues during second cycles. In contrary, the peak corresponding to solvent decomposition is very weak and flattened for biphenyl-containing coin half-cells. In that case, the electrolyte oxidation must be hindered by the polymer on the NMC surface.

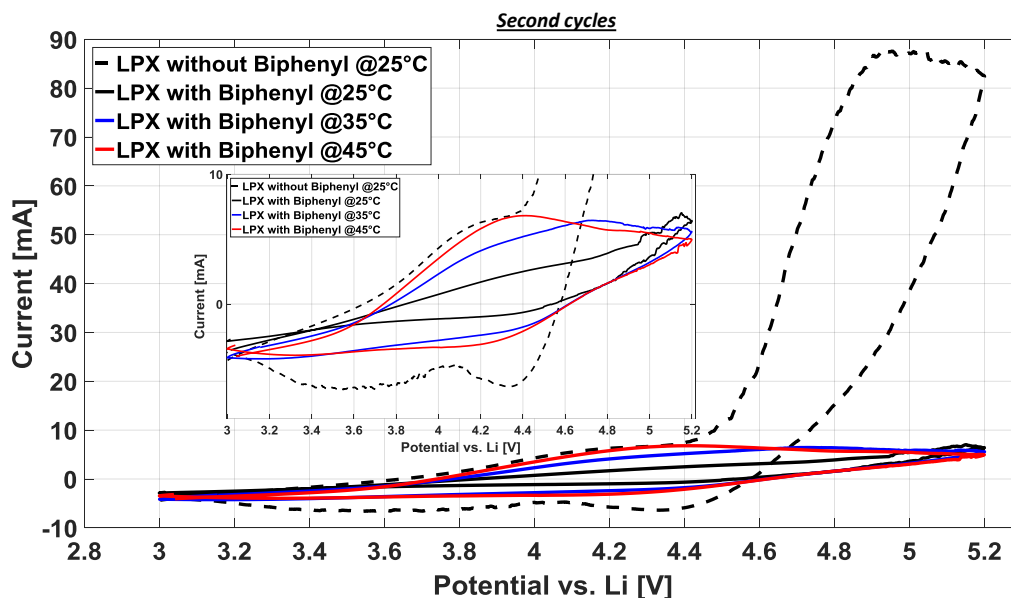


Figure IV-9 : Second cycles of CV measurements. Effects of the temperature increasing on biphenyl polymerization potentials.

At the third cycles, as illustrated in **Figure IV-10**, the intensity of the corresponding peak has seriously decreased.

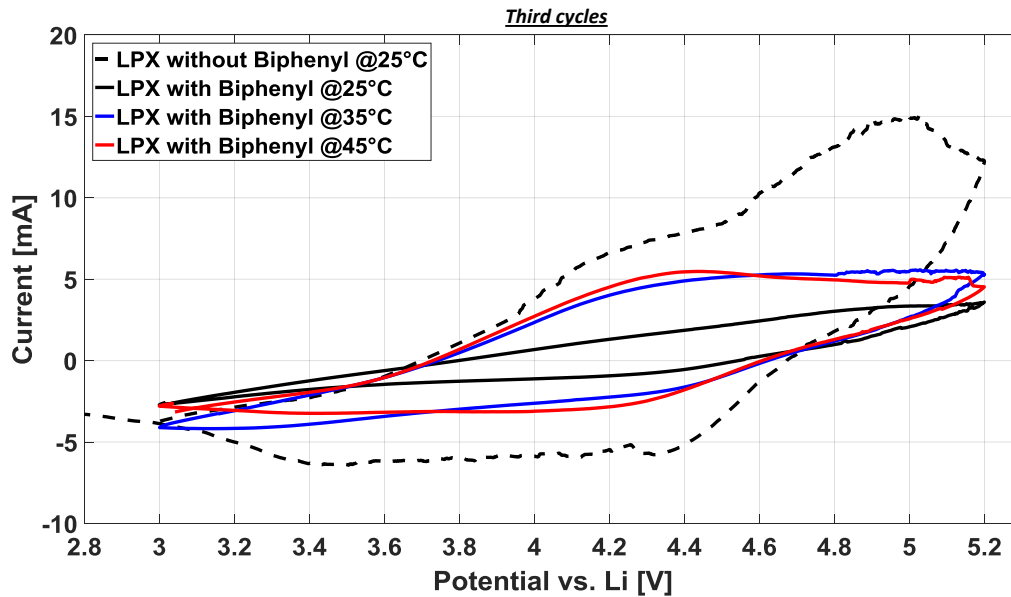


Figure IV-10 : Third cycles of CV measurements. Effects of the temperature increasing on biphenyl polymerization potentials.

It should be noted that the cell voltage is equal to 4.2 V when the cell is stored at 100 % of SOC. This means that the potential of NMC electrode can reach 4.3 V vs. Li/Li⁺, triggering the polymerization of biphenyl at high temperature. In the case of commercial cells stored at 45 °C and 60 °C and at 100 % of SOC, biphenyl has certainly polymerized at potentials much lower than in the range of 4.3 – 5.5 V vs. Li⁺/Li, as reported in the literature, leading to local lithium depositions on graphite electrodes.

The two coin half-cells (with and without biphenyl as an additive in the electrolyte) used for CV measurements at 25 °C, were disassembled for a visual inspection as illustrated in **Figure IV-11**.

The NMC electrode and the separator of the coin half-cell without biphenyl does not show significant defects.

The coin cell containing biphenyl presents white areas on the NMC electrode surface and its separator turned brown. It is noteworthy that the brown coloration of the separator appears stronger in presence of biphenyl. The same morphology was found on commercial cells after calendar aging at high temperature (see in **Figure IV-2** and **Figure IV-3**). We suggest that at high temperature, biphenyl could polymerize at lower voltages (without overcharge), leading to gas formation, which generates local electrolyte depletion in the separator that creates white zones / dry areas.

IV. Study of aging mechanisms at high temperature

Electrolyte composition	Components	
	Pristine NMC	Celgard® 2400 Separator
1:1:1: wt EC:DMC:EMC + 1M LiPF ₆		
1:1:1: wt EC:DMC:EMC + 1M LiPF ₆ + 2%wt of Biphenyl		

Figure IV-11 : Visual inspection of Li metal/NMC coin cells components after two cycles of cyclic voltammetry at 25°C

4.3. Model of local Li deposition at high temperature

Figure IV-12 presents a scheme that explains the formation of local lithium metal deposition in calendar aging at high temperatures and high states of charge.

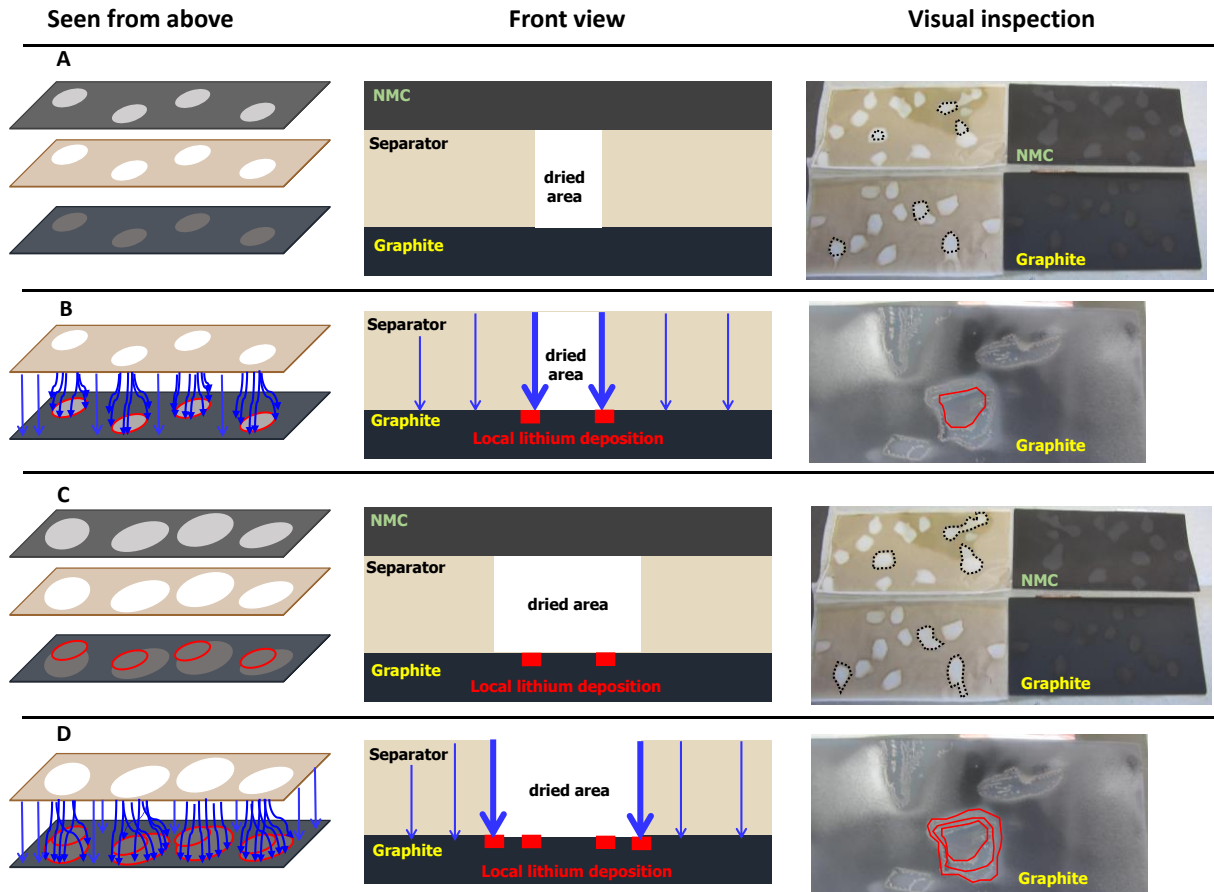


Figure IV-12 : Local Lithium metal deposition development process during storage at high temperature and high state of charge interrupted by regular charges, with biphenyl-containing electrolyte in Graphite/NMC Li-ion cell.

During the storage period at elevated temperature (above ~ 45 °C) and at high state of charge (at around 100 % of SOC), the potential of the positive electrode vs. Li/Li^+ is at its highest level. At this temperature, biphenyl additive can polymerize and generate gas inside the cell. The progressive formation of gas bubbles causes a contact disconnection between the electrodes and the separator, especially in the areas where those bubbles are formed. This creates insulated zones separating the two electrodes. Due to the “stacked” geometry of cells, these white dry zones on the separator symmetrically impregnate both electrodes surfaces (**Step A**).

These dry zones are very resistive and then the current will be forced to pass through the border of these latter regions. In fact, in the anode, the lithium depleted region presents a little voltage gradient to drive Li migration due the high resistance of this region. This assumption is consistent with A.H. Zimmerman et al. works [203] about mechanisms leading to lithium deposition due to depleted regions on anodes. As a

IV. Study of aging mechanisms at high temperature

result, during the periodic check-up test performed at 25 °C, metallic lithium is then deposited on the border of these dry zones due to the local high current density and the resulting local more negative potential vs. Li/Li⁺ (**Step B**).

If the storage period at high temperature and high state of charge is prolonged, then biphenyl polymerization may evolve over time, forming larger dry zones (**Step C**) that will create additional metallic lithium depositions at each check-up test (**Step D**).

This explains the presence of several concentric lithium depositions nearby as well as the lower capacity of the cell with check-ups at 60 °C compared to the cell without check-ups. The difference is therefore probably due to the loss related to "dead metal Li".

In the calendar aging test without check-ups, although the same white dry areas were observed on the separator and on the surface of the NMC electrode, absolutely no lithium deposition was found on graphite electrode.

4.4. Conclusions

Unexpected localized metallic lithium depositions were found on top of graphite electrodes of commercial 16 Ah Li-ion pouch cells, dismantled at discharged state, after calendar aging at high temperature and high state of charge.

We determined that the presence of the biphenyl additive contained in the electrolyte in combination with periodic capacity tests are at the origin of this degradation mechanism.

Polymerization of biphenyl results in the formation of a gas that can occur at 45 °C when the voltage of the positive electrode reaches 4.27 V vs Li/Li⁺, corresponding to the calendar aging conditions used in our work (45 and 60 °C; 100 % of SOC).

The polymerization reaction is irreversible and results in electrolyte-free zones (or dry areas) which are highly resistive to Li-ions transport.

During periodic capacity tests, high current densities are generated at the circumference of these zones leading to lithium metal depositions. This aging protocol can be compared to the use of Li-ion cells in applications such as electric vehicles with long rest time (calendar aging) and regular cycling phases (periodic capacity tests). It is therefore imperative for the EV industry to perform similar protocols to test the battery in 'real life' operating conditions.

IV. Study of aging mechanisms at high temperature

V. Aging modeling

A semi-empirical approach of aging modeling based on the evolution of capacity, resulting from the experimental aging campaign of commercial cells, is proposed in the first section of this chapter. The SEI growth as well as the loss of capacity caused by biphenyl polymerization are both considered in the calendar aging model. In addition to the calendar effect, the cycling aging model also includes an equation expressing the loss induced by capacity throughput. Thereafter, the model is evaluated by comparison with experimental measurements.

The second part addresses the development of a diagnostic and prognostic aging model based on electrodes shifts. Incremental capacity (IC) depicts a capacity change associated with a voltage step ($\Delta Q/\Delta V$). Each peak in the incremental capacity curve has a unique shape, intensity, and position, and it exhibits an electrochemical process taking place in the cell. In this section, degradation modes affecting the performance of Li-ion cells are represented and identified as resulting from either a “shifting” or a “decreasing” of peak. This aging mechanism identification methodology is developed by exploiting the signatures of incremental capacity curves.

5.1 Synthesis of aging mechanisms studied

For pedagogical reasons, the different aging mechanisms of Li-ion batteries, studied in the two preceding chapters of this thesis are summarized in the **Table V-1** below. LLI refers to loss of lithium inventory while LAM means loss of active material (surface / sites). NE and PE respectively relate to the negative electrode and the positive electrode.

	Main aging mechanisms	Category	Conditions
Literature	Lithium depositions	<i>caused by LAM on the NE [204]</i>	Low temperatures High cycling rates
	SEI growth	LLI [45]	High temperatures and SOC
	Exfoliation, contact loss of particles	LAM [45]	Overcharge High cycling rate and DOD
Chapter 3	Anode porosity clogging	LAM on the NE	Low temperatures Full cycling at 1 C
	Lithium depositions	<i>caused by LAM on the NE</i>	Low temperatures High polarization due to anode pore clogging
Chapter 4	Apparition of dry areas	LAM on the NE LAM on the PE	Storage at high temperatures and SOC
	Local lithium depositions	<i>caused by LAM on the NE</i>	Storage at high temperatures and SOC Checkups at 1 C and at 25 °C

Table V-1 : Lithium-ion anode aging mechanisms – category, conditions and modeling in behalf of this thesis.

The loss of porosity at the negative electrode and the resulting metallic Li depositions on its surface will not be taken into account in the semi-empirical aging model, since the corresponding condition of cycling leads to a particular fast loss of capacity. All these two mechanisms will only be studied with incremental capacity curves.

Similarly, local metallic Li depositions observed after calendar aging will also not be considered in the calendar aging model since this mechanism occurred by applying a charge current. It is thus not inherent to pure calendar aging.

Subsequently, in the semi-empirical aging model, the loss of active material (LAM) is considered to be related to the apparition of dry areas on both electrodes.

5.2. Semi-empirical aging modeling

5.2.1. Introduction

The degradation phenomena of Li-ion batteries are so complex and interdependent that the development of a comprehensive aging model remains a challenge. Even when an aging mechanism is well understood, it is still necessary to achieve a satisfactory corresponding equation. Consequently, in order to predict the lifetime of the Li-ion cells, the most useful approach consists in developing an empirical aging model.

In the literature, some authors have worked on the development of empirical Li-ion cells aging models. However, the equations that have been used do not always have any physical significance. J. Wang et al. [205] established a life model for graphite-LiFePO₄ cells by adopting a power law equation in which the capacity loss followed a power law relation with time or charge throughput while an Arrhenius correlation accounted for the temperature effect. Recently, M. Petit et al. [206] have also used the same approach by coupling this type of empirical capacity loss model to an empirical electrothermal model. I. Baghdadi et al. [207] proposed an empirical model of capacity fade and resistance increase based on the square root of time. The approach consisting in considering an empirical equation based on the square root of time has thus been used by different researchers.

In this chapter, we propose an aging model for the commercial 16 Ah Li-ion cell by considering main aging mechanisms discussed in the previous chapters (see in **Table V-1**). This aging model is developed to be used as a model for predicting the lifetime of the cell for different types of solicitations.

5.2.2. Model equations

5.2.2.1. Calendar aging

5.2.2.1.1. The SEI growth

The SEI growth is the phenomenon of degradation which has been the subject of the greatest number of modeling works. This mechanism is favored by high temperature and high SOC conditions, especially in calendar aging mode. G. Kaneko et al. [208] developed a degradation prediction model of calendar capacity loss following the reaction rate of SEI films. Their results show that the capacity loss progressed linearly with the square root of time. More specially, M. Broussely et al. [209] presented a physical approach expressing the loss of capacity linked to the SEI growth. We present here the path which has led them to the determination of the equation.

The kinetics rate is considered to be limited by electronic mobility of Li^+ in the SEI layer, thus proportional to the SEI electronic conductance \mathbf{X} :

$$\frac{dx}{dt} = kX = k \frac{\sigma s}{e} \quad (5.1)$$

In the expression above, \mathbf{x} represents the number of moles of Li being reacting to form the SEI, \mathbf{k} is the proportional term, σ is the specific conductivity, \mathbf{s} is the interface area and \mathbf{e} stands for the thickness of the layer.

The parasitic reaction of SEI leads to the apparition of different products. Some of them are soluble (\mathbf{P}_s) and create reversible self-discharge, which is compensated by equivalent charging current during constant voltage phases. Whereas, insoluble products (\mathbf{P}_i) trap lithium and lead to irreversible capacity loss. The insoluble products are then proportional to the number of Li moles \mathbf{x} that have reacted:

$$P_i = nx \quad (5.2)$$

Where \mathbf{n} is the proportional term

The layer conductance will decrease with time as the amount of insoluble products will increase. As a result, the average layer thickness should be expressed as follows:

$$e = e_o + cP_i \quad (5.3)$$

Note that \mathbf{e}_o represents the initial thickness after the formation and \mathbf{c} is a constant coefficient related to the average molar volume of the layer. By incorporating equations (5.2) and (5.3) into the (5.1), the kinetics rate can be expressed as follows:

$$\frac{dx}{dt} = k \frac{\sigma s}{e_o + cnx} \quad (5.4)$$

The expression above can be simplified as follows:

$$\frac{dx}{dt} = \frac{J_{SEI}}{1 + A_{SEI}x} \quad (5.5)$$

With:

$$\begin{aligned} J_{SEI} &= k \frac{\sigma s}{e_o} \\ A_{SEI} &= \frac{cn}{e_o} \end{aligned} \quad (5.6)$$

Since the variable x expresses the number of Li moles irreversibly lost, it can be replaced by Q_{loss} and thus, the expression of capacity loss related to the SEI growth can be expressed as follows:

$$\frac{dQ_{\text{loss}}}{dt} = \frac{J_{\text{SEI}}}{1 + A_{\text{SEI}}Q_{\text{loss}}} \quad (5.7)$$

The Broussely's equation describes capacity loss of lithium-ion cells in calendar aging caused by the SEI growth with a parabolic relation between aging time and loss of lithium. In the literature, the equation of calendar aging model developed by S. Grolleau et al. [210] is quite similar to the equation proposed by Broussely.

5.2.2.1.2. The apparition of dry areas

As seen in the Chapter 4, the expansion of dry areas during calendar life constitute an additional loss of capacity of the cell called "loss of active material (surface)". It is then indispensable to integrate it as an additional degradation mode into the calendar aging model.

As reported by C. Delacourt et al. [211], the LAM has been the subject of far fewer modeling studies than the parasitic reactions leading to the LLI. Its origin is often poorly known and, in fact, it is a big challenge to put the problem into equations. A simple physical model of this degradation is a challenge, and in general an empirical correlation of the current density, the temperature, and the lithium content in the active material is used [212].

However, in our specific case, we can obtain an equation of loss of capacity caused by the expansion of gas bubbles by analogy with the same approach undertaken by Broussely. The expansion of this gas leads to the active surface loss on both electrodes by insulating the concerned areas during calendar life. It may be assumed that Li moles being not accessible are proportional to the expansion of these dry areas.

So that, the kinetic of rate of this reaction can be expressed as a function of number of Li being unavailable. For simplicity reasons, we consider here a linear proportionality:

$$\frac{dx}{dt} = k(ax + b)^\beta \quad (5.8)$$

The expression above can be simplified as follows:

$$\frac{dx}{dt} = \frac{J_{\text{LAM}}}{(1 + A_{\text{LAM}}x)^{\alpha_{\text{LAM}}}} \quad (5.9)$$

With:

$$\begin{aligned} J_{LAM} &= k \frac{1}{b^{-\beta}} \\ A_{LAM} &= \frac{a}{b} \\ \alpha_{LAM} &= -\beta \end{aligned} \quad (5.10)$$

Since the variable x expresses the number of Li moles irreversibly lost, it can be replaced by Q_{loss} and thus, the expression of capacity loss related to the loss of active material (surface) can be expressed as follows:

$$\frac{dQ_{loss}}{dt} = \frac{J_{LAM}}{(1 + A_{LAM} Q_{loss})^{\alpha_{LAM}}} \quad (5.11)$$

5.2.2.1.3. Calendar loss

Finally, the expression of the loss of capacity in calendar aging for the 16 Ah commercial Li-ion cells is the sum of the SEI and LAM contribution:

$$Q_{loss}^{CAL} = Q_{loss}^{SEI} + Q_{loss}^{LAM} \quad (5.12)$$

For respecting the principle of cumulative damage (the Palmgren-Miner rule) (see in the *Appendix of the Chapter 5*), as reported by M. T. Todinov [213], A_{SEI} , A_{LAM} and α_{LAM} respectively in equations (5.7) and (5.11) must thus be constant. For reasons of optimization of computation time, we decided that $A_{SEI} = A_{LAM} = A$.

The parameters J_{SEI} and J_{LAM} depend on the temperature and the SOC. All the parameters are identified by global optimization methods (see in the following section).

5.2.2.2. Cycling aging

For cycling aging modeling, a similar approach based on the equation (5.7) is considered with $A_{CYC} = A$. In this case, the capacity loss due to cycling is influenced by the temperature, the current and the state of charge. The formulation encountered is then:

$$\frac{dQ_{loss}}{dQ_{th}} = \frac{J_{CYC}}{1 + A Q_{loss}} \quad (5.13)$$

In this expression, Q_{th} represents the capacity throughput, J_{CYC} refers to the kinetics of the reaction, which depends on the temperature, the current and the state of charge. Note that the parameter J_{CYC} is identified on cycling conditions after subtracting the part of capacity loss due to calendar aging from cycling aging.

5.2.2.3. Total capacity loss

Finally, the total loss of capacity can be expressed as the sum of the calendar and cycling capacity loss:

$$dQ_{\text{loss}} = \frac{\partial Q_{\text{loss}}}{\partial t} dt + \frac{\partial Q_{\text{loss}}}{\partial Q_{\text{th}}} dQ_{\text{th}} \quad (5.14)$$

$$Q_{\text{loss}}^{\text{TOT}} = Q_{\text{loss}}^{\text{CAL}} + Q_{\text{loss}}^{\text{CYC}}$$

5.2.3. Identification of model parameters

5.2.3.1. Calendar aging identification results

As described in the previous chapter, 29 commercial C/NMC Li-ion cells (16 Ah) were aged in calendar mode using 3 different SOC, namely 50 %, 90 % and 100 % and 4 different temperatures, namely 5 °C, 25 °C, 45 °C and 60 °C.

In order to identify the model parameters, the first step is to generate profiles of SOC and temperature corresponding to each calendar condition.

In the previous chapter, we have shown that biphenyl polymerization leading to LAM occurred only at temperature higher than or equal to 45 °C and at 100 % of SOC.

Based on this information, the parameter J_{SEI} related to the SEI growth needs to be determined only with calendar conditions for which no polymerization of biphenyl occurred. In fact, in these selected conditions (highlighted in green in **Table V-2**), the SEI growth is the only aging mechanism involved in the loss of capacity.

So that, the value of the parameter J_{SEI} corresponding to the following conditions (45 °C and 60 °C for SOC = 100 %) will be determined by extrapolations methods.

T (°C)	SOC (%)		
	50	90	100
5	x2 CIDETEC		x3 CIDETEC
25	x2 EIGSI	x3 EIGSI	x3 EIGSI
45	x2 CEA	x3 CEA	x3 CEA
60	x2 VITO	x2 VITO	x3 VITO
			x1 CEA**

	SEI
	SEI + LAM
	SEI + LAM + Li Plating
	SEI + <i>potentially</i> LAM + Li Plating

Table V-2 : Calendar aging conditions (** condition without periodic checkup test).

Note that unfortunately only Li-ion cells stored at 100 % of SOC were dismantled for post-mortem investigations. Using Li metal/NMC coin half-cells, we also demonstrated that the polymerization of biphenyl occurs at a potential of 4.47 V, 4.4 V and 4.27 V vs Li/Li⁺ at 25 °C, 35 °C and 45 °C, respectively.

It thus may be assumed that the polymerization of biphenyl did not occur inside cells stored at 45 °C and 90 % of SOC, given the fact that at this the value of SOC, the potential of the positive electrode is lower than 4.27 V vs Li/Li⁺.

Besides, the corresponding cell voltage at 90 % of SOC is measured to be equal to 4.054 V. The positive electrode potential is thus certainly not sufficient to activate gas bubbles formation inside cells stored at 45 °C and at 90 % of SOC.

In contrary, it is not sure that biphenyl polymerization has occurred inside cells stored at 60 °C and 90 % of SOC since no cyclic voltammetry measurements have been performed with this condition (neither post-mortem analyses). Nevertheless, two arguments can be advanced to consider that the polymerization mechanism can take place with this storage condition:

- The first argument is that by extrapolating the polymerization potential of biphenyl at 60 °C and for 90 % of SOC, we find a value of the positive electrode potential closed to 4.075 V vs Li/Li⁺. Yet at this potential value of the positive electrode, the corresponding cell voltage is less than 4.2 V, and therefore the corresponding SOC of the cell is rather less than 100 %, and even less than 90 %.
- The second argument is that with the aging model based on electrodes shift, it is able to identify the LAM as a part of capacity loss in this condition of storage (60 °C and 90 % of SOC) based on incremental capacity measurements exploitations. We will discuss this type of model in the following sections [5.3.3.3].

Based on the two arguments, we consider the LAM (due to dry areas) as a part of capacity loss in this storage condition (60 °C and 90 % of SOC as illustrated in **Table V-2**.

5.2.3.1.1. Identification of the model parameter related to the SEI growth

Since the identification of the model parameters is based on a global optimization method including all the aging conditions at the same time, we have considered the following input conditions:

- $T^{\text{REF}} = 45 \text{ °C}$
- $\text{SOC}^{\text{REF}} = 100 \text{ %}$
- $J_{\text{SEI}}^{\text{REF}} = \theta(1)$

- $AF_{SEI}^T = [\theta(2) \ \theta(3) \ 1 \ \theta(4)]$
- $T = [5 \ 25 \ 45 \ 60]$
- $AF_{SEI}^{SOC} = [\theta(5) \ \theta(6) \ 1 \]$
- $SOC = [50 \ 90 \ 100]$

T^{REF} and SOC^{REF} represent the reference temperature and SOC, respectively while J_{SEI}^{REF} is the value of the parameter J_{SEI} at reference conditions.

$AF_{SEI}^{T/SOC}$ is the vector containing values of acceleration factors (**AF**) in function of each temperature / SOC breakpoint of vectors **T** / **SOC**.

Since 45 °C as well 100 % of SOC are the reference conditions, we consider that the acceleration factors at these temperature and SOC are equal to 1.

The parameter θ is thus determined using the powerful function *lsqcurvefit* of MATLAB software. This nonlinear least-squares solver is used to determine model parameters to get the best fitting ever between the equation (5.7) related to the SEI growth and experimental data.

Once, the parameter θ is obtained, it is then possible to determine vectors AF_{SEI}^T and AF_{SEI}^{SOC} . We chose to use a linear interpolation method to obtain AF_{SEI}^{SOC} values between **SOC** breakpoints. Based on the Arrhenius equation, it was possible to fit and to obtain AF_{SEI}^T values between **T** breakpoints. We have made the assumption that the AF_{SEI}^T follows Arrhenius's law in function of the temperature. As a result, the activation energy (E_a) determined for this reaction (by optimization) is equal to **58625** J.mol⁻¹. This value is consistent with that of found by B. Y. Liaw et al. [214] which is 55 kJ.mol⁻¹.

Finally,

$$J_{SEI}^{(T,SOC)} = J_{SEI}^{REF} * AF_{SEI}^{(T)} * AF_{SEI}^{(SOC)} \quad (5.15)$$

Figure V-1 presents the cartography of the parameter J_{SEI} obtained from calendar conditions for which the SEI growth is determined to be the main aging mechanism. The value of the parameter **A** identified is equal to **0.1043**.

These parameters will thus be used to extract the part of capacity loss due to the SEI growth from calendar conditions where both SEI growth and LAM (activated by biphenyl polymerization) are the aging mechanisms determined. It is then feasible identifying parameters inherent to the LAM by subtracting the contribution of the SEI growth.

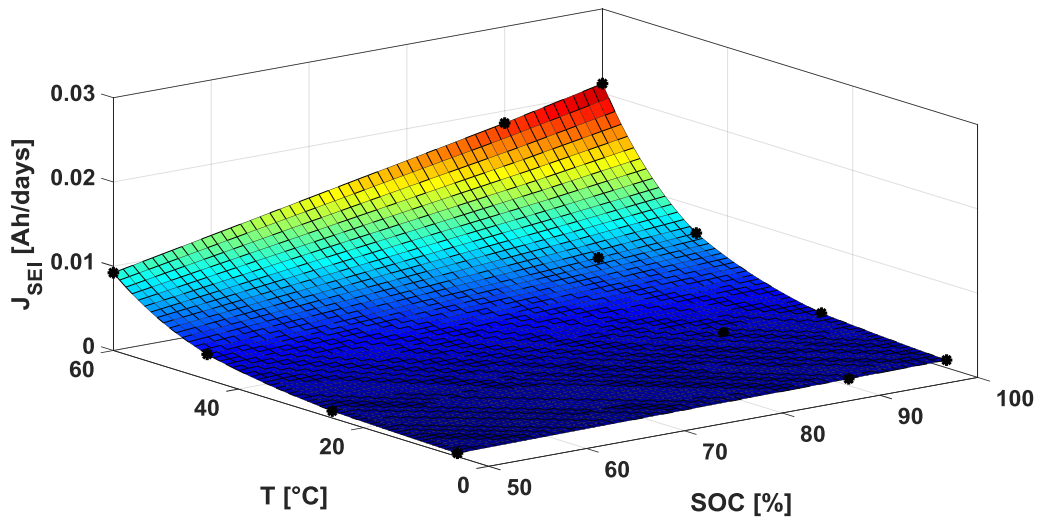


Figure V-1 : Cartography of the parameter J_{SEI} .

5.2.3.1.2. Identification of the model parameter related to the loss of active material

In this section, the aim is to identify the parameters J_{LAM} and α_{LAM} related to the LAM activated by biphenyl polymerization. Unfortunately, there is only one condition (60 °C, 100 % of SOC **without periodic checkups, highlighted in blue in **Table V-2**) where the loss of capacity is caused by the SEI growth and the LAM (see also visual inspections in **Figure IV-2**). It will be thus not possible to interpolate the parameters J_{LAM} and α_{LAM} with only one calendar condition.

That being said, we decided to add also the condition at 45 °C and 100 % of SOC, although local metallic lithium was found on graphite electrodes. In fact, we make the assumption that the part of capacity loss due the apparition of metallic lithium depositions is negligible compared to the loss of active surface. This assumption is supported by visual inspections in **Figure IV-2** where it can be observed that metallic lithium are deposited only in the border of dry areas of graphite electrodes of this cell.

Indeed, metallic lithium is less pronounced compared to cells stored at 60 °C with periodic check-up tests for which metallic deposits are completely covering the surface of graphite electrodes.

On the contrary, it will not be reasonable to consider the storage condition at 60 °C and 90 % of SOC for the determination of model parameters inherent to pure LAM. Although we may consider the LAM as a part of capacity loss in this condition, the part due to local metallic lithium cannot be underestimated.

So, the model parameter related to the LAM at 60 °C and 90 % of SOC will be determined by extrapolations methods.

Anyway, it is necessary to extract the part of capacity loss due the SEI growth from these conditions ($T = 45 \text{ }^\circ\text{C}$ / $T = 60 \text{ }^\circ\text{C}$ at SOC = 100 %) using the cartography presented in **Figure V-1** and the equation (5.7).

The capacity loss related to LAM can then be extracted by using the equation (5.12). As a result, the parameters J_{LAM} and α_{LAM} related to the LAM can be identified. We have considered the following input conditions:

- $T^{\text{REF}} = 45 \text{ }^\circ\text{C}$
- $\text{SOC}^{\text{REF}} = 100 \%$
- $J_{\text{LAM}}^{\text{REF}} = \theta(1)$
- $\text{SOC} = [50 \ 89.9 \ 90 \ 100]$
- $T = [5 \ 25 \ 44.9 \ 45 \ 60]$
- $\alpha_{\text{LAM}} = \theta(4)$

Since the LAM is activated at $45 \text{ }^\circ\text{C}$ at 100 % of SOC and at $60 \text{ }^\circ\text{C}$ at 90 % of SOC, we have defined an interaction factor ($\text{IF}_{\text{LAM}}^{T \leftrightarrow \text{SOC}}$) between the temperature and the SOC considering that:

- For temperatures lower than $45 \text{ }^\circ\text{C}$, there is no interaction
- At $45 \text{ }^\circ\text{C}$, the interaction factor is equal to 1 for 100 % of SOC (reference condition) and equal to 0 for other SOC.
- At $60 \text{ }^\circ\text{C}$, the interaction factors are parameters $\theta(2)$ and $\theta(3)$ for 90 % and 100 % of SOC, respectively. IF is equal to 0 for SOC lower than 90 %. θ is determined by optimization by fitting with experimental data.

At $60 \text{ }^\circ\text{C}$, the interaction factor at 90 % of SOC is determined by assuming a linear evolution of the cell voltage between 90 % ($U = 4.054 \text{ V}$) and 100 % of SOC ($U = 4.2 \text{ V}$). It is then possible to determine parameters values between **SOC** and **T** breakpoints by interpolation for 2-D gridded data using the function *interp2* of MATLAB software.

Finally, the parameter J_{LAM} is expressed as follows:

$$J_{\text{LAM}}^{(T, \text{SOC})} = J_{\text{LAM}}^{\text{REF}} * \text{IF}_{\text{LAM}}^{(T \leftrightarrow \text{SOC})} \quad (5.16)$$

This cartography obtained (see in **Figure V-2**) is consistent with post-mortem results as well as with assumptions we have made showing that the LAM occurs at 100 % of SOC for temperatures higher or equal to $45 \text{ }^\circ\text{C}$, and at 90 % of SOC for temperatures higher or equal to $60 \text{ }^\circ\text{C}$. The value of the parameter α_{LAM} determined by global optimization methods is equal to **-2.1568**.

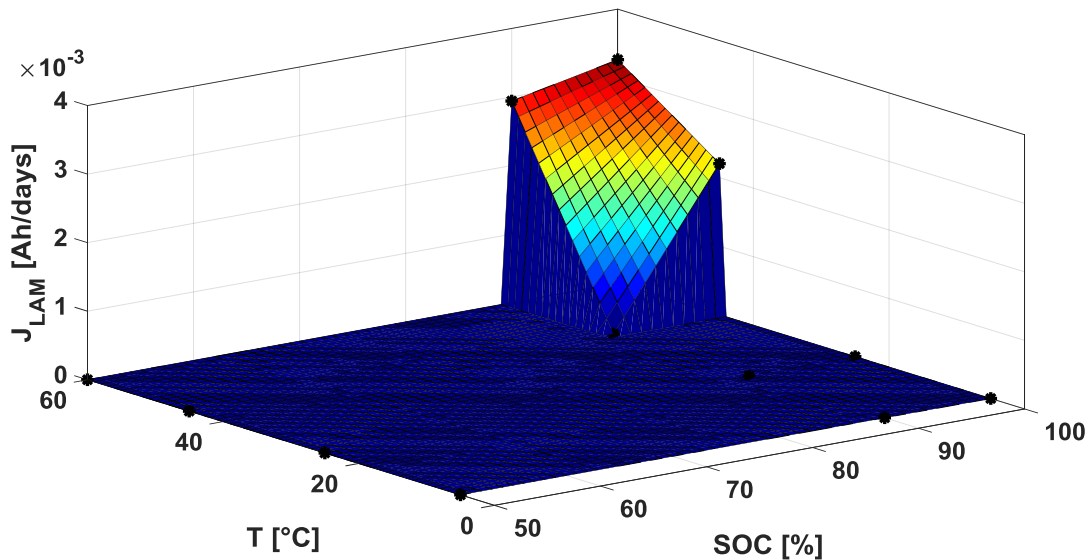


Figure V-2 : Cartography of the parameter J_{LAM} .

5.2.3.2. Cycling aging identification results

In order to study cycling aging, as discussed in the Chapter 3, 42 commercial Li-ion cells with a capacity of 16 Ah were studied in 21 different cycling conditions. The following conditions were studied:

- 3 conditions for temperatures: 5 °C, 25 °C and 45 °C
- 4 state of charge windows: {0 - 80 %; 0 – 100 %; 10 – 90 %, 20 – 100 %}
- 3 charge current rates: 1 C, 2 C and 3 C.

The first step consists in the generation of cycling profiles for each condition. In the framework of the Mat4Bat project, it has been decided to manage cycling SOC windows in function of the corresponding voltage thresholds.

For this reason, the profile generation tool implemented with Matlab software has been parameterized for each cycling condition on the basis of the measured values (temperature measured at the skin of the cell and SOC windows based on measured capacities) instead of theoretical values in order to better reflect the reality.

This method makes it possible to obtain a dependence of the parameter J_{cyc} as a function of the SOC points rather than the SOC ranges, since these latter are entangled in the experimental setup. As a result, the aging model could then be used to simulate the aging for any SOC range.

The sinequanone condition is that the simulated capacity loss and capacity throughput (for example in discharge), obtained from the generated profile must be equal to those that have been measured from the cell (see in the *Appendix of the Chapter 5*).

For each condition, the SOC corresponding to the end-of-charge with constant current as well as the SOC corresponding to end-of-charge with constant voltage are also included in the cycling profile. In addition, the mean temperature measured during checkups is also considered as well as the SOC at the end of checkups.

We did not really considered the evolution of SOC windows with aging. However, we did not notice a significant variation in SOC range values between the 1st and the last CU. The measured values used for generating cycling profiles can be found in the *Appendix of the Chapter 5*.

The same algorithm used for the identification of calendar model parameters is also used for cycling model. The parameter J_{CYC} is identified on cycling conditions after subtracting the part due to calendar aging.

Note that cycling conditions at 45 °C from 2.7 to 3.98 V (0 to 80 % of SOC, theoretically) and from 3.49 to 4.2 V (20 to 100 % of SOC, theoretically) are not considered for the identification of J_{CYC} . These latter conditions will rather be used for the model validation [5.2.5].

The identification of model parameters is based on a global optimization method including all the considered aging conditions at the same time. This method is suitable to manage issues with entangled SOC ranges. We have thus considered the following input conditions:

- $T^{REF} = 45 \text{ °C}$
- $SOC^{REF} = 20 \%$
- $J_{CYC}^{REF} = \theta(1)$

- $AF_{CYC}^T = [\theta(2) \ \theta(3) \ 1 \ \theta(4)]$
- $T = [5 \ 25 \ 45 \ 53]$

- $AF_{CYC}^{SOC} = [\theta(5) \ \theta(6) \ 1 \ \theta(7) \ \theta(8) \ \theta(9)]$
- $SOC = [0 \ 10 \ 20 \ 80 \ 90 \ 100]$

- $AF_{CYC}^{C-rate} = [0 \ 1 \ \theta(10) \ \theta(11)]$
- $C-rate = [0 \ 1 \ 2 \ 3]$

AF_{CYC}^T is the acceleration factor vector following the corresponding temperature breakpoints T while AF_{CYC}^{SOC} is that of following **SOC** breakpoints. Besides, the vector AF_{CYC}^{C-rate} includes values of acceleration factors in function **C-rates**.

Note that we have found that during cycling at 3 C / 1 C and at 45 °C, the skin temperature of cells has reached the temperature of 53 °C. For this reason, we have implemented in the model the maximum temperature at 53 °C.

In addition, we have observed the influence of C-rate is barely different between 2 C and 3 C except at 5 °C (see in **Figure III-1**). For this reason, we have added a supplementary parameter expressing the interaction factor ($IF_{CYC}^{T \leftrightarrow C-rate}$) between temperature and C-rate.

The **Figure V-3** shows the cartography of the parameter J_{CYC} . Linear interpolations methods are used to estimate the values of parameters for SOC (between 50 % and 100 %) and C-rate (between 1 C and 3 C), respectively and an exponential law for intermediate temperature (between 5 °C and 53 °C). The interaction factor values for other temperature and C-rates are obtained by 2-D interpolations.

$$J_{CYC}^{(T,SOC,C-rate)} = J_{CYC}^{REF} * AF_{CYC}^{(T)} * AF_{CYC}^{(SOC)} * AF_{CYC}^{(C-rate)} * IF_{CYC}^{(T \leftrightarrow C-rate)} \quad (5.17)$$

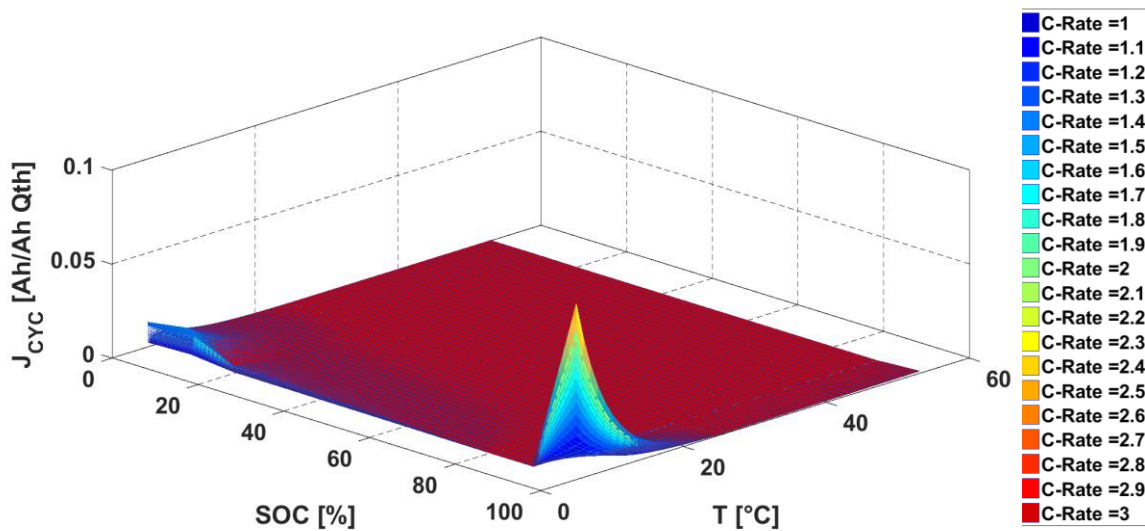


Figure V-3 : Cartography of the parameter J_{CYC} .

The cartography of the parameter J_{CYC} shows a high intensity, especially at 5 °C. This observation is very pronounced at high SOC (between 90 and 100 %) and low SOC (between 0 and 20 % - rather with less intensity) than for medium SOC (between 20 and 80 %).

This behavior has also been observed by J. Jiang et al. [215]. Indeed, the authors have conducted cycling aging tests at 25 °C in four different SOC ranges, which are 0 to 25 %, 25 to 50 %, 50 to 75 % and 75 to 100 % with 20 Ah LiFePO₄/Graphite cells. Their results showed that cycling in the mid-SOC ranges, such as 25 % to 50 % and 50 to 75 %, leads to slowest capacity fade. In contrary, cycling performed in the range of 75 to 100 % as well as 0 to 25 % exhibits the fastest capacity degradation.

This difference can be attributed to the significant side reactions that occur between electrodes and electrolytes and the significant structural change of electrodes materials at the ends of the SOC range. It thus may be assumed that the cartography of the parameter J_{CYC} following the SOC is consistent with the literature.

Accordingly to the temperature, the intensity of J_{cyc} is particularly elevated at temperatures lower than 20 °C (see also **Figure V-3**). This illustration is consistent with the sudden capacity drop observed in the beginning of aging of cells cycled at 5 °C (see in **Figure III-1**). Finally, following the C-rate we can see that the intensity of J_{cyc} naturally increases with C-rate.

5.2.4. Model evaluation

5.2.4.1. Calendar aging validation results

Figure V-4 presents the comparison between the calendar aging model taking into account only on the SEI growth versus experimental data for the 4 temperatures.

At 5 °C and 25 °C, there is a very good correspondence between the model and the experimental data whatever the SOC indicated. At both temperatures, the error estimated is less than 2 %.

At 45 °C, the model does not fit well with experimental data only for 100 % of SOC, the estimated error is reaching 25 % with aging evolution while for the other SOC (50 and 90 %), the error is lower than 5 %. Moreover, we can see that experimental SOH does not follow a square root dependency in function of time.

Nevertheless, when the equation expressing the LAM is also considered in the model, as illustrated in **Figure V-5**, a better agreement with experimental data is finally obtained. The estimated error becomes then less than 6 %.

Besides, it can be observed that coupling the two equations (5.7) and (5.12) allows to follow the slope rupture, observed with the condition at 45 °C and 100 % of SOC.

Furthermore at 60 °C, there is a good correspondence between experimental data and the model only at 50 % of SOC (with an estimated error less than 5%). We can see that the Broussely's law is not enough to obtain a good agreement at 60 °C for SOC higher or equal to 90 % (the error reaching 10 % at 90 % of SOC and almost 20 % at 100 % of SOC).

In contrary, as shown in **Figure V-5**, by adding the contribution of the LAM, a better fitting is obtained. As a result, there is a good correspondence between the model and the condition of storage without periodic checkups where no metallic Li depositions were found on graphite electrodes. However, in conditions where local metallic lithium was found covering all the graphite electrodes surface (60 °C, 100 % of SOC see in **Figure IV-2**), there is a certain gap between the model and experimental measurements. This gap can be attributed to the part of capacity loss due to local metallic Li depositions that the calendar model does not account for.

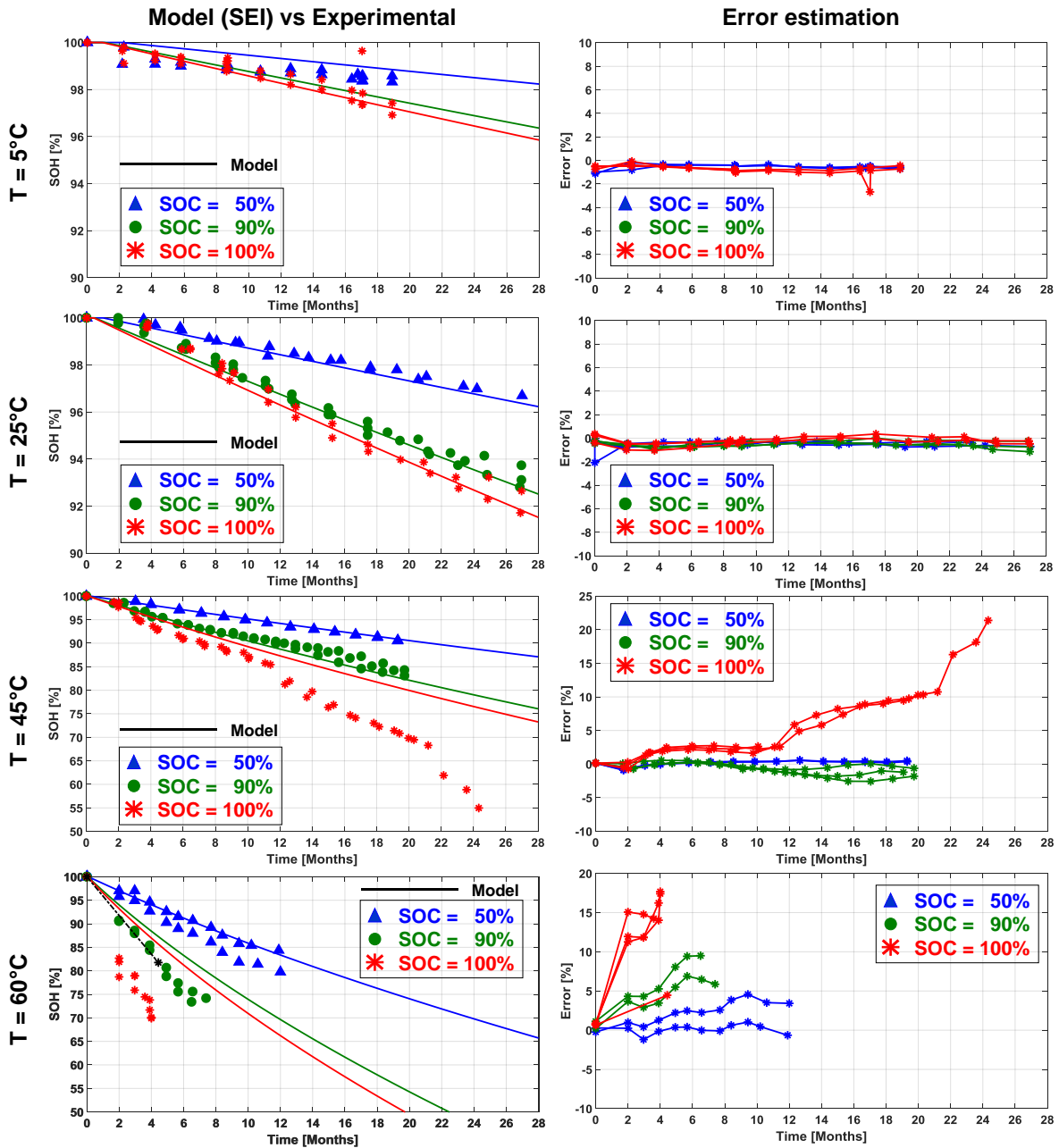


Figure V-4: Comparison between calendar model based only on SEI growth (Broussely's law) versus experimental data.

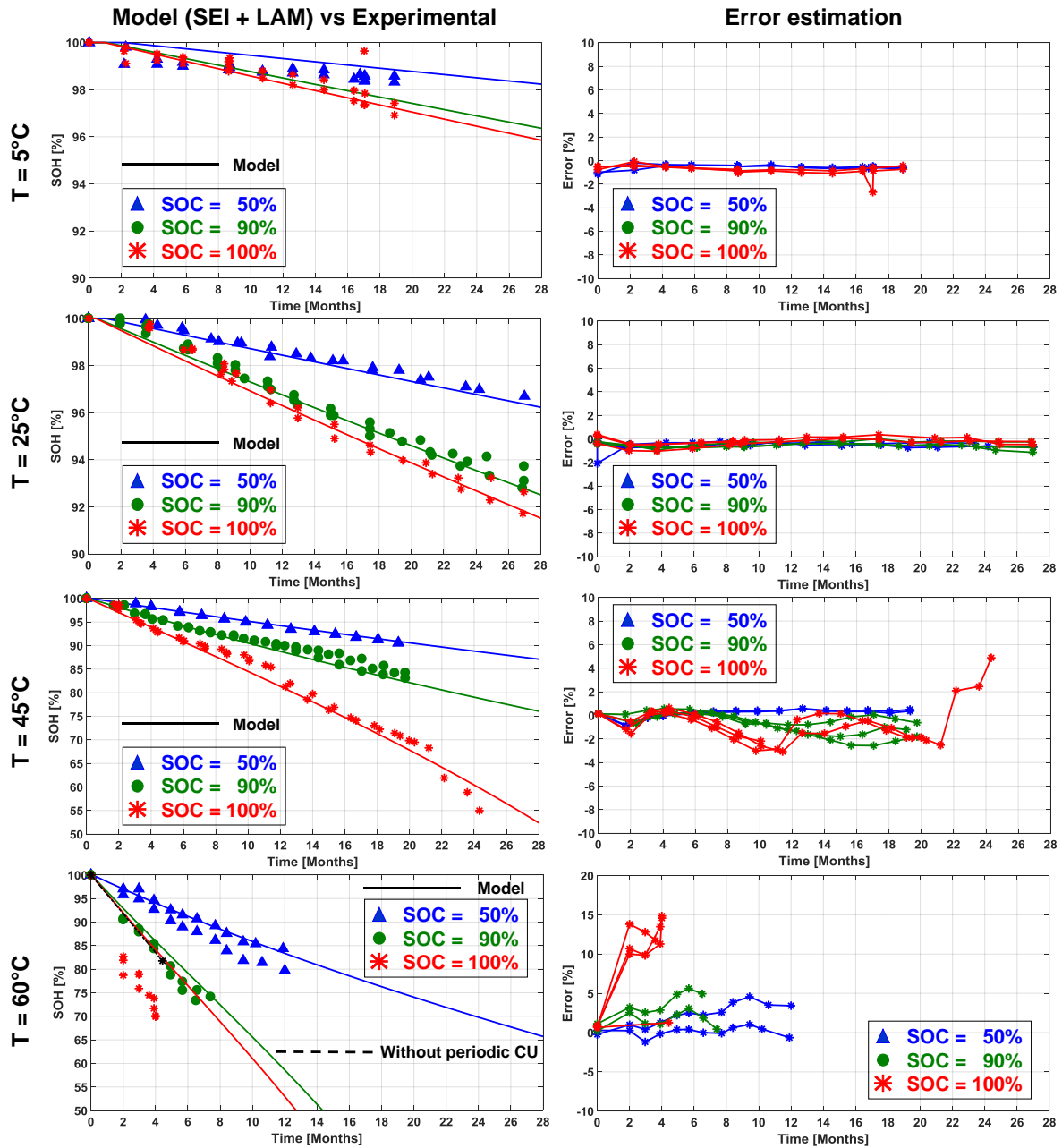


Figure V-5 : Comparison between calendar model based on both SEI growth and LAM versus experimental data.

Finally, **Figure V-6** presents the simulated contribution of each aging mechanism during calendar aging for each calendar condition. Under the severe conditions ($T = 45\text{ }^{\circ}\text{C}$ and $\text{SOC} = 100\%$, $T = 60\text{ }^{\circ}\text{C}$ and $\text{SOC} = 90\%$, $T = 60\text{ }^{\circ}\text{C}$ and $\text{SOC} = 100\%$), the contribution of the LAM (due to dry areas) appears.

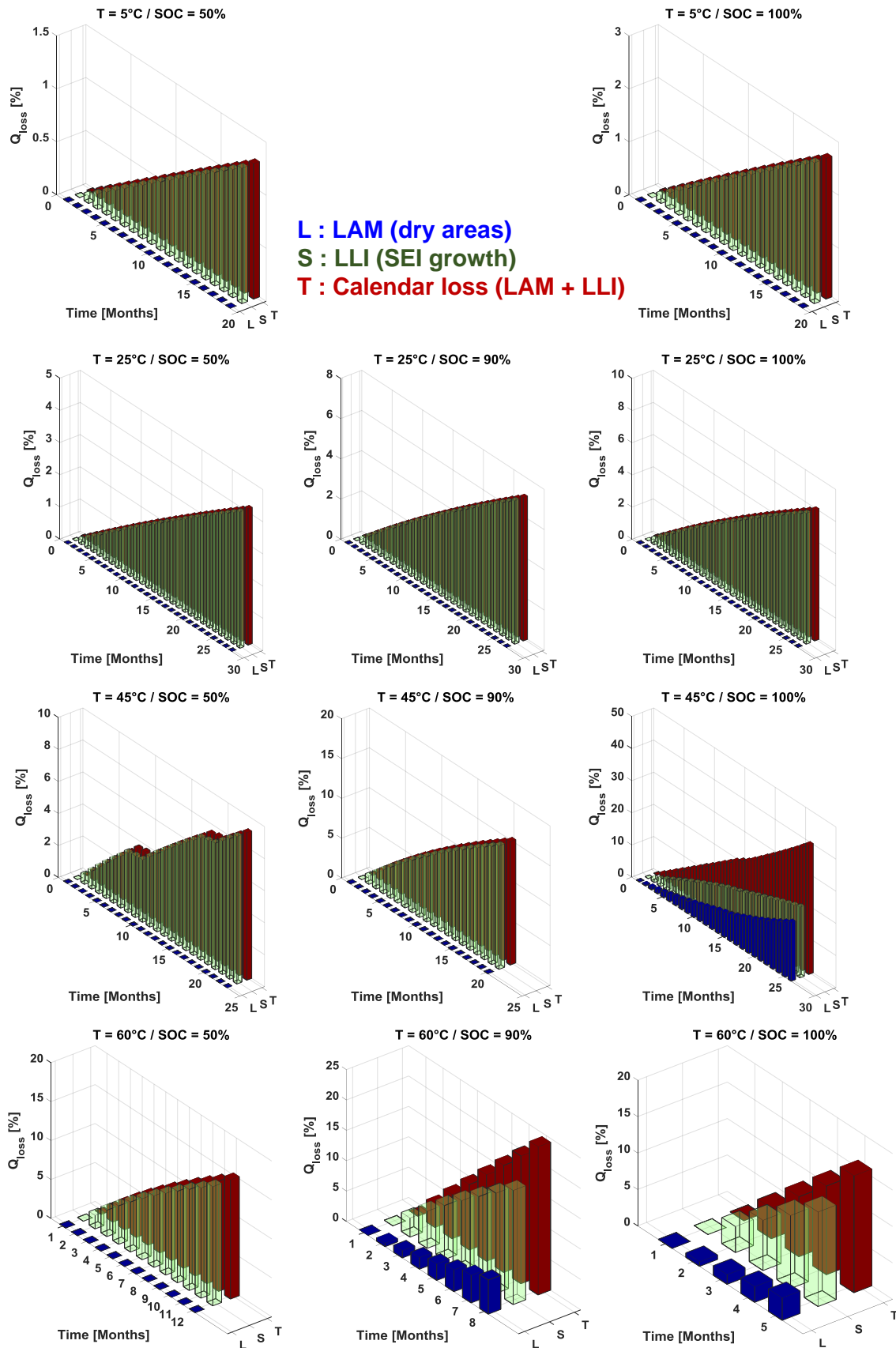


Figure V-6 : Contribution of each aging mechanism into the capacity loss during calendar aging.

5.2.4.2. Cycling aging validation results

5.2.4.2.1. Results obtained for cycling tests performed at 5 °C

Note that, for cycling tests performed at 5 °C between 3.42 V and 4.08 V (theoretical SOC window from 10 to 90 %), the corresponding SOC range measured was rather determined between 8 and 44 % of SOC at 1 C and slightly constricted at 2 C and 3 C (see in *Appendix of the Chapter 5*). It is hence very far from the expected SOC, but this result is not surprising since it is due to the fact that the limiting voltage thresholds are quickly reached because of the high cell resistance at low temperature. Therefore, the amount of capacity throughput is less important.

It can be observed in **Figure V-7** that the model can predict the sudden drop at the beginning of aging. However, it does not follow the curved shape of experimental data especially at 2 C and 3 C between 0 and 2 months. This behavior results in an estimated error of almost 10 % in the first two months and less than 2 % in the last twelve months.

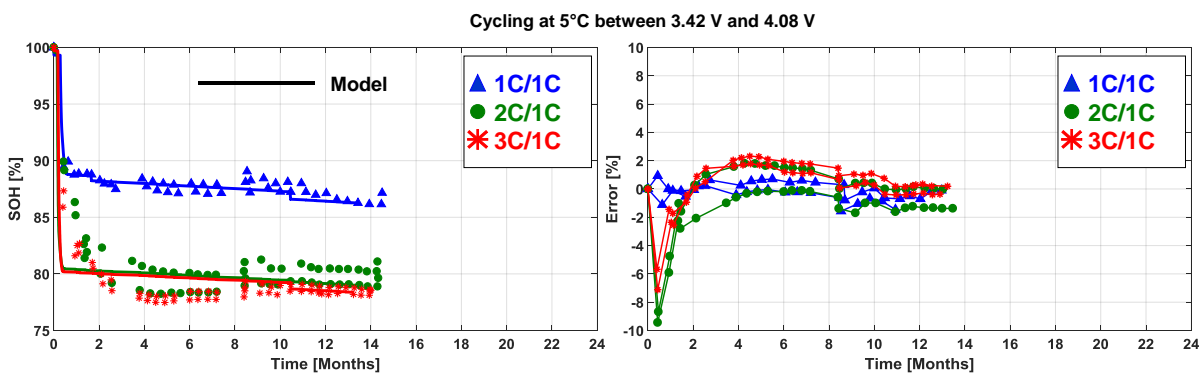


Figure V-7 : Model versus experimental data for cycling tests performed at 5 °C.

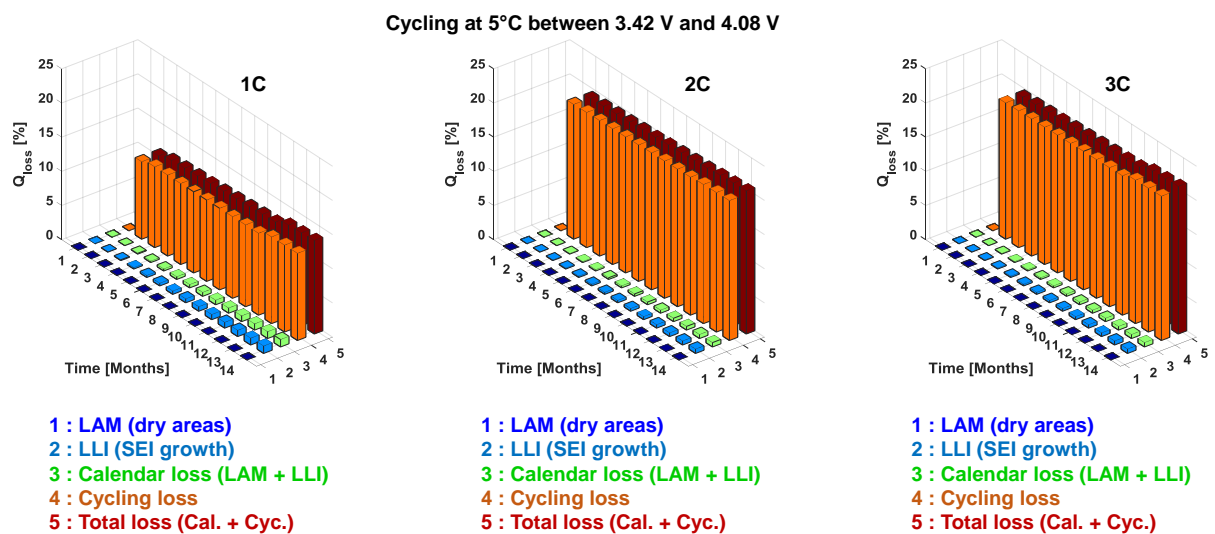


Figure V-8 : Contribution of each aging mechanism into the capacity loss during cycling aging at 5 °C.

The contribution of each aging mechanism illustrated in bar plots of **Figure V-8** shows that the total capacity loss is mainly due to cycling and a negligible part is attributed to the SEI growth.

5.2.4.2.2. Results obtained for cycling tests performed at 25 °C

The model allows to obtain a better fitting at 25 °C, especially for the condition of cycling between 3.42 V and 4.08 V (from 10 to 90 % of SOC, theoretically) as illustrated in **Figure V-9**. The estimated error between the model prediction and experimental data is less than 2 %. For this condition, the measured SOC range (used in the generation of cycling profile) rather varies between 10 and 74 %, practically. Besides, the temperature measured at the skin of the cell is higher than 25 °C in charge as in discharge, reaching 35 °C during charging phase at rate of 3 C (see in *Appendix of the Chapter 5*).

For the condition of cycling at 25 °C between 2.7 V and 4.2 V (from 0 to 100 % of SOC), a good agreement is observed between the model and experimental data, especially at the rates of 1 C and 2 C where the estimated error is less than 2 %. At the rate of 3 C, the model struggles to follow the dynamic of experimental data at the beginning of aging, between 0 and 4 months. Nevertheless, it eventually catch the gap towards the end of aging reducing the estimated error from 6 % to almost 0 %.

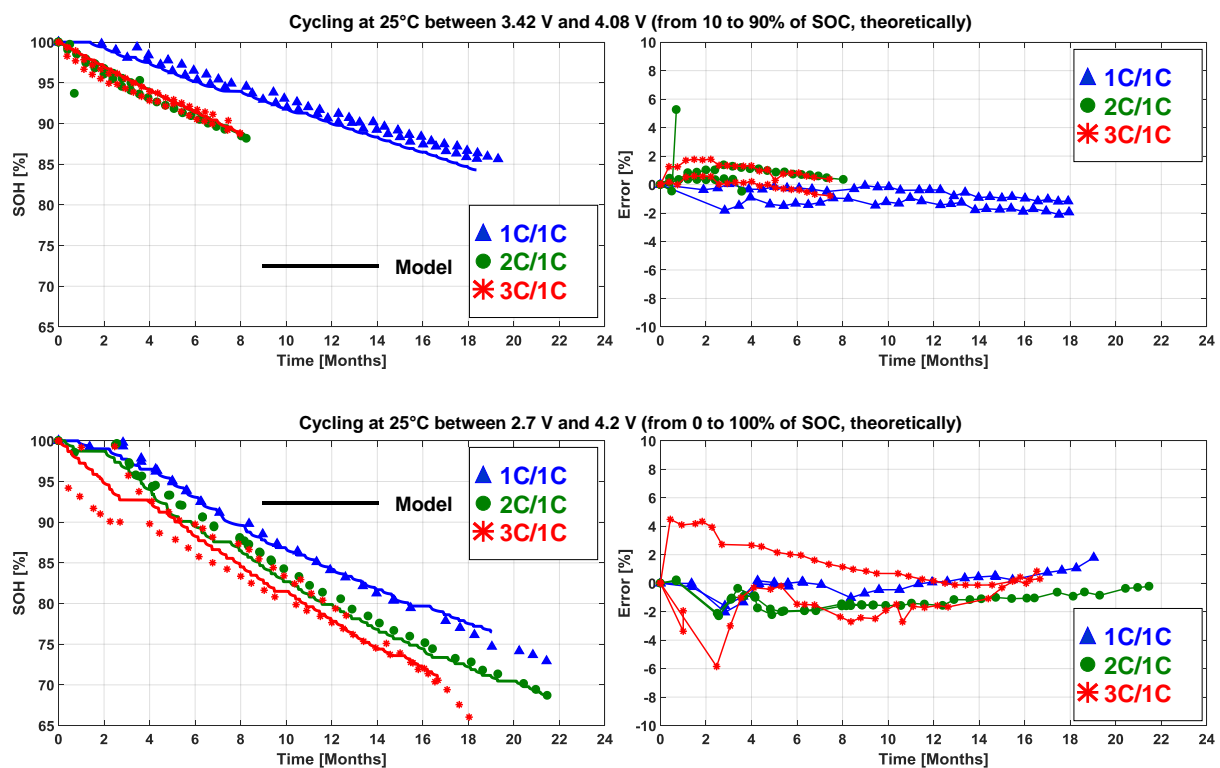


Figure V-9 : Model versus experimental data for tests performed at 25 °C.

In addition, **Figure V-10** shows that cycling between 3.42 V and 4.08 V (from 10 to 90 % of SOC, theoretically) leads to less capacity fade than cycling between 2.7 V and 4.2 V (from 0 to 100 % of SOC).

In both cases, as expected, the total capacity loss is mainly due to the cycling with a few contribution of the SEI growth. For the same duration of aging, calendar losses are quite equivalent between the two strategies of SOC range whatever the C-rate.

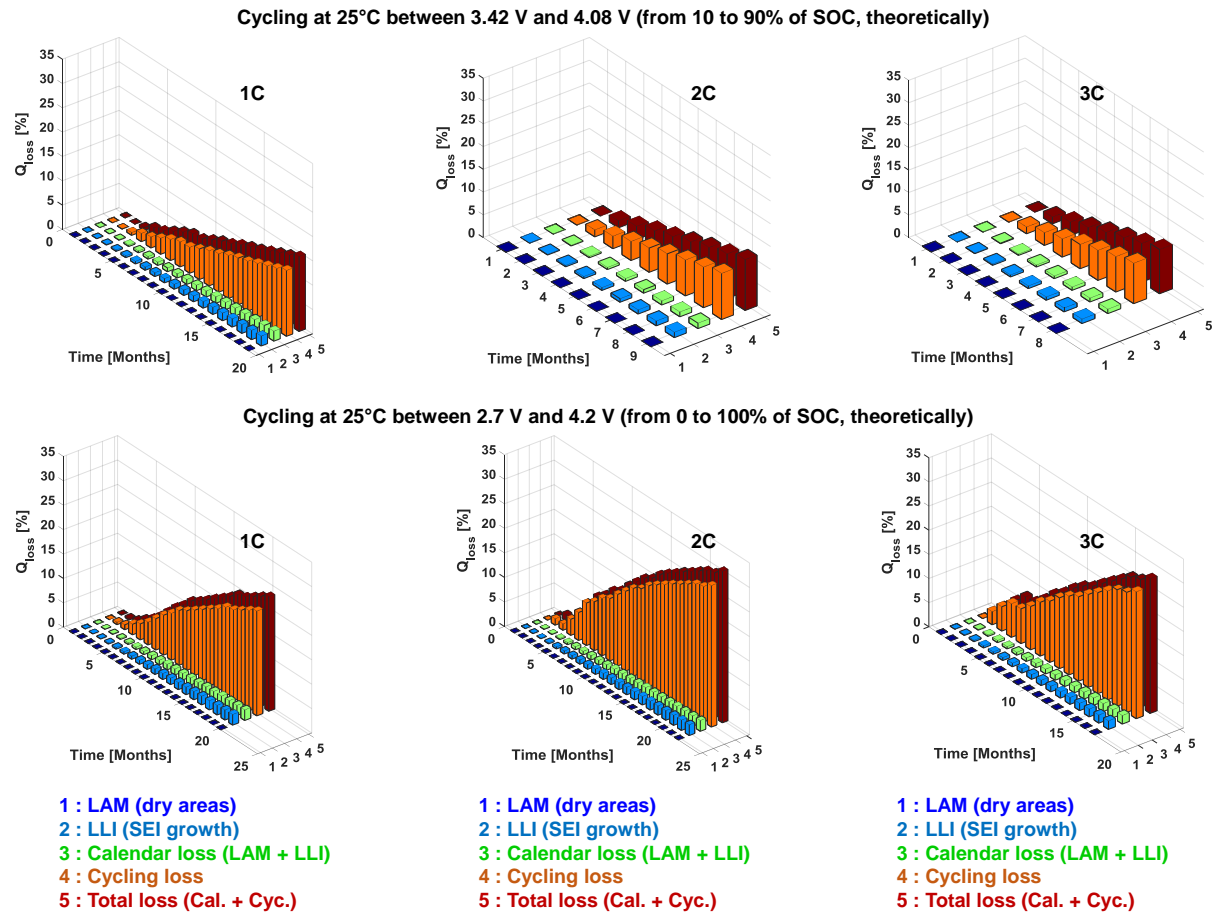


Figure V-10 : Contribution of each aging mechanism into the capacity loss during cycling aging at 25 °C.

5.2.4.2.3. Results obtained for cycling tests performed at 45 °C

Figure V-11 shows the good correspondence between the model and experimental data for cycling performed between 3.42 V and 4.08 V (from 10 to 90 % of SOC, theoretically), especially for the C-rates of 1 C and 2 C. The estimated errors are less than 4 %. In the absence of good reproducibility at a rate of 3 C, the model fits well only with the experimental data corresponding to one cell. The error is then less than 2 % with this cell while it reaches 8 % with the cell presenting the shortest aging duration. Note that at rate of 3 C, the skin temperature of the cell reaches 50 °C in charge and 47 °C in discharge (see in *Appendix of the Chapter 5*). Those measurements were implemented in the generation of usage profile.

When the full cycling condition is considered (from 0 to 100 % of SOC), there is also a good agreement between the model and experimental data at the rate of 1 C, although the model does not fit the slope failure observed around the 10th month of aging. In the literature, as reported by X.-G. Yang et al. [216], this slope failure was attributed to the clogging of anode porosity by the end of cycling resulting in a sharp resistance rise. No cycling test was performed at a rate of 2 C with this SOC range condition.

For the rate of 3 C, it can be seen that capacity fails much faster. On one hand, it has been reported that some cells have exhibited unexpected thermal behavior leading to a rise in temperature above 60 °C. On the other hand, the test was ended due to some cells overcharge. It may thus be assumed that full cycling at 45 °C and a rate of 3 C could have led to additional aging mechanisms according to unexpected behaviors mentioned above. This could be for these reasons that the model does not present a good fitting with experimental data with this condition where the estimated error reaches 8 %.

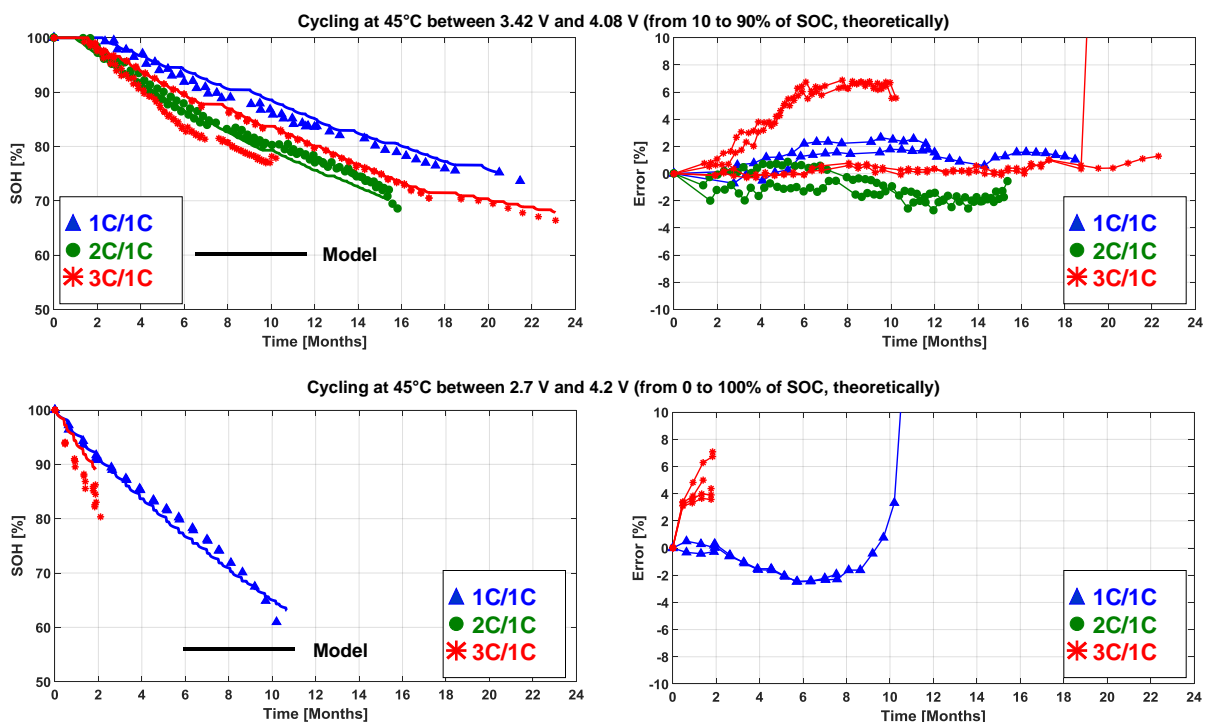


Figure V-11 : Model versus experimental data for tests performed at 45 °C.

Figure V-12 shows the contribution of aging mechanisms into the total loss of capacity over aging duration.

For both SOC ranges strategies, given the fact that the measured temperature exceeded 45 °C (see in *Appendix of the Chapter 5*) and the maximum SOC threshold is above 90 %, it is thus normal to observe a contribution of the LAM in such conditions. However, the part due to this aging mechanism remains negligible compared to the impact of the SEI.

Indeed, the duration spent in critical SOC is actually less important because of SOC fluctuations during cycling. This observation is much more obvious by considering cycling tests performed at a rate of 3 C where the charging phase time is estimated at 20 minutes and the total aging time was only 2 months. Anyway, the major contributor in total capacity loss remains the cycling effect whatever the cycling conditions.

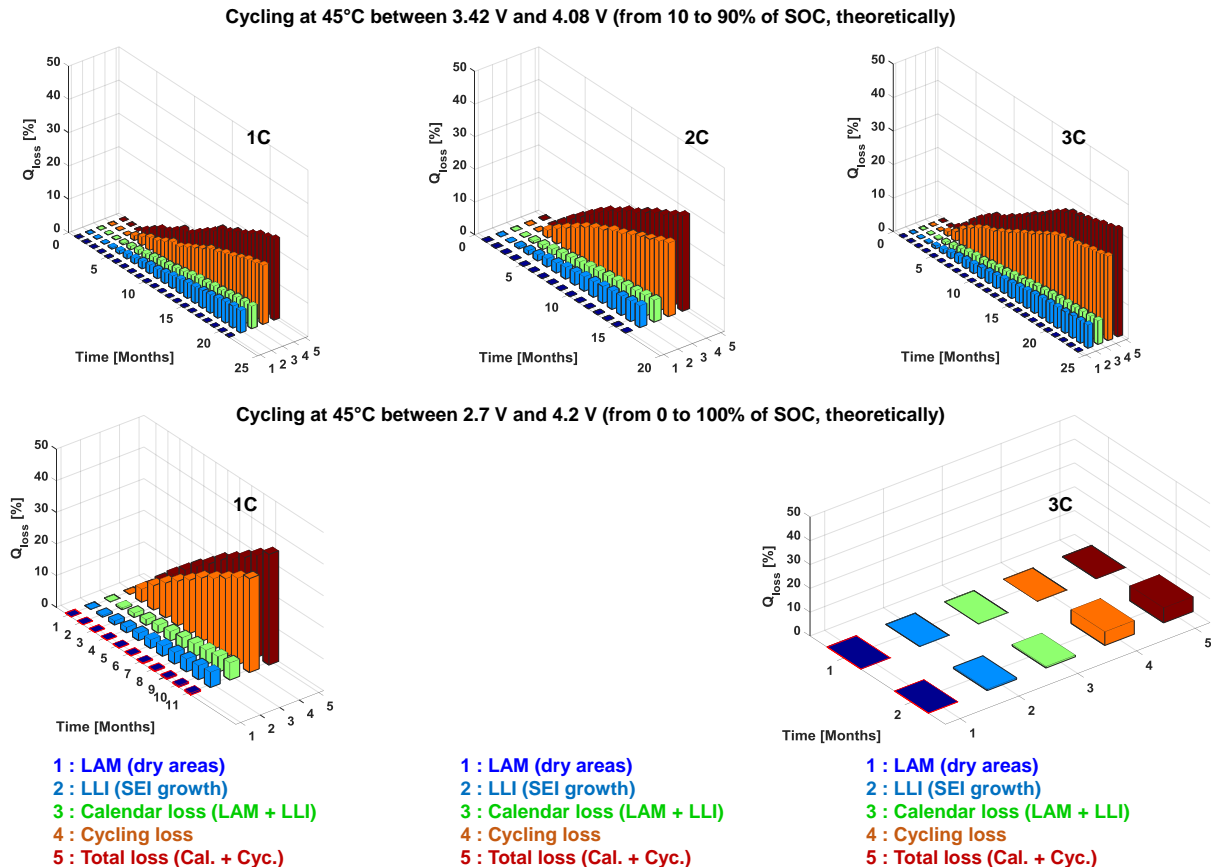


Figure V-12 : Contribution of each aging mechanism into the capacity loss during cycling aging at 45 °C.

5.2.5. Model validation

The model validation is obtained on cycling conditions that were not been taken into account in the identification of the parameter J_{cyc} . These are cycling tests performed at 45 °C from 2.7 to 3.98 V (0 to 80 % of SOC, theoretically) and from 3.49 to 4.2 V (20 to 100 % of SOC, theoretically).

Figure V-13 highlights the good agreement between experimental data and the model for the cycling condition at 45 °C from 2.7 to 3.98 V (0 to 80 % of SOC, theoretically). The estimated error remains less than 6 % for both rates of 1 C and 2 C and less than 2 % for 3 C. This result allows to validate the model in such condition.

By considering the cycling SOC range between 20 and 100 %, it is ascertained that model presents a tolerable agreement only at the rate of 1 C. The model moderately fits with experimental data until the apparition of the slope failure around the 8th month. In that period, the estimated error reaches 4 %.

Besides, this slope failure appears earlier at high C-rates, so that the model cannot fit well at both rates of 2 C and 3 C. This slope break indicates an additional aging mechanism, graphite pore clogging as reported by J. Dahn [46; 181] and X.-G. Yang et al. [216] that model does not simulate. The apparition of this slope failure was also observed in the conditions of cycling at 45 °C between 0 and 100 % of SOC (from 2.7 to 4.2 V), with more accentuation (see in **Figure V-11**). It thus be concluded that prolonged cycling using a maximum voltage threshold maintained at 4.2 V induces an additional aging mechanism, not integrated in the present model.

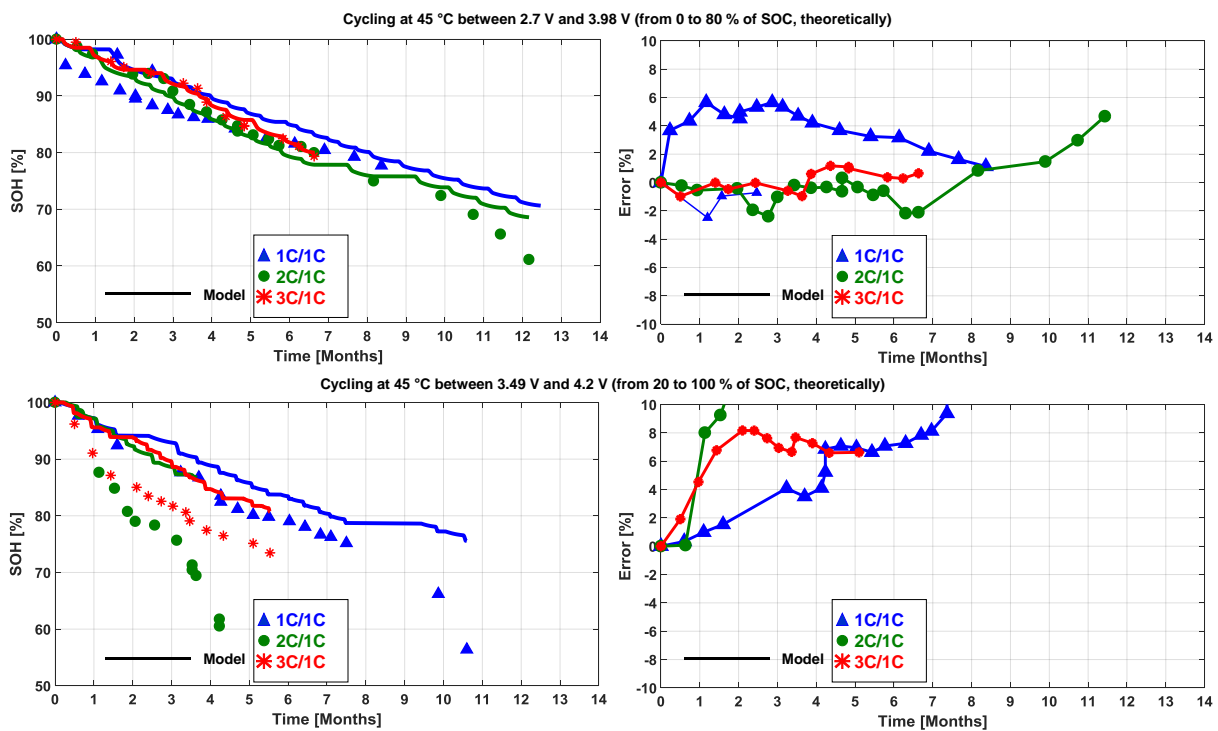


Figure V-13 : Model validation at 45 °C.

As expected, there is no contribution of dry zones in the capacity loss for the SOC range between 0 and 80 % (see in **Figure V-14**). In contrary, a few contribution of LAM can be pointed out in the SOC range between 0 and 100 % since the maximum SOC threshold is higher than 90 % and the measured temperature is higher than 47 °C (see in *Appendix of the Chapter 5*). However, the loss due to cycling remains the most important contributor.

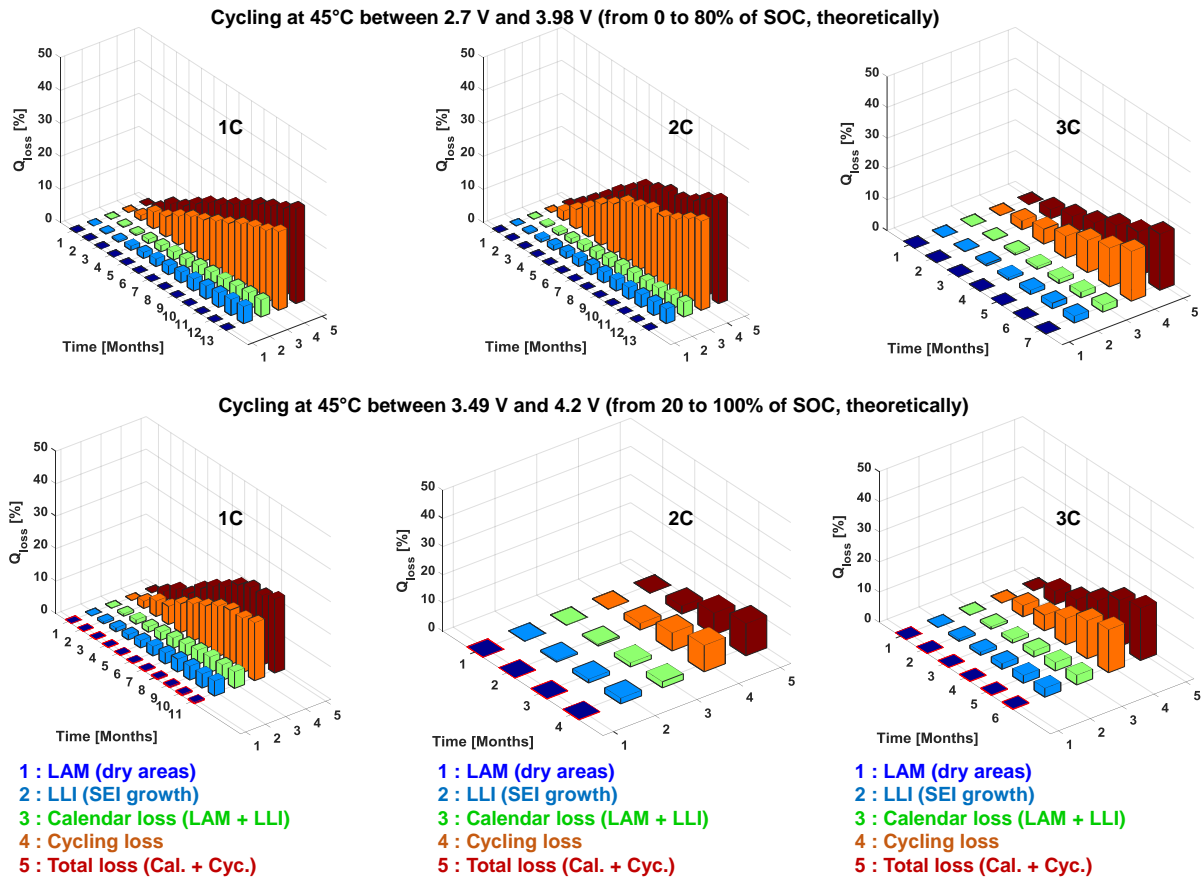


Figure V-14 : Contribution of each aging mechanism into the capacity loss during cycling aging at 45 °C.

5.3. Prognostic aging model based on electrodes shifts

5.3.1. Principles and model descriptions

In most of the works about the use of incremental capacity analysis (ICA) ($\Delta Q/\Delta U$ vs U), the authors distinguish four types of loss of active material (LAM) effects: (1) loss of lithiated negative electrode (LAM_{LiNE}), (2) loss of delithiated negative electrode (LAM_{deNE}), (3) loss of lithiated positive electrode (LAM_{LiPE}), and (4) loss of delithiated positive electrode (LAM_{dePE}) materials. However, in this thesis, we only consider the LAM as an entity for each electrode. The loss of lithium inventory (LLI) mainly suggests the loss of lithium in the SEI growth.

The principle underlying the aging degradation modes and their effects on the OCV of cells and electrodes is well detailed in the papers mentioned in the Chapter 1 [1.3.3]. However, since authors have worked with half-cells based on harvested electrodes materials, they have been forced to perform some operations in order to reconstruct the cell voltage based on individual electrodes potentials. In fact, it was necessary to adjust some parameters such as the ratio of the capacity in the negative electrode (NE) versus the positive electrode (PE) and initial offset (OFS). The initial OFS can be defined as the SOC gap of the NE compared to the PE.

The theory in question relies essentially on the electrode slippage specific to each aging mechanism and its effect on the voltage and IC curves. In order to ensure that the cell operates under an approximate equilibrium state, IC must be calculated from voltage measurements obtained at very small current such as at a rate of $C / 25$.

In the Chapter 2, we have discussed about the integration of reference electrodes inside a fresh commercial 16 Ah Li-ion cell. We have performed electrochemical measurements at different C-rates such as $C / 25$ and under different temperatures. These data will thus be used as reference measurements for the prognostic aging model based on electrodes shifts. Furthermore, it will be able to correlate electrodes shifts characteristic to each aging mode and their impacts even on electrodes potentials and IC curves.

Moreover, insertion of reference electrodes into the commercial cell presents many advantages. Indeed, for each value of the cell voltage, there is already the corresponding value of the potential of each electrode and the corresponding value of charged or discharged capacity. Therefore, there is no need to calculate the ratio of the capacity in both electrodes neither the initial offset.

In the following sections, the representation of different aging mechanism modes is inspired by schematics proposed by M. Dubarry et al. [79], A. Marongiu et al. [217] and C. R. Birkel et al. [218].

The voltage curves of the reference (REF) case are depicted as broken lines while those corresponding to the aging (AG) case are characterized by full lines.

Q_{Loss} represents the capacity loss in the cell. Q_0 and Q_{end} represent respectively the initial and the last breakpoint of relative capacity before aging while Q'_0 and Q'_{end} are those corresponding to relative capacity after aging.

In the framework of this thesis, we have observed the LAM symmetrically on both electrodes (dry areas phenomenon). However, in order to understand the effect of the LAM on each of the two electrodes taken individually, it is appropriate to represent each effect of LAM on the PE and on the NE separately, before representing the overall effect.

5.3.1.1. Loss of Lithium Inventory

LLI is caused by the consumption of reversible Li cations by parasitic reactions of which the major remains the SEI growth on the negative electrode (NE). This reaction is reported to be the main aging mechanism of Li-ion cells in calendar life. However, in some cases, a passivation layer consuming Li can also grow on the positive electrode (PE). The scenario involving LLI and its effects on C / 25 voltage curves is pointed out in **Figure V-15**. The LLI is represented by a left shift of the NE in respect to the PE curve. As a result, the initial capacity interval (from Q_0 to Q_{end}) is reduced due to the decrease of capacity into a new capacity interval (from Q'_0 to Q'_{end}).

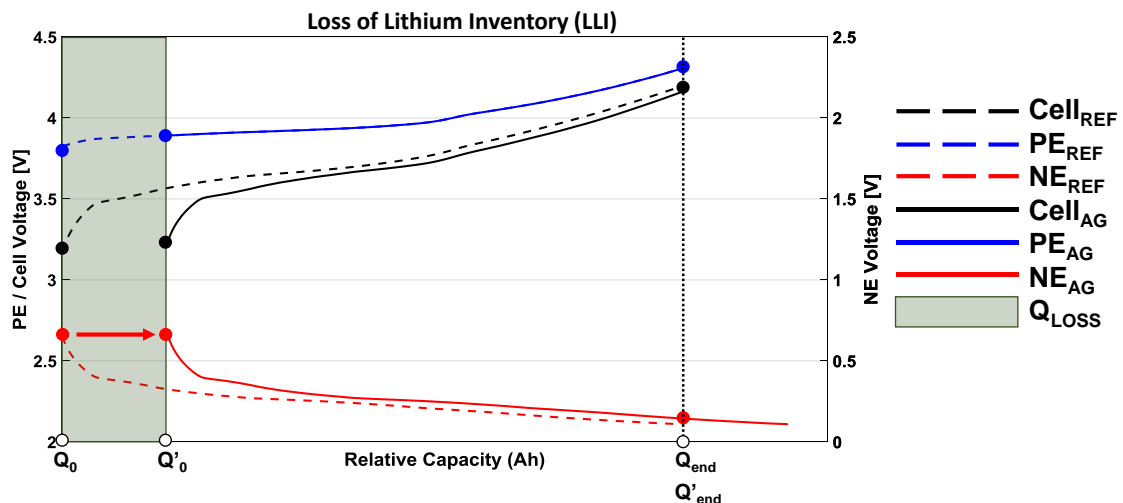


Figure V-15 : Simulation of the LLI degradation mode at C / 25.

During storage at high SOC, the NE voltage is low enough and thus it leads to more consumption of Li ions at the NE / electrolyte interface resulting in an accelerated formation of SEI. As a consequence, at the OCV, the NE potential at the end-of-charge (EOC) will be affected. Due to lithium consumption, the NE voltage at the EOC (100 % of SOC) of the cell becomes higher than in a fresh cell. On the opposite, the NE potential at 0 % of SOC normally remains unchanged.

Thereupon, the PE voltage at the end-of-discharge (EOD) (0 % of SOC) of the cell becomes higher than in a fresh cell. Indeed, after consumption of Li by LLI, the amount of Li present in the NE is now reduced. Thus, by discharging the cell, the PE is no longer completely filled with Li compared to the state before. As a result, its voltage at EOD is higher than it would be in a fresh cell.

Therefore, the minimum cell voltage of 2.7 V is reached by polarization effect which will force more lithium extraction from the NE to be inserted into the PE by an abrupt increase of the NE voltage at the EOD of the cell. Correspondingly, during charging, the maximum cell voltage of 4.2 V will be reached only by the same polarization effect by imposing the PE to reach higher voltages. However, we do not consider the voltage sharp rise in the NE at EOD neither in the PE at the EOC to ensure respectively reaching 2.7 V or 4.2 V at the cell level.

Figure V-16 illustrates the simulation of 5 %, 10 %, 15 % and 20 % of capacity loss for LLI degradation mode at a rate of $C / 25$ and the effects on the voltage and IC curves.

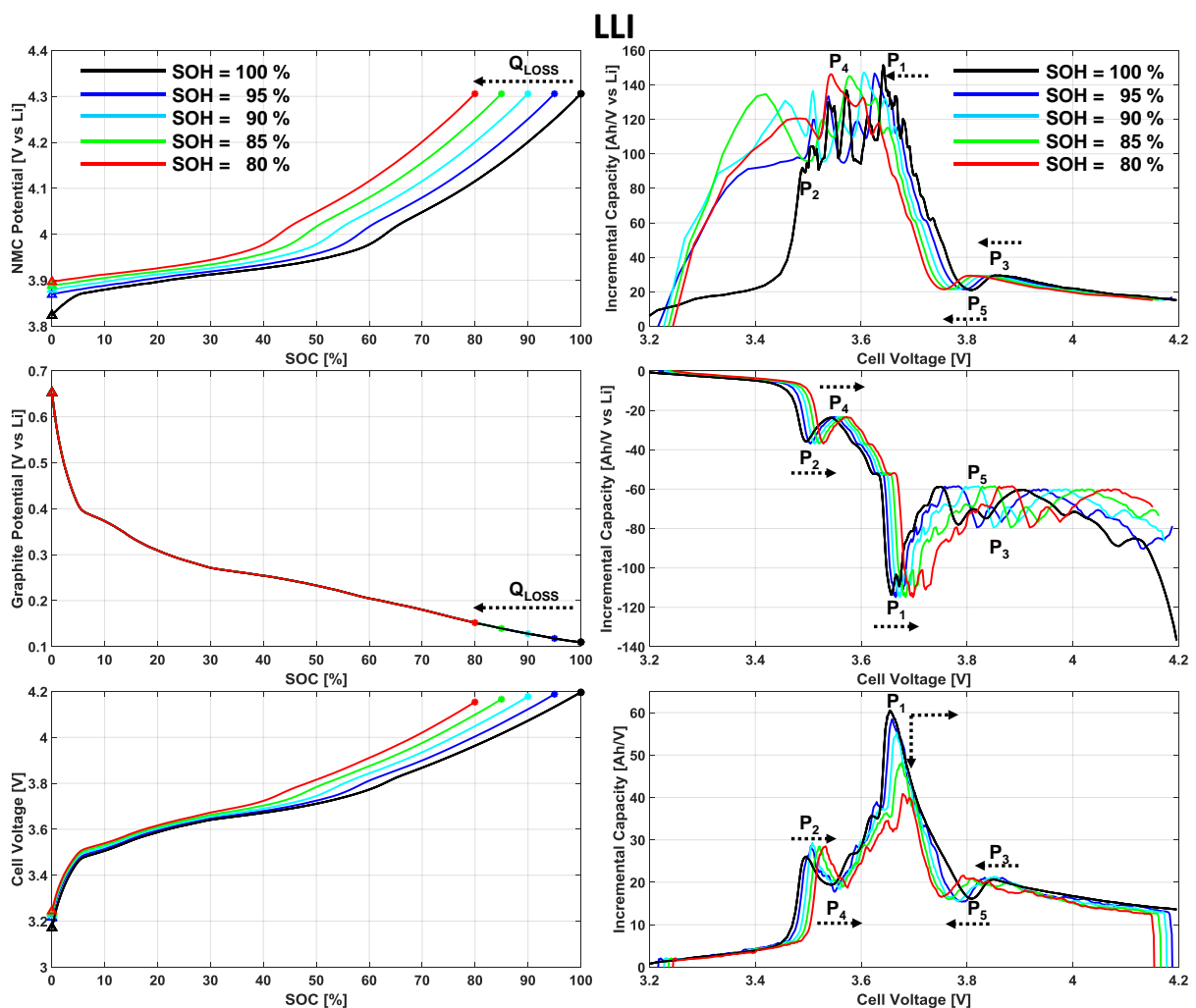


Figure V-16 : Simulation of the LLI degradation mode at $C / 25$ and effects on IC curves.

According to the protocol, this charge at rate of $C / 25$ was preceded by a discharge operated at a rate of $1 C$ followed by a rest of 30 min. The voltage relaxing effect during the rest explains the fact that at the beginning of the charge the cell voltage starts at 3.2 V instead of 2.7 V.

It is pointed out that the NE voltage at the EOC is more and more high due to Li consumption. The presence of 5 characteristic peaks (P_1 , P_2 , P_3 , P_4 and P_5) can be distinguished on the IC curves corresponding to the complete cell.

The peaks P_2 and P_4 are less evident on the IC curves related to the PE (due to numerous fluctuations), while the peaks P_3 and P_5 are less conspicuous on the IC curves associated to the NE.

Based on the cell IC curves, LLI is characterized by the reduction of P_1 which in addition tends to go in the direction of higher voltages, and the shifts of P_2 and P_4 towards higher voltages (without any decrease), while P_3 and P_5 seem to go near lower potentials.

In fact, it can be noticed that the shift of P_1 is more influenced by the graphite electrode while its decrease is rather controlled by both electrodes. Additionally, the shifts of P_2 and P_4 are guided by the NE while P_3 and P_5 are rather handled by the PE.

5.3.1.2. Loss of Active Material on the Positive Electrode

The LAM whether in the PE or in the NE can be represented as the shrinkage of the designed electrode voltage curve compared to its original extent due to, for example, the loss of electronic contact in some electrode areas.

In the case of the LAM on the PE electrode only, as illustrated in **Figure V-17**, since Li becomes not available in the lost areas, the amount of the remained Li in the PE thus becomes insufficient for filling the NE compared to the initial state.

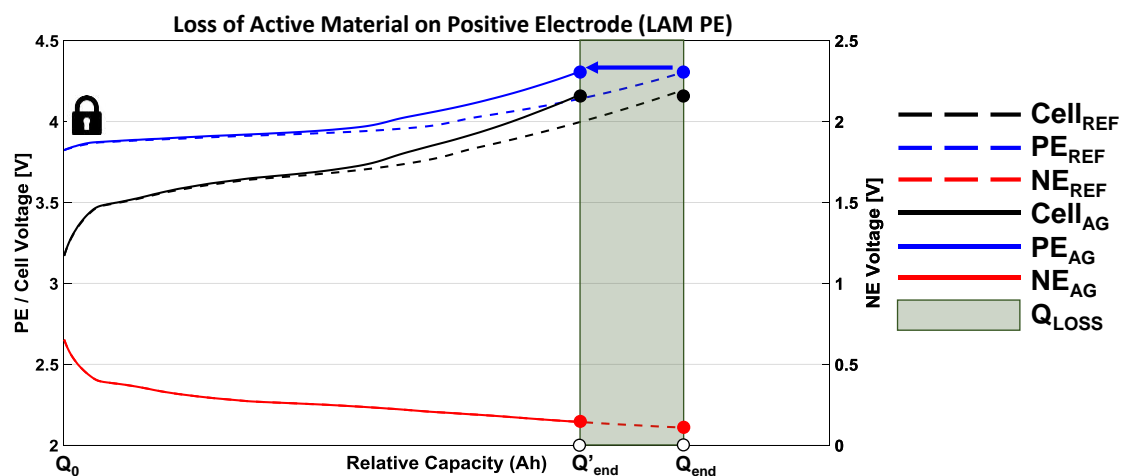


Figure V-17 : Simulation of the LAM degradation mode on the PE at $C / 25$.

At the EOC, less lithium will thus be inserted into the NE so that its potential will stay at a higher values at OCV as illustrated in **Figure V-18**.

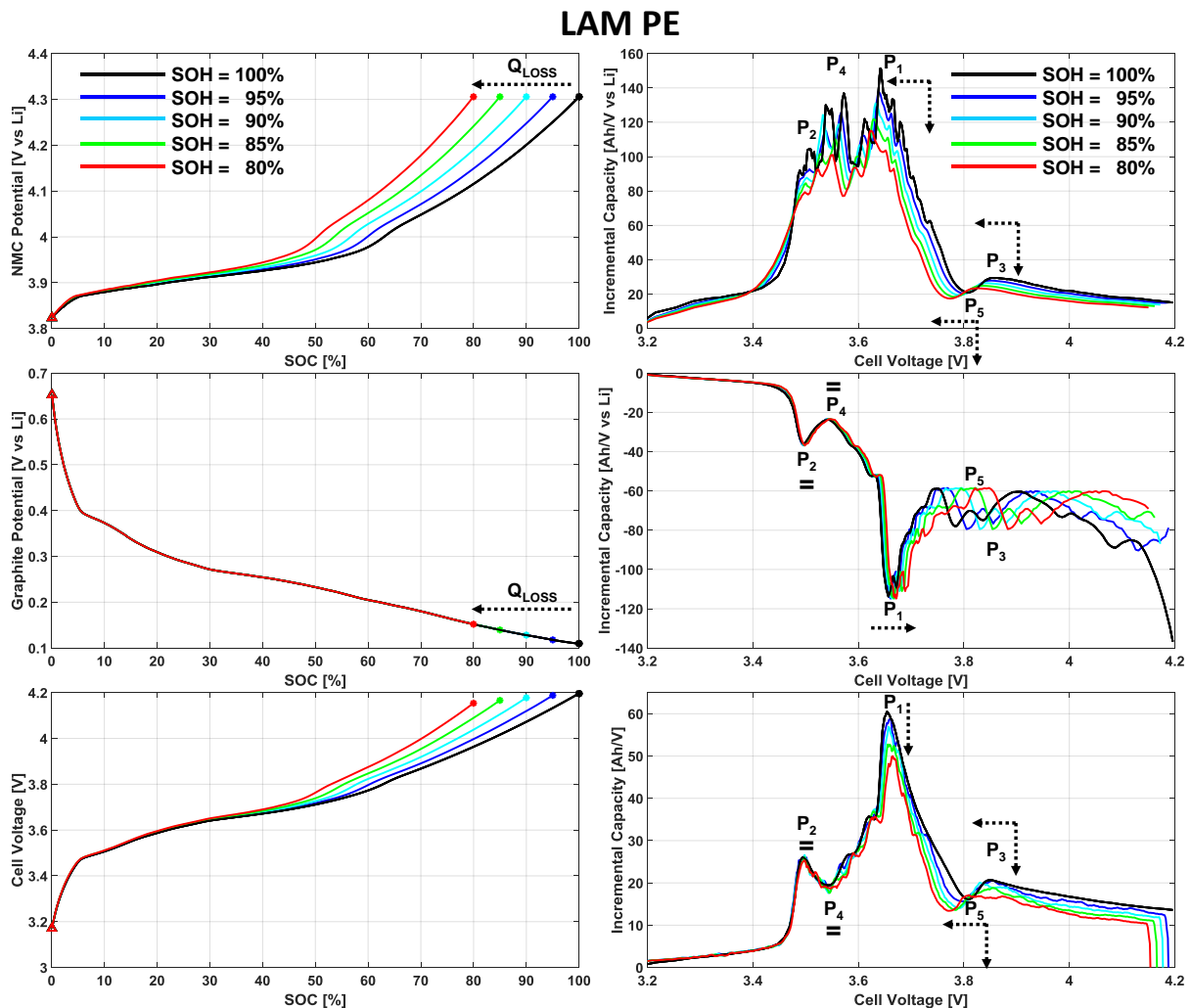


Figure V-18 : Simulation of the LAM degradation mode on the PE at C / 25 and effects on the IC curves.

Based on the cell IC curves, LAM on the PE is identified by the reduction of P_1 with a negligible shift to the right while P_2 and P_4 remain unchanged. Moreover, P_3 and P_5 are slipped to lower potentials with a small diminution.

It can be perceived that the decrease of P_1 is influenced by the PE and the small shift related to the NE. In fact, on IC curves of the PE, P_1 is decreasing while pointing towards lower potentials. Equivalently, IC curves of the NE exhibit only a small shift of P_1 towards higher potentials. Furthermore, the invariance of P_2 and P_4 are managed by the NE while the shifts P_3 and P_5 are rather directed by the PE.

5.3.1.3. Loss of Active Material on the Negative Electrode

The same analogy can be done in the event of the LAM on the NE only. The voltage of the NE remains the same but actually for a reduced capacity because of the inaccessibility to Li ions into disconnected zones for example. As a consequence, by discharging the cell, the amount of the remained Li in the NE becomes deficient to fulfill the PE leaving it at higher potential at the EOD (see in **Figure V-19**).

By the same token, since the cell is constrained to its lower voltage threshold of 2.7 V, the PE may be driven to lower potentials at the EOD by current polarization effects in order to reach the cell minimum voltage.

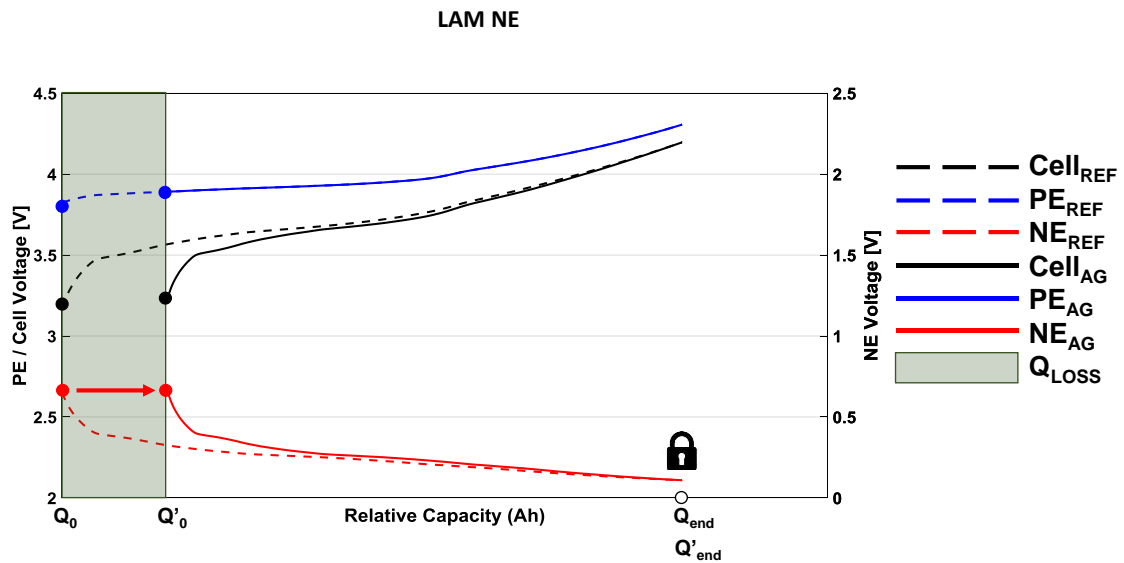


Figure V-19 : Simulation of the LAM degradation mode on the NE at C / 25.

Figure V-20 shows that the PE voltage at 0 % of SOC is more and more high due to the contraction of the NE curve voltage caused by the LAM.

Based on cell IC curves, LAM on the NE is determined by the diminution of P_1 with a small deviation approaching higher voltages. The intensity of P_2 and P_4 also decreases but rather with significant deflection to the right. Moreover, P_3 and P_5 are shifted to the lower voltages. It is ascertained that the shift of P_1 is more driven by the NE. Besides, the move of P_2 and P_4 also depends on the NE while that of P_3 and P_5 are rather conditioned by the PE.

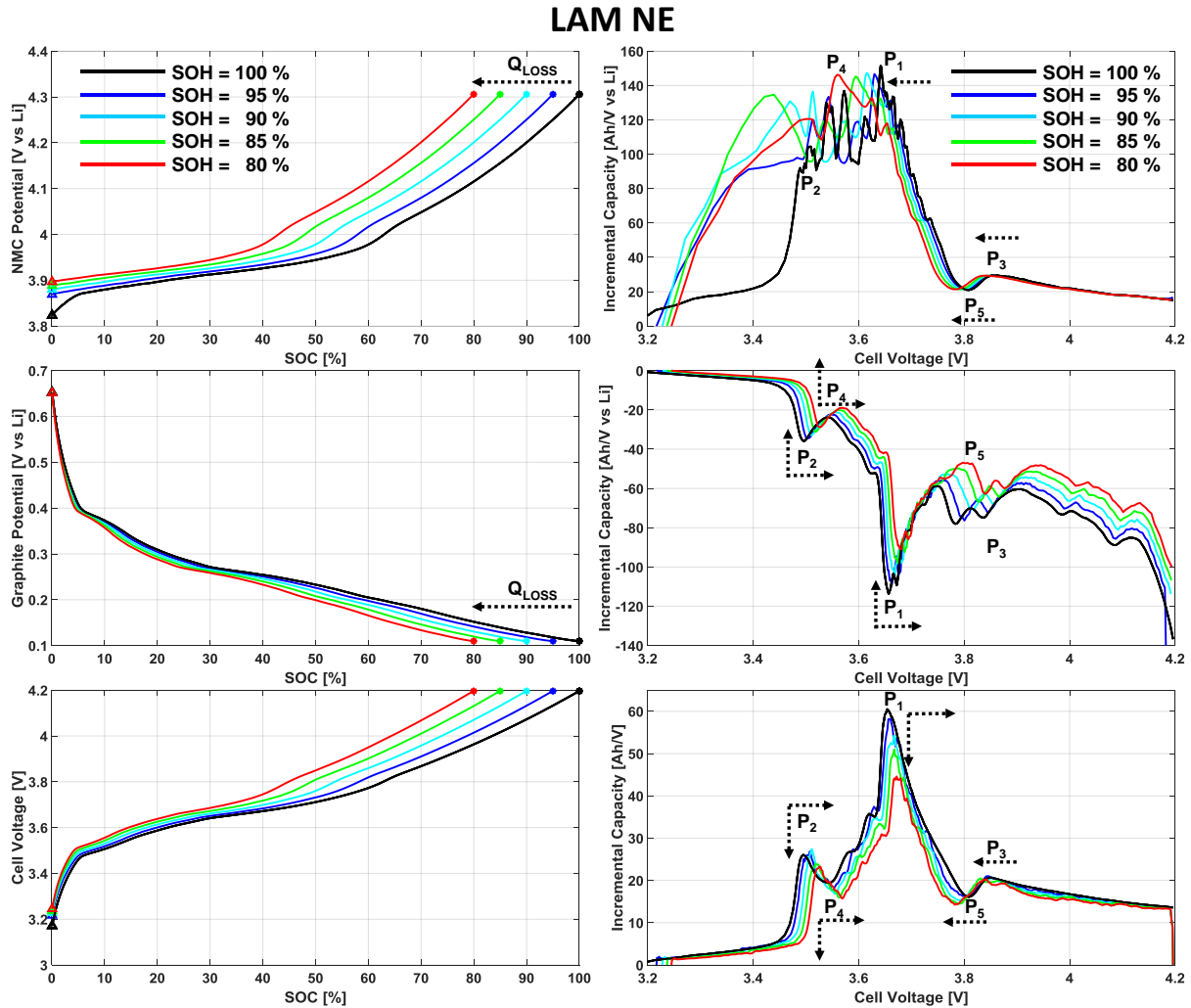


Figure V-20 : Simulation of the LAM degradation mode on the NE at C / 25 and effects on the IC curves.

5.3.1.4. Loss of Active Material on both electrodes

We also consider the LAM on both electrodes at the same time, which is one of the aging case studied in this thesis (Chapter 4). We have observed the LAM exactly in the same areas on both electrodes after calendar aging at high temperature and SOC.

This degradation mode then consists in the shrinkage of voltage curves of both electrodes for an equal loss of capacity. Indeed, since the areas lost are symmetrical for both electrodes, it may be considered that the amount of unreachable Li ions into those dry zones are equivalent.

Figure V-21 illustrates the LAM on both electrodes. It can be seen that the voltage curves of both electrodes are the same but are actualized for a shortened capacity. The effects of electrodes shrinkage on voltage and IC curves are exhibited in **Figure V-22**. The LAM on both electrodes is characterized by the lessening of the intensity of all the peaks.

LAM PE and NE

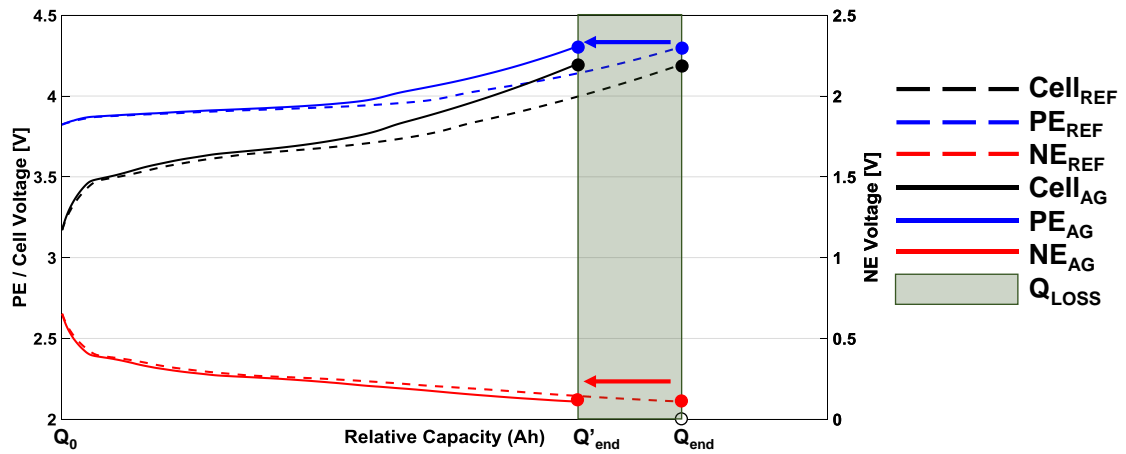


Figure V-21 : Simulation of the LAM degradation mode on both electrodes at C / 25

LAM PE and NE

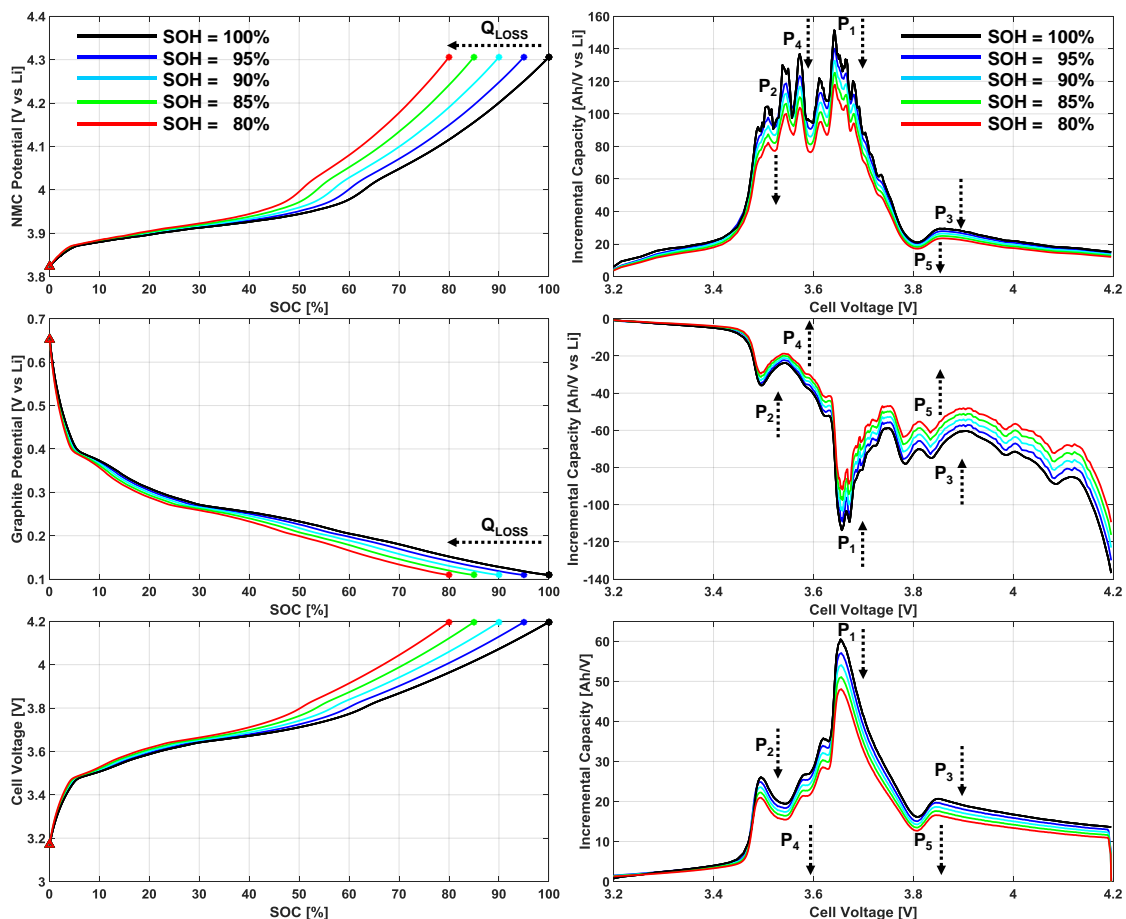


Figure V-22 : Simulation of the LAM degradation mode on both electrodes at C / 25 and effects on the IC curves.

5.3.1.5. Synthesis of the impact of different aging mechanisms on peaks displacement

The impact of different aging mechanisms on peaks displacement are synthetized in the **Table V-3**.

	LLI	LAM on the PE	LAM on the NE	LAM on both electrodes
P ₁	▼ ▶ higher voltages	▼ → small shift	▼ ▶ higher voltages	▼
P ₂	No decrease ▶ higher voltages	= Unchanged	▼ ▶ higher voltages	▼
P ₃	No decrease ◀ lower voltages	▼ ◀ lower voltages	No decrease ◀ lower voltages	▼
P ₄	No decrease ▶ higher voltages	= Unchanged	▼ ▶ higher voltages	▼
P ₅	No decrease ◀ lower voltages	▼ ◀ lower voltages	Low decrease ◀ lower voltages	▼

Table V-3 : Synthesis of the impact of different aging mechanisms on peaks displacement

The intensity of **P₁** decreases whatever the aging mechanism. However, its shift towards higher voltages is observed with all the aging mechanisms except with the LAM on both electrodes.

The decrease of **P₂** is only observed with the LAM on the NE and on both electrodes. Its slippage towards higher voltages is only noticed in the case of LLI and LAM on the NE. However, this peak remains unchanged in the case of the LAM on the PE.

The displacement of **P₄** is similar to that of the **P₂**. As mentioned above, **P₂** and **P₄** are managed by the NE.

The intensity of **P₃** is reduced in the cases of LAM on the PE and LAM on both electrodes. The shift of this latest peak toward lower voltages is determined in all the aging mechanisms except in the case of LAM on both electrodes.

The displacement of **P₅** is equivalent to that of the **P₃**, although a low decrease is observed with LAM on the NE. In addition, the displacement of the peaks **P₃** and **P₅** are handled by the PE.

5.3.2. Identification of aging mechanisms during cycling at low temperatures

In the Chapter 3, we have discussed aging mechanisms that occurred during cycling at low temperatures. According to post-mortem and ante-mortem investigations results, it was found that the fast irreversible capacity fade (around 75 % in less than 100 cycles) observed during fully cycling at 5 °C and at a rate of 1 C was mainly attributed to the loss of porosity in the graphite electrode. As a result, lithium was found trapped into graphite cavities. In addition, metallic depositions were determined on its surface (due to the high polarization), caused by the hindrance of graphite pores due to the accumulation of electrolyte degradation products.

On the contrary, the condition of cycling in a constricted SOC has led to a limited capacity loss (around 12 % in 1509 cycles) without significant visual degradation of the components.

On one hand, the analysis of incremental capacity curves in **Figure V-23 - A** shows the disappearance of all the Li insertion peaks after full cycling at 5 °C. A strong decrease in the intensity of the main peak **P₁** and peaks **P₂** and **P₄** (depending on the graphite electrode) is observed with a high shift towards higher voltages. The position of the peaks **P₃** and **P₅** (controlled by the NMC electrode) are no longer visible at all on the IC curve after aging. The total disappearance of all the peaks on IC curves makes it impossible to determine the associated mode of degradation

On the other hand, **Figure V-23 - B** shows the decrease of **P₁** while shifting to the right. In addition, the shift of **P₂** and **P₄** towards higher voltages with no decreasing of their intensities is pointed out. Nevertheless, the displacement with aging of the peaks **P₃** and **P₅** towards higher voltages does not correspond to the description of any aging mode synthesized in **Table V-3**. Two assertions can be proposed to explain this behavior:

- It may be assumed that there is an additional aging mechanism for the positive electrode which is unknown therefore not taken into account in the synthesis of aging modes.
- The polarization effect to force the cell voltage to reach its reference voltage thresholds is not considered in the prognostic model. Consequently, an influence on the displacements of peaks **P₃** and **P₅** on IC curves after electrodes shifts may not be underestimated.

Be that as it may, the displacement of the peaks **P₁**, **P₂** and **P₄** is consistent with the LLI mode. However, it should be noted that the LLI, in this case, does not relate only to the SEI growth which, moreover, is not favored at low temperatures. The loss of lithium by cycling effect is also involved.

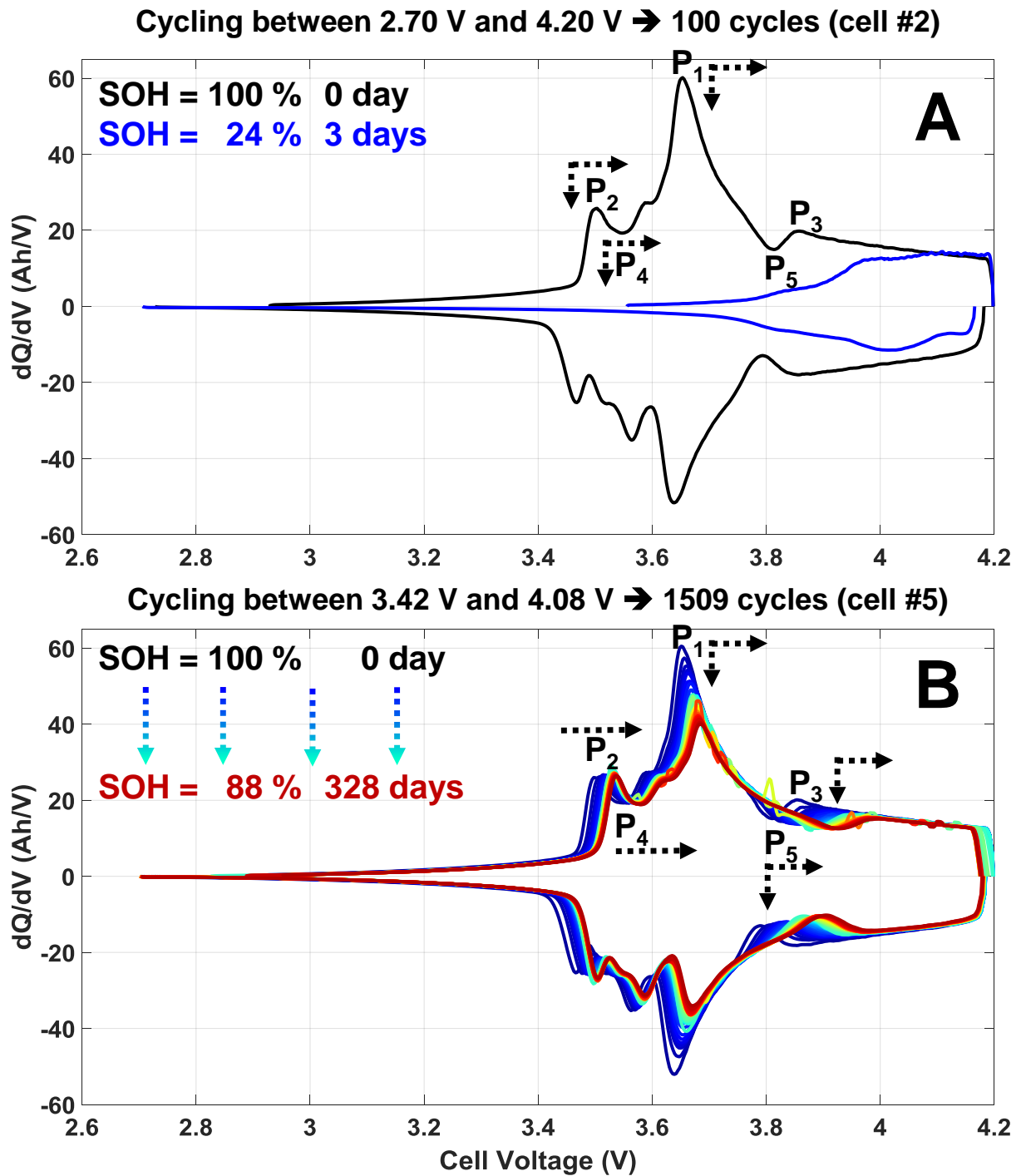


Figure V-23 : Evolution of IC curves during cycling aging at low temperatures.

5.3.3. Identification of aging mechanisms during storage at high temperatures

We still would like to mention that in order to follow the evolution of individual electrodes potentials with aging, two additional commercial 16 Ah Li-ion cells (KOK56 and KOK57) were instrumented with Li metal used as reference electrode, according to the protocol described in Chapter 2.

Unfortunately, after the first phase of calendar aging, we observed a derivation of the potential of reference electrodes in the two additional instrumented cells. As a result, it was not possible to obtain the evolution of individual electrode potentials with aging.

Nevertheless, both additional cells (KOK56 and KOK57) were submitted to calendar aging at 60 °C and at 100 % of SOC with particular CUs performed at 25 °C every ten days. It has been possible to exploit charge / discharge measurements in order to well evaluate the impact of checkups C-rates on IC curves.

	Residual DCH	Rest	CHA/DCH Cycles	Rest	CHA	Rest	DCH	Rest	CHA
KOK56	C/2	30 min		30 min	C/25	30 min	C/25	30 min	C/15
KOK57			10 at 1C						1C

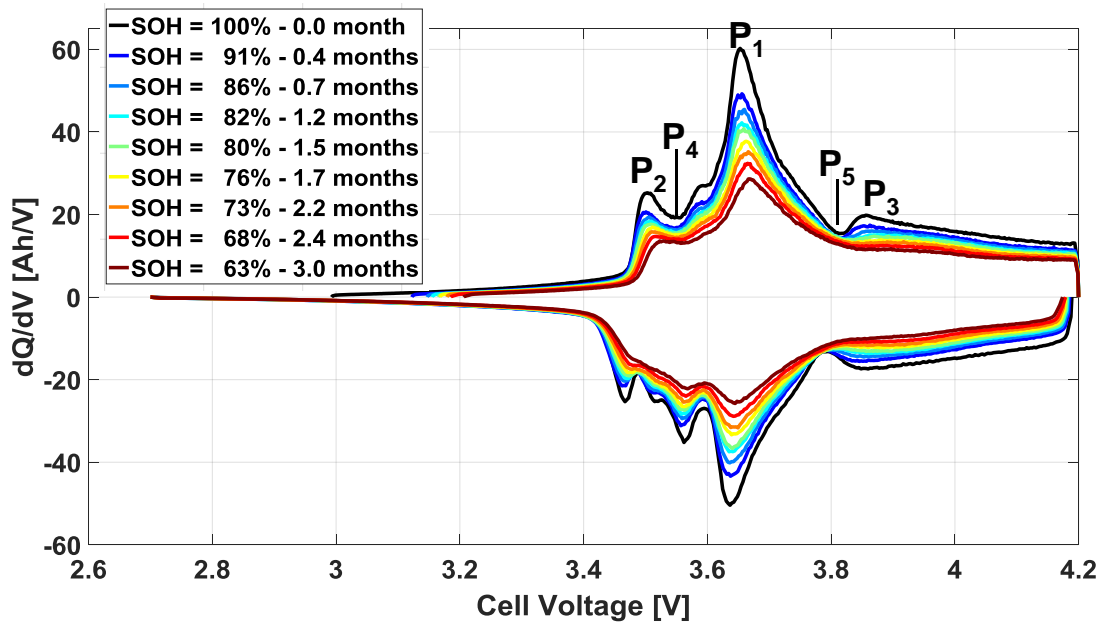
Table V-4 : Protocol of CU for additional commercial KOK56 and KOK57.

The CU of KOK56 consisted in a residual discharge performed at C / 2 followed by one charge / discharge cycle performed at C / 25. At the end, the setting to 100 % of SOC is carried out at C / 15. A rest of 30 min is included between each phase.

The use of the charge low C-rates of C / 25 and C / 15 is necessary to avoid metallic Li depositions that could be formed in the border of dry zones on graphite electrode after biphenyl polymerization.

For the CU of KOK57, 10 charge / discharge cycles at 1 C were added between the residual discharge at C / 2 and the charge / discharge cycle at C / 25. Besides, the protocol ends with a charge set a rate of 1 C with a constant voltage phase until the current drops to C / 20. The purpose here was to evaluate the incidence of 1 C on metallic Li deposition.

KOK56 : T = 60°C / SOC = 100% Periodic Cus without cycles at 1C



KOK 57 : T = 60°C / SOC = 100% Periodic Cus including cycles at 1C

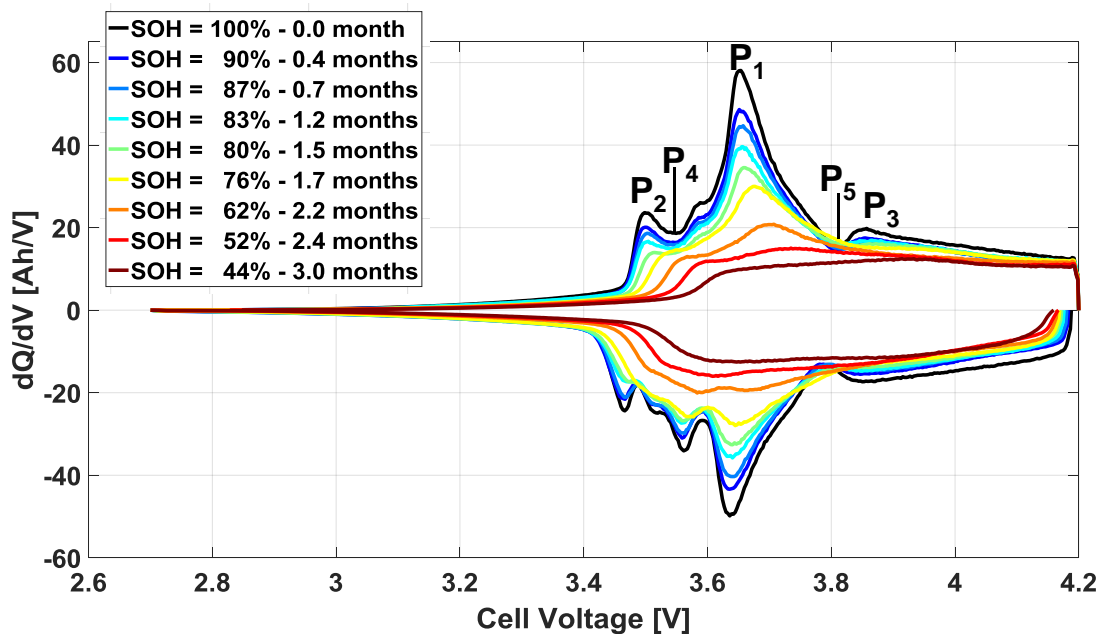


Figure V-24 : Comparison between the evolution of IC curves with aging between KOK56 and KOK57.

It worth mentioning on **Figure V-24** that the evolution of IC curves obtained from KOK56 (with C / 25 as maximum C-rate) present a signature that corresponds to the LAM on both electrodes degradation mode (here due to the formation of dry areas), showing a vertical decrease of all the peaks until the disappearance of **P₃** and **P₅**.

The effects of the SEI growth (LLI mode) seems to appear at 86 % of SOH showing a small “shifting” effect to the right. Note that here, the SOH is calculated based on charged capacities obtained at a rate of C / 25.

In contrary, the evolution of IC curves of KOK57 presents a quite different signature. A vertical decrease of all the peaks is noticeable from 100 % to 80 % of SOH (LAM on both electrodes: dry areas). In this range, a small shift of peaks related to the SEI growth (LLI mode) starts at 87 % of SOH.

However, at lower SOH (i.e. SOH < 76 %), a considerable shift of all the peaks towards higher voltages, in particular that of the **P₁**, **P₂** and **P₄** is observed. Moreover, the disappearance of all the peaks except for **P₂** is clearly pointed out with the acceleration of aging. In fact, for a SOH lower than 76 %, an additional mechanism to dry areas is involved and then the SOH drops very quickly compared to KOK56.

Based on results discussed in the Chapter 4, it may be assumed that the use of the C-rate of 1 C during CUs at 25 °C has led to local metallic Li depositions in KOK57 around the high resistive areas formed on graphite electrodes.

The scenario of electrodes shifts corresponding to metallic Li depositions is few described in the literature. However, in recent paper of Dubarry's group [204], the authors demonstrated that lithium plating was induced by a loss of delithiated negative electrode active material (LAM_{deNE}) in a graphite / LFP cell. Indeed, the shrinkage of the NE will lead it to be fully lithiated well before the PE becomes delithiated. As a result, the remaining Li cations in the PE, which could not be inserted in the NE, will be deposited at the NE surface. Besides, irreversible lithium plating might cause additional degradation such as progressive SEI growth (LLI mode) which accelerate aging.

On the basis of this remark, we therefore consider metallic Li depositions, in the case of the “dead Li”, as a mechanism caused by a LAM on the NE. In addition, as illustrated in **Figure V-24** for KOK57, below 76 % of SOH, the significant decrease and shift of **P₁**, **P₂** and **P₄** towards higher voltages (attributed to local metallic Li depositions) is characteristic of LAM on the NE degradation mode (see in **Table V-3**).

In the following sections, we present the comparison between the evolution of experimental measurements (U vs Q and $\Delta Q/\Delta U$ vs U) with aging to simulated ones. Starting from measurements of potentials of each electrode obtained at the BOL (at 25 °C and at C / 25) from the cell successfully instrumented with reference electrode (cell #4 see in **Table III-3** in Chapter 3), we apply an electrode shift according to the corresponding degradation mode(s). Note that only charge measurements were performed with that cell at the rate of C / 25. Therefore, for each condition, electrodes shifts are performed considering the capacity loss that is experimentally measured. Since there is no notable loss of capacity (less than 5 %) in calendar aging at 5 °C and 25 °C, we will only present results for temperatures ranging from 45 °C to 60 °C for different SOCs.

5.3.3.1. Aging mechanism: SEI growth

We consider in this section all the conditions under which only the SEI is determined to be the aging mechanism responsible for the loss of capacity.

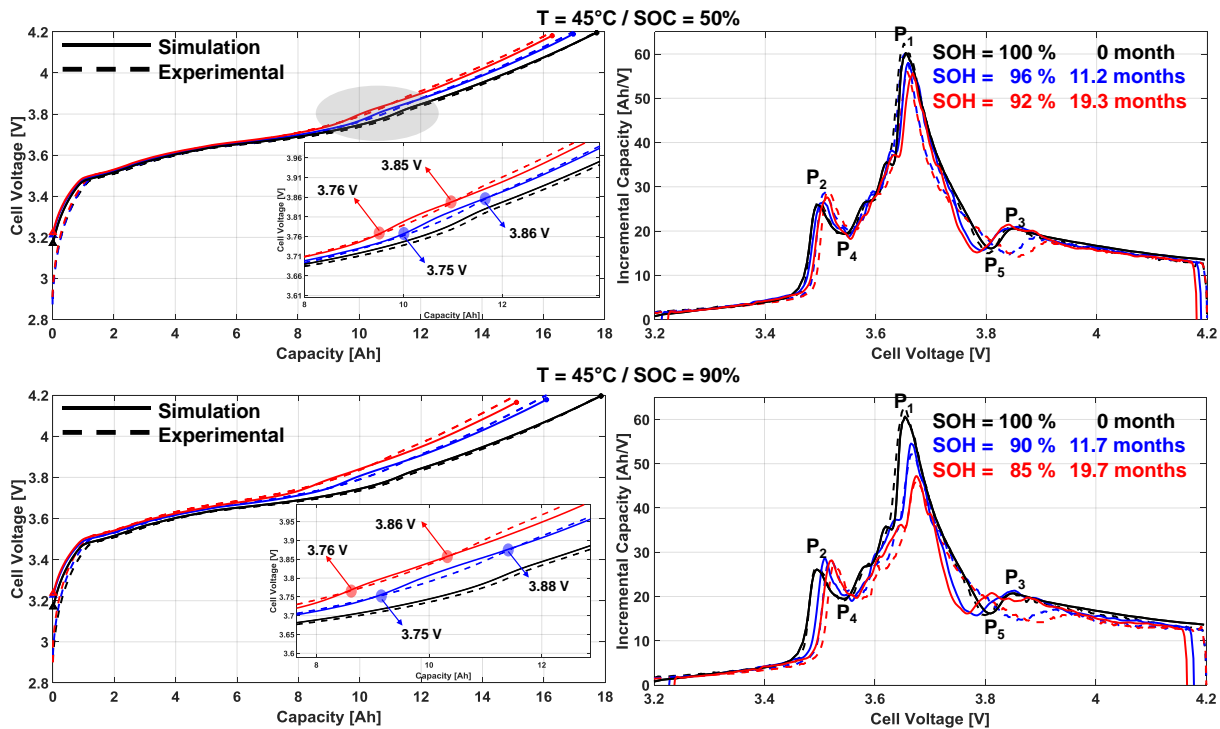


Figure V-25 : Comparison between experimental and simulations measurements corresponding to the case of the SEI growth at 45 °C.

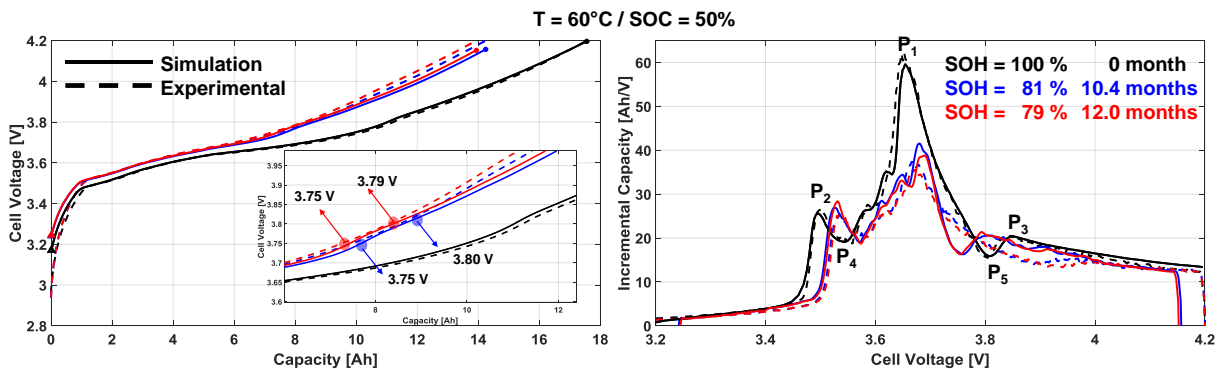


Figure V-26 : Comparison between experimental and simulations measurements corresponding to the case of the growth of the SEI at 60 °C.

At 45 °C (**Figure V-25**) as well as at 60 °C (**Figure V-26**), there is a fairly good correspondence between experimental and simulated measurements of cell voltage and IC curves. However, the evolution with aging of **P₃** and **P₅** from simulation seems to present a different trend compared to that of experimental data. Two assumptions were proposed above to explain this behavior [5.3.2]. A supplementary explanation can be added here by considering the shoulder between 3.75 V and 3.88 V only on simulated cell voltage curves (after capacity loss). Consequently, when these voltage curves are derived, the peaks **P₃** and **P₅** corresponding to these variations clearly appear.

5.3.3.2. Aging mechanisms: SEI growth and dry areas

We aim to simulate an aging situation where the LLI by the SEI growth and the LAM (here caused by dry areas) are both aging mechanisms involved. For this purpose, it is essential to quantify the contribution of each aging mechanism in the total measured capacity loss in order to apply the offset attributed to the corresponding degradation mode.

It may be proposed to estimate the contribution of the LLI as the capacity loss necessary to obtain a shift of P_2 until its abscissa fit the experimental one. The remaining contribution is therefore allocated to the LAM.

The choice of fixing first P_2 is supported by the fact that it is the only peak (P_3 and P_5 cannot be considered based on reasons mentioned above) correctly shifting without any reduction of its intensity in the LLI mode.

This methodology can also be done in the opposite direction, that means firstly by determining the contribution of the LAM which corresponds to the capacity loss necessary to obtain a vertically diminution of P_2 to fit experimental data.

The condition of storage at 60 °C and at 100 % of SOC during 4 months without checkups allows to observe both SEI growth and the LAM on both electrodes as the aging mechanisms involved. **Figure V-27** shows that both methodologies (LLI then LAM or LAM then LLI) lead to the same result.

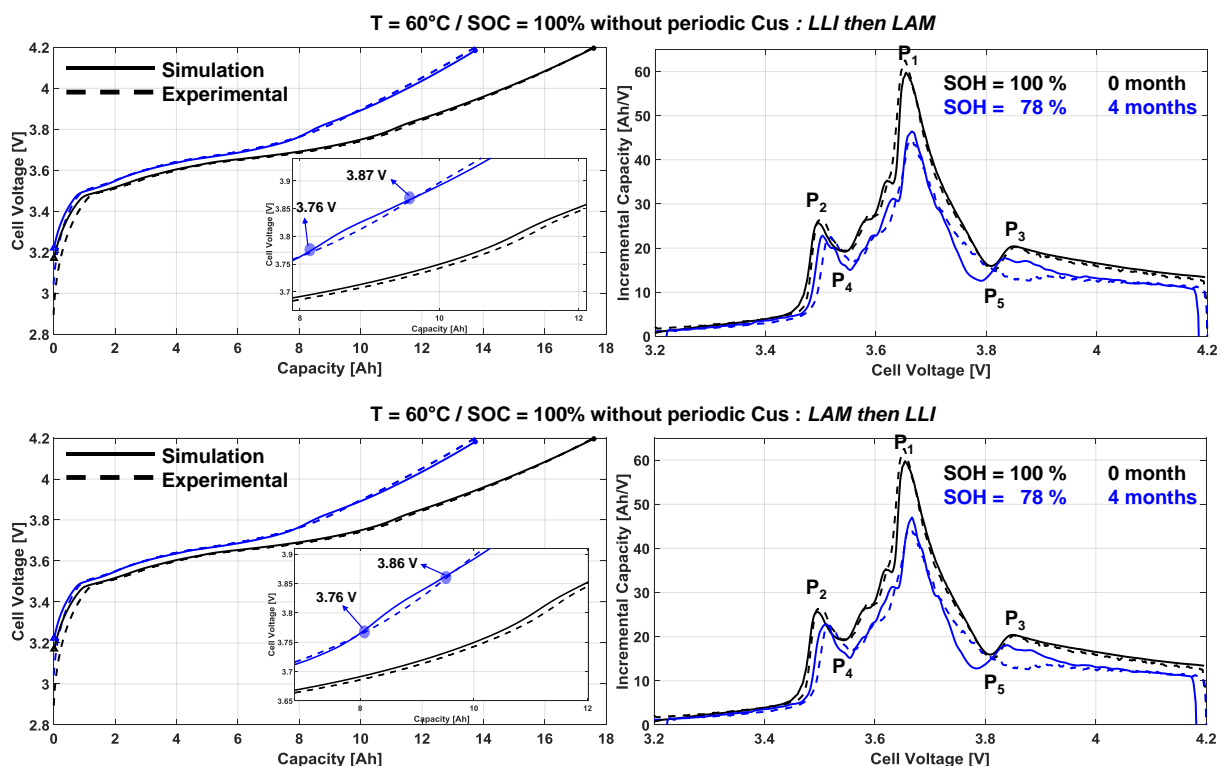


Figure V-27 : Comparison between experimental and simulations measurements corresponding to the case of the growth of the SEI and the LAM at 60 °C.

The simulation still struggles to follow the evolution of the peaks P_3 and P_5 because of the shoulder visible on voltages curves. Nevertheless, there is a good agreement between the simulations and experimental data.

5.3.3.3. Aging mechanisms: SEI growth, dry areas and local Li depositions

Metallic Li depositions were found on graphite electrodes in the border of dry zones created by biphenyl polymerization during storage at 45 °C (100 % of SOC) and at 60 °C (100 % of SOC). As explained above, we have considered metallic Li depositions as a mechanism caused by the LAM on the NE.

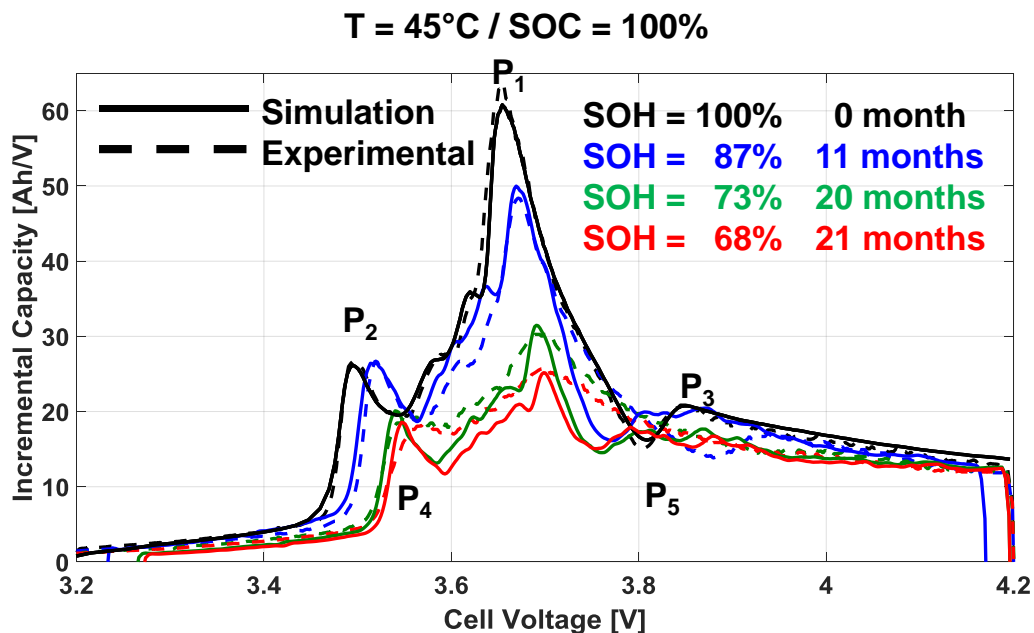


Figure V-28 : Comparison between experimental and simulations measurements corresponding to the case of the growth of the SEI, the LAM and Li plating at 45 °C.

Figure V-28 shows a shift of P_2 and P_4 towards higher voltages without any decrease of its intensity between 100 % and 87 % of SOH. In that same range of SOH, P_1 decreases while tending to the right. This signature is characteristic of the LLI degradation mode where the move of P_2 and P_4 are handled by the NE. This means that during the first 11 months of storage at 45 °C at 100 % of SOC, the SEI growth has been the main aging mechanism

The decrease of P_2 and P_4 with a significant shift towards higher voltages starts 9 months later at 73 % of SOH. This suggests the combined effects of the SEI growth, the LAM on both electrodes due to biphenyl polymerization and local metallic Li depositions.

However, the evolution of P_3 and P_5 are rather different from the experimental ones. In summary, this result shows that the biphenyl polymerization effects are activated beyond 11 months of storage at 45 °C and at 100 % of SOC.

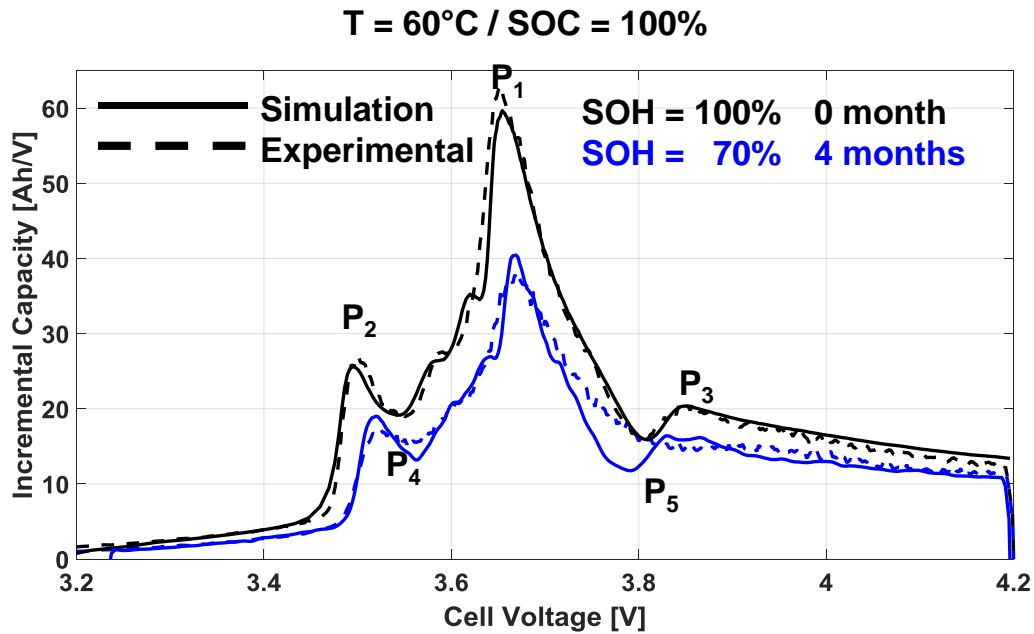


Figure V-29 : Comparison between experimental and simulations measurements corresponding to the case of SEI growth, the LAM and local metallic Li depositions at 60 °C and for 100 % of SOC.

At 60 °C and for 100 % of SOC (see in **Figure V-30**), there is a good match between the simulation and the experimental measurements. All the three mechanisms are involved in the capacity fade as illustrated by visual inspections (see in **Figure IV-2**).

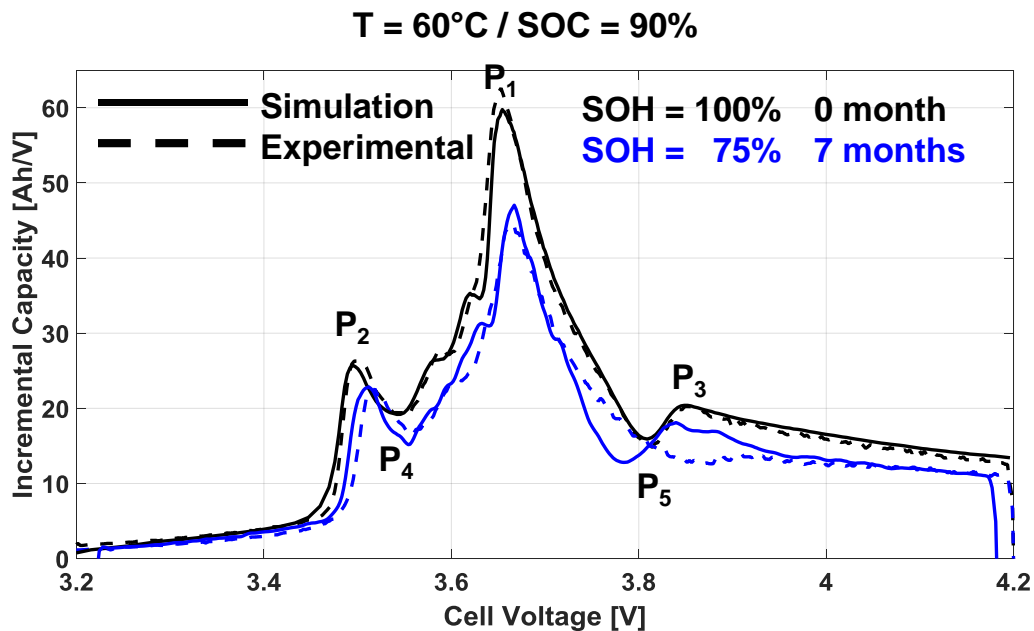


Figure V-30 : Comparison between experimental and simulations measurements corresponding to the case of SEI growth, the LAM and local metallic Li depositions at 60 °C and for 90 % of SOC.

Note that no cell stored at 60 °C and at 90 % of SOC was opened for post-mortem investigations. However, the evolution of IC curves (see in **Figure V-30**), showing a decrease of all the peaks and a shift of **P₂** and **P₄** towards higher voltages, indicates that the LAM on both electrodes (dry areas) is also involved in the capacity fade in addition to the SEI growth. Moreover, as CUs included the rates of 1 C, local metallic Li depositions was also considered in the simulation as an additional LAM on the NE.

Indeed, by considering only the SEI growth as the only aging mechanism with this condition (60 °C / 100 % of SOC), there would be no decrease of **P₂** and **P₄**. Therefore, it would not have been possible to fit well with the experimental IC curve.

5.4. Conclusions

This chapter addressed aging modeling of commercial 16 Ah C/NMC Li-ion cells, studied in this thesis. On one hand, a semi-empirical aging model based on the evolution of capacity has been implemented taking into account aging mechanisms discussed in the previous chapter. On the other hand, a diagnostic aging model on the basis of electrodes potentials shifts has been developed in order to identify degradation mode using the signature of incremental capacity curves.

The semi-empirical model is a combination of calendar and pure cycling models. The calendar aging model is itself based on differential equations expressing both SEI growth and dry areas mechanisms. The SEI growth has been identified as the main aging mechanism in calendar life according to the literature. The equation expressing the capacity loss caused by this parasite reaction has been determined using the approach proposed by Broussely.

In addition, the physical law associated to the apparition of dry areas on both electrodes, driven by biphenyl polymerization, has been established by analogy with Broussely's method.

Otherwise, the pure cycling aging model only relates to the capacity throughput induced by repeated charge / discharge cycles. In this case, simulated cycling profiles has been conceived considering parameters experimentally measured (cell skin temperature in charge as in discharge, SOC thresholds at the end-of-charge with constant current as well as at end-of-charge with constant voltage).

In general, the model has shown a satisfactory agreement compared to calendar as well as cycling experimental measurements. In addition, this model allow to estimate the contribution of each aging mechanism involved.

In calendar aging, it appeared that the SEI growth was the main aging mechanism compared to the loss of active surface, according to the model estimations. In cycling, it resulted rather that the loss caused purely by the effect of repeated cycles was dominant. It should be noted that this aging model can be used for the prediction of the Li-ion cell lifetime. It just requires input temperature, SOC and current profiles to estimate the capacity loss for a given duration.

The prognostic aging model based on electrodes potentials shifts supports the principle that the evolution of incremental capacity curves presents a signature specific to a given degradation mode. Four main types of degradation modes have been distinguished according to the literature and mechanisms discussed in this work: LLI, LAM on the NE, LAM on the PE and LAM on both electrodes.

This diagnostic tool was developed based on electrode potentials measurements obtained in charge at a rate of C / 25 with the commercial cell successfully instrumented with a Li metal as reference electrode.

The incremental capacity curves are characterized by distinctive peaks of graphite convoluted with NMC electrode. Consequently, the displacement of two peaks (P_2 and P_4) was attributed to the NE while that of P_3 and P_5 was rather associated with the PE. However, it was not simple to relate those peaks with the corresponding plateaus of graphite neither the NMC phase transformation.

On the basis of the signature of incremental capacity curves, it was not able to identify the degradation mode in the condition of fully cycling at 5 °C. On the contrary, the LLI was identified as the degradation mode in the condition of cycling at 5 ° C with a constricted SOC range.

According to the simulations, the apparition of dry areas observed in calendar aging at high temperature and at high SOC matched with the LAM on both electrodes, showing a vertical decrease of all the peaks. In addition, local metallic Li depositions found in the border of these high resistive zones rather matched with a LAM on the NE leading to capacity loss. This consideration was supported by a recent research work.

It can be concluded that incremental capacity curves can really be used as a diagnostic tool to identify the aging mechanisms that cause capacity losses. It is therefore a qualitative approach to be used in complementary to the aging model in order to distinguish aging conditions leading to LLI and / or LAM.

Conclusions and perspectives

The main objectives of this PhD thesis work was to consolidate new knowledge on aging mechanisms prone to reduce the performance of commercial Li-ion batteries under normal conditions, to develop aging models taking into account these mechanisms and to propose a diagnostic tool for their identification, which may be complementary to post-mortem investigations.

Predominant aging mechanisms, namely SEI growth, metallic lithium depositions on graphite electrode as well as pore clogging and degradation of active material, have been detailed in the first chapter, on the basis of a bibliographic study. In the battery field, post-mortem techniques, the use of reference electrodes and the incremental capacity analysis, have been identified as the most required methods for investigating these mechanisms.

The second chapter was devoted to the description of all the experimental protocols. The chosen battery technology was the commercial high power Graphite/NMC Li-ion polymer pouch cell with a nominal capacity of 16 Ah. The introduction of the reference electrodes into a commercial Li-ion cell has been successfully undertaken. It was then possible to perform electrochemical tests at different temperatures and different C-rates in order to validate the correct functioning of the instrumented cells. Data obtained at the beginning of life at 25 °C were used in the calibration of the two-electrode prognostic aging model. Moreover, this latest experiment also allowed to follow up the evolution of the potentials of each electrode during cycling at 5 °C, as discussed in the third Chapter.

The protocol for the disassembly of cells as well as electrochemical characterizations of reassembled electrodes with coin cells was then described. The different physico-chemical methods required for this work have been featured into categories as following: electrolyte analysis (GC-MS), microscopy analysis (SEM and MET), chemical methods sensitive to electrode surface (EDX and XPS) and chemical methods sensitive to the bulk (^7Li NMR, XRD and FIB/ToF-SIMS).

Results obtained from cycling aging have been exploited in the third chapter. The cycling condition at 5 °C between 0 and 100 % of SOC presented more interesting features to investigate given that a rapid capacity fade, around 75 %, was observed in less than 100 cycles. This behavior was also reproducible with the commercial instrumented cells. In addition, the internal resistance of the cell, measured at 25 °C and at 40 % of SOC with pulses measurements, has increased of about 400 %. Visual inspections, after cells were dismantled at a discharged state, showed that all the 24 bifacial graphite electrodes remained unexpectedly lithiated,

exhibiting a brown color. The analysis of the electrolyte with GC-MS leads to the detection of many electrolyte degradation products caused by a considerable solvents decomposition.

Measurements obtained from the instrumented cells showed that during cycling, the potential of graphite electrode went only below 0 V vs. Li^+/Li over the last 6 cycles. Moreover, they demonstrated that it was difficult to extract more lithium cations from graphite in order to be inserted to the NMC electrode. Furthermore, electrochemical measurements with coin half-cells based on harvested electrodes showed that Li was trapped into graphite electrode while the harvested NMC electrode did not loss at all its capacity of insertion. This result was then confirmed by XRD measurements where the concurrent presence of intercalation compounds (LiC_6 , LiC_{12} and LiC_{24}) was astoundingly found into the aged graphite.

It appeared clearly that only the negative electrode was involved in the loss of capacity, and Li de/re-intercalation mechanisms were then obstructed into the graphite electrode due to the accumulation of electrolyte degradation products into its porosity. These results were consistent with the interpretation from FIB/ToF-SIMS suggesting that Li was trapped in the regions corresponding to the cavities between or within graphite particles. Species such as C-O bonding groups; Li_2O ; Li carbonates; PVDF, LiPF_6 and its degradation products were identified by XPS as the elements constituting the thick layer impeding the graphite electrode porosity. Consequently, as the entrance of Li ions into pores of graphite electrodes were hindered by the growing of the layer made of electrolyte degradation products, metallic Li depositions occurred on the surface of the anode due to the high polarization. This approach was also supported by ^7Li NMR results where metallic Li was detected with a lower peak compared to Li in graphite planes and Li in oxidized forms.

Contrary to the general conclusions commonly encountered in the literature about charging at low temperature, metallic Li depositions do not appear here as the main mechanism, but rather as a parasitic surface reaction resulting from the loss of Li ions pathways in the graphite electrode.

Perspectives regarding this first section:

Based on the results from this study, it may be considered that the porosity as well as the thickness and the particles sizes of graphite, are the three parameters to investigate in order to improve Li cations transport through this electrode at low temperatures.

According to the literature, the hindrance of Li ions transport in the electrode pores may also be induced by Li ions depletion in these pores at high current rates, caused by the limitation of Li ions diffusion in these pores.

Furthermore, it is presumed that the diffusion pathways for Li ions are shorter for thinner electrodes and smaller graphite particles. When a more porous negative electrode is considered, pores should normally remain open to Li cations transport since electrolyte reduced products cannot accumulate into these pores.

In this study, the thickness of one sheet of both electrodes was estimated at 110 μm . The influence of the thickness was not an objective of this work, so that thickness as well as measurements of particles size or porosity were not performed. It should be pointed out that the thickness of the electrodes defines the typology of the cells.

For example, typically power-typed batteries present electrodes less thick than energy-typed cells. The influence of these parameters (thickness, particles sizes and porosity) on aging mechanisms at low temperature remains unknown, so that it may be the subject of future research works.

Still in order to generate new knowledge about the aging mechanisms of Li-ion batteries, investigations were performed on cells aged in calendar life. Unexpected localized metallic Li depositions were found on the surface of graphite electrodes of cells stored at high temperature and SOC, although these cells were disassembled in discharged state. Contrary to the cycling at low temperature, in this case, it was determined by GC-MS that the polymerization of biphenyl used at 7 % wt in the electrolyte in combination with periodic checkups, were at the origin of the apparition of these deposits. Indeed, biphenyl is a shutdown aromatic compound used as an overcharge protection agent. It was determined that the polymerization of biphenyl occurred at lower potentials when the temperature increased. For example, at 45 °C, its polymerization occurred when the potential of the positive electrode reaches 4.27 V vs Li/Li⁺ (without overcharge). This latest polymerization potential corresponds to a SOC of 100 % at the cell level. The progressive formation of gas bubbles caused by biphenyl polymerization results in contacts disconnection between the electrodes and the separator. The dry areas created are then very resistive to Li ions transport. Consequently, during checkups performed at 25 °C, metallic Li is then deposited on the border of these dry areas due to the local high current densities and the resulting local more negative potential vs. Li/Li⁺.

According to the literature, the capacity loss in calendar life is attributed to the SEI growth. However, this study demonstrated that the contribution of the loss of active surface, caused by biphenyl polymerization, needs also to be integrated in the capacity fade during storage. Moreover, although it remains a mechanism not inherent to calendar aging, metallic Li also has its part, especially at 60 °C where it is seen covering all the graphite surface.

This protocol is quite similar to the use of Li-ion cells in electric vehicles, combining long rest time and regular charge / discharge phases. This is an alarm for the electric vehicle field: batteries need to be tested using similar protocols in order to reflect real operating conditions.

Perspectives regarding this second section:

It was found that protective agents used in the electrolyte might induce unexpected aging mechanisms prone to accelerate capacity fading. Research could be directed towards the development of electrolyte protective additives whose decomposition at high voltage (necessary to avoid overcharge) would be accompanied by another system to make the cell inoperative, rather than by gas production. In addition, these materials should exhibit tolerable sensitivity at elevated temperatures. This remains a big challenge to deal with.

It was able to propose satisfactory equations expressing capacity losses caused by the aging mechanisms discussed in this work and to develop an associated semi-empirical aging model. The calendar aging model was based on the SEI growth and the dry areas mechanisms while that of cycling only related to capacity throughput. The combination of both calendar and cycling models constituted the complete aging model for the 16 Ah commercial Li-ion cell. Suitable agreement was obtained between the model and experimental data. However, it was shown that cycling conditions including charging until 4.2 V induced an additional aging mechanism which was not considered in the model.

In parallel, a diagnostic aging model based on electrodes potentials shifts has been developed in order to determine the associated degradation mode(s) using the signature of incremental capacity curves. This prognostic model was developed by shifting electrodes potentials obtained in charge at a rate of C / 25 from one commercial instrumented cell.

The LLI was identified as the degradation mode in the condition of cycling at 5 ° C between 3.42 V and 4.08 V while in the condition of fully cycling, it was not able to attribute a degradation mode because of the total disappearance of all the peaks.

The apparition of dry areas observed in storage at high temperature and SOC was attributed to the LAM on both electrodes, leading to a vertical decrease of all the peaks.

This diagnostic tool appeared useful for the identification of degradation mode in Li-ion batteries, to be used in complementary to post-mortem analyses and to the aging model. However, it is not yet finalized to make quantitative measurements of each aging mode contribution.

Perspectives regarding this last section:

It would be interesting to develop a physics-based Li-ion battery aging model accounting for the SEI growth, the evolution dry areas and also the pore clogging observed in the graphite electrode. In this study, this latter mechanism was observed at low temperature leading to a rapid and considerable capacity fade. In the

literature, it is often reported to be observed after prolonged cycles at high temperatures, by the end-of life. Nevertheless, it remains a challenge to propose a suitable and satisfying equation to express this mechanism.

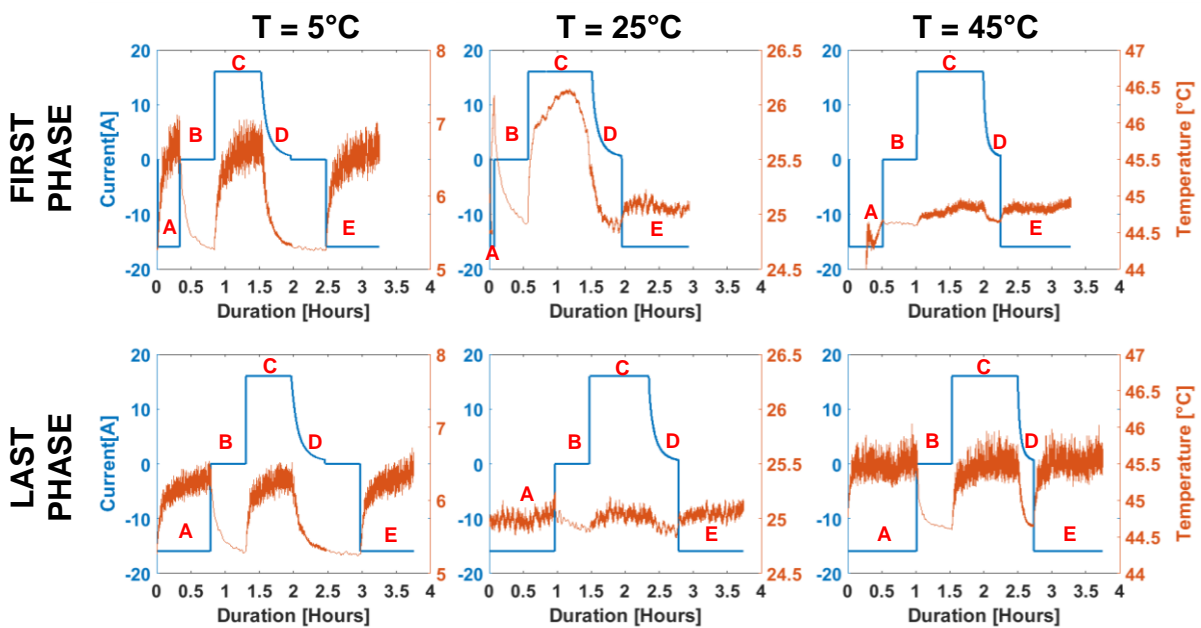
It would still be very useful to automate the incremental capacity tool, so that it is directly integrated into the aging model loop. This would make it possible to build a more robust aging model.

Appendix

Appendix of the Chapter 2

Thermal behavior of the instrumented cell between the first and the last charge at the rate of 1 C

The thermal behavior of the cell during the first and the last phase of the electrochemical test performed respectively at 25 °C, 45 °C and 5 °C is presented in the Figure below.



A : Previous Discharge | B : Rest | C : Constant Current Charge at 1C | D : Constant Voltage Charge until C/20 | E : Next Discharge

Figure A: Comparison of thermal behavior during the first and the last phase (at 1 C / 1C) for all different temperatures.

Note that this is the temperature measured at the level of the skin of the cell using temperature sensors, so that the temperature inside should normally be higher.

The thermal behavior during the first and the last charge at 1 C are quite similar at 5 °C. This ascertainment could explain the similar behavior of electrodes potential curves between the first and the last charge performed at 1 C and at 5 °C as seen in **Figure II-8**.

By contrast, the thermal behavior presents a different signature when the first and the last charge (at 1 C) are considered, for both conditions of 25 °C and 45 °C. Nevertheless, the temperature increases remains quite small and lower than 1 °C.

Checkups sequences description

❖ A residual discharge at 1 C followed by two capability tests at 1 C (CC-CV and then C / 20)

The cell is completely discharged from its residual charge with a constant current (CC) applied at 16 A (1 C). Then, it is first recharged at constant current (CC) at a rate of 1 C until the maximum voltage of 4.2 V is reached and then at constant voltage (CV) until the current drops to 0.8 A (C / 20). This recharge is followed by a total discharge at constant current performed at 1 C until minimum voltage of 2.7 V, and then with at constant voltage until the current reaches the value of 0.8 A (C / 20). This capacity test carried out at CC-CV mode and then C / 20 is repeated once before the last recharge under the same conditions. These cycles are used to determine the actual capacity of the cell after recharge. The capacity value measured at the end of the second discharge is considered to be the "reference capacity" in order to measure the loss of relative capacity due to aging.

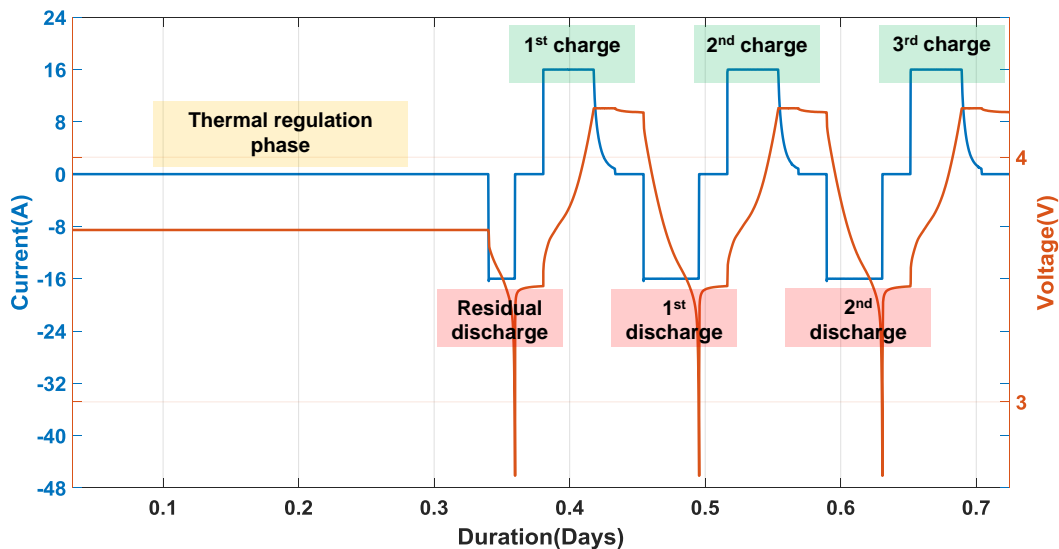


Figure B: Illustration of the sequence corresponding to the residual discharge and two tests of capacities performed at 1C.

❖ Dynamic Stress Test (DST)

Dynamic Stress Test (DST) is a discharge power test profile as presented in **Figure C**. It is an American standard cycles test modeled on the functioning of the Renault ZOE electric vehicle in order to simulate driving conditions and serve as a basis for comparison. The discharge profile is repeated until the battery is fully discharged. The DST can be used, for example, to evaluate the performance of model-based algorithms for the estimation of the SOC of Li-ion batteries in electric vehicles [219; 220]. Other types of cycles tests such as New European Driving Cycle (NEDC), ARTEMIS (corresponding to the European Artemis project), FTP (Federal Test Procedure) can also be used to evaluate driving conditions, but only the DST has been implemented here.

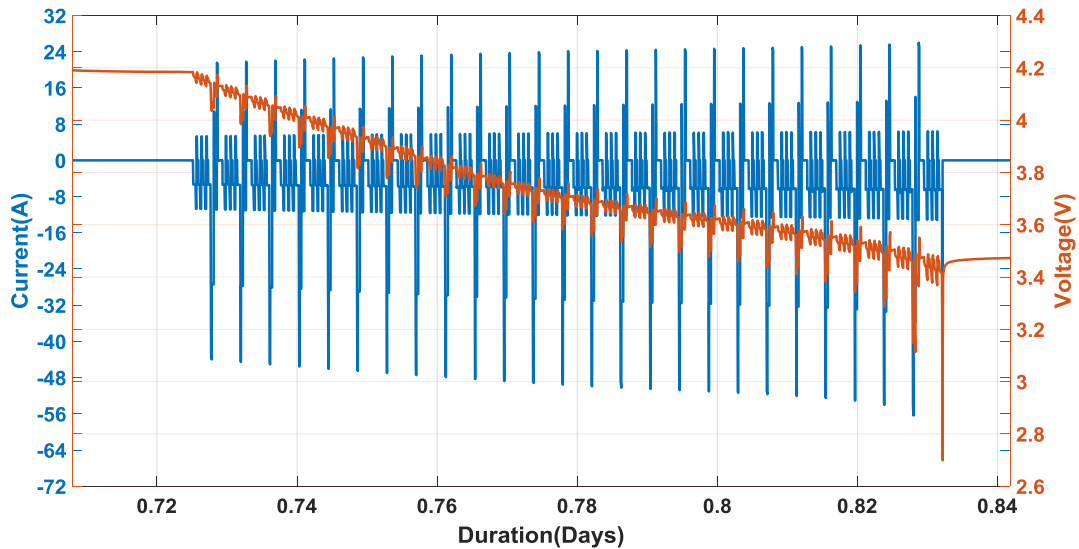


Figure C: Illustration of the sequence of Dynamic Stress Test (DST)

❖ Capacity tests at different C-rates

This sequence starts with a discharge performed at 0.64 A (C/25) followed by a charge/discharge cycle performed at the same rate. Then, the cell is subjected at different discharge current rates respectively performed at 3.2 A (C/5), 8 A (C/25), 32 A (2 C), 48 A (3 C) and 16 A (1 C).

Between each discharge phase, the cells is recharged at a rate of 1 C which is the maximum current charge rate used in this protocol.

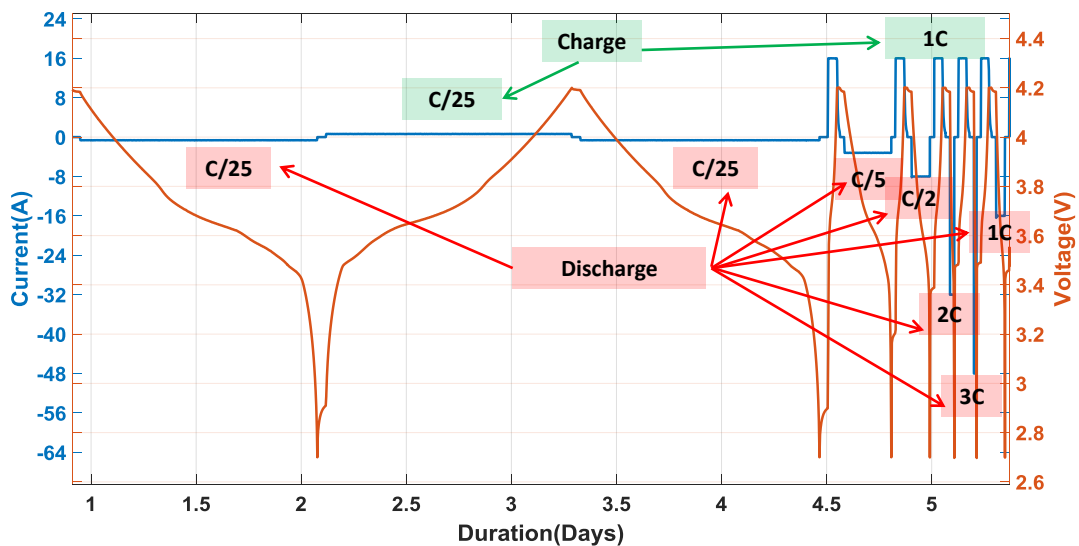


Figure D: Illustration of the sequence of capacity tests performed at different discharge current rates

❖ Charge and discharge pulses sequence

The pulses sequence is used to simulate the acceleration or braking phases in the case of the electric vehicle and make it possible to calculate the direct current (DC) internal resistance (referring to the previous section [2.2.3.2] in which internal resistance of batteries by pulses measurements was shown) which is correlated to the available power.

Pulses with a duration of 30 s are implemented in charge as in discharge at rate of 1 C and performed respectively at 100 %, 95 %, 90 %, 80 %, 60 %, 40 %, 20 %, 10 %, 5 % of state of charge.

At the end of the protocol, the cell is fully recharged in to be subjected to the cycling aging or calendar aging protocol.

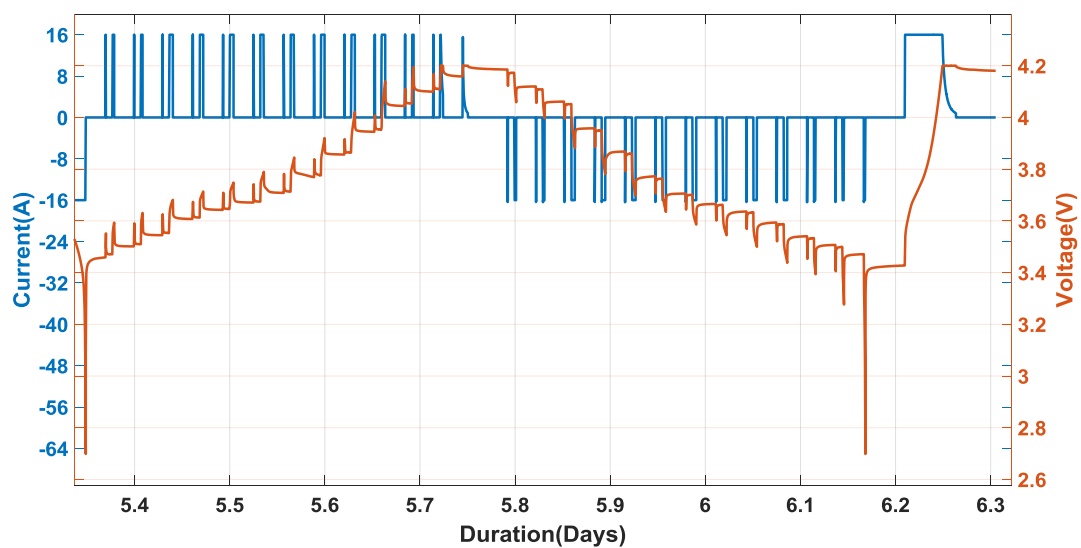


Figure E: Illustration of the sequence of pulses performed in charge as in discharge.

Appendix of the Chapter 3

Profiles of current, voltage and capacity evolution during cycling of commercial 16 Ah commercial Li-ion cells at 5 °C between 2.7 V and 4.2 V

The charge has been performed without a CV phase. For safety reasons, we have stopped the cycling test at the 38th cycle because the capacity was decreasing rapidly. The SOH based on measurements at 25 °C is 20.2 %. After the 2nd check-up at 25 °C, the cell #1 was stored in a climate chamber at 12 °C as backup.

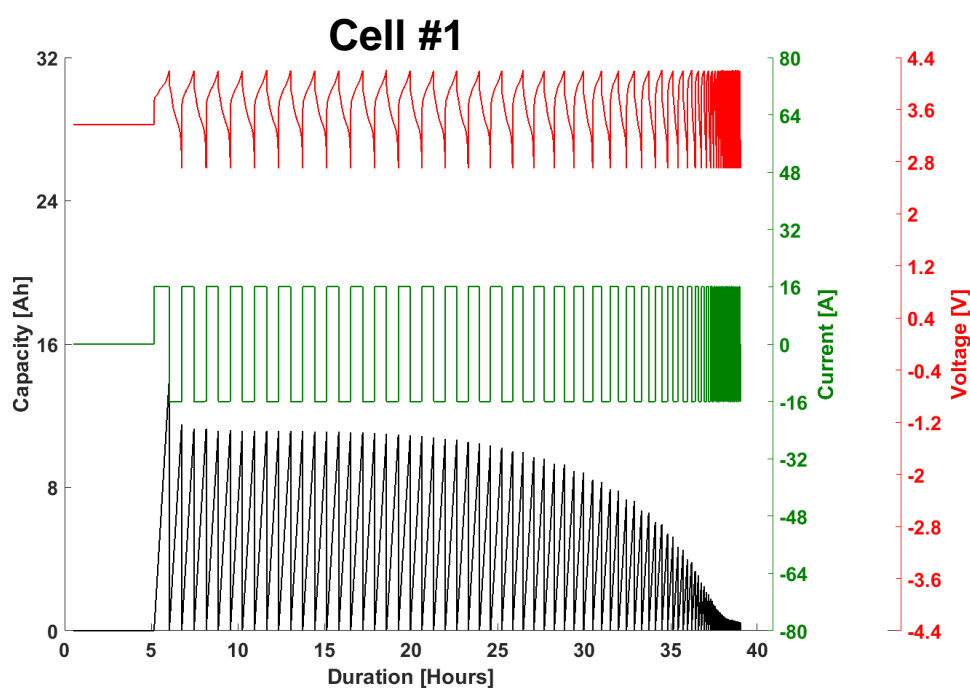


Figure F: Profiles of current, voltage and capacity evolution during cycling of the cell #1 at 5 °C between 2.7 V and 4.2 V.

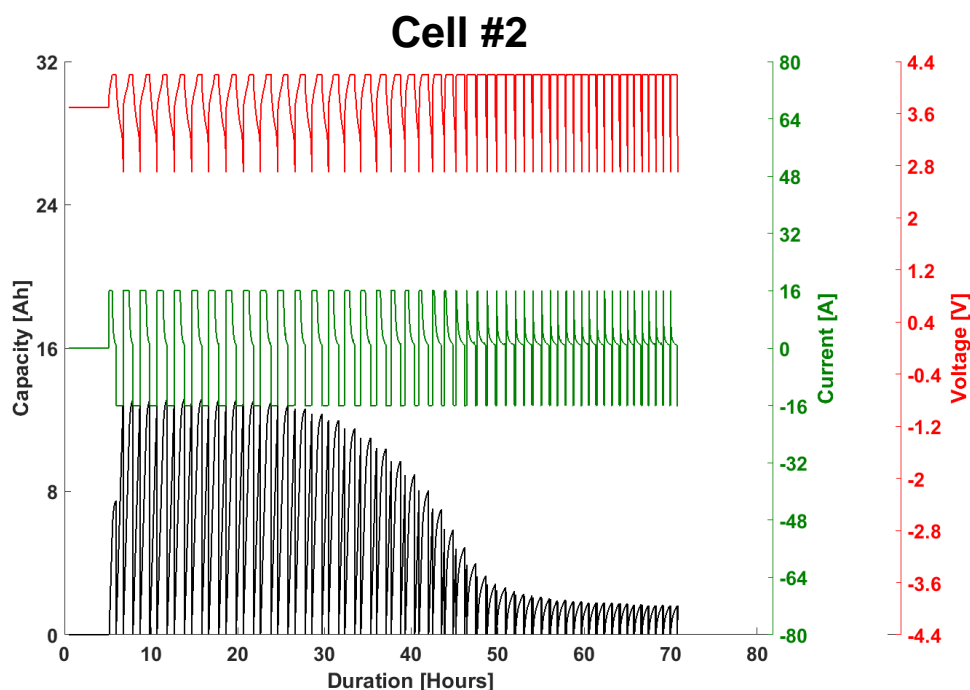


Figure G: Profiles of current, voltage and capacity evolution during cycling of the cell #2 at 5 °C between 2.7 V and 4.2 V.

The charge has been performed with a CV phase. In fact, based on the fast capacity fade observed with the previous cell (cell #1), it was believed that the absence of CV phase could be responsible of the fast capacity loss. 100 cycles were then programmed. We can see that as the number of cycles increases, the end-of-charge voltage is reached more rapidly. The cell is essentially being charged in CV mode. However, the same fast capacity fade was again observed with cell #2 although the charge was done with a CV phase. The SOH based on measurements at 25°C is 23.6 %. After the 2nd check-up at 25°C, the cell #2 has swollen in the climate chamber at 12°C. For safety reasons, it was thrown away.

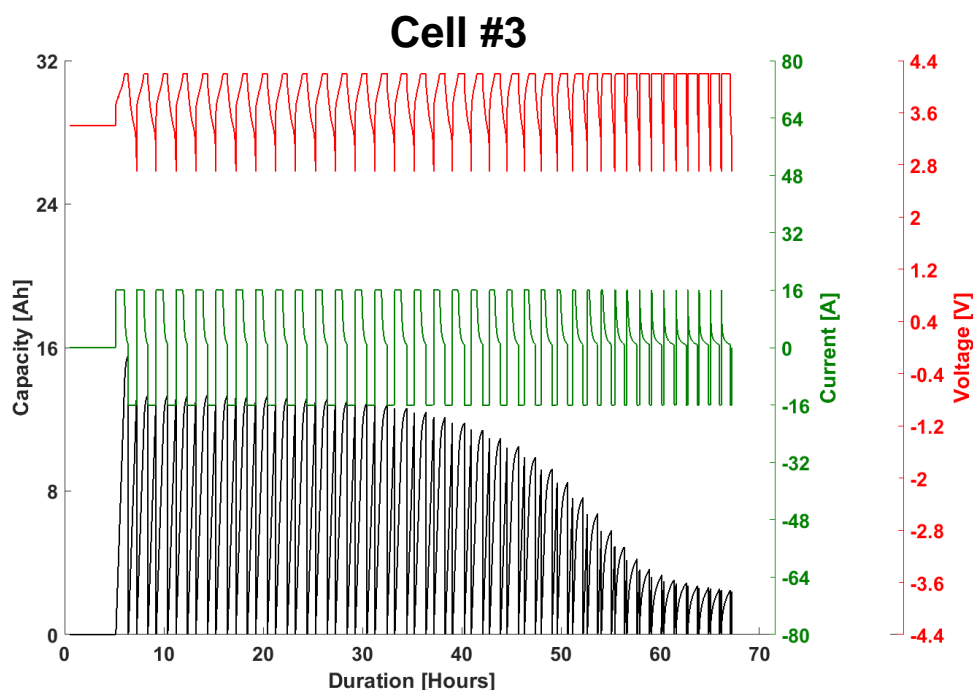


Figure H: Profiles of current, voltage and capacity evolution during cycling of the cell #3 at 5°C between 2.7 V and 4.2 V.

The charge has been performed with a CV phase. For safety reasons, we have stopped the cycling test at the 73th cycle. The SOH based on measurements at 25°C is 28.3 %. After the 2nd check-up at 25°C, the cell #3 was dismantled for post-mortem analyses.

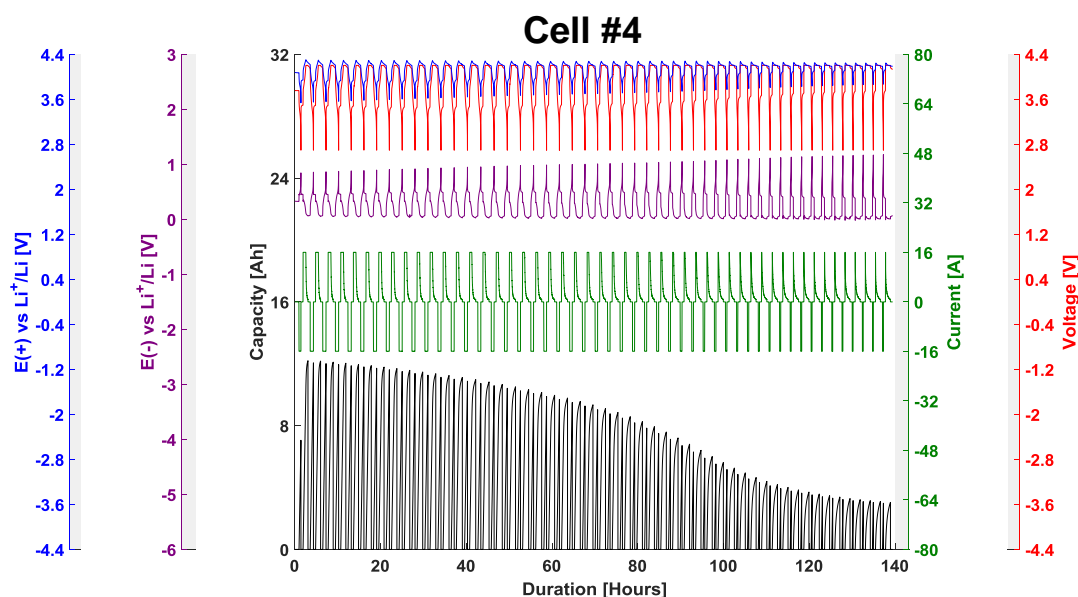


Figure I: Profiles of current, voltage and capacity evolution during cycling of the cell #4 at 5°C between 2.7 V and 4.2 V.

Appendix of the Chapter 4

Quantitative analyses of the electrolyte composition recovered from cells aged in calendar at 100 % of SOC

Content (%) of additive per time of storage in function of the sum of all detected carbonates					
Materials		With periodic checkups			Without periodic checkup
		Fresh	Cal @25°C	Cal @45°C	Cal @60°C
EMC + EC + other detected carbonates		100.00	100.00	100.00	100.00
VC		0.12	0.00	0.00	0.00
FEC		1.02	0.08	0.04	0.07
Biphenyl		12.28	1.34	0.64	2.55
1,3-PS		2.79	0.26	0.10	0.13
Content (%) of each component					
Type	Component	With periodic check-ups			Without periodic checkup
		Fresh	Cal @25°C	Cal @45°C	Cal @60°C
Solvents	EMC	53.52	49.20	46.45	53.52
	EC	32.53	32.53	32.53	21.66
Additives	VC	0.10	0.00	0.00	0.00
	FEC	0.88	0.62	0.34	0.21
	Biphenyl	10.57	9.98	5.23	7.84
	1,3-PS	2.40	1.95	0.84	0.40
Decomposition products	DMC	0.00	0.00	0.28	0.29
	DEC	0.00	0.00	1.14	0.88
	2-methoxycarbonyloxyethyl methyl carbonate	0.00	0.00	0.06	0.00
	2-ethoxycarbonyloxyethyl methyl carbonate	0.00	0.00	0.00	0.46
Gas and/or non detected material		0.00	5.73	13.13	14.74

Table A: Content (%) of each component of the electrolyte determined by GC-MS.

Post-mortem electrochemical measurements with Li metal/NMC coin half-cells

Post-mortem electrochemical measurements of harvested graphite and NMC electrodes recovered from commercial 16 Ah Li-ion cells aged at 25 °C, 45 °C and 60 °C respectively, were conducted with coin half cells. Four CR2032 NMC/Li metal coin half-cells are assembled in 1:1:1 wt EC:DMC:EMC + 1 M LiPF₆ electrolyte. Each of them contain harvested NMC electrodes from a fresh cell and cells aged at 100 % of SOC and at 25 °C, 45 °C and 60 °C, respectively. The protocol of NMC/Li metal coin half cells starts with a discharge step performed at a rate of 0.1 C which is a low C-rate. The aim is to delithiate those electrodes so that the residual capacity of each of the respective electrodes, after dismantling of the cell, can be determined. Thereafter, the capacity of these coin half cells is also measured at other different C-rates (0.1 C, 0.2 C, 0.5 C, 1 C and 2 C). No notable loss of capacity is observed for all these harvested NMC electrodes. The trend of initial state of lithiation is consistent with aging duration and temperature.

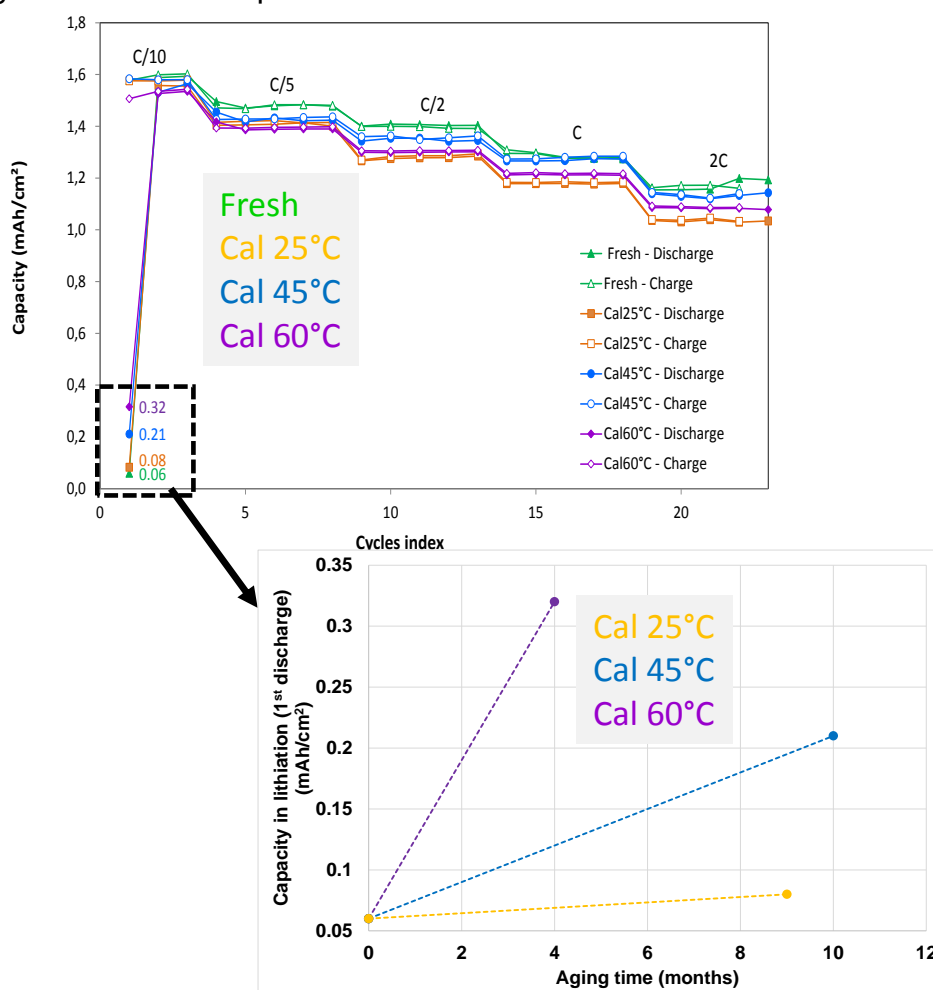
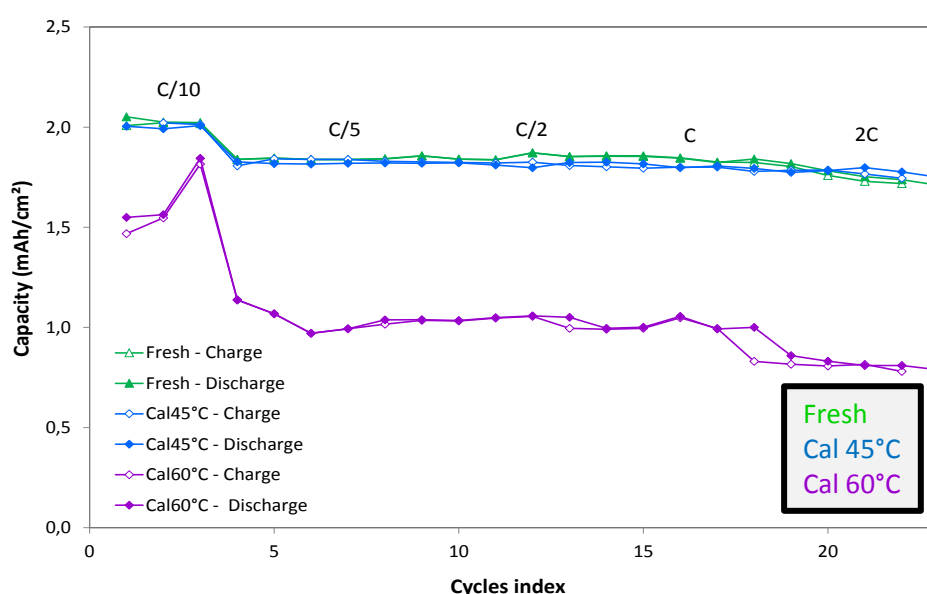


Figure J: Post-mortem electrochemical measurements with Li metal/NMC coin half cells based on harvested NMC electrodes recovered from a fresh commercial 16 Ah Li-ion and cells aged at 25 °C, 45 °C and 60 °C, respectively.

Post-mortem electrochemical measurements with Li metal/Graphite coin half-cells

Three CR2032 Graphite/Li metal coin half-cells are assembled in 1:1:1 wt EC:DMC:EMC + 1 M LiPF₆ electrolyte. Each of them is based on graphite electrodes from a fresh cell and cells aged at 100 % of SOC and at 45 °C and 60 °C, respectively. The protocol of Graphite/Li metal coin half cells starts with a charge step performed at a rate of 0.1 C which is a low C-rate. The aim is to delithiate those electrodes so that the residual capacity of each of the respective electrodes, after dismantling of the cell, can be determined. Thereafter, the capacity of these coin half cells is also measured at other different C-rates.

Electrodes recovered on areas without visible deposits



Impact of deposits on the capacity of the electrode (T=60°C)

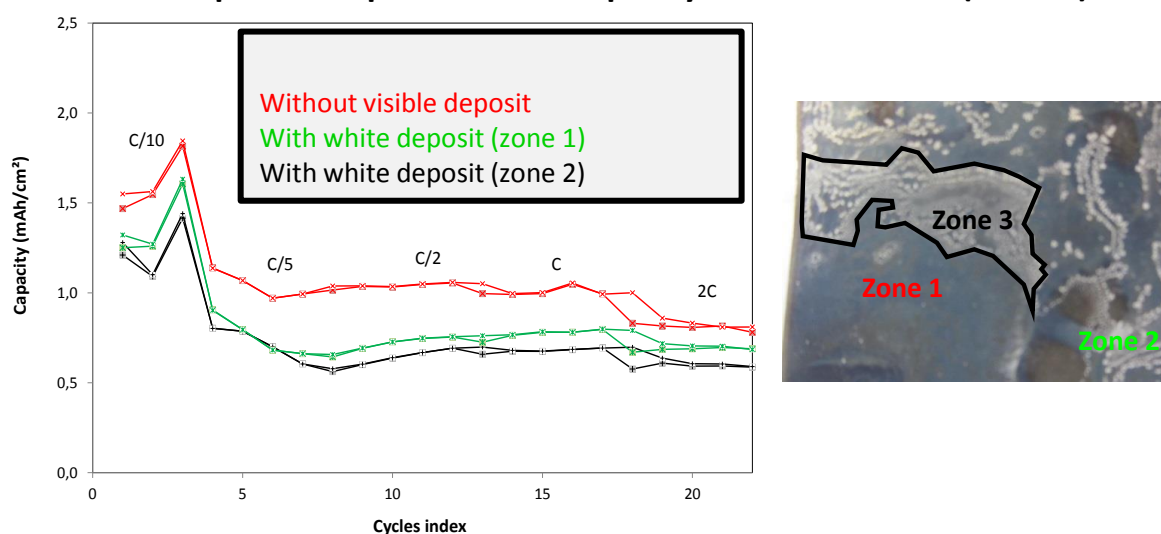


Figure K: Post-mortem electrochemical measurements with Li metal/graphite coin half cells based on harvested graphite electrodes recovered from a fresh commercial 16 Ah Li-ion cells and cells aged at 45°C and 60°C, respectively.

No loss of capacity is observed for the fresh electrode and even for the coin half-cell based on graphite electrode from the Li-ion cell aged at 45°C. Dramatic loss of capacity is observed on coin half-cell based on harvested graphite from the Li-ion cell aged at 60°C. The loss of capacity is higher where white deposits are found on the surface of electrode.

Appendix of the Chapter 5

Runge-Kutta Method

The Runge-Kutta methods (so called RK4) are algorithms used for numerically solving differential equations. They are based on iterative methods. In this work, the most popular algorithm of the Runge-Kutta methods, referred as the Fourth Order Runge-Kutta method (RK4), has been implemented in order to have finer approximate solutions of the semi-empirical model differential equations.

Let consider the following equations:

$$\begin{aligned} y' &= f(t, y) \\ y(t_0) &= y_0 \end{aligned} \quad (5.21)$$

In the equation above, y is the function of time t that needs to be approximate. The function y' depends of both y and t , it can be considered as the rate at which y varies.

The function f (considered as the model equation) and the data t_0 and y_0 are well known.

The RK4 method is given by the equation below:

$$y_{n+1} = y_n + \frac{h}{6}(k_1 + 2k_2 + 2k_3 + k_4) \quad (5.22)$$

Where

$$\begin{aligned} k_1 &= f(t_n, y_n) \\ k_2 &= f\left(t_n + \frac{h}{2}, y_n + \frac{h}{2}k_1\right) \\ k_3 &= f\left(t_n + \frac{h}{2}, y_n + \frac{h}{2}k_2\right) \\ k_4 &= f(t_n + h, y_n + hk_3) \end{aligned} \quad (5.23)$$

With

- k_1 represents the slope at the beginning of the interval.
- k_2 is the increment based on the slope at the midpoint of the interval using k_1 to calculate y .
- k_3 is the increment based on the slope at the midpoint of the interval using k_2 to calculate y .
- k_4 stands for the slope at the end of the interval.

Palmgren-Miner Rule

In the general case of analysis of a fatigue structure, the Palmgren-Miner rule can be used. This law stipulates that the corresponding damage is additive, speaking of linear accumulation. Breakage therefore occurs when the sum of the damage related to each amplitude reaches the unity.

$$\sum_{i=1}^M \frac{n_i}{n_i^f} = 1 \quad (5.24)$$

The term in the denominator is the number of cycles needed to attain the specified amount of damage at a constant stress amplitude. The term in the numerator denotes the number of stress cycles with a constant amplitude.

The Palmgren-Miner rule can be used for fatigue life predictions, if and only if, the damage development rate ($d\varepsilon(n)/dn$) at a constant parameter p can be presented as a product of a function $\varphi_1(\varepsilon)$ of the current amount of damage and a function $\varphi_2(p)$ of the parameter (amplitude) p :

$$\frac{d\varepsilon(n)}{dn} = \varphi_1(\varepsilon)\varphi_2(p) \quad (5.25)$$

Finally, equations (5.7) and (5.12) can be expressed as following:

$$\frac{dQ_{\text{loss}}(t)}{dt} = \varphi_1(Q_{\text{loss}})\varphi_2(p) \quad (5.26)$$

With:

- $\varphi_1(Q_{\text{loss}})$ expressing function of the current amount of damage
- $\varphi_2(p)$ expressing function of parameters.

In order to respect the Palmgren-Miner rule, the parameters A_{SEI} , A_{LAM} and A_{CYC} must be constant.

Measured values for generating cycling life profile

		SOC windows strategies (%)					
		Min	0	10	0	20	
Cycling at 1C/1C at 5 °C	Theoretical SOC windows	Min	0	10	0	20	
		Max	100	90	80	100	
	Measured SOC windows	Min		8			
		Max CC		29			
		Max CC-CV		44			
	Charge	Temperature (°C)					
		Min		4.3			
		Max		6.3			
	Discharge	Min		4.3			
		Max		6.2			
		Mean		5.4			
	Cycling at 2C/1C at 5 °C	Theoretical SOC windows	Min	0	10	0	20
Max			100	90	80	100	
Measured SOC windows		Min		9			
		Max CC		16			
		Max CC-CV		42			
Charge		Temperature (°C)					
		Min		4.3			
		Max		8.0			
Discharge		Min		4.4			
		Max		6.2			
		Mean		5.3			
Cycling at 3C/1C at 5 °C		Theoretical SOC windows	Min	0	10	0	20
	Max		100	90	80	100	
	Measured SOC windows	Min		8			
		Max CC		14			
		Max CC-CV		36			
	Charge	Temperature (°C)					
		Min		4.4			
		Max		8.0			
	Discharge	Min		4.5			
		Max		6.5			
		Mean		5.5			
	Cycling at 1C/1C at 25 °C	Theoretical SOC windows	Min	0	10	0	20
Max			100	90	80	100	
Measured SOC windows		Min	0	10			
		Max CC	91	65			
		Max CC-CV	100	74			
Charge		Temperature (°C)					
		Min	25	25			
		Max	27	27			
Discharge		Min	25	25			
		Max	27	27			
		Mean	26	26			
Cycling at 2C/1C at 25 °C		Theoretical SOC windows	Min	0	10	0	20
	Max		100	90	80	100	
	Measured SOC windows	Min	0	10			
		Max CC	91	65			
		Max CC-CV	100	74			
	Charge	Temperature (°C)					
		Min	28	28			
		Max	34	34			
	Discharge	Min	25	25			
		Max	27	27			
		Mean	26	26			
	Cycling at 3C/1C at 25 °C	Theoretical SOC windows	Min	0	10	0	20
Max			100	90	80	100	
Measured SOC windows		Min	0	10			
		Max CC	91	65			
		Max CC-CV	100	74			
Charge		Temperature (°C)					
		Min	34	34			
		Max	36	36			
Discharge		Min	25	25			
		Max	27	27			
		Mean	26	26			
Cycling at 1C/1C at 45 °C		Theoretical SOC windows	Min	0	10	0	20
	Max		100	90	80	100	
	Measured SOC windows	Min	0	10	0	20	
		Max CC	96	88	77	95	
		Max CC-CV	100	92	83	100	
	Charge	Temperature (°C)					
		Min	45	45	46	47	
		Max	48	46	48	48	
	Discharge	Min	45	45	46	46	
		Max	48	46	47	47	
		Mean	46	45	46	46	
	Cycling at 2C/1C at 45 °C	Theoretical SOC windows	Min	0	10	0	20
Max			100	90	80	100	
Measured SOC windows		Min		9.9	0	19	
		Max CC		81	72	92	
		Max CC-CV		91	84	100	
Charge		Temperature (°C)					
		Min		47	47	46	
		Max		51	48	56	
Discharge		Min		46	46	46	
		Max		48	48	52	
		Mean		47	46	48	
Cycling at 3C/1C at 45 °C		Theoretical SOC windows	Min	0	10	0	20
	Max		100	90	80	100	
	Measured SOC windows	Min	0	9.9	0	19	
		Max CC	89	81	72	91	
		Max CC-CV	100	91	84	100	
	Charge	Temperature (°C)					
		Min	47	47	47	46	
		Max	51	51	48	56	
	Discharge	Min	46	46	46	46	
		Max	48	48	48	52	
		Mean	47	47	46	48	

Table B: Measured values for generating cycling life profile.

Figure L shows an example of a profile illustrating cycling aging performed at 45 °C between 3.42 V and 4.08 V (corresponding to a SOC window of 10 to 90 %) and a rate of 3 C in charge and 1 C in discharge. This profile has been generated based on measured values presented in the *Appendix*. The **Figure M** presents a comparison of capacity loss and capacity throughput obtained in these conditions.

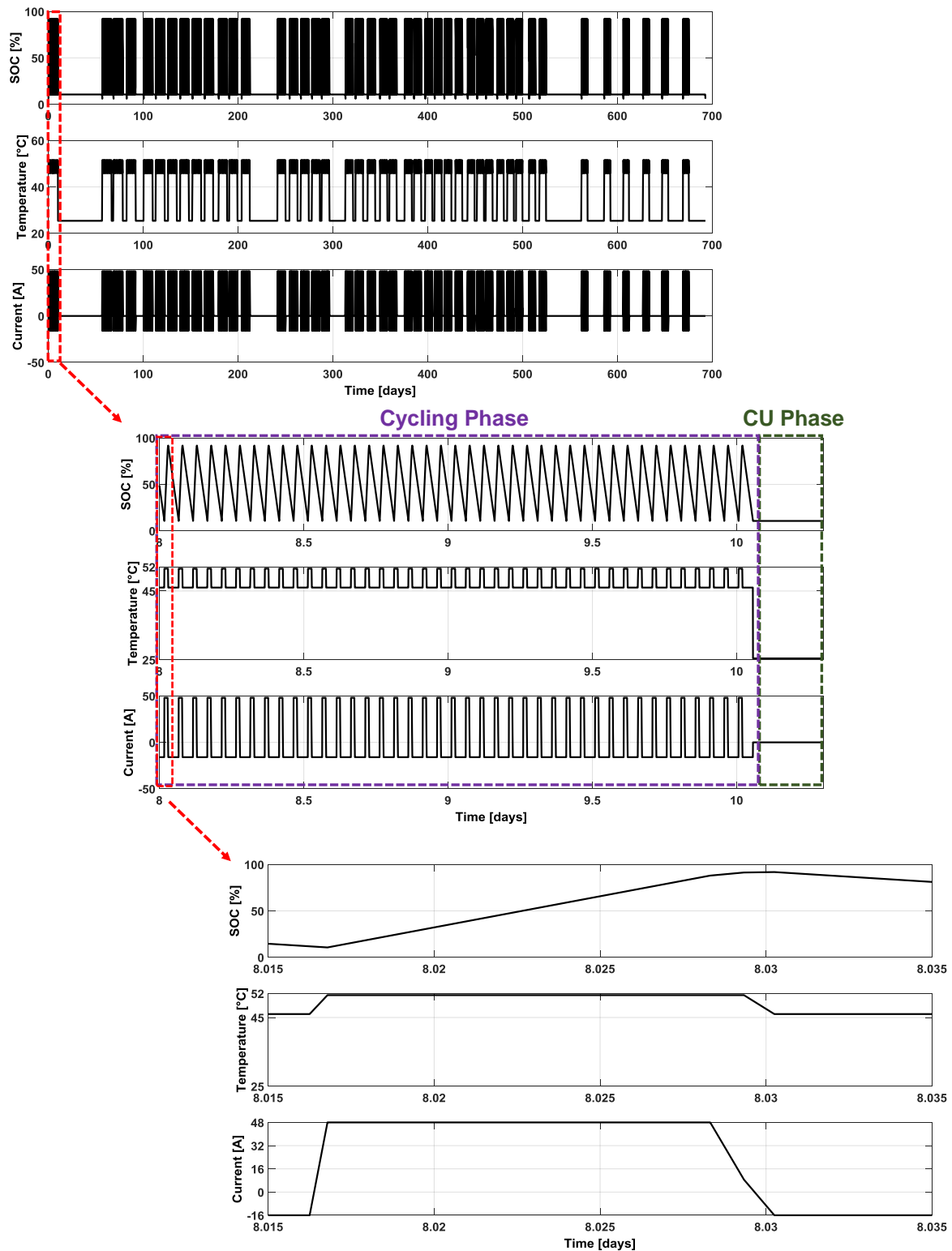


Figure L: Example of a profile representing cycling aging at $T = 45^{\circ}\text{C}$ ($\text{SOC}_{\min} = 10\%$, $\text{SOC}_{\max} = 90\%$, $3\text{ C} / 1\text{ C}$).

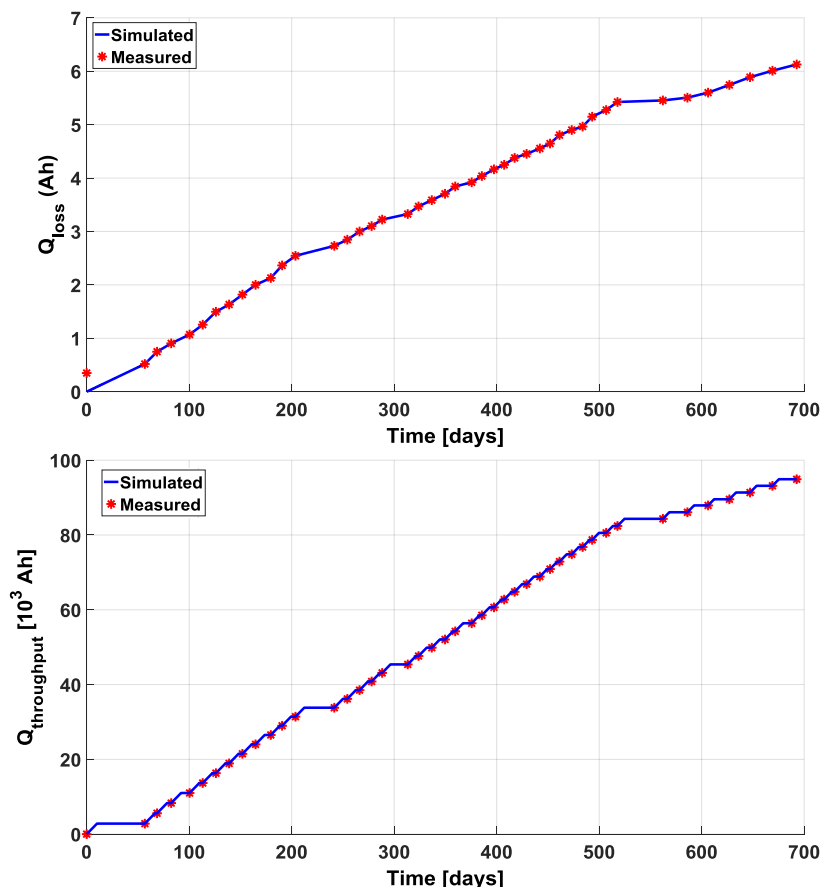


Figure M: Comparison of capacity loss and capacity throughput obtained from the use profile corresponding to cycling at 3 C / 1 C at 45 °C (between 10 and 90 % of SOC, theoretically) with values obtained from measurements.

Characteristic values of peaks determined on incremental capacity curves at 100 % of SOH

The Table below present the characteristic values of all the peaks determined on incremental capacity curves (based on charge measurements obtained at a rate of C / 25) at 100 % of SOH.

Peaks	Cell voltage (V)	PE voltage (V vs. Li)	NE voltage (V vs. Li)	SOC (%)	Electrodes
P ₁	3.65	3.92	0.26	35	Both
P ₂	3.49	3.87	0.38	8	NE
P ₃	3.85	4.04	0.18	68	PE
P ₄	3.54	3.88	0.34	14	NE
P ₅	3.80	4.00	0.19	63	PE

Table C: Characteristic values of peaks determined on IC curves at 100 % of SOH.

Evolution of incremental capacity curves with other cycling conditions

We present here incremental capacity measurements obtained from commercial cells aged in cycling at CEA.

At 25 °C (Erreur ! Source du renvoi introuvable.) as well as at 45 °C (from Erreur ! Source du renvoi introuvable. to Erreur ! Source du renvoi introuvable.), the signature of the displacement incremental capacity peaks are characteristic of a combination between LLI and LAM on the NE modes. Indeed, the decrease of P_1 and its shift towards higher voltages are typical of LLI while the shifts of both P_2 and P_4 are specific to LAM on the NE.

Concerning the aging mechanisms, the SEI growth as the effects of repeated cycles can be considered in the LLI in cycling, more pronounced at 45 °C.

On one hand, at 25 °C, the apparition of dry areas cannot occurred at this temperature. In this case, the LAM on the NE is certainly caused by another physical mechanism leading to loss of active surface on graphite electrodes.

On the other hand, at 45 °C, biphenyl polymerization should be negligible when cycling is performed between 3.42 V and 4.08 V (from 10 to 90 % of SOC, theoretically). Although, the cell temperature can reach 50 °C during charging (especially at 3 C), the little time spent in the maximum SOC threshold (due SOC variations during cycling) is not sufficient to lead to a significant biphenyl polymerization. Consequently, the LAM on the NE here might be also caused by an additional aging mechanism.

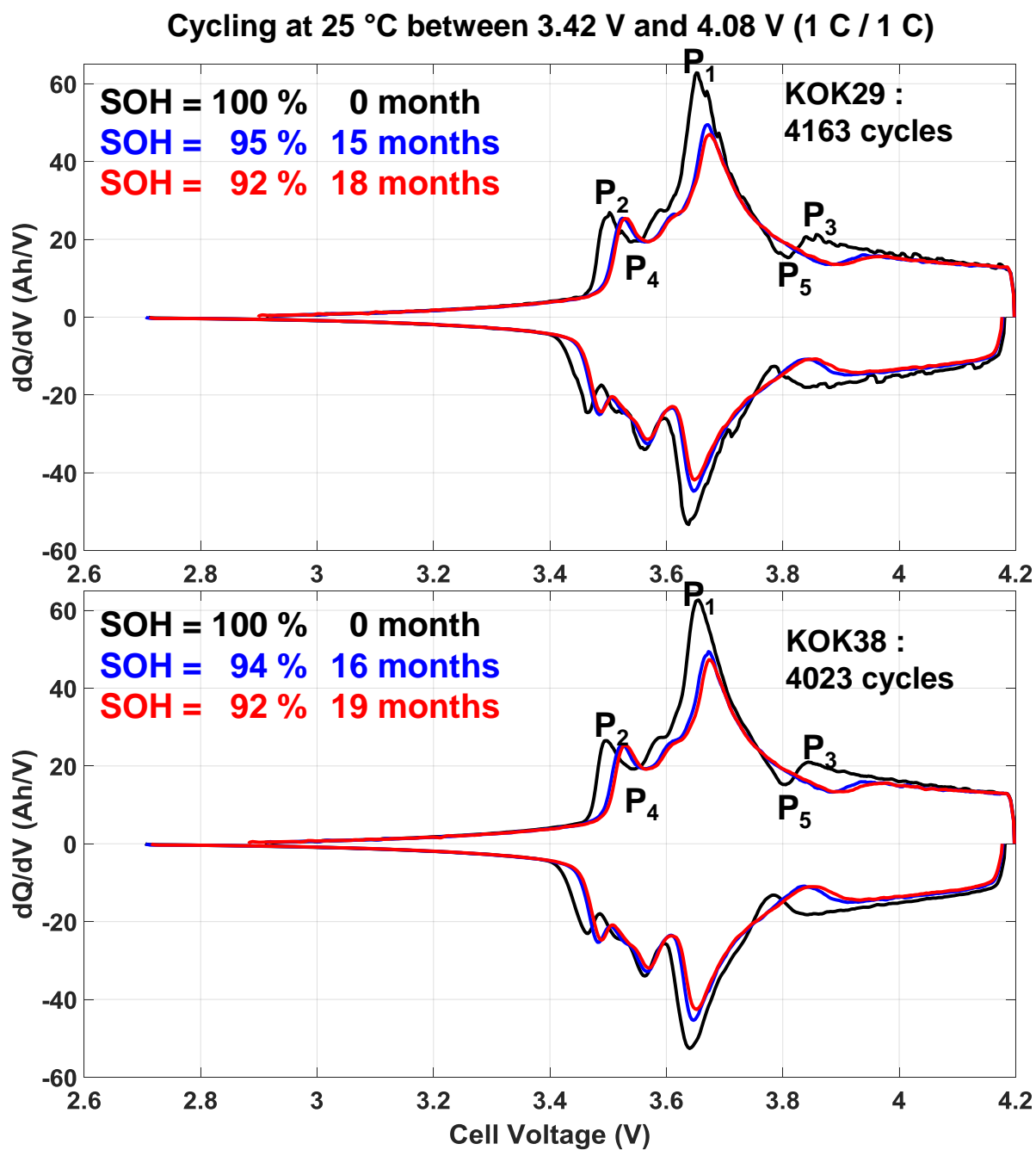


Figure N: Evolution of IC curves during cycling aging at 25 °C between 3.42 V and 4.08 V and at a rate of 1 C in charge as in discharge.

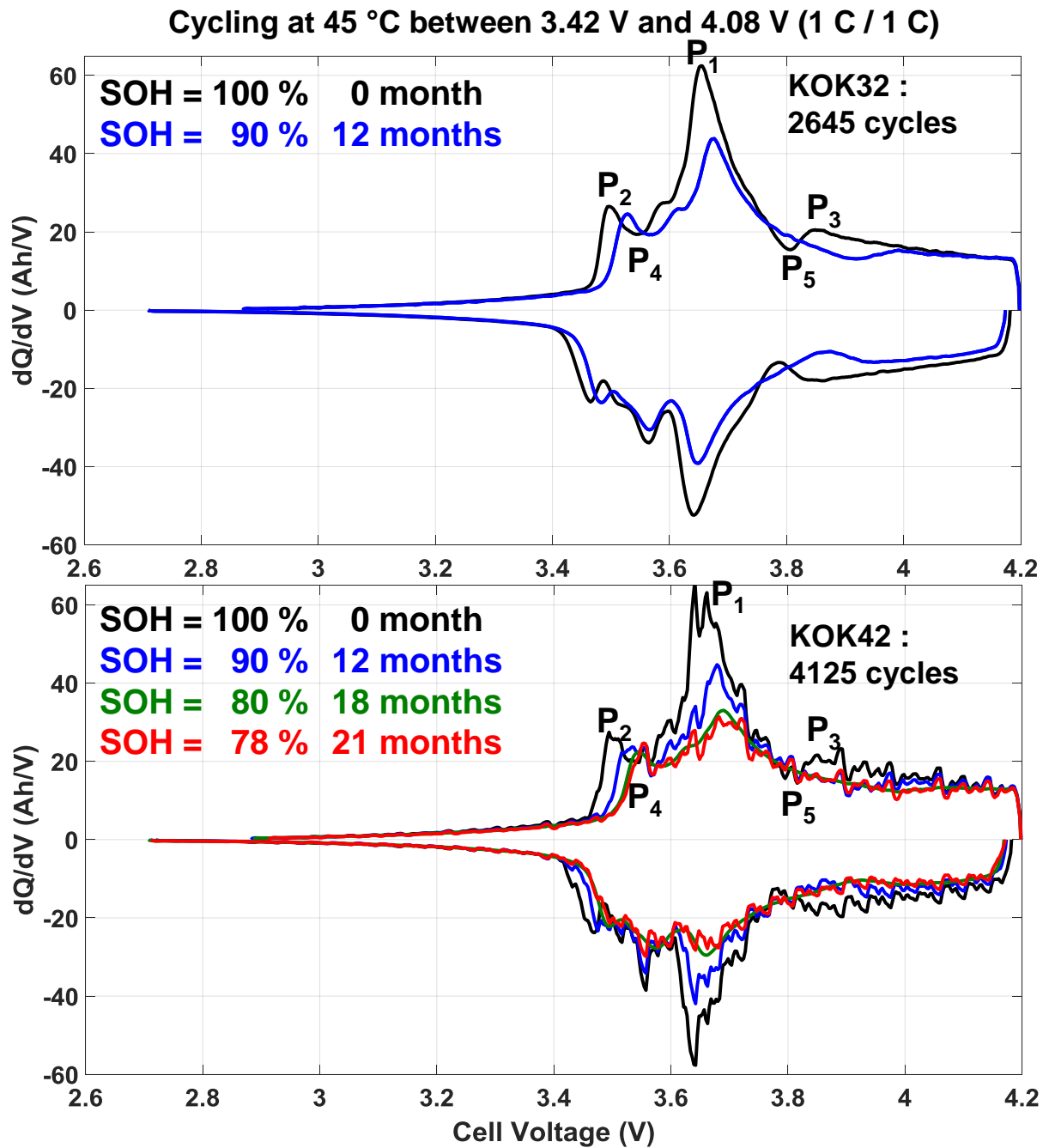


Figure O: Evolution of IC curves during cycling aging at 45 °C between 3.42 V and 4.08 V and at a rate of 1 C in charge as in discharge.

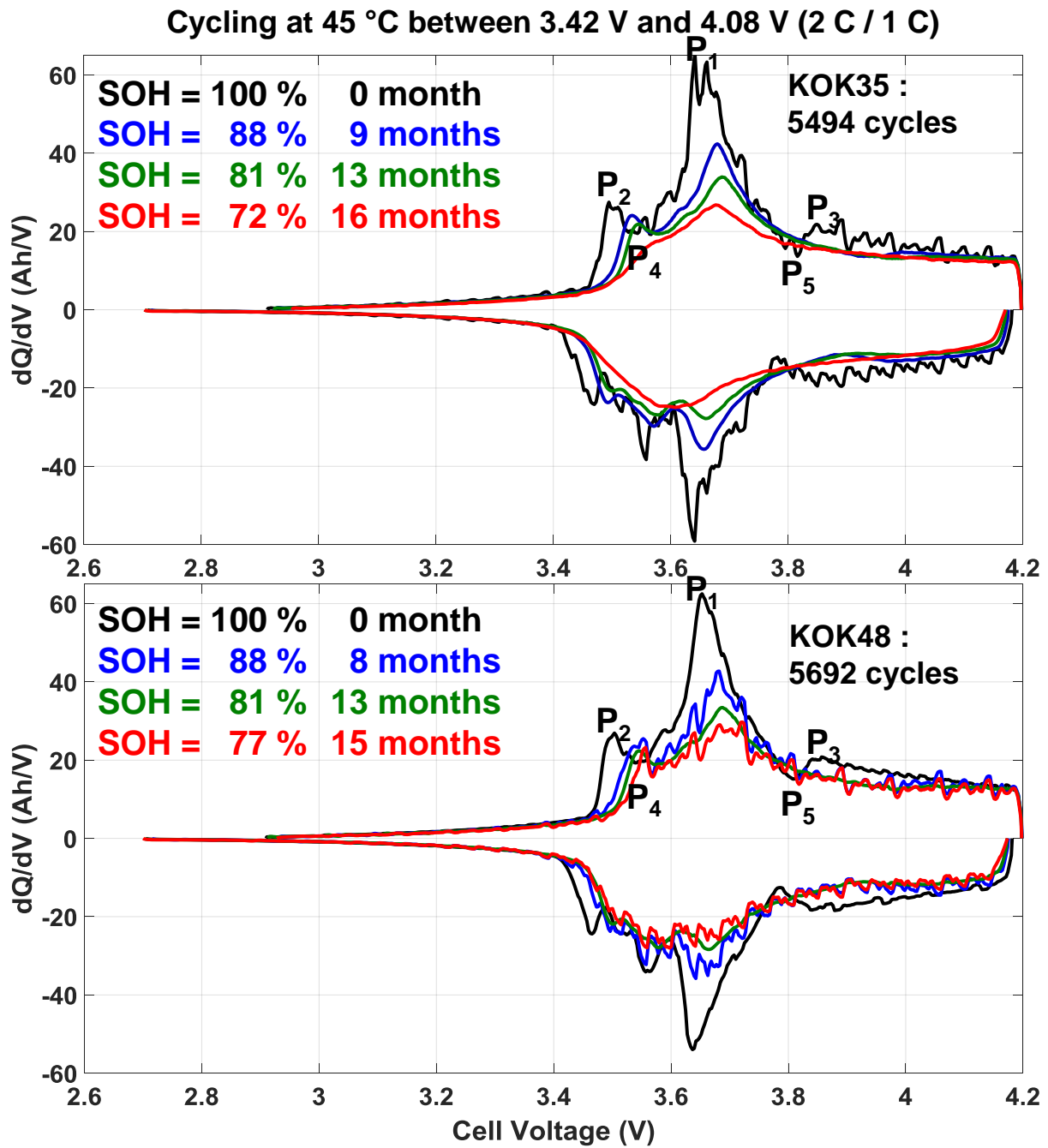


Figure P: Evolution of IC curves during cycling aging at 45 °C between 3.42 V and 4.08 V and at a rate of 2 C in charge as in discharge.

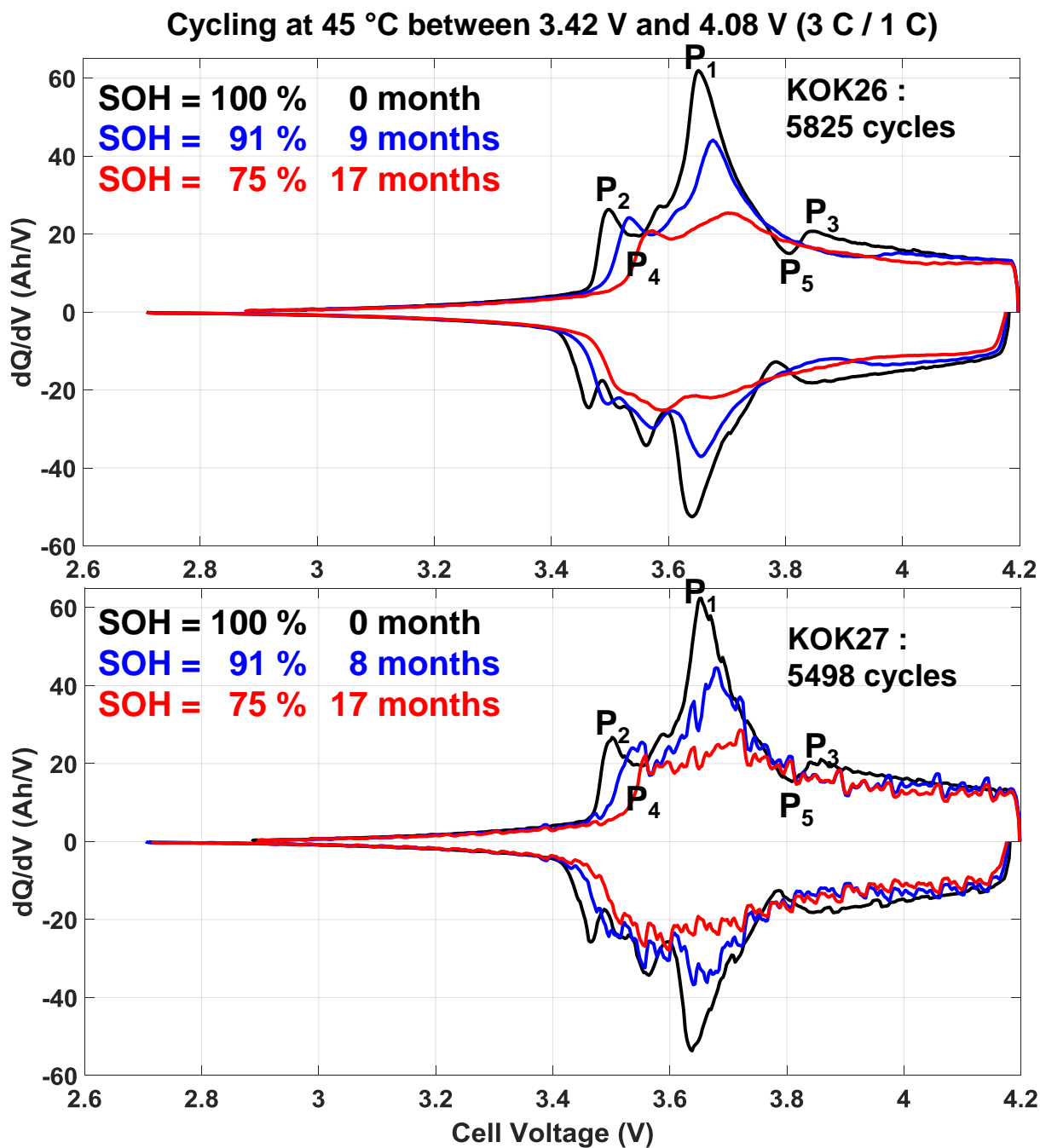


Figure Q: Evolution of IC curves during cycling aging at 45 °C between 3.42 V and 4.08 V and at a rate of 3 C in charge and 1 C in discharge.

List of illustrations

Figure I-1 : The worldwide battery market between 1990 and 2015 ^[3]	16
Figure I-2 : Li-ion technology main applications – M Wh ^[3]	17
Figure I-3 : Schematic illustration of a typical Li-ion battery [□]	18
Figure I-4 : Crystalline structures for each type of positive electrode insertion material [□]	20
Figure I-5 : Plans of graphene between which the Li is inserted ^[10]	20
Figure I-6 : Principle of overcharge agents based on the representation made by J. Garche et al. ^[16]	22
Figure I-7 : Overcharge agents: mechanism of redox shuttle type (A) and mechanism of shutdown type (B) based on the representation made by J. Garche et al. ^[16]	23
Figure I-8 : Development of the SEI at the graphite electrode [□]	27
Figure I-9 : Example of gradual capacity loss (A) and fast rollover capacity loss (B) due to the reduction of porosity on graphite electrode ^[46]	28
Figure I-10 : Impact of the exposure of electrodes to the atmosphere of the anhydrous room before assembling into reconstructed 3-electrodes system.....	32
Figure I-11 : Incremental capacity of a Graphite / LFP Li-ion cell obtained at the rate of C / 10. (This Figure originates from an internal project of the Laboratory).....	33
Figure I-12 : Incremental capacity of a Graphite / NMC Li-ion cell obtained at the rate of C / 25. (This Figure originates from this thesis work).....	34
Figure II-1 : 16 Ah commercial Li-ion cell (Kokam SLPB 78205130H).....	39
Figure II-2 : Internal order of electrodes inside the 16 Ah commercial Li-ion cell (Kokam SLPB 78205130H).....	39
Figure II-3 : Dimensions of positive and negative electrodes in the 16 Ah commercial Li-ion cell (Kokam SLPB 78205130H).....	40
Figure II-4 : Illustration of the reference electrode which will be inserted inside the 16 Ah commercial Li-ion cells (Kokam SLPB 78205130H).....	42
Figure II-5 : Steps of insertion of reference electrodes into the 16 Ah commercial Li-ion cell (Kokam SLPB 78205130H).....	43
Figure II-6 : Impedance curves before and after the insertion of the reference electrodes into the first commercial 16 Ah pouch-cell.....	43
Figure II-7 : Electrochemical characterizations performed at 25 °C, 45 °C and 5 °C at different C-rates with the 16 Ah commercial Li-ion cell instrumented with Li metal as reference electrode.....	45
Figure II-8 : Evolution of the potential of each electrode compared to the lithium potential in function of the charge current and the temperature.....	46
Figure II-9 : Evolution of the potential of each electrode compared to the Li potential in function of the discharge current (1 C) and the temperature.....	47
Figure II-10 : Measurement of internal resistance according direct current test procedure. ..	48
Figure II-11 : Comparison of the DC resistance obtained directly from cell and those calculated by addition of the DC resistance of each electrodes for different temperatures....	48
Figure II-12 : DC resistance corresponding to the positive electrode in function of the SOC and for the different pulses duration (5s, 10s and 30s).....	49
Figure II-13 : DC resistance corresponding to the negative electrode in function of the SOC and for the different pulses duration (5 s, 10 s and 30 s).....	50
Figure II-14 : Mapping of DC resistances measured during pulses in charge at 10 s.....	50
Figure II-15 : Protocol of Extended Check-Up (ECU) test performed at 25 °C at the beginning of life, at the middle of life and at the end of life of the commercial cell.....	51

Figure II-16 : Protocol of Short Check-Up (SCU) test performed at 25 °C after every 200 cycles.....	52
Figure II-17 : Flow chart for the disassembly of Li-ion cells and analysis of components.	53
Figure II-18 : Scheme of the cell disassembly and coin cells types for post-mortem electrochemical analyses.	55
Figure II-19 : Overview of components inside the commercial 16 Ah Li-ion pouch cell and various methods of sampling specific to each physico-chemical method for post-mortem analyses. (1) Electrolyte analysis; (2) Electron microscopy methods; (3) chemical methods sensitive to electrode surface; (4) chemical methods sensitive to electrode bulk.....	56
Figure II-20 : Schematics of principle of each analysis method.	57
Figure III-1 : Evolution of the SOH of commercial 16 Ah Li-ion cells in cycling aging in the framework of the Mat4Bat project.	68
Figure III-2 : Evolution of the increase of DC resistance over aging as function of the capacity decrease and the equivalent cycles.....	69
Figure III-3 : Evolution of the charged capacity (A), Faraday Efficiency (B) and Energy Efficiency (C) measured at each cycle during cycling test at 5 °C between 2.7 V and 4.2 V (A).	71
Figure III-4 : Evolution of the potential of both positive and negative electrodes corresponding to discharge during cycling aging test at 5 °C.....	75
Figure III-5 : Evolution of the potential of both positive and negative electrodes corresponding to charge during cycling aging test at 5 °C.....	76
Figure III-6 : Evolution of the end-of-charge / discharge potential in function of number of cycles of both positive and negative electrodes during cycling aging test at 5 °C.	77
Figure III-7 : Visual inspections of both negative and positive electrodes and separators of 16 Ah C/NMC commercial Li-ion pouch cells after cycling at 5 °C.....	78
Figure III-8 : SEM analysis performed on a sample of graphite electrode recovered from the fresh commercial cell and on a sample graphite electrode from the cell #3 (after cycling between 2.7 V and 4.2 V).....	80
Figure III-9 : TEM images obtained from a sample of graphite electrode respectively recovered from the cell #5 (cycling between 3.42 V and 4.08 V) and from the cell #3 (2.7 V and 4.2 V).	81
Figure III-10 : TEM / EDS analysis of a sample of graphite electrode recovered from the cell #5.	82
Figure III-11 : TEM / EDS analysis of a sample of graphite electrode recovered from the cell #3.	83
Figure III-12 : Electrochemical characterizations at 25 °C with Graphite / Li metal and NMC / Li metal coin half-cells.....	85
Figure III-13 : XRD studies of the cathode $\text{Li}_x(\text{Mn}_{0.4}\text{Co}_{0.2}\text{Ni}_{0.4})\text{O}_2$ material. In situ XRD measurements are performed on a sample of a fresh cathode electrode in order to obtain a calibration curve of lattice parameters in function of Li rate.....	87
Figure III-14 : XRD studies of the anode material.	89
Figure III-15 : Evolution of the charged capacity measured at each cycle during cycling test at 5 °C between 2.7 V and 4.2 V with coin full cells based on six different types of electrolyte composition.	92
Figure III-16 : Visual inspections of both negative and positive electrodes and separators of coin full cells after cycling at 5 °C and at a rate of 1 C between 2.7 V and 4.2 V.	93
Figure III-17 : ^7Li NMR analysis on graphite electrodes.	94
Figure III-18 : ToF-SIMS images: Standardization of the rate of each characteristic element in function of the graphite "carbon" rate.	96

Figure III-19 : Spectroscopic analysis of graphite electrodes with XPS technique	97
Figure III-20 : Profilometric analysis graphite electrodes with XPS technique.....	100
Figure III-21 : Representation of the mechanism leading to the hindrance of Li diffusion into graphite electrodes, observed during cycling at 5 °C between 2.7 V and 4.2 V.....	102
Figure IV-1 : Evolution of the state of health and the resistance increase of 16Ah commercial Li-ion cells in calendar aging.	109
Figure IV-2 : Visual inspections of negative and positive electrodes and separators of commercial 16 Ah Graphite/NMC pouch cells (at discharged state) aged in calendar mode (SOC=100%).....	111
Figure IV-3 : Calendar aging at 45 °C and at 100 % of SOC.	113
Figure IV-4 : ⁷ Li NMR analysis on graphite electrode after calendar aging at 60°C and 100 % of SOC with periodic checkups.	114
Figure IV-5 : Content of each carbonate in % normalized regarding the quantity of EC and in accordance with time of storage.....	116
Figure IV-6 : Content (%) of additive per time of storage in function of the sum of all detected carbonates.	117
Figure IV-7 : Visual inspection of Graphite/NMC coin cells components after 24 days of calendar aging at 45 °C and 100 % of SOC.....	118
Figure IV-8 : First cycles of CV measurements. Effects of the temperature increasing on biphenyl polymerization potentials.	119
Figure IV-9 : Second cycles of CV measurements. Effects of the temperature increasing on biphenyl polymerization potentials.	120
Figure IV-10 : Third cycles of CV measurements. Effects of the temperature increasing on biphenyl polymerization potentials.	121
Figure IV-11 : Visual inspection of Li metal/NMC coin cells components after two cycles of cyclic voltammetry at 25°C.....	122
Figure IV-12 : Local Lithium metal deposition development process during storage at high temperature and high state of charge interrupted by regular charges, with biphenyl-containing electrolyte in Graphite/NMC Li-ion cell.....	123
Figure V-1 : Cartography of the parameter J_{SEI}	136
Figure V-2 : Cartography of the parameter J_{LAM}	138
Figure V-3 : Cartography of the parameter J_{CYC}	140
Figure V-4 : Comparison between calendar model based only on SEI growth (Broussely's law) versus experimental data.....	142
Figure V-5 : Comparison between calendar model based on both SEI growth and LAM versus experimental data.	143
Figure V-6 : Contribution of each aging mechanism into the capacity loss during calendar aging.	144
Figure V-7 : Model versus experimental data for cycling tests performed at 5 °C.	145
Figure V-8 : Contribution of each aging mechanism into the capacity loss during cycling aging at 5 °C.....	145
Figure V-9 : Model versus experimental data for tests performed at 25 °C.	146
Figure V-10 : Contribution of each aging mechanism into the capacity loss during cycling aging at 25 °C.	147
Figure V-11 : Model versus experimental data for tests performed at 45 °C.	148
Figure V-12 : Contribution of each aging mechanism into the capacity loss during cycling aging at 45 °C.	149
Figure V-13 : Model validation at 45 °C.	150

Figure V-14 : Contribution of each aging mechanism into the capacity loss during cycling aging at 45 °C.	151
Figure V-15 : Simulation of the LLI degradation mode at C / 25.	153
Figure V-16 : Simulation of the LLI degradation mode at C / 25 and effects on IC curves... ..	154
Figure V-17 : Simulation of the LAM degradation mode on the PE at C / 25.....	155
Figure V-18 : Simulation of the LAM degradation mode on the PE at C / 25 and effects on the IC curves.	156
Figure V-19 : Simulation of the LAM degradation mode on the NE at C / 25.	157
Figure V-20 : Simulation of the LAM degradation mode on the NE at C / 25 and effects on the IC curves.	158
Figure V-21 : Simulation of the LAM degradation mode on both electrodes at C / 25	159
Figure V-22 : Simulation of the LAM degradation mode on both electrodes at C / 25 and effects on the IC curves.	159
Figure V-23 : Evolution of IC curves during cycling aging at low temperatures.	162
Figure V-24 : Comparison between the evolution of IC curves with aging between KOK56 and KOK57.	164
Figure V-25 : Comparison between experimental and simulations measurements corresponding to the case of the SEI growth at 45 °C.....	166
Figure V-26 : Comparison between experimental and simulations measurements corresponding to the case of the growth of the SEI at 60 °C.....	166
Figure V-27 : Comparison between experimental and simulations measurements corresponding to the case of the growth of the SEI and the LAM at 60 °C.....	167
Figure V-28 : Comparison between experimental and simulations measurements corresponding to the case of the growth of the SEI, the LAM and Li plating at 45 °C.....	168
Figure V-29 : Comparison between experimental and simulations measurements corresponding to the case of SEI growth, the LAM and local metallic Li depositions at 60 °C and for 100 % of SOC.....	169
Figure V-30 : Comparison between experimental and simulations measurements corresponding to the case of SEI growth, the LAM and local metallic Li depositions at 60 °C and for 90 % of SOC.....	169

List of tables

Table II-1 : Common specifications of 16 Ah commercial Li-ion pouch cells (Kokam SLPB 78205130H).....	38
Table III-1 :Correspondence between SOC windows and voltage thresholds at 25 °C as defined for cycling aging by the consortium in the Mat4Bat project.	66
Table III-2 : Illustration of experimental conditions for cycling aging of commercial Li-ion cells in the framework of the Mat4Bat project.	67
Table III-3 : Protocol of cycling at 5 °C according to the following voltage limits strategies. ..	74
Table III-4 : Percentage of each element detected with SEM / EDS on samples of graphite electrodes respectively recovered from a fresh cell and from the cell #3.	80
Table III-5 : Post-mortem electrochemical measurements (performed at 25 °C) of single components (from the cell #3) with coin half cells.	84
Table III-6 : Content (%) of each component of the electrolyte detected with GC-MS analysis performed on samples recovered from a fresh cell and from cell #3.	90
Table III-7 : Composition of different electrolytes based on elements detected from the fresh electrolyte with GC-MS [3.4.3.1].	91
Table III-8 : The average of capacity loss of coin full cells per type of electrolyte.	92
Table III-9 : Percentage of each element detected with XPS on the surface of samples of graphite electrodes respectively recovered from the cell #3 (cycled between 2.70 V and 4.20 V) and from the cell #5 (cycled between 3.42 V and 4.08 V).	99
Table IV-1 : Calendar aging conditions (condition without any periodic check-up test but only two check-ups, at BOL and EOL respectively).	108
Table V-1 : Lithium-ion anode aging mechanisms – category, conditions and modeling in behalf of this thesis.....	128
Table V-2 : Calendar aging conditions (** condition without periodic checkup test).....	133
Table V-3 : Synthesis of the impact of different aging mechanisms on peaks displacement	160
Table V-4 : Protocol of CU for additional commercial KOK56 and KOK57.	163

References

- [1] K. Mizushima, P. C. Jones, P. J. Wiseman, and J. Goodenough, "Li_xCoO₂ (0 < x < -1): A new cathode material for batteries of high energy density", *Materials Res. Bull.*, 15, 783 (1980).
- [2] R. Yazami and P. Touzain, "A reversible graphite-lithium negative electrode for electrochemical generators", *J. Power Sources*, 9, 365 (1983).
- [3] <http://www.batteriesevent.com>
- [4] H. Lee, M. Yanilmaz, O. Toprakci, K. Fu and X. Zhang, A review of recent developments in membrane separators for rechargeable lithium-ion batteries, *Energy Environ. Sci.*, 2014,7, 3857-3886, [doi:10.1039/C4EE01432D](https://doi.org/10.1039/C4EE01432D).
- [5] R. Masse, G. Cao, C. Li, Energy storage through intercalation reactions : electrodes for rechargeable batteries, *National Science Review*, 4:26-53, (2017), doi: 10.1093/nsr/nww093
- [6] V. Agubra, J. Fergus, Lithium Ion Battery Anode Aging Mechanisms, *Materials*. (2013), 6, 1310–1325. [doi:10.3390/ma6041310](https://doi.org/10.3390/ma6041310).
- [7] Z. Li, J. Huang, B. Y. Liaw, V. Metzler, J. Zhang, A review of lithium deposition in lithium-ion and lithium metal secondary batteries, *J. Power Sources*. 254 (2014) 184-186. [doi:10.1016/j.jpowsour.2013.12.099](https://doi.org/10.1016/j.jpowsour.2013.12.099).
- [8] Z. Guo, J. Zhu, J. Feng and S. Du, Direct *in situ* observation and explanation of lithium dendrite of commercial graphite electrodes, *RSC Adv.* (2015), 5, 69514–69521. [doi:10.1039/c5ra13289d](https://doi.org/10.1039/c5ra13289d).
- [9] T. Waldmann, B-I. Hogg, M. Kasper, S. Grolleau, C. Gutiérrez Couceiro, K. Trad, B. Pilipili Matadi and M. Wohlfahrt-Mehrens, Interplay of Operational Parameters on Lithium Deposition in Lithium-ion cells: Systematic Measurements with Reconstructed 3-Electrode Pouch Full Cells, *J. Electrochem. Soc.* 163, 7, (2016) A1–A7. [doi: 10.1149/2.0591607jes](https://doi.org/10.1149/2.0591607jes).
- [10] C. Glaize, S. Geniès, Accumulateurs électrochimiques au lithium, haute température et à circulation d'électrolyte, (2013), Lavoisier, Paris.
- [11] N. Job, « Matériaux carbonés poreux de texture contrôlée synthétisés par procédé sol-gel et leur utilisation en catalyse hétérogène », Thèse-Université de Liège, ISSN 0075-9333 (2006).
- [12] T. Tran, B. Yebka, X. Song, G. Nazri, K. Kinoshita, D. Curtis, « Thermal and electrochemical studies of carbons for Li-ion batteries 2. Correlation of active sites and irreversible capacity loss », *J. Power Sources*, 85 (2000) 269–278, [doi: 10.1016/S0378-7753\(99\)00343-2](https://doi.org/10.1016/S0378-7753(99)00343-2).

-
- [13] M. Nie, J. Demeaux, B. T. Young, D. R. Heskett, Y. Chen, A. Bose, J. C. Woicik and B. L. Lucht, Effect of Vinylene Carbonate and Fluoroethylene Carbonate on SEI Formation on Graphitic Anodes in Li-Ion Batteries, *Journal of The Electrochemical Society*, 162 (13) A7008-A7014 (2015), [doi: 10.1149/2.0021513jes](https://doi.org/10.1149/2.0021513jes).
- [14] S.L. Li, X.P. Ai, J.K. Feng, Y.L. Cao, H.X. Yang, Diphenylamine: A safety electrolyte additive for reversible overcharge protection of 3.6 V-class lithium ion batteries, *Journal of Power Sources* 184 (2008) 553–556, [doi:10.1016/j.jpowsour.2008.02.041](https://doi.org/10.1016/j.jpowsour.2008.02.041)
- [15] M. Adachi, K. Tanaka, and K. Sekai, Aromatic Compounds as Redox Shuttle Additives for 4 V Class Secondary Lithium Batteries, *Journal of The Electrochemical Society*, 146 (4) 1256-1261 (1999)
- [16] J. Garche, C. K. Dyer, P. T. Moseley, Z. Ogumi, D.A. J. Rand, B. Scrosati, *Encyclopedia of Electrochemical Power Sources, Secondary Batteries – Lithium Rechargeable Systems / Electrolytes: Nonaqueous*, p. 80-81, Elsevier Science (2009).
- [17] W. K. Behl, Overcharge Protection in Ambient Temperature Lithium and Lithium-Ion Cells: A Literature Survey, Army Research Laboratory, Adelphi, MD 20783-1197, 1998
- [18] S. S. Zhang, A review on electrolyte additives for lithium-ion batteries, *Journal of Power Sources* 162 (2006) 1379–1394
- [19] H. Mao and U. Sacken, U.S. Patent 5,776,627 (1998).
- [20] Polymerizable Aromatic Additives for Overcharge Protection in Non-Aqueous Rechargeable Lithium Batteries, APPLICATION FOR CANADIAN PATENT
- [21] C-H. Doh and A. Veluchamy, Thermo-chemical process associated with lithium cobalt oxide cathode in lithium ion batteries, *Next generation lithium ion batteries 36 for electrical vehicles*, p 41.
- [22] K. Abe, T. Takaya, H. Yoshitake, Y. Ushigoe, M. Yoshio and H. Wang, Functional electrolyte: additive for improving the cyclability of cathode materials, *Electrochem Solid-State Lett.* (2004), issue 12, A462-A465.
- [23] Y. Zhang, A-Q. Zhang, Y-H. Gui, L-Z. Wang, X.-B. Wu, C.-F. Zhang, P. Zhang, Application of biphenyl additive in electrolyte for liquid state Al-plastic film lithium-ion batteries, *Journal of Power Sources* 185 (2008) 492–500, [doi:10.1016/j.jpowsour.2008.07.001](https://doi.org/10.1016/j.jpowsour.2008.07.001)
- [24] L. Xiao, X. Ai*, Y. Cao, H. Yang, Electrochemical behavior of biphenyl as polymerizable additive for overcharge protection of lithium ion batteries, *Electrochimica Acta.* 49 (2014) 4189–4196. [doi:10.1016/j.electacta.2004.04.013](https://doi.org/10.1016/j.electacta.2004.04.013).

-
- [25] N. Choi, J-G. Han, S-Y. Ha, I. Park and C-K. Back, Recent advances in the electrolytes for interfacial stability of high-voltage cathodes in lithium-ion batteries, *RSC Adv.* (2015), 5, 2732. [doi:10.1039/c4ra11575a](https://doi.org/10.1039/c4ra11575a).
- [26] A. Dinger, R. Martin, X. Mosquet, M. Rabl, D. Rizoulis, M. Rousso and G. Sticher, « Batteries for electric cars – Challenges, opportunities, and the Outlook to 2020 », The Boston Consulting Group, Inc., (2010).
- [27] K. Uddin, R. Gough, J. Radcliffe, J. Marco, P. Jennings, Techno-economic analysis of the viability of residential photovoltaic systems using lithium-ion batteries for energy storage in the United Kingdom, *Applied Energy* 206 (2017) 12-21, <http://dx.doi.org/10.1016/j.apenergy.2017.08.170>.
- [28] B. Guangxing, W. Pingfeng, « A generic model-free approach for lithium-ion battery health management », IIE Annual Conference and Expo, pp. 3291-3300 (2013).
- [29] R.P. Ramasamy, R.E. White, B.N. Popov, « Calendar life performance of pouch lithium-ion cells », *Journal of Power Sources*, vol.141 pp. 298–306 (2005). [doi:10.1016/j.jpowsour.2004.09.024](https://doi.org/10.1016/j.jpowsour.2004.09.024).
- [30] J. Nadeau, « Effets du vieillissement de la batterie Li-ion sur les performances d'un véhicule récréatif hybride branchable à trois roues », Mémoire de Maîtrise – Université de Sherbrooke, Sherbrooke, Canada (2013).
- [31] L. LAM, « A Practical Circuitbased Model for State of Health Estimation of Li ion Battery Cells in Electric Vehicles », Master of Science Thesis – University of Technology Delft.
- [32] M. Gauthier, T.J. Carney, A. Grimaud, L. Giordano, N. Pour, H-H. Chang, D. P. Fenning, S.F. Lux, O. Paschos, C. Bauer, F. Maglia, S. Lupart, P. Lamp and Y. Shao-Horn, Electrode-Electrolyte Interface in Li-ion Batteries: Current Understanding and New Insights, *J. Phys. Chem. Lett.* (2015), 6, 4653–4672. [doi:10.1021/acs.jpcllett.5b01727](https://doi.org/10.1021/acs.jpcllett.5b01727).
- [33] W. A. van Schalkwijk and B. Scrosati, *Advances in lithium-ion batteries*, Klumer Academics Publishers, 155-181.
- [34] D. Takamatsu, Y. Orikasa, S. Mori, T. Nakatsutsumi, K. Yamamoto, Y. Koyama, T. Minato, T. Hirano, H. Tanida, H. Arai, Y. Uchimoto, Z. Ogumi, Effect of an electrolyte additive of vinylene carbonate on the electronic structure at the surface of a lithium cobalt oxide electrode under battery operating conditions, *J. Phys. Chem. C* (2015), 119, 9791–9797. [doi: 10.1021/jp511405g](https://doi.org/10.1021/jp511405g).
- [35] E. Markevich, G. Salitra, K. Fridman, R. Sharabi, G. Gershinky, A. Garsuch, G. Semrau, M.A. Schimdt, D. Aurbach, Fluoroethylene carbonate as important component in electrolyte solutions for high-voltage lithium batteries: role of surface chemistry on the cathode, *Langmuir*, (2014), 30 (25), 7414–7424, [doi: 10.1021/la501368y](https://doi.org/10.1021/la501368y).

-
- [36] Y. Ein-Eli, Dimethyl carbonates (DMC) electrolytes - the effect of solvent purity on Li-ion intercalation into graphite anodes, *Electrochemistry communications*, (2002), 4, 644-648. [doi:10.1016/S1388-2481\(02\)00407-1](https://doi.org/10.1016/S1388-2481(02)00407-1).
- [37] B. Zhang, M. Metzger, S. Solchenbach, M. Payne, S. Meini, H.A. Gasteiger, A. Garsuch, B.L. Lucht, Role of 1,3-propane sultone and vinylene carbonate in solid electrolyte interface formation and gas generation, *J. Phys. Chem, C* (2015), 119, 11337-11348. [doi: 10.1021/acs.jpcc.5b00072](https://doi.org/10.1021/acs.jpcc.5b00072).
- [38] T. R. Jow, K. Xu, O. Borodin, M. Ue, Electrolytes for lithium and lithium-ion batteries, *Johnson Matthey Technol. Rev.*, 2015, 59, (1), 30–33.
- [39] R. Imnhof and P. Novák, Oxydative electrolyte solvent degradation in lithium-ion batteries: an *in situ* differential electrochemical mass spectrometry investigation, *J. Electrochem. Soc.* 146, issue 5, (1999) 1702–1706. [doi: 10.1149/1.1391829](https://doi.org/10.1149/1.1391829).
- [40] B. Pilipili Matadi, S. Geniès, A. Delaille, T. Waldmann, M. Kasper, M. Wohlfahrt-Mehrens, F. Aguesse, E. Bekaert, I. Jiménez-Gordon, L. Daniel, X. Fleury, M. Bardet, J.-F. Martin and Y. Bultel, Effects of Biphenyl polymerization on lithium deposition in commercial Graphite/NMC lithium-ion pouch-cells during calendar aging at high temperature, *J. Electrochem. Soc.* 164, issue 6, (2017) A1089–A1097. [doi: 10.1149/2.0631706jes](https://doi.org/10.1149/2.0631706jes).
- [41] P. Niehoff, E. Kraemer, M. Winter, Parametrisation of the influence of different cycling conditions on the capacity fade and the internal resistance increase for lithium nickel manganese cobalt oxide/graphite cells, *J. Electroanal. Chem.*, 707 (2013), pp. 110–116. <http://dx.doi.org/10.1016/j.jelechem.2013.08.032>.
- [42] K. Amine, J. Liu, I. Belharouak, High-temperature storage and cycling of C-LiFePO₄/graphite Li-ion cells, *Electrochemistry communications*, (2005), 7, 669-673. [doi:10.1016/j.elecom.2005.04.018](https://doi.org/10.1016/j.elecom.2005.04.018).
- [43] S. Grolleau, A. Delaille, H. Gaulous, P. Gyan, R. Revel, J. Bernard, E. Redondo-Iglesias, J. Peter, On behalf of the SIMACL Network, Calendar aging of commercial graphite/LFP cell - Predicting capacity fade under time dependent storage conditions, *J. Power Sources*. 225 (2014) 450–458. [doi:10.1016/j.jpowsour.2013.11.098](https://doi.org/10.1016/j.jpowsour.2013.11.098).
- [44] S. Käbitz, J. B. Gerschler, M. Ecker, Y. Yurdagel, B. Emmermacher, D. André, T. Mitsch, D. Uwe Sauer, Cycle and calendar life study of a graphite|LiNi_{1/3}Mn_{1/3}Co_{1/3}O₂ Li-ion high energy system. Part A: Full cell characterization, *J. Power Sources*. 239 (2013) 572–583. [doi:10.1016/j.jpowsour.2013.03.045](https://doi.org/10.1016/j.jpowsour.2013.03.045).
- [45] J. Vetter, P. Novák, M.R. Wagner, C. Veit, K.-C. Möller, J.O. Besenhard, M. Winter, M. Wohlfahrt-Mehrens, C. Vogler, A. Hammouche, Ageing mechanisms in lithium-ion batteries, *J. Power Sources*. 145 (2005) 269–281. [doi:10.1016/j.jpowsour.2005.01.006](https://doi.org/10.1016/j.jpowsour.2005.01.006).

-
- [46] J. C. Burns, A. Kassam, N. N. Sinha, L. E. Downie, L. Solnickova, B. M. Way and J. R. Dahn, « Predicting and Extending the Lifetime of Li-Ion Batteries », *Journal of the Electrochemical Society*, vol. 160, no. 9, A1451–A1456, (2013).
- [47] M.C. Smart, B.V. Ratnakumar, S. Surampudi, Electrolytes for Low-Temperature Lithium Batteries Based on Ternary Mixtures of Aliphatic Carbonates, *J. Electrochem. Soc.*, 146 (1999), p. 486.
- [48] C.-K. Huang, J.S. Sakamoto, J. Wolfenstine, S. Surampudi, The Limits of Low-Temperature Performance of Li-Ion Cells, *J. Electrochem. Soc.*, 147 (2000), 2893 – 2896.
- [49] M. Winter, The Solid Electrolyte Interphase - The Most Important and the Least Understood Solid Electrolyte in Rechargeable Li Batteries, *Z. Phys. Chem.*, 223 (2009), 1395–1406. [doi: 10.1524.zpch.2009.6086](https://doi.org/10.1524/zpch.2009.6086).
- [50] M. Petzl, M. A. Danzer, Nondestructive detection, characterization, and qualification of lithium plating in commercial lithium ion batteries, *J. Power Sources*. 254 (2014) 80–87. [doi:10.1016/j.jpowsour.2013.12.060](https://doi.org/10.1016/j.jpowsour.2013.12.060).
- [51] M. Petzl, M. Kasper, M.A. Danzer, Lithium plating in a commercial lithium-ion battery – A low-temperature aging study, *J. Power Sources*. 275 (2015) 799–807. [doi:10.1016/j.jpowsour.2014.11.065](https://doi.org/10.1016/j.jpowsour.2014.11.065).
- [52] S. Schindler, M. Bauer, M. Petzl, M.A. Danzer., Voltage relaxation and impedance spectroscopy as in-operando methods for the detection of lithium plating on graphitic anodes in commercial lithium-ion cells, *J. Power Sources*. 304 (2016) 170-180. [doi:10.1016/j.jpowsour.2015.11.044](https://doi.org/10.1016/j.jpowsour.2015.11.044).
- [53] M. C. Smart, B. V. Ratnakumar, Effects of electrolyte composition on lithium plating in lithium-ion cells, *J. Electrochem. Soc.* 158, issue 4, (2011) A379–A389. [doi: 10.1149/1.3544439](https://doi.org/10.1149/1.3544439).
- [54] M. Wakihara, O. Yamamoto, *Lithium ion batteries: Fundamentals and Performance*, Kodansha (1998).
- [55] H. Zheng, L. Tan, L. Zhang, Q. Qu, Z. Wan, Y. Wang, M. Shen, H. Zheng, Correlation between lithium deposition on graphite electrode and the capacity loss for LiFePO₄/graphite cells, *Electrochimica Acta*. 173 (2015) 323–330. [doi:10.1016/j.electacta.2015.05.039](https://doi.org/10.1016/j.electacta.2015.05.039).
- [56] NASA Engineering and Safety Center Technical Report, NASA Aerospace Flight Battery Program, RP-08-75.
- [57] L.-E. Downie, L.-J. Krause, J.-C. Burns, L.-D. Jensen, V.-L. Chevrier and J.-R. Dahn, *In situ* detection of lithium plating on graphite electrodes by electrochemical calorimetry, *J. Electrochem. Soc.* 160, issue 4, (2013) A588–A594.

-
- [58] J.-C. Burns, D.A. Stevens and J.-R. Dahn, *In situ* detection of lithium plating using high precision coulometry, J. Electrochem. Soc. 162, issue 6, (2015) A959–A964 [doi: 10.1149/2.0621506jes](https://doi.org/10.1149/2.0621506jes).
- [59] J. Cannarella, C. B. Arnold, The effects of defects on localized plating in Lithium-ion Batteries, J. Electrochem. Soc. 162, issue 7, (2015) A1365–A1373 [doi: 10.1149/2.1051507jes](https://doi.org/10.1149/2.1051507jes).
- [60] D. Aurbach, Electrode–solution interactions in Li-ion batteries: a short summary and new insights, Journal of Power Sources 119–121 (2003) 497–503, [doi:10.1016/S0378-7753\(03\)00273-8](https://doi.org/10.1016/S0378-7753(03)00273-8)
- [61] D.P. Abraham, J. Liu, C.H. Chen, Y.E. Hyung, M. Stoll, N. Elsen, S. MacLaren, R. Twisten, R. Haasch, E. Sammann, I. Petrov, K. Amine, G. Henriksen, Diagnosis of power fade mechanisms in high-power lithium-ion cells, Journal of Power Sources 119–121 (2003) 511–516, [doi:10.1016/S0378-7753\(03\)00275-1](https://doi.org/10.1016/S0378-7753(03)00275-1)
- [62] A. Eddahech, « Modélisation du vieillissement et détermination de l'état de santé de batteries lithium-ion pour application véhicule électrique et hybride », Thèse de Doctorat - Université Bordeaux 1 (2013).
- [63] M. Maccario, « Caractérisation de nanomatériaux C-LiFePO₄ optimisés pour matériaux d'électrode positive pour batteries lithium – ion. Détermination du mécanisme de désintercalation / intercalation du lithium à partir de ces matériaux », Thèse de Doctorat - Université Bordeaux 1 (2007).
- [64] S. J. Harris, A. Timmons, D. R. Baker, C. Monroe, Direct *in situ* measurements of Li transport in Li-ion battery negative electrodes, Chemical Physics Letters 485 (2010) 265–274. [doi:10.1016/j.cplett.2009.12.033](https://doi.org/10.1016/j.cplett.2009.12.033).
- [65] C. Uhlmann, J. Illig, M. Ender, R. Schuster, E. Ivers-Tiffée, *In situ* detection of lithium metal plating on graphite in experimental cells, J. Power Sources. 279 (2015) 428-438. [doi: dx.doi.org/10.1016/j.jpowsour.2015.01.046](https://doi.org/10.1016/j.jpowsour.2015.01.046).
- [66] J. Steiger, D. Kramer, R. Mönig, Mechanisms of dendritic growth investigated by *in situ* light microscopy during electrodeposition and dissolution of lithium, J. Power Sources. 261 (2014) 112-119. [doi: doi.org/10.1016/j.jpowsour.2014.03.029](https://doi.org/10.1016/j.jpowsour.2014.03.029).
- [67] O. Crowther and A. C. West, Effect of Electrolyte Composition on Lithium Dendrite Growth, J. Electrochem. Soc. 155, issue 11, (2008) A806–A811. [doi: 10.1149/1.2969424](https://doi.org/10.1149/1.2969424).
- [68] H. Wu, D. Zhuo, D. Kong and Y. Cui, Improving battery safety by early detection of internal shorting with a bifunctional separator, Nature Communications, 5, 5193 (2014), [doi: 10.1038/ncomms6193](https://doi.org/10.1038/ncomms6193).
- [69] R. G. Lerner and G. L. Trigg, Encyclopedia of physics, VCH, New York (1991).

-
- [70] H.-P. Lin, D. Chua, M. Salomon, H.-C. Shiao, M. Hendrickson, E. Plichta et al., Low-Temperature Behavior of Li-Ion Cells, *Electrochem. Solid-State Lett.* 4, A71 534 (2001) [doi: 10.1149/1.1368736](https://doi.org/10.1149/1.1368736).
- [71] T. Waldmann, M. Kasper, and M. Wohlfahrt-Mehrens, Optimization of Charging Strategy by Prevention of Lithium Deposition on Anodes in high-energy Lithium-ion Batteries – Electrochemical Experiments, *Electrochimica Acta.* 178, 525 (2015). [doi:10.1016/j.electacta.2015.08.056](https://doi.org/10.1016/j.electacta.2015.08.056).
- [72] E. McTurk, C. R. Birkl, M. R. Roberts, D. A. Howey, and P. G. Bruce, Minimally Invasive Insertion of Reference Electrodes into Commercial Lithium-Ion Pouch Cells, *ECS Electrochem. Lett.* 4, A145 (2015). [doi: 10.1149/2.0081512eel](https://doi.org/10.1149/2.0081512eel).
- [73] T. Waldmann, B.-I. Hogg, M. Kasper, S. Grolleau, C. Gutiérrez Couceiro, K. Trad, B. Pilipili Matadi and M. Wohlfahrt-Mehrens, Interplay of Operational Parameters on Lithium Deposition in Li-ion cells: Systematic Measurements with Reconstructed 3-Electrode Pouch Full Cells, *J. Electrochem. Soc.* 163, 7, (2016) A1–A7. [doi: 10.1149/2.0591607jes](https://doi.org/10.1149/2.0591607jes).
- [74] G. Nagasubramanian, Two- and three-electrode impedance studies on 18650 Li-ion cells, *Journal of Power Sources* 87 (2000) 226–229.
- [75] J. R. Belt, D. M. Bernardi and V. Utgikar, Development and Use of a Lithium-Metal Reference Electrode in Aging Studies of Lithium-Ion Batteries, *Journal of The Electrochemical Society*, 161 (6) A1116-A1126 (2014), [doi: 10.1149/2.062406jes](https://doi.org/10.1149/2.062406jes).
- [76] E. McTurk, C. R. Birkl, M. R. Roberts, D. A. Howey and P. G. Bruce, Minimally Invasive Insertion of Reference Electrodes into Commercial Lithium-Ion Pouch Cells, *ECS Electrochemistry Letters*, 4 (12) A145-A147 (2015), [doi: 10.1149/2.0081512eel](https://doi.org/10.1149/2.0081512eel)
- [77] C. Edouard, Vieillissement des batteries Li-ion de traction : des mécanismes vers le vieillissement accéléré, Thèse de doctorat de l'Université de technologie de Compiègne, (2015)
- [78] M. Dubarry, V. Svoboda, R. Hwu, and B. Y. Liaw, Incremental Capacity Analysis and Close-to-Equilibrium OCV Measurements to Quantify Capacity Fade in Commercial Rechargeable Lithium Batteries, *Electrochemical and Solid-State Letters*, 9 (10) A454-A457 (2006), [DOI: 10.1149/1.2221767](https://doi.org/10.1149/1.2221767).
- [79] M. Dubarry, C. Truchot, B. Y. Liaw, Synthesize battery degradation modes via a diagnostic and prognostic model, *Journal of Power Sources* 219 (2012) 204-216, [DOI: 10.1016/j.jpowsour.2012.07.016](https://doi.org/10.1016/j.jpowsour.2012.07.016).
- [80] A. Devie, M. Dubarry, and B. Y. Liaw, Overcharge Study in Li₄Ti₅O₁₂ Based Lithium-Ion Pouch Cell I. Quantitative Diagnosis of Degradation Modes, *Journal of The Electrochemical Society*, 162 (6) A1033-A1040 (2015), [doi: 10.1149/2.0941506jes](https://doi.org/10.1149/2.0941506jes).

-
- [81] M. Safari and C. Delacourt, Aging of a Commercial Graphite/LiFePO₄ Cell, *Journal of The Electrochemical Society*, 158 (10) A1123-A1135 (2011), [doi: 10.1149/1.3614529](https://doi.org/10.1149/1.3614529).
- [82] X. Han, M. Ouyang, L. Lu, J. Li, Y. Zheng, Z. Li, A comparative study of commercial lithium ion battery cycle life in electrical vehicle: Aging mechanism identification, *Journal of Power Sources* 251 (2014) 38-54, <http://dx.doi.org/10.1016/j.jpowsour.2013.11.029>.
- [83] S. Torai, M. Nakagomi, S. Yoshitake, S. Yamaguchi, N. Oyama, State-of-health estimation of LiFePO₄/graphite batteries based on a model using differential capacity, *Journal of Power Sources* 306 (2016) 62-69, <http://dx.doi.org/10.1016/j.jpowsour.2015.11.070>.
- [84] Z. Ma, J. Jiang, W. Shi, W. Zhang, C. C. Mi, Investigation of path dependence in commercial lithium-ion cells for pure electric bus applications: Aging mechanism identification, *Journal of Power Sources* 274 (2015) 29-40, <http://dx.doi.org/10.1016/j.jpowsour.2014.10.006>.
- [85] M. Kassem, J. Bernard, R. Revel, S. Pélissier, F. Duclaud, C. Delacourt, Calendar aging of a graphite/LiFePO₄ cell, *Journal of Power Sources* 208 (2012) 296–305, [doi:10.1016/j.jpowsour.2012.02.068](https://doi.org/10.1016/j.jpowsour.2012.02.068)
- [86] E. Sarasketa-Zabala, I. Gandiaga, L.M. Rodriguez-Martinez, I. Villarreal, Calendar ageing analysis of a LiFePO₄/graphite cell with dynamic model validations: Towards realistic lifetime predictions, *Journal of Power Sources* 272 (2014) 45e57, <http://dx.doi.org/10.1016/j.jpowsour.2014.08.051>.
- [87] C.-K. Huang, J.S. Sakamoto, J. Wolfenstine, S. Surampudi, The Limits of Low-Temperature Performance of Li-Ion Cells, *J. Electrochem. Soc.*, 147 (2000), 2893 – 2896.
- [88] F. La Mantia, C.D. Wessells, H.D. Deshazer, Yi Cui, Reliable reference electrodes for Li-ion batteries, *Electrochemistry Communications* 31 (2013) 141–144, <http://dx.doi.org/10.1016/j.elecom.2013.03.015>.
- [89] J.L. Gómez-Cámer, P. Novák, Electrochemical impedance spectroscopy: Understanding the role of the reference electrode, *Electrochemistry Communications* 34 (2013) 208–210, <http://dx.doi.org/10.1016/j.elecom.2013.06.016>.
- [90] H. Nara, D. Mukoyama, T. Yokoshima, T. Momma and T. Osaka, Impedance Analysis with Transmission Line Model for Reaction Distribution in a Pouch Type Li-ion Battery by Using Micro Reference Electrode, *Journal of The Electrochemical Society*, 163 (3) A434-A441 (2016), [DOI: 10.1149/2.0341603jes](https://doi.org/10.1149/2.0341603jes).
- [91] M. Dollé, F. Orsini, A. S. Gozdz and J.-M. Tarascon, Development of Reliable Three-Electrode Impedance Measurements in Plastic Li-Ion Batteries, *Journal of the Electrochemical Society*, 148 (8) A851-A857 (2001), [DOI: 10.1149/1.1381071](https://doi.org/10.1149/1.1381071).

-
- [92] Y. Hamon, T. Brousse, F. Jousse, P. Topart, P. Buvat, D.M. Schleich, Aluminium negative electrode in lithium ion batteries, *Journal of Power Sources* 97-98 (2001) 185-187.
- [93] A. Braun, X-ray Studies on Electrochemical Systems: Synchrotron Methods for Energy Materials, 3.1. X-ray diffraction - p.71, Walter de Gruyter GmbH & Co KG (2017).
- [94] M. Doyle, E. Takeushi, K. M. Abraham, Rechargeable Lithium Batteries: Proceedings of the International Symposium, p.233, The Electrochemical Society (2001).
- [95] Y. Avigal, lithium- lithium tetrachloroaluminate reference electrode in thionyl chloride, *J. Electroanal. Chem.*, 76 (1977) 135—138.
- [96] Z. Zeng, W.-I Liang, H.-G. Liao, H. L. Xin, Y.-H. Chu and H. Zheng, Visualization of Electrode–Electrolyte Interfaces in LiPF₆/EC/DEC Electrolyte for Lithium Ion Batteries via in Situ TEM, *Nano Lett.* (2014), 14, 1745–1750, [dx.doi.org/10.1021/nl403922u](https://doi.org/10.1021/nl403922u).
- [97] M. Yao, K. Okuno, T. Iwaki, M. Kato, S. Tanase, K. Emura, T. Sakai, LiFePO₄-based electrode using micro-porous current collector for high power lithium ion battery, *Journal of Power Sources* 173 (2007) 545–549, [doi:10.1016/j.jpowsour.2007.08.014](https://doi.org/10.1016/j.jpowsour.2007.08.014).
- [98] Myth and Reality about the Origin of Inductive Loops in Impedance Spectra of Li-ion Electrodes —A Critical Experimental Approach, *Electrochimica Acta* 207 (2016) 218 – 223, <http://dx.doi.org/10.1016/j.electacta.2016.03.126>.
- [99] E. Barsoukov, J. R. Macdonald, Impedance Spectroscopy Theory, Experiment, and Applications, 4.4.6. Corrosion Mechanisms p.359-381, John Wiley & Sons, Inc., Hoboken, New Jersey, (2005).
- [100] V. V. Elkin, A. I. Marshakov, A. A. Rybkina, and M. A. Maleeva, Interpretation of the Impedance Comprising Negative Capacitance and Constant Phase Elements on Iron Electrode in Weakly Acidic Media, *Russian Journal of Electrochemistry*, (2011), Vol. 47, No. 2, pp. 136–146, [DOI: 10.1134/S1023193511020054](https://doi.org/10.1134/S1023193511020054)
- [101] R. Arrabal, A. Pardo, M.C. Merino, M. Mohedano, P. Casajús, K. Paucar, G. Garcés, Effect of Nd on the corrosion behaviour of AM50 and AZ91D magnesium alloys in 3.5 wt.% NaCl solution, *Corrosion Science* 55 (2012) 301–312, [doi:10.1016/j.corsci.2011.10.033](https://doi.org/10.1016/j.corsci.2011.10.033)
- [102] H.-G. Schweiger, O. Obeidi, O. Komesker, A. Raschke, M. Schiemann, C. Zehner, M. Gehnen, M. Keller and P. Birke, Comparison of Several Methods for Determining the Internal Resistance of Lithium Ion Cells, *Sensors* 2010, 10, 5604-5625; [doi:10.3390/s100605604](https://doi.org/10.3390/s100605604).

-
- [103] B.V. Ratnakumar, M.C. Smart, L.D. Whitcanack, R.C. Ewell, The impedance characteristics of Mars Exploration Rover Li-ion batteries, *Journal of Power Sources* 159 (2006) 1428–1439, [doi:10.1016/j.jpowsour.2005.11.085](https://doi.org/10.1016/j.jpowsour.2005.11.085).
- [104] A. Samba, N. Omar, H. Gualous, Y. Firouz, P.V. den Bossche, J. V. Mierlo, Tala I. Boubekour, Development of an Advanced Two-Dimensional Thermal Model for Large size Li-ion Pouch Cells, *Electrochimica Acta* 117 (2014) 246– 254, <http://dx.doi.org/10.1016/j.electacta.2013.11.113>
- [105] S. Goutam, J.-M. Timmermans, N. Omar, P. V. den Bossche and J. Van Mierlo, Comparative Study of Surface Temperature Behavior of Commercial Li-Ion Pouch Cells of Different Chemistries and Capacities by Infrared Thermography, *Energies* 2015, 8, 8175-8192; [doi:10.3390/en8088175](https://doi.org/10.3390/en8088175).
- [106] M. Muratori, Thermal Characterization of Li-ion battery cell, Politecnico Di Milano, Facoltà di Ingegneria Industriale, Anno Accademico 2008 – 2009.
- [107] <http://mat4bat.eu/>
- [108] M. Klett, R. Eriksson, J. Groot, P. Svens, K. C. Högström, R. W. Lindström, H. Berg, T. Gustafson, G. Lindbergh, K. Edström, Non-uniform aging of cycled commercial LiFePO₄/graphite cylindrical cells revealed by post-mortem analysis, *Journal of Power Sources* 257 (2014) 126-137, <http://dx.doi.org/10.1016/j.jpowsour.2014.01.105>
- [109] T. Waldmann, M. Wilka, M. Kasper, M. Fleischhammer, M. Wohlfahrt-Mehrens, Temperature dependent ageing mechanisms in Li-ion batteries - A Post-Mortem study, *Journal of Power Sources* 262 (2014) 129-135, <http://dx.doi.org/10.1016/j.jpowsour.2014.03.112>
- [110] Y. Kobayashi, T. Kobayashi, K. Shono, Y. Ohno, Y. Mita and H. Miyashiro, Decrease in Capacity in Mn-Based/Graphite Commercial Li-ion Batteries, I. Imbalance Proof of Electrode Operation Capacities by Cell Disassembly, *Journal of The Electrochemical Society*, 160 (8) A1181-A1186 (2013), [DOI: 10.1149/2.071308jes](https://doi.org/10.1149/2.071308jes)
- [111] J. C. Burns, D. A. Stevens, and J. R. Dahn, In-Situ Detection of Lithium Plating Using High Precision Coulometry, *Journal of The Electrochemical Society*, 162 (6) A959-A964 (2015), [DOI: 10.1149/2.0621506jes](https://doi.org/10.1149/2.0621506jes)
- [112] R. Kostecky, J. Lei, F. McLarnon, J. Shim and K. Striebel, Diagnostic Evaluation of Detrimental Phenomena in High-Power Li-ion Batteries, *Journal of The Electrochemical Society*, 153 (4) A669-A672 (2006), [DOI: 10.1149/1.2170551](https://doi.org/10.1149/1.2170551).
- [113] N. Williard, B. Sood, M. Osterman and M. Pecht, Disassembly methodology for conducting failure analysis on lithium-ion batteries, *J Mater Sci: Mater Electron* (2011) 22:1616–1630, [DOI 10.1007/s10854-011-0452-4](https://doi.org/10.1007/s10854-011-0452-4).

-
- [114] D. Aurbach, B. Markovsky, A. Rodkin, M. Cojocaru, E. Levi, H.-J Kim, An analysis of rechargeable Li-ion batteries after prolonged cycling, *Electrochimica Acta* 00 (2002) 1 – 13.
- [115] Q. Wang, J. Sun, X. Yao, C. Chen, Thermal stability of LiPF₆/EC + DEC electrolyte with charged electrodes for lithium ion batteries, *Thermochimica Acta* 437 (2005) 12–16, [doi:10.1016/j.tca.2005.06.010](https://doi.org/10.1016/j.tca.2005.06.010).
- [116] T. Waldmann, A. Iturrondobeitia, M. Kasper, N. Ghanbari, F. Aguesse, E. Bekaert, L. Daniel, S. Geniès, I. Jimenez Gordon, M. W. Loble, E. De Vito and M. Wohlfahrt-Mehrens, Review—Post-Mortem Analysis of Aged Li-ion Batteries: Disassembly Methodology and Physico-Chemical Analysis Techniques, *J. Power Sources*. 163 (2016) A2149-A2164. [doi: 10.1149/2.1211609jes](https://doi.org/10.1149/2.1211609jes).
- [117] D.P. Abraham, J.L. Knuth, D.W. Dees, I. Bloom, J.P. Christophersen, Performance degradation of high-power Li-ion cells - Electrochemistry of harvested electrodes, *Journal of Power Sources* 170 (2007) 465–475, [doi:10.1016/j.jpowsour.2007.03.071](https://doi.org/10.1016/j.jpowsour.2007.03.071).
- [118] L. Somerville, J. Bareño, P. Jennings, A. McGordon, C. Lyness, I. Bloom, The Effect of Pre-Analysis Washing on the Surface Film of Graphite Electrodes, *Electrochimica Acta* 206 (2016) 70–76, <http://dx.doi.org/10.1016/j.electacta.2016.04.133>.
- [119] T. Waldmann, M. Kasper, M. Wohlfahrt-Mehrens, Optimization of Charging Strategy by Prevention of Lithium Deposition on Anodes in high-energy Li-ion Batteries – Electrochemical Experiments, *Electrochimica Acta* 178 (2015) 525–532, <http://dx.doi.org/10.1016/j.electacta.2015.08.056>.
- [120] G. Gachot, P. Ribièrè, D. Mathiron, S. Grugeon, M. Armand, J.-B. Leriche, S. Pilard and S. Laruelle, Gas Chromatography/Mass Spectrometry As a Suitable Tool for the Li-Ion Battery Electrolyte Degradation Mechanisms Study, *Anal. Chem.* (2011), 83, 478–485
- [121] G. Gachot, S. Grugeon, I. Jimenez-Gordon, G. G. Eshetu, S. Boyanov, A. Lecocq, G. Marlair, S. Pilarde and S. Laruelle, Gas chromatography/Fourier transform infrared/mass spectrometry coupling: a tool for Li-ion battery safety field investigation, *Anal. Methods*, (2014), 6, 6120, [DOI: 10.1039/c4ay00054d](https://doi.org/10.1039/c4ay00054d)
- [122] M. Grütze, V. Kraft, B. Hoffmann, S. Klamor, J. Diekmann, A. Kwade, M. Winter, S. Nowak, Aging investigations of a Li-ion battery electrolyte from a field-tested hybrid electric vehicle, *Journal of Power Sources* 273 (2015) 83-88, <http://dx.doi.org/10.1016/j.jpowsour.2014.09.064>
- [123] Kazuma Kumai), Hajime Miyashiro, Yo Kobayashi, Katsuhito Takei, Rikio Ishikawa, Gas generation mechanism due to electrolyte decomposition in commercial Li-ion cell, *Journal of Power Sources* 81–82 (1999) 715–719.

-
- [124] R. G. Lerner and G. L. Trigg, *Encyclopedia of physics*, VCH, New York (1991).
- [125] H. Honbo, K. Takei, Y. Ishii, T. Nishida, Electrochemical properties and Li deposition morphologies of surface modified graphite after grinding, *J. Power Sources*. 189 (2009) 337–343. <https://doi.org/10.1016/j.jpowsour.2008.08.048>.
- [126] F. Lin, I. M. Markus, M. M. Doeff and H. L. Xin, Chemical and Structural Stability of Li-ion Battery Electrode Materials under Electron Beam, *Scientific Reports* | 4 : 5694 | [DOI: 10.1038/srep05694](https://doi.org/10.1038/srep05694)
- [127] Y. Shao-Horn, Chapter 16 - Understanding phase transformations in lithium battery materials by transmission electron microscopy, *Science and Technology of Lithium Batteries – Kluwer Academic Publishers (2003)* Eds. Nazri, G. A. N. & Pistoia G. P. 478
- [128] Y. Shao-Horn, L. Croguennec, C. Delmas, E. C. Nelson & M. A. O'Keefe, Atomic resolution of lithium ions in LiCoO₂, *Nature Materials* 2, 464-467 (2003), [doi:10.1038/nmat922](https://doi.org/10.1038/nmat922).
- [129] F. Wang, S.-W. Kim, L. Wu, D. Su, Y. Zhu, and J. Graetz, *In Situ* TEM-EELS for Tracking Lithium Reactions in Battery Electrodes, *Microsc. Microanal.* 19 (Suppl 2), 2013, [doi:10.1017/S1431927613009446](https://doi.org/10.1017/S1431927613009446).
- [130] M. T. Janish, *In-situ TEM Lithiation of Alternative Battery Electrode Materials*, University of Connecticut, 2017.
- [131] S. J. Harris, R. D. Deshpande, Y. Qi, I. Dutta, Y.T. Cheng , Mesopores inside electrode particles can change the Li-ion transport mechanism and diffusion-induced stress, *J. Mater. Res.*, 25, 1433 (2010).
- [132] M. Zier, F. Scheiba, S. Oswald, J. Thomas, D. Goers, T. Scherer, M. Klose, H. Ehrenberg, J. Eckert, Lithium dendrite and solid electrolyte interphase investigation using OsO₄, *Journal of Power Sources* 266 (2014) 198-207, <http://dx.doi.org/10.1016/j.jpowsour.2014.04.134>
- [133] Y. Kramer, C. Birkenmaier, J. Feinauer, A. Hintennach, C. L. Bender, M. Meiler, V. Schmidt, R. E. Dinnebier and T. Schleid, A New Method for Quantitative Marking of Deposited Lithium by Chemical Treatment on Graphite Anodes in Li-ion Cells, *Chem. Eur. J.* (2015), 21, 6062 – 6065, <http://dx.doi.org/10.1002/chem.201406606>.
- [134] M. Klett, P. Svens, C. Tengstedt, A. Seyeux, J. Światowska, G. Lindbergh and R. W. Lindström, Uneven Film Formation across Depth of Porous Graphite Electrodes in Cycled Commercial Li-Ion Batteries, *J. Phys. Chem. C* (2015), 119, 90–100, [dx.doi.org/10.1021/jp509665e](https://doi.org/10.1021/jp509665e).
- [135] ThermoFisher Scientific, Detecting Li with EDS, October 2014, <https://tools.thermofisher.com/content/sfs/brochures/WS52730-Detecting-Lithium-EDS.pdf>

-
- [136] P.N. Ross, Catalysis and Interfacial Chemistry in Lithium Batteries: A Surface Science Approach, *Catal Lett* (2014) 144:1370–1376 [DOI 10.1007/s10562-014-1287-4](https://doi.org/10.1007/s10562-014-1287-4)
- [137] T. Kajita, R. Yuge, K. Nakahara, J. Iriyama, H. Takahashi, R. Kasahara, T. Numata, S. Serizawa and K. Utsugi, Deterioration Analysis in Cycling Test at High Temperature of 60°C for Li-Ion Cells Using SiO Anode, *Journal of The Electrochemical Society*, 161 (5) A708-A711 (2014), [DOI: 10.1149/2.042405jes](https://doi.org/10.1149/2.042405jes)
- [138] G. Kilibarda, S. Schlabach, V. Winkler, M. Bruns, T. Hanemann, D.V. Szabó, Electrochemical performance of tin-based nano-composite electrodes using a vinylene carbonate-containing electrolyte for Li-ion cells, *Journal of Power Sources* 263 (2014) 145e153, <http://dx.doi.org/10.1016/j.jpowsour.2014.04.030>
- [139] B. Ziv, V. Borgel, D. Aurbach, J.-H. Kim, X. Xiao and B. R. Powell, Investigation of the Reasons for Capacity Fading in Li-Ion Battery Cells, *Journal of The Electrochemical Society*, 161 (10) A1672-A1680 (2014), [DOI: 10.1149/2.0731410jes](https://doi.org/10.1149/2.0731410jes)
- [140] Y. Zheng, Y.-B. He, K. Qian, B. Li, X. Wang, J. Li, C. Miao, F. Kang, Effects of state of charge on the degradation of LiFePO₄/graphite batteries during accelerated storage test, *Journal of Alloys and Compounds* 639 (2015) 406–414, <http://dx.doi.org/10.1016/j.jallcom.2015.03.169>
- [141] L. Boulet-Roblin, M. El Kazzi, P. Novak and C. Villevieille, Surface/Interface Study on Full xLi₂MnO₃·(1 - x)LiMO₂ (M = Ni, Mn, Co)/Graphite Cells, *Journal of The Electrochemical Society*, 162 (7) A1297-A1300 (2015), [DOI: 10.1149/2.0491507jes](https://doi.org/10.1149/2.0491507jes)
- [142] R. Castaing, P. Moreau, Y. Reynier, D. Schleich, S. Jouanneau Si Larbi, D. Guyomard, N. Dupré, *Electrochimica Acta*, 155, 391 (2015), <http://dx.doi.org/10.1016/j.electacta.2014.12.049>.
- [143] W.-C. Oh, ⁷Li-NMR and Thermal Analysis for Lithium Inserted into Artificial Carbon Material, *Bull. Korean Chem. Soc.* 2001, Vol. 22, No. 4.
- [144] C. L. Campion, W. Li and B.L. Lucht, Thermal Decomposition of LiPF₆-Based Electrolytes for Li-ion Batteries, *Journal of the Electrochemical Society*, 152 (12) A2327-A2334 (2005), [DOI: 10.1149/1.2083267](https://doi.org/10.1149/1.2083267).
- [145] W. Li and Brett L. Lucht, Li-ion Batteries: Thermal Reactions of Electrolyte with the Surface of Metal Oxide Cathode Particles, *Journal of The Electrochemical Society*, 153 (8) A1617-A1625 (2006), [DOI: 10.1149/1.2210588](https://doi.org/10.1149/1.2210588).
- [146] I. Buchberger, S. Seidlmayer, A. Pokharel, M. Piana, J. Hattendorff, P. Kudejova, R. Gilles and H. A. Gasteiger, Aging Analysis of Graphite/LiNi_{1/3}Mn_{1/3}Co_{1/3}O₂ Cells Using XRD, PGAA, and AC Impedance, *J. Electrochem. Soc.* 162, issue 14, (2015) A2737–A2746. [doi: 10.1149/2.0721514jes](https://doi.org/10.1149/2.0721514jes).

-
- [147] S.-C. Yin, Y.-H. Rho, I. Swainson and L. F. Nazar, X-ray/Neutron Diffraction and Electrochemical Studies of Lithium De/Re-Intercalation in $\text{Li}_{1-x}\text{Co}_{1/3}\text{Ni}_{1/3}\text{Mn}_{1/3}\text{O}_2$ ($x = 0 \rightarrow 1$), *Chem. Mater.* (2006), 18, 1901-1910.
- [148] J. Choi, A. Manthiram, Role of Chemical and Structural Stabilities on the Electrochemical Properties of Layered $\text{LiNi}_{1/3}\text{Mn}_{1/3}\text{Co}_{1/3}\text{O}_2$ Cathodes, *J. Electrochem. Soc.* 152, issue 9, (2005) A1714–A1718. [doi: 10.1149/1.1954927](https://doi.org/10.1149/1.1954927).
- [149] D.-C. Li, T. Muta, L.-Q. Zhang, M. Yoshio, H. Noguchi, Effect of synthesis method on the electrochemical performance of $\text{LiNi}_{1/3}\text{Mn}_{1/3}\text{Co}_{1/3}\text{O}_2$ Cathodes, *J. Power Sources.* 132 (2004) 150-155. [doi: 10.1016/j.jpowsour.2004.01.016](https://doi.org/10.1016/j.jpowsour.2004.01.016).
- [150] C.G. Marxer, M. L. Kraft, P. K. Weber, I. D. Hutcheon and S. G. Boxer, Supported Membrane Composition Analysis by Secondary Ion Mass Spectrometry with High Lateral Resolution, *Biophysical Journal* Volume 88 April (2005) 2965–2975.
- [151] E. Peled, D. Bar Tow, A. Merson, and L. Burstein, Microphase structure of SEI on HOPG, *Journal of New Materials for Electrochemical Systems*, 3, 321-328 (2000).
- [152] E. Peled, D. Bar Tow, A. Merson, A. Gladkikh, L. Burstein and D. Golodnitsky, Composition, depth profiles and lateral distribution of materials in the SEI built on HOPG-TOF SIMS and XPS studies, *Journal of Power Sources*, 97-98 (2001) 52-57.
- [153] A. Bordes, E. De Vito, C. Haon, A. Boulineau, A. Montani, P. Marcus, Multiscale Investigation of Silicon Anode Li Insertion Mechanisms by Time-of-Flight Secondary Ion Mass Spectrometer Imaging Performed on an In Situ Focused Ion Beam Cross Section, *Chem. Mater.*, 2016, 28 (5), pp 1566–1573, [DOI: 10.1021/acs.chemmater.6b00155](https://doi.org/10.1021/acs.chemmater.6b00155).
- [154] T. Waldmann, M. Wilka, M. Kasper, M. Fleischhammer, M. Wohlfahrt-Mehrens, Temperature dependent ageing mechanisms in Lithium-ion batteries - A Post-Mortem study, *Journal of Power Sources* 262 (2014) 129-135, <http://dx.doi.org/10.1016/j.jpowsour.2014.03.112>.
- [155] K. Amine, J. Liu, I. Belharouak, High-temperature storage and cycling of C-LiFePO₄/graphite Li-ion cells, *Electrochemistry communications*, (2005), 7, 669-673. [doi:10.1016/j.elecom.2005.04.018](https://doi.org/10.1016/j.elecom.2005.04.018).
- [156] S. Grolleau, A. Delaille, H. Gaulous, P. Gyan, R. Revel, J. Bernard, E. Redondo-Iglesias, J. Peter, On behalf of the SIMACL Network, Calendar aging of commercial graphite/LFP cell - Predicting capacity fade under time dependent storage conditions, *J. Power Sources.* 225 (2014) 450–458. [doi:10.1016/j.jpowsour.2013.11.098](https://doi.org/10.1016/j.jpowsour.2013.11.098).
- [157] S. Käbitz, J. B. Gerschler, M. Ecker, Y. Yurdagel, B. Emmermacher, D. André, T. Mitsch, D. Uwe Sauer, Cycle and calendar life study of a graphite| $\text{LiNi}_{1/3}\text{Mn}_{1/3}\text{Co}_{1/3}\text{O}_2$ Li-ion high energy system. Part A: Full cell characterization, *J. Power Sources.* 239 (2013) 572–583. [doi:10.1016/j.jpowsour.2013.03.045](https://doi.org/10.1016/j.jpowsour.2013.03.045).

-
- [158] M. Ecker, J. B. Gerschler, J. Vogel, S. Käbitz, F. Hust, P. Dechent, D. Uwe Sauer, Development of a lifetime prediction model for lithium-ion batteries based on extended accelerated aging test data, *J. Power Sources*. 215 (2012) 248–257. [doi:10.1016/j.jpowsour.2012.05.012](https://doi.org/10.1016/j.jpowsour.2012.05.012).
- [159] K. Amine, C.H. Chen, J. Liu, M. Hammond, A. Jansen, D. Dees, I. Bloom, D. Vissers, G. Henriksen, Factors responsible for impedance rise in high power lithium-ion batteries, *J. Power Sources*. 97-98 (2001) 684–687
- [160] A. Friesen, F. Horsthemke, X. Monnighoff, G. Brunklaus, R. Krafft, M. Borner, T. Risthaus, M. Winter, F. M. Schappacher, Impact of cycling at low temperatures on the safety behavior of 18650-type lithium ion cells: Combined study of mechanical and thermal abuse testing accompanied by post-mortem analysis, *Journal of Power Sources* 334 (2016) 1-11, [doi : http://dx.doi.org/10.1016/j.jpowsour.2016.09.120](http://dx.doi.org/10.1016/j.jpowsour.2016.09.120).
- [161] J. Fan and S.Tan, Studies on Charging Lithium-Ion Cells at Low Temperatures, *Journal of The Electrochemical Society*, 153 (6) A1081-A1092 (2006), [doi: 10.1149/1.2190029](https://doi.org/10.1149/1.2190029).
- [162] V. Zinth, C. Von Lüders, M. Hofmann, J. Hattendorff, I. Buchberger, S. Erhard, J. Rebelo-Kornmeier, A. Jossen, Ralph Gilles, Lithium plating in lithium-ion batteries at sub-ambient temperatures investigated by in situ neutron diffraction, *Journal of Power Sources* 271 (2014) 152-159, <http://dx.doi.org/10.1016/j.jpowsour.2014.07.168>.
- [163] T. Waldmann, M. Wohlfahrt-Mehrens, Effects of rest time after Li plating on safety behavior—ARC tests with commercial high-energy 18650 Li-ion cells, *Electrochimica Acta* 230 (2017) 454–460, <http://dx.doi.org/10.1016/j.electacta.2017.02.036>.
- [164] W. Bao, J. Wan, X. Han, X. Cai, H. Zhu, D. Kim, D. Ma, Y. Xu, J. N. Munday, H. D. Drew, M. S. Fuhrer and L. Hu, Approaching the limits of transparency and conductivity in graphitic materials through lithium intercalation, *Nature Communications*, |5:4224| (2014). [doi: 10.1038/ncomms5224](https://doi.org/10.1038/ncomms5224).
- [165] Y. Qi and S. J. Harris, In Situ Observation of Strains during Lithiation of a Graphite Electrode, *J. Power Sources*. 157 (2010) A741-A747. [doi: 10.1149/1.3377130](https://doi.org/10.1149/1.3377130).
- [166] C. Uhlmann , J. Illig, M. Ender, R. Schuster, E. Ivers-Tiffée, In situ detection of lithium metal plating on graphite in experimental cells, *J. Power Sources*. 259 (2015) 428-438. [doi: 10.1016/j.jpowsour.2015.01.046](https://doi.org/10.1016/j.jpowsour.2015.01.046).
- [167] X.-L. Wang, K. An, L. Cai, Z. Feng, S. E. Nagler, C. Daniel, K. J. Rhodes, A. D. Stoica, H. D. Skorpenske, C. Liang, W. Zhang, J. Kim, Y. Qi and S. J. Harris, Visualizing the chemistry and structure dynamics in lithium-ion batteries by in-situ neutron diffraction, *Scientific Reports*. (2012) |2:747| [doi: 10.1038/srep00747](https://doi.org/10.1038/srep00747).

-
- [168] H. Honbo, K. Takei, Y. Ishii, T. Nishida, Electrochemical properties and Li deposition morphologies of surface modified graphite after grinding, *Journal of Power Sources* 189 (2009) 337–343 [doi:10.1016/j.jpowsour.2008.08.048](https://doi.org/10.1016/j.jpowsour.2008.08.048).
- [169] M. Nie, J. Demeaux, B. T. Young, D. R. Heskett, Y. Chen, A. Bose, J. C. Woicik and B. L. Lucht, Effect of Vinylene Carbonate and Fluoroethylene Carbonate on SEI Formation on Graphitic Anodes in Li-Ion Batteries, *Journal of The Electrochemical Society*, 162 (13) A7008-A7014 (2015), [doi: 10.1149/2.0021513jes](https://doi.org/10.1149/2.0021513jes).
- [170] I. Buchberger, S. Seidlmayer, A. Pokharel, M. Piana, J. Hattendorff, P. Kudejova, R. Gilles and H. A. Gasteiger, Aging Analysis of Graphite/LiNi_{1/3}Mn_{1/3}Co_{1/3}O₂ Cells Using XRD, PGAA, and AC Impedance, *J. Electrochem. Soc.* 162, issue 14, (2015) A2737–A2746. [doi: 10.1149/2.0721514jes](https://doi.org/10.1149/2.0721514jes).
- [171] S.-C. Yin, Y.-H. Rho, I. Swainson and L. F. Nazar, X-ray/Neutron Diffraction and Electrochemical Studies of Lithium De/Re-Intercalation in Li_{1-x}Co_{1/3}Ni_{1/3}Mn_{1/3}O₂ (x = 0 → 1), *Chem. Mater.* (2006), 18, 1901-1910.
- [172] J. Choi, A. Manthiram, Role of Chemical and Structural Stabilities on the Electrochemical Properties of Layered LiNi_{1/3}Mn_{1/3}Co_{1/3}O₂ Cathodes, *J. Electrochem. Soc.* 152, issue 9, (2005) A1714–A1718. [doi: 10.1149/1.1954927](https://doi.org/10.1149/1.1954927).
- [173] D.-C. Li, T. Muta, L.-Q. Zhang, M. Yoshio, H. Noguchi, Effect of synthesis method on the electrochemical performance of LiNi_{1/3}Mn_{1/3}Co_{1/3}O₂ Cathodes, *J. Power Sources*. 132 (2004) 150-155. [doi: 10.1016/j.jpowsour.2004.01.016](https://doi.org/10.1016/j.jpowsour.2004.01.016) .
- [174] N. Yabuuchi, Y. Makimura and T. Ohzuku, Solid-State Chemistry and Electrochemistry of LiCo_{1/3}Ni_{1/3}Mn_{1/3}O₂ for Advanced Lithium-Ion Batteries. III. Rechargeable Capacity and Cycleability, *J. Electrochem. Soc.* 154, issue 4, (2007) A314–A321. [doi: 10.1149/1.2455585](https://doi.org/10.1149/1.2455585).
- [175] A. M. Rodriguez, D. Ingersoll, and D. H. Doughty, *Adv. X-Ray Anal.*, 45, 182 (2002).
- [176] B. Zhang, M. Metzger, S. Solchenbach, M. Payne, S. Meini, H.A. Gasteiger, A. Garsuch, B.L. Lucht, Role of 1,3-propane sultone and vinylene carbonate in solid electrolyte interface formation and gas generation, *J. Phys. Chem, C* (2015), 119, 11337-11348. [doi: 10.1021/acs.jpcc.5b00072](https://doi.org/10.1021/acs.jpcc.5b00072).
- [177] G. Gachot, S. Grugeon, M. Armand, S. Pilard, P. Guenet, J-M. Tarascon and S. Laruelle, Deciphering the multi-step degradation mechanisms of carbonate-based electrolyte in Li batteries, *J. Power Sources*. 178 (2008) 409–421. [doi: 10.1016/j.jpowsour.2007.11.110](https://doi.org/10.1016/j.jpowsour.2007.11.110).
- [178] H. Kim, S. Grugeon, G. Gachot, M. Armand, L. Sannier, and S. Laruelle, Ethylene bis-carbonates as telltales of SEI and electrolyte health, role of carbonate type and new additives, *Electrochimica Acta*. 136 (2014) 157–165. [doi:10.1016/j.electacta.2014.05.072](https://doi.org/10.1016/j.electacta.2014.05.072).

-
- [179] Y. Zhang, A-Q. Zhang, Y-H. Gui, L-Z. Wang, X.-B. Wu, C.-F. Zhang, P. Zhang, Application of biphenyl additive in electrolyte for liquid state Al-plastic film lithium-ion batteries, *Journal of Power Sources* 185 (2008) 492–500, [doi:10.1016/j.jpowsour.2008.07.001](https://doi.org/10.1016/j.jpowsour.2008.07.001)
- [180] S. J. An, J. Li, C. Daniel, D. Mohanty, S. Nagpure, D. L. Wood III, The state of understanding of the lithium-ion-battery graphite solid electrolyte interphase (SEI) and its relationship to formation cycling, *Carbon* 105 (2016) 52-76, <http://dx.doi.org/10.1016/j.carbon.2016.04.008>
- [181] Professor Jeff Dahn – Win Seminar Series, Waterloo Institute of Nanotechnology, 42' – 45', <https://www.youtube.com/watch?v=9qi03QawZEK>
- [182] W.-C. Oh, 7Li-NMR and Thermal Analysis for Lithium Inserted into Artificial Carbon Material, *Bull. Korean Chem. Soc.* 2001, Vol. 22, No. 4.
- [183] C. Xu, T. Gustadsson, K. Edström, D. Brandell and M. Hahlin, Interface layer formation in solid polymer electrolyte lithium batteries: an XPS study, *J. Mater. Chem. A*, 2014, 2, 7256-7264.
- [184] R. A. Quinlan, Y.-C. Lu, D. Kwabi, Y. Shao-Horn and A. N. Mansour, XPS Investigation of the Electrolyte Induced Stabilization of LiCoO₂ and “AlPO₄”-Coated LiCoO₂ Composite Electrodes, *Journal of The Electrochemical Society*, 163 (2) A300-A308 (2016), [doi:10.1149/2.0851602jes](https://doi.org/10.1149/2.0851602jes).
- [185] V. Eshkenazi, E. Peled, L. Burstein, D. Golodnitsky, XPS analysis of the SEI formed on carbonaceous materials, *Solid State Ionics* 170 (2004) 83–91.
- [186] M. Lu, H. Cheng, Y. Yang, A comparison of solid electrolyte interphase (SEI) on the artificial graphite anode of the aged and cycled commercial lithium ion cells, *Electrochimica Acta* 53 (2008) 3539–3546.
- [187] H. Liu, Q. Xu, C. Yan, Y. Qiao, Corrosion behavior of a positive graphite electrode in vanadium redox flow battery, *Electrochimica Acta* 56 (2011) 8783– 8790.
- [188] C.N. Taylor, J.P. Allain, B. Heim, P.S. Krstic, C.H. Skinner, H.W. Kugel, Surface chemistry and physics of deuterium retention in lithiated graphite, *Journal of Nuclear Materials* 415 (2011) S777–S780.
- [189] X-G. Yang, Y. Leng, G. Zhang, S. Ge, C-Y. Wang, Modeling of lithium plating induced aging of lithium-ion batteries: Transition from linear to nonlinear aging, *Journal of Power Sources* 360 (2017) 28-40, <http://dx.doi.org/10.1016/j.jpowsour.2017.05.110>
- [190] M. Ecker, N. Nieto, S. Käbitz, J. Schmalstieg, H. Blanke, A. Warnecke, D. Uwe Sauer, Calendar and cycle life study of Li(NiMnCo)O₂-based 18650 lithium-ion batteries, *J. Power Sources*. 248 (2014) 839–851.

-
- [191] P. Keil, S. F. Schuster, J. Wilhem, J. Travi, A. Hauser, R. C. Karl and A. Jossen, Calendar Aging of Lithium-Ion Batteries I. Impact of the Graphite Anode on Capacity Fade, *J. Electrochem. Soc.* 163, 9, (2016) A1872–A1880. [doi: 10.1149/2.0411609jes](https://doi.org/10.1149/2.0411609jes)
- [192] K. Amine, J. Liu, I. Belharouak, High-temperature storage and cycling of C-LiFePO₄/graphite Li-ion cells, *Electrochemistry communications*, (2005), 7, 669-673. [doi:10.1016/j.elecom.2005.04.018](https://doi.org/10.1016/j.elecom.2005.04.018).
- [193] S. Grolleau, A. Delaille, H. Gaulous, P. Gyan, R. Revel, J. Bernard, E. Redondo-Iglesias, J. Peter, On behalf of the SIMACL Network, Calendar aging of commercial graphite/LFP cell - Predicting capacity fade under time dependent storage conditions, *J. Power Sources*. 225 (2014) 450–458. [doi:10.1016/j.jpowsour.2013.11.098](https://doi.org/10.1016/j.jpowsour.2013.11.098).
- [194] S. Käbitz, J. B. Gerschler, M. Ecker, Y. Yurdagel, B. Emmermacher, D. André, T. Mitsch, D. Uwe Sauer, Cycle and calendar life study of a graphite|LiNi_{1/3}Mn_{1/3}Co_{1/3}O₂ Li-ion high energy system. Part A: Full cell characterization, *J. Power Sources*. 239 (2013) 572–583. [doi:10.1016/j.jpowsour.2013.03.045](https://doi.org/10.1016/j.jpowsour.2013.03.045).
- [195] M. Ecker, J. B. Gerschler, J. Vogel, S. Käbitz, F. Hust, P. Dechent, D. Uwe Sauer, Development of a lifetime prediction model for lithium-ion batteries based on extended accelerated aging test data, *J. Power Sources*. 215 (2012) 248–257. [doi:10.1016/j.jpowsour.2012.05.012](https://doi.org/10.1016/j.jpowsour.2012.05.012).
- [196] K. Jalkanen, J. Karppinen, L. Skogström, T. Laurila, M. Nisula and K. Vuorilehto Cycle aging of commercial NMC/graphite pouch cells at different temperatures, *Applied Energy*. 154 (2015) 160–172.
- [197] N. Nagasubramanian, Comparison of the thermal and electrochemical properties of LiPF₆ and Li(SO₂C₂F₅)₂ salts in organic electrolytes, *J. Power Sources*. 119-121 (2003) 811–814. [doi:10.1016/S0378-7753\(03\)00246-5](https://doi.org/10.1016/S0378-7753(03)00246-5).
- [198] S.S. Zhang, K. Xu and T.R. Jow, A thermal stabilizer for LiPF₆-based electrolytes of Li-ion cells, *Electrochemical and Solid-State Letters*, (2002), 5 (9), A206–A208. [doi: 10.1149/1.1499669](https://doi.org/10.1149/1.1499669).
- [199] D. J. Xiong, R. Petibon, M. Nie, L. Ma, J. Xia and J. R. Dahn, Interactions between Positive and Negative Electrodes in Li-Ion Cells Operated at High Temperature and High Voltage, *Journal of The Electrochemical Society*, 163 (3) A546-A551 (2016), [doi: 10.1149/2.0951603jes](https://doi.org/10.1149/2.0951603jes).
- [200] R. Bhattacharyya, B. Key, H. Chen, A. S. Best, A. F. Hollenkamp and C. P. Grey, In situ NMR observation of the formation metallic lithium microstructures in lithium batteries, *Nature materials*. (2010), vol.9, 504-510. [doi:10.1038/NMAT2764](https://doi.org/10.1038/NMAT2764).
- [201] J. Arai, Y. Okada, T. Sugiyama, M. Izuka, K. Gotoh, and K. Takeda, In Situ Solid State ⁷Li NMR Observations of Lithium Metal Deposition during Overcharge in

Lithium Ion Batteries, J. Electrochem. Soc. 162, issue 6, (2015) A952-A958. [doi:10.1149/2.0411506jes](https://doi.org/10.1149/2.0411506jes).

[202] M. Fleischhammer, T. Waldmann, G. Bisle, B-I. Hogg and M. Wohlfahrt-Mehrens, Interaction of cyclic aging at high-rate and low temperatures and safety in lithium-ion batteries, J. Power Sources. 274 (2015) 432–439. [doi:10.1016/j.jpowsour.2014.08.135](https://doi.org/10.1016/j.jpowsour.2014.08.135).

[203] A. H. Zimmerman and M. V. Quinzio, Lithium Plating in Lithium-Ion Cells, The Aerospace Corporation, NASA Battery Workshop, 16-18 November 2010 Huntsville, AL

[204] D. Anseán, M. Dubarry, A. Devie, B.Y. Liaw, V.M. García, J.C. Viera, M. Gonzalez, Operando lithium plating quantification and early detection of a commercial LiFePO₄ cell cycled under dynamic driving schedule, Journal of Power Sources 356 (2017) 36-46, <http://dx.doi.org/10.1016/j.jpowsour.2017.04.072>

[205] J. Wang, P. Liu, J. Hicks-Garner, E. Sherman, S. Soukiazian, M. Verbrugge, H. Tatara, J. Musser, P. Finamore, Cycle-life model for graphite-LiFePO₄ cells, Journal of Power Sources 196 (2011) 3942–3948, [doi:10.1016/j.jpowsour.2010.11.134](https://doi.org/10.1016/j.jpowsour.2010.11.134).

[206] M. Petit, E. Prada, V. Sauvant-Moynot, Development of an empirical aging model for Li-ion batteries and application to assess the impact of Vehicle-to-Grid strategies on battery lifetime, Applied Energy 172 (2016) 398–407, <http://dx.doi.org/10.1016/j.apenergy.2016.03.119>

[207] I. Baghdadi, O. Briat, J.-Y. Delétage, P. Gyan, J.-M. Vinassa, Lithium battery aging model based on Dakin's degradation approach, Journal of Power Sources 325 (2016) 273-285, <http://dx.doi.org/10.1016/j.jpowsour.2016.06.036>

[208] G. Kaneko, S. Inoue, K. Taniguchi, T. Hirota, Y. Kamiya, Y. Daisho, S. Inami, Analysis of Degradation Mechanism of Lithium Iron Phosphate Battery, The 27th International Electric Vehicle Symposium & Exhibition, Barcelona, Spain, 17th – 20th November (2013)

[209] M. Broussely, S. Herreyre, P. Biensan, P. Kasztejna, K. Nechev, R. J. Staniewicz, Aging mechanism in Li ion cells and calendar life predictions, Journal of Power Sources 97-98 (2001) 13-21.

[210] S. Grolleau, A. Delaille, H. Gualous, P. Gyan, R. Revel, J. Bernard, E. Redondo-Iglesias, J. Peter, Calendar aging of commercial graphite/LiFePO₄ cell - Predicting capacity fade under time dependent storage conditions, Journal of Power Sources 255 (2014) 450-458. <http://dx.doi.org/10.1016/j.jpowsour.2013.11.098>

[211] C. Delacourt, C. Ades, Q. Badey, Vieillessement des accumulateurs Li-ion dans l'automobile, Techniques de l'ingénieur, RE231 (2014).

[212] C. Delacourt and M. Safari, Life Simulation of a Graphite/LiFePO₄ Cell under Cycling and Storage, *Journal of the Electrochemical Society*, **159** (8) A1283-A1291 (2012), [DOI: 10.1149/2.049208jes](https://doi.org/10.1149/2.049208jes)

[213] M.T. Todinov, Necessary and sufficient condition for additivity in the sense of the Palmgren-Miner rule, *Computational Materials Science* 21 (2001) 101-110.

[214] B. Y. Liaw, E. P. Roth, R. G. Jungst, G. Nagasubramanian, H. L. Case, and D. H. Doughty, "Correlation of arrhenius behaviors in power and capacity fades with cell impedance and heat generation in cylindrical lithium-ion cells," *Journal of Power Sources*, vol. 119, pp. 874–886, (2005), [doi:10.1016/S0378-7753\(03\)00196-4](https://doi.org/10.1016/S0378-7753(03)00196-4)

[215] J. Jiang, W. Shi, J. Zheng, P. Zuo, J. Xiao, X. Chen, W. Xu and J.-G. Zhang, Optimized Operating Range for Large-Format LiFePO₄/Graphite Batteries, *Journal of The Electrochemical Society*, 161 (3) A336-A341 (2014), [DOI: [10.1149/2.052403jes](https://doi.org/10.1149/2.052403jes)]

[216] X-G. Yang, Y. Leng, G. Zhang, S. Ge, C-Y. Wang, Modeling of lithium plating induced aging of lithium-ion batteries: Transition from linear to nonlinear aging, *Journal of Power Sources* 360 (2017) 28-40, <http://dx.doi.org/10.1016/j.jpowsour.2017.05.110>

[217] A. Marongiu, N. Nlandi, Y. Rong, D. U. Sauer, On-board capacity estimation of lithium iron phosphate batteries by means of half-cell curves, *Journal of Power Sources* 324 (2016) 158-169, <http://dx.doi.org/10.1016/j.jpowsour.2016.05.041>

[218] C. R. Birkl, M. R. Roberts, E. McTurk, P. G. Bruce, D. A. Howey, Degradation diagnostics for lithium ion cells, *Journal of Power Sources* 341 (2017) 373-386, <http://dx.doi.org/10.1016/j.jpowsour.2016.12.011>.

[219] Y. Tian, B. Xia, M. Wang, W. Sun and Z. Xu, Comparison Study on Two Model-Based Adaptive Algorithms for SOC Estimation of Lithium-Ion Batteries in Electric Vehicles, *Energies* 2014, 7, 8446-8464; [doi:10.3390/en7128446](https://doi.org/10.3390/en7128446)

[220] X. Zhang, Y. Wang, D. Yang, Z. Chen, Behavior data of battery and battery pack SOC estimation under different working conditions, *Data in Brief* 9 (2016) 737–740, <https://doi.org/10.1016/j.dib.2016.10.012>.



Abstract

In order to deepen the understanding of the aging mechanisms of Li-ion batteries, post-mortem investigations were performed on C/NMC Li-ion commercial cells. These autopsies revealed unexpected degradations that question current knowledge about the aging mechanisms of these cells. Thus, it appears that the parasitic reaction of Li metal depositions on the graphite electrode, nowadays associated in the literature with charging at low temperature and / or high C-rates, would have various origins depending on the chemistry and conditions of use of the battery. In this thesis work, local Li deposits were observed on cells aged in calendar at high temperatures, due to the apparition of dry areas. Paradoxically, under low temperature cycling conditions, this Li resulted from anode porosity hindrance. Besides, a semi-empirical aging model, taking into account cycling losses as well as those caused by the SEI growth and the biphenyl polymerization, is proposed. Finally, a method of identifying degradation modes using incremental capacity measurements has been undertaken, based on the potential shifts of each of the electrodes.

Keywords

Li deposition; Pore clogging; Reference electrode into commercial cell; Biphenyl; Aging modeling; Incremental capacity; Loss of Li inventory; Loss of active material.

Résumé

Afin d'approfondir la compréhension des mécanismes de vieillissement des batteries Li-ion, des analyses post-mortem ont été effectuées sur des cellules commerciales Li-ion C/NMC. Ces autopsies ont révélé des dégradations inattendues qui remettent en question les connaissances actuelles sur les mécanismes de vieillissement de ces cellules. Ainsi, il semble que la réaction parasite des dépôts de Li métallique sur l'électrode en graphite, actuellement associée dans la littérature à des charges à basses températures et / ou à courants élevés, aurait diverses origines selon la chimie et les conditions d'utilisation de la batterie. Dans ce travail de thèse, des dépôts locaux de Li métallique ont été observés sur des cellules vieilles en calendrier à haute température. Paradoxalement, dans des conditions de cyclage à basse température, ce dépôt de Li métallique a résulté de la perte de porosité au niveau de l'électrode négative. Par ailleurs, un modèle de vieillissement semi-empirique, prenant compte les pertes en cyclage ainsi que celles causées par la croissance de la SEI et la polymérisation du biphényle, est proposé. Pour finir, une méthode d'identification des modes de dégradation grâce à des mesures de capacité incrémentale a été entreprise, sur la base du décalage des potentiels de chacune des électrodes.

Mots clés

Dépôts de Li ; Blocage des pores ; Electrode de référence dans une cellule commerciale ; Biphényle ; Modélisation de vieillissement ; Capacité incrémentale ; Perte de Li cyclable ; Perte de matière active.